Spatio-temporal analysis of the turbulent boundary layer and an investigation of the effects of periodic disturbances

Thesis by

Jeffrey Allen LeHew

In Partial Fulfillment of the Requirements

for the Degree of

Doctor of Philosophy

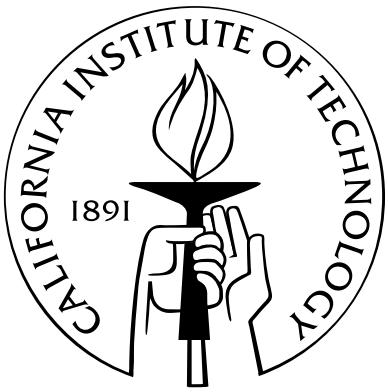

California Institute of Technology

Pasadena, California

2012

(Defended May 1, 2012)

© 2012
Jeffrey Allen LeHew
All Rights Reserved

Acknowledgements

I would like to begin by thanking my advisor, Beverley McKeon, for her guidance and support of my research for the past five years. I have thoroughly enjoyed my time in her research group and feel that I have grown tremendously as a researcher under her guidance.

I would also like to thank both my candidacy and thesis committee members: Tim Colonius, Mory Gharib, Dale Pullin, and Ravi Ravichandran for taking time to review and discuss my research.

A large portion of the experimental work for this thesis was performed in collaboration with Dr. Michele Guala. Michele taught me a great deal about performing PIV experiments and was extremely helpful both in setting up and running the experiments. I am also appreciative of his comments and feedback on my work and analysis of the PIV results.

I would also like to thank Prof. Haecheon Choi at Seoul National University for hosting me for a two-month stay to perform research in his lab. I am also appreciative of his group members who helped me with my experiments and living arrangements during my stay. In particular I would like to thank Jooha Kim for taking care of my housing, cell phone, and much more, as well as Hongwon Lee, Hoon Lee, and Duho Je for their help with the experimental setup.

I am appreciative of the aeroshop staff for their work on several experimental setups. Also, thanks to Petros Arakelian for producing the rough surface I used in this work and Prof. Chiara Daraio for allowing me to use her group's 3D printer for this purpose.

Last, but not least, I would like to thank all of my friends at Caltech for their inspiration. In particular I would like to thank Ian Jacobi for making the office an entertaining place to work and for all of our discussions on research as well as non-academic topics. I would especially like to thank Toni Lee for her support of my research as well as being a great person in general. Finally, I would like to thank my family for their kindness and support over the years.

Support for this research through the Air Force Office of Scientific Research under award # FA9550-09-1-0701, as well as from the National Science Foundation through the EAPSI fellowship, was greatly appreciated.

Abstract

The purpose of this study was to investigate the turbulent boundary layer to learn more about the dynamics of the flow and how it might be controlled through the input of spatially and/or temporally periodic disturbances. The first part of this work studies the structure of a zero-pressure-gradient turbulent boundary layer using time-resolved particle image velocimetry in both wall-normal and wall-parallel planes. Using data from wall-parallel measurements, a 3D spectrum over streamwise, spanwise, and temporal wavelengths was constructed for the first time, a major focus of this work. Among several uses, this spectrum allows the calculation of a scale-based convection velocity, that is, a convection velocity for each streamwise-spanwise scale pair present in the flow. This data set also provided a method for investigating the temporal evolution of coherent structures in the flow, of which, swirling coherent structures (SCS), indicative of vortices, and low-momentum regions were investigated thoroughly. The convection velocity and lifetime of the SCS were measured; using histograms of the SCS convection velocity in multiple wall-parallel planes, it was possible to statistically infer different SCS structures that could be categorized as "attached" or "detached" from the wall.

A study was also performed on the response of the turbulent boundary layer to a stationary periodic roughness inspired by the scale pattern on the sailfish. The roughness was relatively sparse with element spacing on the order of the boundary layer thickness allowing the measurement of turbulent statistics at different points along the roughness as well as below the crests of the roughness elements, a region not commonly accessible in rough-wall boundary layer studies. The streamwise turbulent statistics were studied using hotwire anemometry from which it was found that while the outer part of the flow remained similar, the near-wall region was perturbed by structures of size similar to the roughness spacing.

Contents

List of Figures

List of Tables

List of Variables

$\overline{(\,)}$	Mean value
$\hat{(\,)}$	Estimate
$\tilde{(\,)}$	Small-scale envelope
$\breve{(\,)}$	Measured value
$\acute{(\,)}$	Tilted coordinate system
$(\,)^+$	Inner scaled quantity
$(\,)^*$	Complex conjugate
$(\,)'$	Value of a conditional average about the conditioned point
$(\,)^A$	Average over the laser sheet thickness
$<\ >$	Ensemble average
$(\,) \star (\,)$	Convolution
∇u	Velocity gradient tensor
Γ	Circulation
Δ	Discriminant of the velocity gradient tensor
ΔU^+	Hama roughness function
Δh	Peak-to-peak displacement of the IPMC
Δt	Time between measurements
Δx, Δy, Δz	Streamwise, wall-normal, and spanwise spacing between vectors for PIV data
Δx_T	Spacing calculated using Taylor's hypothesis ($\Delta x_T = \overline{U}(y)\Delta t$)
Θ	Phase angle spectrum
$\Lambda_{c,i}$	Signed swirling strength
Ξ	Attenuation correction for velocity spectrum
Π	Wake strength
$\Psi(i,j)$	Inferred vortex structure that exists between planes y_i and y_j
Ω	Anti-symmetric part of the velocity gradient tensor

α	Vortex inclination angle
β	Cutoff for identifying low-momentum regions
γ	Convection velocity ratio
δ	Boundary layer thickness based on 99% of the free-stream velocity
δ^*	Displacement thickness
δ_0	Incoming boundary layer thickness (δ just upstream of the roughness)
δ_ν	Viscous length (ν/u_τ)
ϵ	Eccentricity of an ellipse
θ	Momentum thickness
θ_t	Vortex trajectory angle
θ_y	Vortex yaw angle
κ	Kármán constant
λ	Eigenvalue
λ_2	Second eigenvalue of the pressure Hessian
$\lambda_{c,i}$	Imaginary part of the complex eigenvalue of ∇u (swirling strength)
$\lambda_{c,r}$	Real part of the complex eigenvalue of ∇u
λ_x, λ_z	Streamwise and spanwise wavelength
ν	Kinematic viscosity
ξ, ζ	Separation/shift in the streamwise and spanwise directions
ρ	Density
τ	Separation/shift in time
τ_L	Temporal window length
τ_w	Shear stress at the wall
ϕ	Power spectrum
ω	Circular frequency
ω_{cut}	Low-pass filter cutoff frequency
ω_y	Wall-normal vorticity

A	Area
B, C	Log law additive constants
C_f	Coefficient of friction
E	Event vector
F	Force
$H(i)$	Histogram for plane y_i
K	Acceleration parameter $(\nu/U_\infty^2(dU_\infty/dx))$
L_D	Distance from the leading edge to the center of the measurement region
L_{LF}	The streamwise length of the large field of view
L_{SF}	The streamwise length of the small field of view
L_{ij}	Coupling coefficient for LSE
L_x	The streamwise length of the measurement window or of a coherent structure
L_y	The wall-normal height of the measurement window
L_z	The spanwise width of the measurement window or of a coherent structure
M	Magnitude spectrum
P, Q, R	Invariants of the velocity gradient tensor
R	Correlation coefficient
Re_θ	Momentum thickness Reynolds number $(\theta U_\infty/\nu)$
Re_τ	Friction Reynolds number $(\delta u_\tau/\nu)$
S	Symmetric part of the velocity gradient tensor
T	Temporal wavelength
T_E	Eddy turnover time (δ/U_∞)
T_L	Vortex lifetime
T_M	Total measurement time
U, V, W	Instantaneous streamwise, wall-normal, and spanwise velocities
U_∞	Free-stream velocity
U_L	Large-scale streamwise velocity signal
U_S	Small-scale streamwise velocity signal
U_c	Convection velocity of a particular streamwise and/or spanwise scale
U_{core}	Vortex convection velocity calculated from the average velocity in the core
U_{traj}	Vortex convection velocity calculated from the vortex trajectory
W_I	Interrogation window size
$W_c(y/\delta)$	Coles wake function

a, b	Major and minor axes of an ellipse
d	Diameter
e	Virtual origin offset
f	Frequency
f_c	Maximum flow frequency ($u_\tau^3/3\nu$)
g_H	3D Hann window
h_d	Displacement relative to position at $t = 0$
h_m	Mean displacement over one cycle relative to the position at $t = 0$
k	Roughness height
k_{cut}	Cutoff wavenumber at which the spectrum is attenuated by 2dB
k_s	Equivalent sand grain roughness height
k_x, k_z	Streamwise and spanwise wavenumbers
l	Length of the hotwire probe
l_t	Laser sheet thickness
p	Probability density function (pdf)
r	Radius
r_{eq}	Equivalent radius ($\sqrt{A/\pi}$)
s_{avg}	Average spacing between roughness elements
t	Time
t_ν	Viscous time scale (ν/u_τ^2)
u, v, w	Streamwise, wall-normal, and spanwise velocity fluctuations
u_τ	Friction velocity ($\sqrt{\tau_w/\rho}$)
u_c	Convection velocity of a particular streamwise and/or spanwise scale with the local mean velocity subtracted
u_{core}	Vortex convection velocity calculated from the average velocity in the core with the local mean velocity subtracted
u_{traj}	Vortex convection velocity calculated from the vortex trajectory with the local mean velocity subtracted
v_n	Out-of-plane velocity
w_g	Gaussian weighting
x, y, z	Streamwise, wall-normal, and spanwise directions
x_{90}	Fraction of time to reach 90% of the maximum displacement

List of Abbreviations

2D2C	2 dimensions and 2 components
CCW	Counter clockwise
CW	Clockwise
DAQ	Data acquisition (board)
DIC	Digital image correlation
IPMC	Ionic polymer-metal composite
LF	Large field of view
LM	Low momentum
LSE	Linear stochastic estimate
LSM	Large-scale motion
PIV	Particle image velocimetry
POD	Proper orthogonal decomposition
SCS	Swirling coherent structure
SF	Small field of view
SG	Savitzky-Golay (filter)
TBL	Turbulent boundary layer
VLSM	Very large scale motion
WN	Wall normal
WP	Wall parallel
ZPG	Zero-pressure gradient
jpdf	Joint probability density function
pdf	Probability density function
rms	Root mean square

Chapter 1

Introduction

1.1 Motivation

High-Reynolds-number wall-bounded shear flows are of intrinsic interest as they are ubiquitous in industrial applications from the boundary layers that form over the surfaces of airplanes, automobiles, ships, and submarines to those which form inside of piping systems. At high Reynolds numbers, these flows become fully turbulent, the skin friction drag imparted increases compared to the laminar case, and they exhibit what, at first glance, appears to be random fluctuations in the velocity field. Careful analysis of these flows show that there is a structure to these velocity fluctuations and they are linked to a cycle of production, transport, and dissipation of turbulent energy. The goal of this work is to gain a deeper understanding of this flow structure and use this knowledge to try and control turbulence. To reach this goal, the dynamics of the turbulent boundary layer are treated as a black box as proposed by Clauser [1956]. Knowing the base state, perturbing the boundary layer, in this case with a spatially and/or temporally periodic perturbation, and observing the changes to the flow, one can back out the effects of these perturbations and tailor them to meet the control objective.

The first part of this work is a study of the canonical zero-pressure-gradient turbulent boundary layer which will act as the base flow. This flow is investigated using time-resolved particle image velocimetry (PIV) in both wall-normal and wall-parallel planes. With this data set, the streamwise and spanwise velocity fluctuations measured in wall-parallel planes can be fully decomposed into a spectrum over streamwise, spanwise, and temporal wavelengths, essentially a decomposition into traveling waves. This decomposition is a new contribution of this work and provides a complete map of the energy in the flow for a given wall-normal location (note that the variation of the velocity statistics in the wall-normal direction makes a Fourier decomposition in the wall-normal direction difficult to interpret). In addition, with the interpretation of the flow as a composition of traveling waves, the convection velocity of various streamwise and spanwise velocity scales in the flow can be analyzed.

This data set also provides information about coherent structure in the flow, where the focus is on swirling coherent structures (SCS) and low-momentum regions associated with Reynolds stress production, and thus regions important for sustaining turbulence. The current data set allows the unique analysis of the lifetime of these structures and also allows the investigation of their evolution in time, both of which have been difficult to study up until now either due to difficulty in performing the experiments or in the computational costs to draw statistically significant conclusions.

With these new insights into the structure of the turbulent boundary layer, a perturbation of the boundary layer in the form of a spatially periodic roughness (in streamwise and spanwise extent) was considered. For simplicity, comparisons between the rough and smooth wall flows were only made using temporal records of the streamwise velocity component measured using hotwire anemometry. With this, the alteration of the streamwise velocity statistics, including the mean and rms velocity profiles as well as the change in the structure of the streamwise velocity spectrum, was studied.

1.2 Background

The literature on turbulent shear flows and, more specifically, wall-bounded turbulent shear flows, which are of interest in the current investigation, is quite vast, but the underlying concepts as well as recent advances will be briefly reviewed to place this research into context.

Note that in the work to follow, the streamwise, wall-normal and spanwise directions are denoted by x, y, and z, respectively. Similarly, the streamwise, wall-normal, and spanwise velocities are denoted by U, V, and W, respectively, where capital letters indicate instantaneous velocities and lower case letters indicate a fluctuation about the local mean.

1.2.1 Canonical wall-bounded shear flows

In order to understand the dynamics of turbulence in wall-bounded shear flows, canonical cases are studied to try and eliminate as many complicating factors as possible. There are three different canonical wall-bounded shear flows generally studied: flow in a circular pipe, flow through a low aspect ratio rectangular channel producing a 2D flow over a majority of the span, and a zero-pressure-gradient boundary layer formed over a flat plate, which is the focus of the present research. In these canonical cases, the surface is smooth, the flow is neutrally buoyant, nonreacting, and is, in general, not perturbed in any way. The general structure of these canonical wall-bounded shear flows are reviewed in classical texts such as Townsend [1976] and Tennekes and Lumley [1972].

An important feature of wall-bounded shear flows is that the flow dynamics depend on two different sets of length and time scales, where the dominance of one scaling over the other depends on the distance from the wall. Near the wall, viscosity is dominant and thus viscous velocity, length, and time scales can be defined. The viscous velocity scale is called the friction velocity, $u_\tau = \sqrt{\tau_w/\rho}$,

where ρ is the density and τ_w is the shear stress at the wall, the viscous length scale is $\delta_\nu = \nu/u_\tau$, where ν is the kinematic viscosity, and the viscous time scale $t_\nu = \nu/u_\tau^2$. Normalization by these quantities is termed "inner" scaling and is denoted by a '+' superscript. The profile of the mean streamwise velocity, $\overline{U}$, near the wall scales according to the "law of the wall", given in Eqn. 1.1, and is "a unique and universal similarity law for every turbulent flow past a smooth surface" [Coles, 1956].

$$\overline{U}^+ = f(y^+) \tag{1.1}$$

The region very near the wall, below a wall-normal distance $y^+ \approx 5$, is called the viscous sublayer and is dominated by the effect of viscosity. The velocity profile is linear here and follows $\overline{U}^+ = y^+$. Immediately above this region is the buffer layer, between about $5 < y^+ < 100$, which is the most active part of the flow where the local turbulence production is the highest.

Far from the wall, viscosity is no longer dominant and the length scale of importance is the outer scale, namely the boundary layer thickness, δ. This is called the "wake region". Due to the thin-layer approximation of the momentum equation, the order of magnitude of the Reynolds stress across the boundary layer is limited by u_τ^2, and thus u_τ is a global velocity scale [Jiménez, 2004], that is, it is important both near and far from the wall. The outer part of the mean velocity profile is determined by the "Defect law" given in Eqn. 1.2, where U_∞ is the free-stream velocity and Π is the wake strength.

$$U_\infty^+ - \overline{U}^+ = F(\Pi, y/\delta) \tag{1.2}$$

At intermediate distances from the wall, if the scale separation is large enough, that is the friction Reynolds number (a.k.a. Kármán number) $Re_\tau = \delta^+ = \delta u_\tau/\nu >> 1$, there exists an inertial sublayer where both δ and δ_ν provide a collapse of the mean velocity profile. Here, the only unique length scale is y, the wall-normal distance, and it follows that the velocity varies logarithmically with y [Millikan, 1938]. This region is aptly named the "log layer" and takes the form of Eqn. 1.3 for inner scaled variables or Eqn. 1.4 for outer scaled variables.

$$\overline{U}^+ = \frac{1}{\kappa}\ln(y^+) + B \tag{1.3}$$

$$\overline{U}^+ - U_\infty^+ = \frac{1}{\kappa}\ln(y/\delta) + C \tag{1.4}$$

The variables κ, B, and C are thought to be universal constants, although recent work by Nagib and Chauhan [2008] shows variations in these constants between the three canonical cases as well as variations with Reynolds number, particularly at lower Reynolds numbers. For the purposes of this

work, the widely used values of the Karman constant, $\kappa = 0.41$ and the additive constant, $B = 5.0$ are taken [Nagib and Chauhan, 2008]. The log layer extends from about $100 \leq y^+ \leq 0.12\delta$, above which is the "wake region". The log and wake regions can be written as one unified profile as given in Eqn. 1.5.

$$\overline{U}^+ = \frac{1}{\kappa}\ln(y^+) + B + \frac{\Pi}{\kappa}W_c\left(\frac{y}{\delta}\right) \tag{1.5}$$

This equation was derived by Coles [1956] and is termed the "law of the wake", where $W_c(y/\delta)$ is a universal function, called the Coles wake function, that is closely approximated by a sine squared function.

Less is known theoretically about the statistics of the velocity fluctuations about the mean. Even the appropriateness of u_τ, U_∞, or some other velocity scaling for the collapse of the fluctuation profiles near the wall is not apparent. A thorough review of data on this topic for the zero-pressure-gradient turbulent boundary layer up until 1996 is provided by Fernholz and Finley [1996].

In a spectral sense, there has been a recent focus on large scales, where a large scale is one whose streamwise coherence is equal to or larger than the boundary layer thickness, δ. These large-scale motions are of interest due to the large amount of turbulent kinetic energy they contain. As discussed by Balakumar and Adrian [2007] in a study of the zero-pressure-gradient boundary layer, streamwise scales longer than 3δ in streamwise extent at all wall-normal locations and Reynolds numbers studied contained at least 40% of the turbulent kinetic energy and at least 30% of the Reynolds shear stress. These scales can become quite large and were found to extend up to 14 times the pipe radius in experiments by Kim and Adrian [1999]. These large scales are present in all of the canonical flows and are grouped into two categories, the large-scale motions (LSMs) with an energetic peak at $\lambda_x/\delta = 2-3$ and the very large scale motions (VLSMs) or superstructures[1], with an energetic peak at $\lambda_x/\delta = 6-10$ as discussed by Hutchins and Marusic [2007], Monty et al. [2009], and Guala et al. [2011], where λ_x is the streamwise wavelength.

In addition to their energy content, recent work by Mathis et al. [2009a] has shown that large scales in the flow modulate the activity of small-scale velocity fluctuations throughout the boundary layer. By applying a low-pass filter to the velocity signal, the large-scale velocity signal can be extracted. When compared to the envelope of the small scales, found using the Hilbert transform in the work of Mathis et al. [2009a], a large positive correlation between the two signals is found near the wall. This indicates that even the small-scale fluctuations in the flow are dependent on the large-scale activity. Being that these large scales are so important, care is required to recover these features in both space and time, as in the experiments of Dennis and Nickels [2008]. In experiments or simulations, measurements must be taken over a large enough domain and/or for a long enough

[1] In the literature, the term superstructure is generally used to refer to structures in the zero pressure gradient boundary layer of size $\lambda_x/\delta = 6$ while the VLSM is generally used for internal flows for structures of size $\lambda_x/\delta = 10$

time to accurately capture the signature of these scales.

While the work of Dennis and Nickels [2008] focused on one wall-parallel plane at $y/\delta = 0.16$, it is of interest to study the varying dynamics both closer to the wall (in the buffer region) and further from the wall (in the wake region). Similarly, it would be of interest to further investigate the applicability of Taylor's hypothesis [Taylor, 1938] which states that the spatial field can be reconstructed from temporal information if the convection velocities of the individual eddies or scales which compose the flow are known. This conversion is performed assuming the eddies are "frozen", or in other words, that their shape does not evolve significantly over the distance projected. Generally, this assumption is used to convert temporal data, such as single-point hotwire measurements, to spatial data using the local mean velocity in order to infer the streamwise coherence of velocity fluctuations. Several studies have shown that this is not always a valid assumption [Morrison et al., 1971, Kim and Hussain, 1993, Krogstad et al., 1998, del Álamo and Jiménez, 2009, Chung and McKeon, 2010, LeHew et al., 2010], with a strong scale dependence generally found near the wall. Recent work by Monty and Chong [2009] compared channel flow computations and experiments under the same conditions and showed explicitly that spatial velocity spectra from computations and temporal velocity spectra from experiments agree well as long as a scale-dependent convection velocity is imposed near the wall.

In addition to statistical measures, coherent structures observed in the turbulent boundary layer are also of interest. One prevalent structure is called the hairpin vortex originally proposed by Theodorsen [1952]. Simulations of hairpins in a turbulent flow by Zhou et al. [1999] were used to study the possibility of the auto-generation of packets of these hairpin vortices, a formation often observed in turbulent boundary layers. Wu and Christensen [2006] studied the distribution of the heads of hairpin vortices in wall-normal planes generally finding a higher density closer to the wall with most existing in the log layer. These heads were found to convect at the local mean velocity on average, with the distribution of convection velocities widening with increasing turbulence intensity, and thus decreasing distance from the wall. These findings agree with those of Carlier and Stanislas [2005] and Stanislas et al. [2008], both of whom extensively studied the shape and conditional flow fields around these structures. Extensive measurements of the inclination angle and other tilting angles of hairpin vortices were made using two-plane stereo PIV by Ganapathisubramani et al. [2006], who confirmed an average inclination angle around 45^o. Furthermore, they were able to classify vortices into forward and backward leaning types, with a decrease of forward leaning vortices away from the wall, as well as identify the shape of the head (Λ or Ω shaped), giving new interpretations to previous planar PIV velocity fields. Gao et al. [2011] analyzed both the data of Ganapathisubramani et al. [2006] as well as DNS data sets to again show the prevalence of forward leaning vortices, where it was much more common to have portions of a vortex that were backward leaning as opposed to a fully backward leaning vortex. Furthermore, they found that the vortices actually convected slightly

slower than the local mean on average (96-98% of the local mean) throughout the boundary layer with stronger vortices convecting slower than weaker ones.

Hairpin vortices are often observed in packets, as shown by Adrian et al. [2000], consisting of regions of uniform low-momentum fluid between the legs of streamwise-aligned hairpin vortices. A series of low Reynolds number experiments showed that these packets are often 1–2δ in streamwise extent, are found often (75% of the 1.2δ long flow fields from Adrian et al. [2000] included at least one uniform momentum region), and contain vortices convecting at similar speeds with a dispersion less than 7% of the free-stream velocity (and can thus be called coherent) [Adrian et al., 2000]. Additional wall-parallel measurements by Tomkins and Adrian [2003] showed that these packets generally extend 2δ or more in the streamwise direction and 0.1–0.4δ in spanwise extent, with size increasing away from the wall. In addition, the spanwise growth mechanism for vortex packets was proposed to be via a merging of adjacent packets, yet, to date, there is no time-resolved study to prove or disprove this hypothesis. In addition to their prevalence, Ganapathisubramani et al. [2003] found that hairpin packets contain a significant amount of the total Reynolds stress and thus may be important in sustaining turbulence.

1.2.2 Rough-wall turbulent boundary layers

A wealth of information exists on rough-wall flows and the review by Jiménez [2004] condenses several decades worth of information. The roughness of interest here is one in which $\delta/k >> 1$, where k is the roughness height, such that the roughness does not disrupt the boundary layer assumption (i.e., the flow remains similar to the smooth wall case outside a thin layer near the wall). In this case, the effect of the roughness on the mean profile is simply to shift the logarithmic region by some amount ΔU^+, called the Hama roughness function [Hama, 1954], such that the log law is governed by Eqn. 1.6.

$$\overline{U}^+ = \frac{1}{\kappa}\ln(y^+) + B - \Delta U^+ \tag{1.6}$$

Another effect of the roughness is to obscure the origin of the wall-normal coordinate, y, such that it exists some distance e, the virtual origin offset, below the crests of the roughness, where e is chosen to best fit the logarithmic velocity profile. To make comparisons to other studies, an equivalent sand grain roughness, k_s, can be calculated by comparing to the careful experiments of Nikuradse [1933], who fit the velocity profile in Eqn. 1.7 to his data, from which the equivalent sand grain roughness can be calculated as in Eqn. 1.8.

$$\overline{U}^+ = \frac{1}{\kappa}\ln(y/k_s) + 8.5 + \frac{\Pi}{\kappa}W_c\,(y/\delta) \tag{1.7}$$

$$k_s^+ = \exp[\kappa(\Delta U^+ + 8.5 - B)] \tag{1.8}$$

To have a flow such that $\delta/k >> 1$, Flack et al. [2005] suggest $\delta/k_s > 40$ while Jiménez [2004] suggests $\delta/k > 50$ as another limit for experimental design since k_s is not known a priori (the relationship between k and k_s is unknown and must be found by experimental measurements). Under these conditions, the flow outside the roughness sublayer (a distance of a few roughness heights, k, above the roughness) is identical to the smooth wall flow, known as Townsend's Reynolds number similarity hypothesis [Townsend, 1976]. This is traditionally interpreted as the flow far from the rough wall being influenced only by the change in u_τ associated with the roughness. Other experiments by Flack et al. [2007] in the turbulent boundary layer show that even large roughnesses whose roughness sublayer extends beyond the log layer, where they define the roughness sublayer as $y > 5k$ or $y > 3k_s$, do not affect the outer layer similarity. They suggest an even more lenient limit on the maximum roughness height of $\delta/k > 19$ or $\delta/k_s > 5.5$.

For roughnesses with an equivalent sand grain roughness, $k_s^+ \leq 5$, there is no discernible effect of the roughness on the flow and the roughness is considered hydrodynamically smooth. On the other end, once the roughness reaches a height $k_s^+ \geq 50$ or so, the flow becomes fully rough; that is the ratio between the effective sand grain roughness and the actual roughness height becomes independent of the roughness Reynolds number, k_s^+. In this case, the near-wall cycle centered in the buffer region is fully disrupted by the roughness [Jiménez, 2004] and the roughness elements develop turbulent wakes, which create an essentially inviscid drag on the surface [Tennekes and Lumley, 1972]. The intermediate range $5 \leq k_s^+ \leq 50$ is considered a "transitional roughness" where the offset of the boundary layer and the relationship between k and k_s is affected by both the roughness Reynolds number and roughness geometry.

Considering the effect of roughness on the structure of the flow, Wu and Christensen [2010] studied a non-ideal industrial-type roughness using proper orthogonal decomposition (POD) and found that the main difference between rough- and smooth-wall flows was a disruption of large coherent structures. It was found that the coherence of the first few modes containing 50% of the turbulent energy was shortened in streamwise extent by the presence of roughness. This was true for modes of the streamwise, spanwise, and wall-normal velocity. On the other hand, the modes containing the other 50% of the turbulent energy looked almost identical over both smooth and rough surfaces.

Considering the effects of a sparse roughness, the hotwire experiments by Monty et al. [2011] showed an attenuation of the largest scales in the streamwise velocity spectrum up to and including the log layer using a small (k^+ = 7–22, $\delta/k > 400$) and sparse roughness. There was also evidence of the existence of a near-wall cycle, similar to the smooth wall, when measurements were taken

between spanwise rows of elements. Measurements behind elements did not show this feature.

The effect of the inclination angle of a periodic roughness was studied by Schultz and Flack [2009]. By systematically varying the height and inclination angle of a close-packed pyramid-type roughness, they found that depending on how steep the roughness was, a different scaling existed between the offset of the velocity profile and the roughness height, and thus the conversion from k_s to k. It was concluded that for steep elements (22^o and 45^o), the drag imposed by the roughness was dominated by the form drag caused by flow separation around the roughness elements. In these cases, the shift of the mean velocity profile scaled on the roughness height. For shallow angles (11^o), the separation was less severe and skin friction dominated leading to a scaling of the shift in the mean velocity profile based on the roughness slope or waviness.

Hong et al. [2011] studied the same roughness elements as Schultz and Flack [2009] with a 16° inclination angle using PIV and were able to investigate the periodic variation of the flow along the roughness as well as the flow beneath the crests of the roughness elements. The periodic variation of flow properties did not extend much more than 2 k from the crests of the roughness elements, but eddies on the order of the roughness height were present throughout the flow.

While the effect of roughness is generally to increase the drag on a surface compared to a smooth condition, certain roughnesses can actually reduce the drag. Riblets, streamwise v-shaped grooves with a small amplitude and spanwise spacing inspired by the tiny grooves found on shark skin [Reif, 1985], can reduce the skin friction imparted by a turbulent boundary layer by as much as 8% when compared to a smooth surface in a narrow range of flow conditions [Walsh, 1982]. The mechanism proposed to explain the drag reduction is a displacement of quasi-streamwise counter-rotating vortex pairs (vortices with their axis of rotation aligned with the bulk fluid flow) away from the wall, thus limiting their interaction to the small area at the tips of the riblets [Choi et al., 1993]. Also motived by the potential for a bio-inspired drag reducing surface, Sagong et al. [2008] studied the scale patterns on the sailfish, the fastest sea animal, able to travel up to 110 km/hr, whose body is covered in protrusions with a much larger spacing than grooves on shark skin. Unfortunately, no combination of scale height and spacing tested demonstrated significant drag reduction in comparison to a smooth surface, and in many cases showed an increase in drag. It is of note, though, that at the maximum speed of the sailfish, nearly an order of magnitude greater than its cruise speed, the spacing between these protrusions is on the order of the boundary layer thickness and k/δ becomes large enough that the protrusions reach into the buffer region and can have an impact on the flow. The large protrusion spacing at these high speeds where the scales act as a roughness suggest that this spacing may be important for optimal performance.

Chapter 2

Experimental Setup

In this chapter, details on the experimental setup and measurement accuracy will be discussed for each set of experiments.

2.1 Smooth-wall PIV experiments

2.1.1 Test facility

The goal of this set of experiments was to study in detail the structure of a fully developed zero pressure gradient turbulent boundary layer using time-resolved particle image velocimetry (PIV) in both wall-normal and wall-parallel planes. Experiments were performed in the free surface water tunnel facility in the Graduate Aerospace Laboratories at the California Institute of Technology. A diagram of the tunnel and a photographs showing the test section and coordinate system are presented in Fig. 2.1. The flow was conditioned by passing it through a perforated plate, a honey comb, three turbulence reducing screens and finally a 6:1 contraction before reaching the 2 m long by 1 m wide test section. These various screens provided a free-stream turbulence intensity ($u_{rms} = \sqrt{\overline{(U - U_\infty)^2}}$) less than 0.1% of the free-stream velocity in the test section. The canonical zero-pressure gradient turbulent boundary layer (the acceleration parameter, $K = \nu/U_\infty^2(dU_\infty/dx) = 2 \times 10^{-7}$, was near the range of values measured in the zero-pressure-gradient boundary layer experiments of DeGraaff and Eaton [2000] with $K = 0.1\text{–}1.1 \times 10^{-7}$) was formed over a 1.1 m long by 0.45 m wide Plexiglas plate with an elliptical leading edge and an adjustable wedge-shaped trailing edge. The plate was submerged 0.12 m below the water and was suspended from the top of the water tunnel. The total water depth was 0.48 m. The boundary layer on the bottom of the plate was studied to avoid any interactions with surface waves. In addition, a shroud with a wedge-shaped leading edge was placed along the sides of the plate to promote a two-dimensional flow. The spanwise variation of the mean streamwise velocity was measured to be less than 1% of the local mean over the 5δ wide field of view of the camera at the measurement location, 0.66 m downstream of the leading edge (this

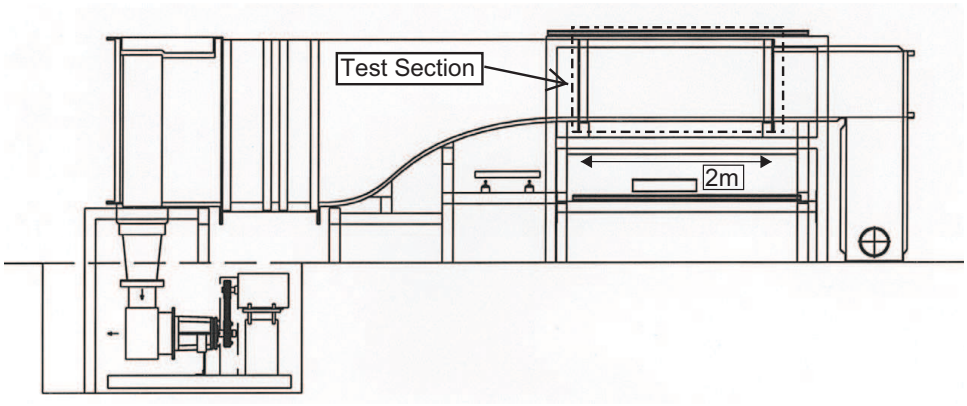

(a) Tunnel diagram [Bobba, 2004]

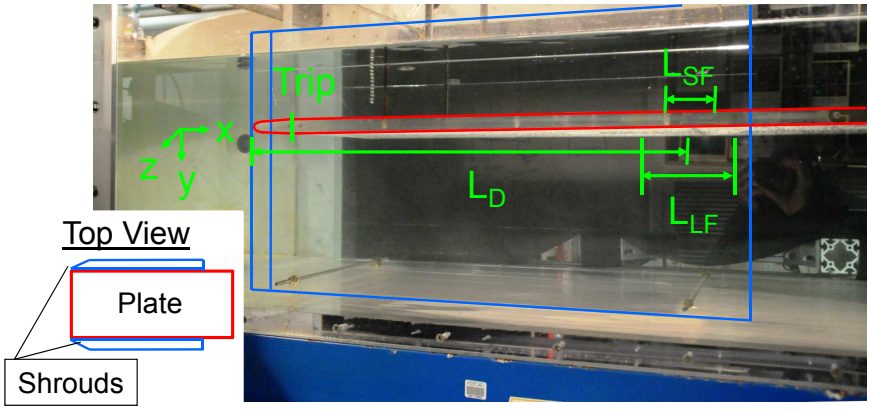

(b) Test section

Figure 2.1: (a): Water tunnel schematic showing the location of the test section. (b): Photograph of the test section; red lines outline the plate and blue lines outline the submerged portion of the shroud and its wedge-shaped leading edge. A top-down view is provided in the inset to clarify the shroud orientation. The lengths L_{SF}, and L_{LF} are defined for each set of experiments in Table 2.2, where L_{SF} and L_{LF} are given under the L_x/δ header.

distance is $L_D = 0.63$ m for set 2). A thin strip of tape (approximately 3 mm wide, 0.25 mm thick, and spanning the width of the plate) was placed immediately downstream of the elliptical leading edge on the measurement side to promote transition and favor the establishment of a turbulent regime at the measurement location. The free-stream velocity, and thus Reynolds number, for these experiments was set to provide the best flow conditions possible (i.e., minimize tunnel vibrations and the density of bubbles entrained in the flow) and to allow a small enough displacement per frame for accurate PIV measurements. Bobba [2004] provides additional information about the water tunnel and flat plate.

Table 2.1: Experimental parameters for both sets of experiments

Set	Re_τ	Re_θ	δ(mm)	θ(mm)	U_∞(m/s)	u_τ(m/s)	$\delta_\nu(\mu$m)
1	470	1280	13.9	1.72	0.67	0.030	29.5
2	410	1085	13.5	1.60	0.63	0.028	32.9

Table 2.2: Parameters for wall-parallel planes. Quantities for the small field of view (SF) are given in parenthesis for the second set of experiments.

Plane	y^+	y/δ	U/U_∞	Δx^+, Δz^+	L_x/δ	L_z/δ	Δt^+	$T_M(T_E)$
1-1	34	0.07	0.59	37.6	10.0	4.9	0.50	2000
1-2	108	0.23	0.73	37.1	9.9	4.8	0.50	2000
1-3	278	0.59	0.90	37.5	10.0	4.9	0.50	2000
2-0	33	0.08	0.65 (0.63)	33 (15)	10.0 (4.3)	5.0 (2.2)	0.84 (0.34)	3800 (950)
2-1	58	0.14	0.68 (0.69)	34 (15)	10.2 (4.3)	5.0 (2.2)	0.84 (0.34)	3800 (950)
2-2	122	0.30	0.76 (0.77)	33 (15)	10.0 (4.4)	4.9 (2.2)	0.84 (0.34)	3800 (950)
2-3	198	0.48	0.86 (0.86)	32 (14)	9.5 (4.3)	4.8 (2.1)	0.56 (0.34)	2500 (950)

2.1.2 Equipment and experimental setup

2.1.2.1 Equipment

Time-resolved 2D2C (two-dimensional velocity field with two in-plane components of velocity) PIV was used to measure the flow field in the wall-normal and wall-parallel planes independently using a LaVision PIV system with 2 Photron Fastcam APX-RS high-speed cameras equipped with Tamron SP AF 180 mm F/5.5 macro lenses. The cameras were capable of taking images up to 3000 fps with 1024 x 1024 pixel resolution (17 μm $\times$ 17 μm pixels). The flow was illuminated by a Photonics DM20-527 solid-state laser providing 20 mJ/pulse and a spherical and cylindrical lens were used to focus the beam into a sheet approximately 1 mm thick. The sheet was thick enough to nearly eliminate out-of-plane loss with $|v_n|\Delta t/l_t < 0.04$, much less than the maximum allowable value of 0.25 suggested by Keane and Adrian [1990], where l_t is the laser sheet thickness, Δt is the time between images, and v_n is the out-of-plane velocity estimated from the rms velocity fluctuations.

2.1.2.2 Setup and experiments

Two sets of experiments were performed and the flow parameters for each are recorded in Table 2.1 where $Re_\theta = \theta U_\infty/\nu$, is the momentum thickness Reynolds number where the momentum thickness is defined in Eqn. 2.1, Δx and Δz are the vector spacings in the x and z directions, respectively, L_x and L_z are the size of the field of view in the x and z directions, respectively, Δt is the time between images, and T_M is the total measurement time.

$$\theta = \int_0^\infty \frac{\overline{U}(y)}{U_\infty}\left(1 - \frac{\overline{U}(y)}{U_\infty}\right) dy \tag{2.1}$$

The goal of the first set of experiments was to obtain time-resolved PIV measurements in wall-

Table 2.3: Parameters for wall-normal planes

Set	$\Delta x^+, \Delta y^+$	Δt^+	L_x/δ	L_y/δ	$T_M(T_E)$
1	10.0	0.50	3.6	3.6	250
2	8.6	0.43	5.0	1.2	2400

parallel planes at various distances from the wall, where the focus was on capturing the largest field possible, and thus recovering the largest scales in the flow. While previous work by Dennis and Nickels [2008] recovered a 6δ long field in one wall-parallel plane at the outer edge of the log region, the present work provides an even larger field of view at various wall-normal locations given in Table 2.2 (planes 1-1 through 1-3 refer to this first set of experiments and 2-0 through 2-3 refer to the second set). For these experiments, the flow was seeded with $10\mu m$ hollow glass spheres with a specific gravity of 1.1.

Measurements were first performed in the wall-normal plane to provide a brief characterization of the boundary layer and extract important scaling parameters such as the boundary layer thickness and friction velocity. In this plane, 5 runs or 2048 images were recorded at 2000 Hz on one camera, providing about 250 eddy turnover times ($T_E = \delta/U_\infty$) worth of data per point. A cartoon of the setup is shown in Fig. 2.2. Additional experimental parameters for these measurements are provided in Table 2.3 where Δy is the vector spacing in y and L_y is the size of the field of view in the wall-normal direction.

Measurements were then taken in three wall-parallel planes located in the buffer layer, log layer, and wake regions (y/δ = 0.07, 0.23, and 0.59) of the boundary layer, respectively. Two cameras were placed side-by-side in the streamwise direction to elongate the streamwise field of view. An overlap between the two camera images of 10–20 pixels was chosen to provide the largest field of view possible while providing enough overlap to accurately stitch the vector fields together after vector processing. With this setup, 40 runs of 2048 images were recorded at 2000 Hz providing nearly $2000\,T_E$ of data per point. A cartoon of this setup is provided in Fig. 2.3. The experimental parameters for this set of data are provided in Table 2.2 (see planes 1-1 through 1-3).

Upon analyzing this first set of data it was apparent that: (1) there was not sufficient data in the wall-normal plane to provide convergence of the spectra and other high order statistics in this plane, (2) while the field was large enough to capture some of the largest fluctuations in the flow, the small-scale fluctuations, in particular the spanwise velocity fluctuations, were not sufficiently well resolved, and (3) the vibration of the tunnel at 24 Hz was evident in the measurements. To remedy these issues a second set of data was taken.

For the second set of wall-normal experiments, the convergence of statistics was improved by recording 25 runs of 4096 images (using half of the camera's CMOS sensor to double the storage space) at 2000 Hz, providing $2400\,T_E$ of data per point. Other relevant parameters are recorded in

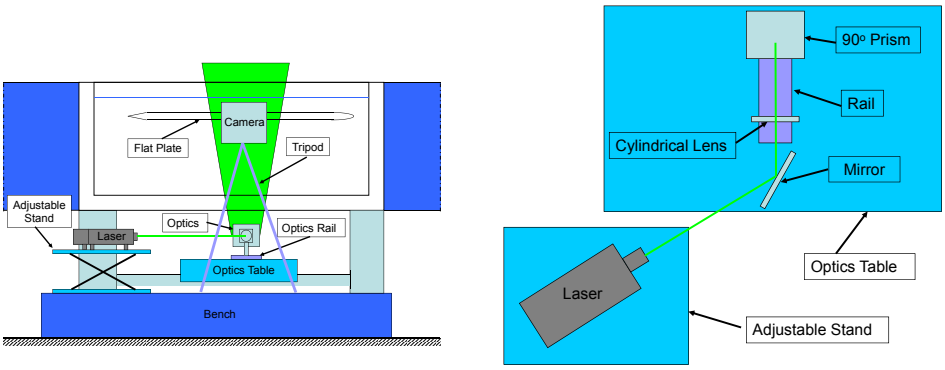

(a) Side View (b) Top View

Figure 2.2: Schematic of the laser and camera setup for set 1 of the wall-normal measurements

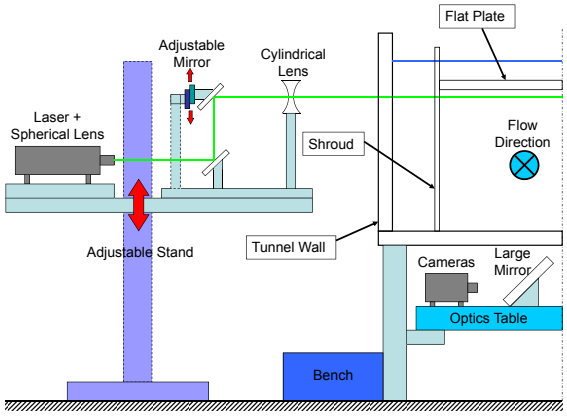

Figure 2.3: Schematic of the laser and camera setup for set 1 of the wall-parallel measurements

Table 2.3. In addition, the setup was altered to help reduce the transmission of tunnel vibrations to the measurement system. In the new setup the laser was placed onto the optics table along with the optics for compactness and the cameras were mounted to the adjustable stand shown in Fig. 2.3 with its base far from the tunnel for improved vibration isolation as shown in Fig. 2.4a. A vibration damping pad was placed between the arm of the adjustable stand and the support from the optics table so that no vibrations were transmitted from the tunnel to the cameras.

For the second set of wall-parallel experiments, a small field of view (SF) about half the size of the large field of view (LF) was used to improve the spatial resolution. For the SF, 25 runs of 2048 images were recorded at 2500 Hz, providing 950 T_E of data per point. The reduced length of recording was justified based on the reduction in the size of the longest wavelengths observable, and thus a shorter time to statistical convergence. In order to compare the LF and SF data, new LF measurements were taken at the same wall-normal locations and under the same conditions as the SF measurements. For these measurements, 40 sets of 2048 images were recorded with a frame rate of 1000 Hz in the three planes nearest the wall and 1500 Hz in the remaining plane, providing approximately 3800 T_E and 2500 T_E of data per point, respectively. Additional experimental parameters are provided in Table 2.2, where parameters for the SF data are provided in parentheses when they differ from the LF values (see planes 2-0 through 2-3). For this second set of wall-parallel measurements, the laser setup remained the same, but the cameras were placed on a stand isolated from the tunnel. In addition, the camera mounts were adjusted to allow the cameras to look up at the tunnel as shown in Fig. 2.4b, eliminating the need for the additional mirror in Fig. 2.3.

In addition to these changes for this second set of experiments, two cameras were placed side-by-side in the streamwise direction to elongate the streamwise field of view for all experiments (wall normal and wall parallel). Also, the seeding in these experiments was further improved using near neutrally buoyant (ρ = 1.016 g/cm^3 at 23^{o}C) Vestosint 2159 particles with an average diameter of 11μm. Finally, the tunnel was run at a slightly slower speed to reduce the tunnel vibrations and further decrease the amount of bubbles present in the flow.

The recording time for the experiments described above may not appear to be long enough for convergence of the spectra and other statistical measures (only a few thousand eddy turnover times), but recall that this is the recording time per point. For example, the SF measurements of set 2 were only recorded for 950 T_E, but this was done at approximately 8000 points in space, and thus, by averaging in the homogeneous spanwise direction and nearly homogeneous streamwise direction, over 7 million eddy turnover times worth of data are actually recovered.

2.1.2.3 Vector processing

For vector calculation, LaVision's Davis software was used with multipass processing and a 50% overlap of interrogation windows for all experiments. The window size is documented for each ex-

(a) New wall-normal setup

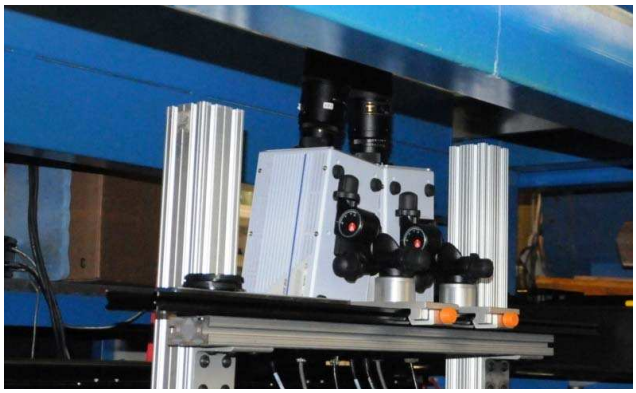

(b) New wall-parallel camera setup

Figure 2.4: (a): The position of the cameras and laser for the second set of wall-normal measurements. (b): The setup of the cameras for the second set of wall-parallel measurements

Table 2.4: Interrogation spot size in pixels for vector processing for wall-normal (WN) and wall-parallel (WP) experiments from each set.

Set-Plane	1st Pass	2nd Pass
1-WN	16 x 16	12 x 12
1-WP	32 x 32	32 x 32
2-WN	32 x 32	16 x 16
2-WP	64 x 64	32 x 32

periment in Table 2.4. Correlation peak fitting was performed using a Gaussian three-point estimator in each coordinate direction independently, image reconstruction was performed using Whittaker reconstruction, and in-plane pair loss was minimized using a window shift. Spurious vectors were removed via interpolation, of which less than 3% were removed in any image so interpolation errors were considered minimal. Smoothing of the vector fields was only performed for the wall-normal measurements of set 1 as this would have adverse effects on the velocity spectra calculated using the other sets of data.

The effect of lens distortions on the captured images were corrected for in the software before vector calculation using an image mapping computed from an image of a 3D calibration target for wall-normal measurements and a 2D target for wall-parallel measurements of set 2. For the wall-parallel measurement of set 1, corrections for lens distortions were made after vector calculation as calibration was performed using a ruler, so a mapping of the lens distortions could not be computed. To develop a correction mapping for this case, the time mean at each point in the flow was calculated and a multiplication factor was applied to each point so that the mean would be identical to a region near the center of the field of view where lens distortions were minimal.

When working with two cameras, vector fields were stitched together after processing. To assure an exact overlap of the processed fields, the original images were cropped before processing to ensure overlap of an integer number of interrogation windows after processing. In addition, due to bubbles

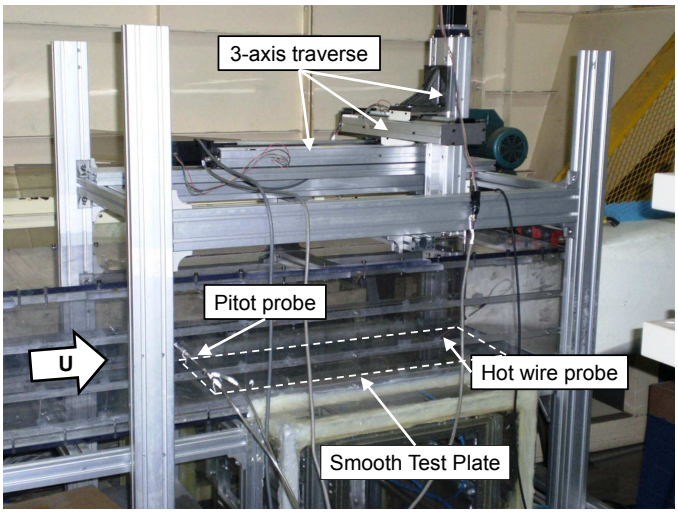

Figure 2.5: The test section and measurement probes

and particles occasionally aggregating at the wall, for plane 1-1 (the plane nearest the wall in set 1), an average was taken over all images and subtracted from each raw image before vector calculation to reduce the effects of stationary tracers on this calculation. For completeness, all processing parameters have been included in Appendix A.

2.2 Rough-wall hotwire experiments

The following section describes the experimental setup and measurement techniques used for analyzing the flow over a spatially periodic rough surface.

2.2.1 Test facility

Experiments were conducted in an open-circuit suction-type wind tunnel at Seoul National University shown in Fig. 2.5. The test section was 2 x 0.4 x 0.3 m (length, width, height) with a ball bearing trip (each with a diameter of 2.6 mm) placed on the floor of the test section 0.1 m downstream of the entrance to promote a turbulent regime over the measurement plate. The test section width expanded to 0.42 m near the exit to produce a near zero pressure gradient along the test section (A value of $K = \nu/U_\infty^2(dU_\infty/dx) = 4.18 \times 10^{-9}$ was noted by Kim [2006]).

Measurements were performed over two different 0.6 x 0.3 m (length, width) test plates mounted flush[1] to the wind tunnel floor 1.2 m downstream of the trip. A slight gap (about 2 mm per side) between the plate and the tunnel wall was present to allow for drag measurements. When performing velocity measurements, this gap was filled with modeling putty. The first test plate was flat and smooth and used as a reference; the second test plate had the roughness pattern shown in Fig. 2.6.

[1]For the rough test plate, the valleys of the roughness elements were made flush with the wall of the wind tunnel.

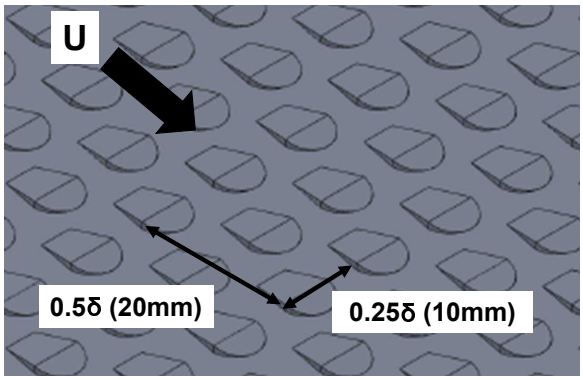

Figure 2.6: A drawing of a portion of the rough surface. The primary flow direction is indicated by the large arrow.

This roughness pattern was chosen to mimic the large streamwise and spanwise spacing of the scale pattern present on the sailfish as discussed in Section 1.2.2, which was investigated thoroughly by Sagong et al. [2008]. The current study focused on the largest roughness spacing investigated by these authors. Due to the choice of roughness height and spacing we will refer to this as a long-wavelength sparse roughness. Other than the spacing, the current roughness did not include any other details of the sailfish scale geometry which was the focus of the research of Sagong et al. [2008]. Interesting interactions between a shallow periodic roughness and the turbulent boundary layer were demonstrated by Schultz and Flack [2009], and as fish scales tend to have a smooth streamwise curvature to them, a ramp like roughness element was used.

The roughness element spacing was approximately 0.25δ (10 mm) in the spanwise direction and approximately 0.5δ (20 mm) in the streamwise direction. Every other row of roughness elements was staggered by 0.125δ (5 mm) in the spanwise direction. The roughness height, k, was 0.8 mm, and the rms roughness height, k_{rms} was 0.26mm. Thus, k/δ = 0.019 and k_{rms}/δ = 0.006 at the last measurement location (δ varied from 36–42 mm along the plate). The roughness was inclined at 9^o on the upstream side and 14^o on the downstream side. The width of the ramp on the upstream side increased from 4 mm in the valley to 6 mm at the crest 5 mm downstream. The ramp on the downstream side was semicircular with a radius of 3 mm.

The maximum free-stream velocity of the tunnel was 30 m/s corresponding to a Reynolds number of $Re_\theta = \theta U_\infty/\nu$ = 8300 measured at the start of the test plate, where θ is the momentum thickness. The free-steam velocity variation along the tunnel is shown in Fig. 2.7a for U_∞ = 17.8 and 23.5 m/s and the variation of the free-stream turbulence intensity with free-stream velocity is shown in Fig. 2.7b. These measurements were taken using hotwire anemometry as described in Section 2.2.2. Fig. 2.7a is normalized so that the difference in free-stream velocities is zero at the location of the Pitot probe upstream of the test plate. This figure shows that the mean velocity slightly increased up to the center of the plate and decreased thereafter with a maximum deviation of 0.9 and 1.4%

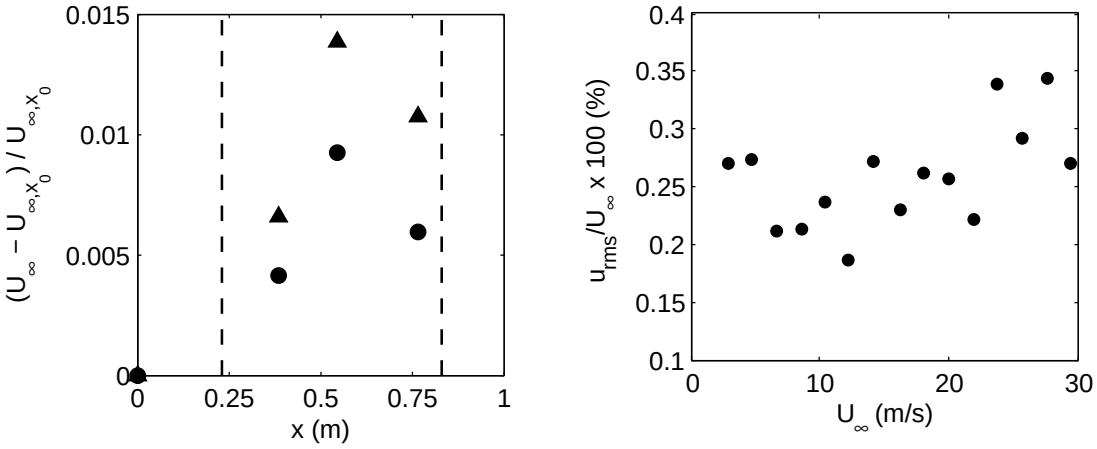

(a) Free-stream variation

(b) Turbulence intensity

Figure 2.7: (a): The variation of the free-stream velocity U_∞ with respect to the Pitot tube location (x_0) with a mean free-stream velocity of 17.8 m/s (•) and 25.3 m/s (▲). The start and end of the test plate are indicated by dashed black lines. (b): The turbulence intensity for various values of U_∞ with a mean value of 0.26% at the center of the test plate, 0.54 m downstream of the Pitot tube

Table 2.5: Test parameters measured at location 7

Surface	Re_τ	Re_θ	δ (mm)	θ (mm)	U_∞ (m/s)	u_τ (m/s)	δ_ν (μm)	δ_0 (mm)	Δt^+
Smooth	2600	7300	42.5	4.5	25.4	0.97	16.2	36.2	2.4
Rough	3000	7900	43.3	4.9	25.3	1.10	14.3	36.2	3.1

of the free-stream velocity for free-stream velocities of 17.8 and 25.3 m/s, respectively. In Fig. 2.7b, it is observed that the turbulence intensity was low (around 0.26% of the free-stream velocity) and approximately the same for all tunnel speeds. Thus, the turbulence intensity was low enough (verified in Fig. 5.4b) to run at the desired speed of 25.3 m/s.

The operating conditions for the experiments are compiled in Table 2.5 for measurements at the most downstream measurement location (location 7, see Fig. 2.8). For measurements over the rough wall, these values were obtained by averaging over all measurement stations (described in Section 2.2.2.2) at location 7.

2.2.2 Equipment and experimental setup

2.2.2.1 Hotwire measurements

Velocity measurements were performed using Dantec 55P05 hotwire probes controlled through an in-house hotwire anemometer. The probes had a length (l) to diameter (d) ratio of l/d = 250 and l^+ = 77 and 85 for the smooth- and rough-wall measurements, respectively. As the wire length was larger than the value of l^+ = 20 suggested by Ligrani and Bradshaw [1987] and further supported by Hutchins et al. [2009], some attenuation of the small-scale turbulent fluctuations was expected,

particularly near the wall (see Fig. 5a of Hutchins et al. [2009], for example). Despite this attenuation, valid comparisons can still be drawn between different experiments as they were all subject to the same attenuation. The probes had a response time of 85–90 μs (calculated from a square wave response), and thus could accurately measure frequencies below 11.1–11.8 kHz without attenuation. To prevent aliasing of high frequency data, a 10 kHz low-pass filter (the closest to the system response available) internal to the anemometer was applied and data was sampled at 25 kHz. A sampling rate of more than twice the filter cutoff was chosen to account for any non-ideal behavior of the filter. Hutchins et al. [2009] suggests a maximum flow frequency of $f_c \geq u_\tau^2/3\nu$ to resolve all energetic temporal scales, where $f_c \approx 20$ kHz for the smooth wall measurements and 25.6 kHz for the rough-wall measurements at the last measurement location. Thus the velocity measurements will have some degree of attenuation of the smallest temporal frequencies. Using Fig. 16b from Hutchins et al. [2009], which simulates the effect of under-resolved temporal scales, a maximum attenuation of the rms velocity of 1.5% could be observed. The overheat ratio of the probes was set to 1.4 and an amplifier internal to the anemometer was used to amplify the output by 10 times to cover the entire -10V to 10V range of the data acquisition board (National Instruments PXI-6259).

Calibration of the hotwire probe was performed with a Pitot static probe placed in the center of the test section 15 cm from the bottom wall and 23 cm upstream of the test plate. As the Pitot probe and hotwire probe were not co-located due to difficulties in mounting them together, the variation of the free-stream velocity with streamwise distance in Fig. 2.7a was noted. Pressure measurements were taken with a MKS Baratron differential capacitance manometer (model #: 220DD-00010B28) with a range of 10 Torr. A calibration curve was created using a 4th order polynomial fit to 10 logarithmically spaced velocity points ranging from 2.5 to 30 m/s, where 250,000 samples were recorded at each velocity, equivalent to about 6,000 eddy turnover times. Calibration was performed before and after profiles were taken at a single streamwise location. In the case of varying calibration curves, the resulting calibration curves were averaged as long as the variance in the free-stream velocity was less than 0.5% between the two calibrations. If the variance was larger than 0.5% between calibrations, the data was discarded and another recording was taken along with another pre- and post-calibration.

For positioning, the hotwire probe was mounted to a three degree-of-freedom traverse with a 20 μm step size in the wall-normal and spanwise directions and a 10 μm step size in the streamwise direction. The traverse was powered by three Vextra PK569-NA stepper motors. The control and measurement of all instruments was handled by a National Instruments PXI-6259 data acquisition board with 16-bit resolution and capable of measuring 10^6 samples per second.

Due to limited optical access in the test section it was not possible to directly monitor the distance between the probe and the wall. To overcome this obstacle and obtain the probe position with respect to the wall, the distance was measured indirectly. To do this, a calibration ruler was

first placed at the measurement location flush to the wall and a calibration image was taken. The ruler was then removed and the probe was placed in position. The probe was moved toward the wall and a photograph of the probe was taken. A distinct mark on the probe was noted and the distance between this mark and the probe tip was known. By comparing the calibration image to the probe image, the position of the probe tip could be inferred. For the sake of safety, the probe was never moved closer to the wall than a few hundred microns in either the rough or smooth measurements.

2.2.2.2 Measurement locations

To confirm that the rough surface was long enough for the flow to reach a fully developed state after the change in boundary conditions from the smooth tunnel wall to the rough test plate, boundary layer profiles were recorded at 7 locations shown in Fig. 2.8 spaced $2.2\delta_0$ (80 mm) apart starting $1.0\delta_0$ (35 mm) from the start of the test plate, where δ_0 is the boundary layer thickness just upstream of the test plate. One measurement was also made just upstream of the test plate (labeled location 0). Previous investigations by Andreopoulos and Wood [1982] suggest a development length of $20\delta_0$ for the smooth to rough transition for a 2D roughness. To study the convergence of the velocity statistics at different positions along the roughness pattern, profiles were taken at 3 different stations shown in Fig. 2.9a. The first station was positioned right between the peaks of two roughness elements in the spanwise direction, the second was in the valley just upstream of a roughness element (4 mm downstream of station 1 and 1 mm upstream of the start of a roughness element), and the third was right above the peak of a roughness element (10 mm downstream of station 1). Profiles were also recorded over the smooth surface at the first station of locations 3 and 7 ($5.4\delta_0$ and $14.2\delta_0$, respectively) for comparison purposes. Each profile consists of measurements at 40 logarithmically spaced wall-normal locations ranging from a point immediately next to the wall to about 2δ from the wall. 5 blocks of 125,000 measurements were taken at each wall-normal location at a rate of 25 kHz providing about 16,000 T_E worth of data.

In addition, longer recordings were taken to resolve the turbulent spectra at several stations shown in Fig. 2.9b at location 7 (the most downstream location) for the rough and smooth wall data. Measuring with respect to station A, located between the peaks of two roughness elements in the spanwise direction, the other stations were located 3.5, 5, 10, 13, and 15 mm downstream. For spectral measurements, each profile was taken at 20 logarithmically spaced wall-normal locations between the point nearest the wall or the peak of the roughness elements and about 2δ. For stations where the hotwire probe could access regions below the roughness peaks, another 4 logarithmically spaced wall-normal locations between the wall and roughness peaks were recorded. At each wall-normal location, 64 blocks of 125,000 measurements were taken at a rate of 25 kHz, providing about 200,000 T_E worth of data.

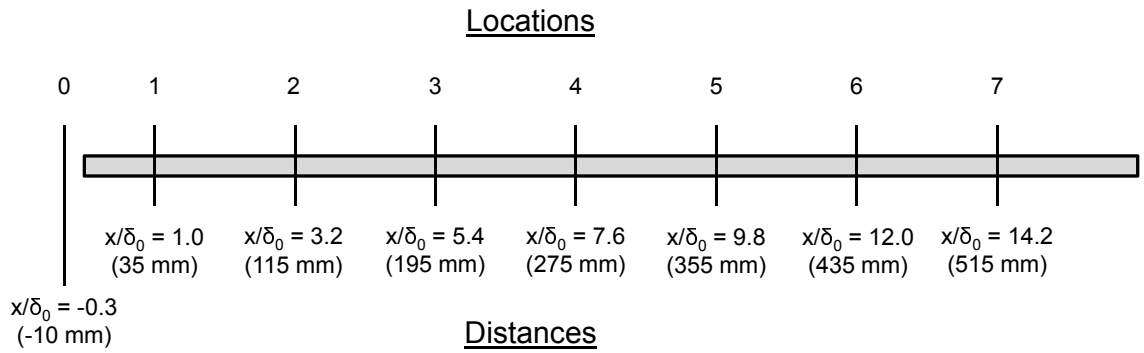

Figure 2.8: The locations at which measurements were taken are labeled with the location number, as well as the downstream distance in terms of incoming boundary layer thicknesses and in absolute units.

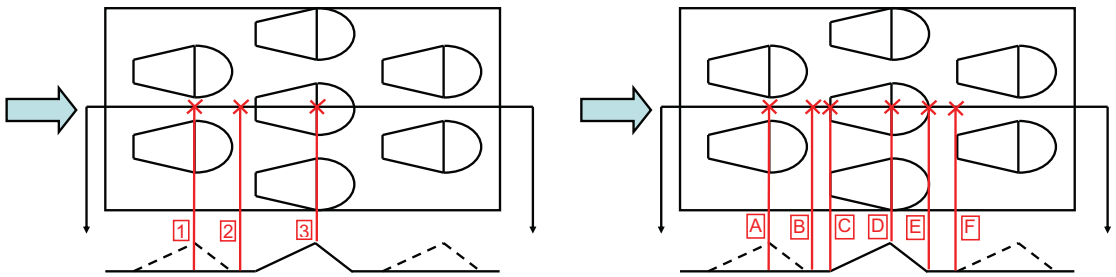

(a) Development measurement stations

(b) Spectra measurement stations

Figure 2.9: The stations along the roughness at which measurements were taken to test the development of the flow are indicated in (a) and the stations along the roughness at which spectra were measured are indicated in (b).

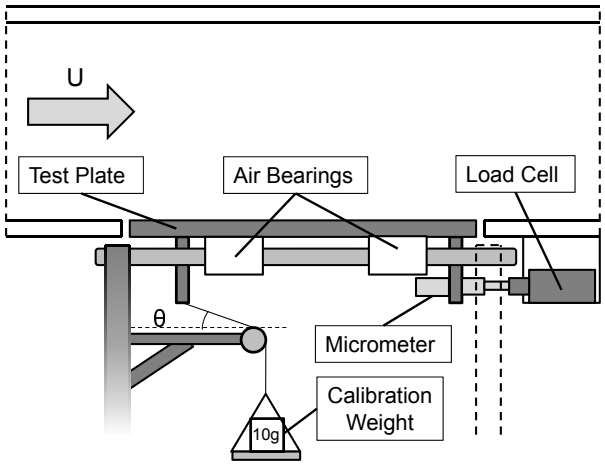

Figure 2.10: The setup for measuring drag on the test plates. The two dark gray regions reaching down from the plate were acrylic blocks rigidly adhered to the bottom of the measurement plate and were used as attachment locations for the weights and the micrometer, respectively.

2.2.2.3 Drag measurements

For drag measurements, test plates were attached to four air bearings which slid freely along two parallel tracks mounted underneath the wind tunnel allowing nearly friction-free measurement of drag on the plate as shown in Fig. 2.10. While a gap was needed between the plate and the test section to allow the plate to move, the gap was small and minimized at the leading edge of the test plate to prevent additional form drag. An AND LC4001 load cell with a 120 g range and an error of ±0.015% was rigidly attached underneath the test section and used to measure the drag force. A micrometer attached to the base of the test plate was adjusted to make contact with this load cell. The loadcell output was amplified by 3000 times using a Vishay Micro-measurements 2310B signal conditioning amplifier, and the results were recorded using the same data acquisition board as used for hotwire measurements. For calibration of the load cell, weights were hung over a pulley and attached to the plate by a string to provide a known lateral force. The calibration curve was linear and weights ranging from 2–100 g were used to assure good accuracy of the linear fit over the expected force range on the order of 10 g_f (this value was backed out from the predicted u_τ obtained by the modified Clauser method to be described in Section 5.1.).

Chapter 3

Flow Statistics and Turbulent Spectra

In this chapter, the time-resolved PIV data will be analyzed statistically looking at the mean and rms velocity profiles, the streamwise and spanwise velocity spectrum over space and time, and these measures will be used to calculate the convection velocity of scales of different sizes as well as investigate the validity of Taylor's hypothesis. A portion of this work has already been published in LeHew et al. [2011] concerning data set 1 in Sections 3.1 and 3.2, with the exception of Sections 3.2.3.2 and 3.2.8.

3.1 Mean and rms statistics

The mean velocity profiles for all PIV experiments are presented in Fig. 3.1a and were calculated by averaging the velocity fields over the homogeneous spanwise direction (for wall-parallel measurements only), the nearly homogeneous streamwise direction (δ may change up to 14% over the largest field of view), and time. Good agreement was found with the measurements of DeGraaff and Eaton [2000] at a similar Reynolds number. Differences in the outer regions of the profiles were expected due to slight differences in Reynolds number between data sets. The friction velocity was extracted from the mean velocity profiles using the Clauser method and the boundary layer thickness, δ, was defined as the height where the velocity reached 99% of the free-stream velocity.

The Clauser method for inferring the friction velocity relies on the existence of a portion of the velocity profile which follows the logarithmic scaling given in Eqn. 1.3 for a smooth surface, which extends over a significant spatial extent for high Reynolds number flows. This region should exist somewhere beyond the buffer layer ($y^+ > 30$ at least) and below the wake region ($y/\delta < 0.2$ at most). The log law can be rearranged in the form of Eqn. 3.1.

$$\frac{\overline{U}(y)}{U_\infty} = \frac{u_\tau}{U_\infty}\frac{1}{\kappa}\ln\left(\frac{yU_\infty}{\nu}\right) + \frac{u_\tau}{U_\infty}\frac{1}{\kappa}\ln\left(\frac{u_\tau}{U_\infty}\right) + \frac{u_\tau}{U_\infty}B \tag{3.1}$$

Using this form, if the velocity profile is plotted in terms of the known quantities yU_∞/ν and $\overline{U}(y)/U_\infty$, the ratio of u_τ/U_∞ in Eqn. 3.1 can be varied to find a best fit line to the data (in a least-squares sense), and thus u_τ can be inferred. This fit was performed over the range $60 \leq y^+ \leq 100$ where the variation between the log profile and the data was less than $0.05u_\tau$ at all points. For this fit, the widely used values of B = 5.0 and κ = 0.41 [Nagib and Chauhan, 2008] were used. The alternative values B = 4.17 and κ = 0.384 suggested by Nagib and Chauhan [2008] for a zero-pressure gradient boundary layer were also tested and showed only a 0.7% difference in the value of u_τ inferred.

The streamwise and spanwise rms velocity fluctuations are presented in Fig. 3.1b for both wall-normal and wall-parallel measurements. The streamwise velocity fluctuations near the wall were attenuated in the wall-normal measurements of set 1 and also for the LF wall-parallel measurements for both sets. For the wall-normal measurements, this was likely from applying a smoothing filter to the data which averaged velocity fluctuations in the region of high shear near the wall and also attenuated small scale velocity fluctuations that were most energetic near the wall (see Fig. 6 in Hutchins et al. [2009] to see the varying contribution of large- and small-scale fluctuations to the streamwise turbulence intensity) . At the same time this smoothing was deemed necessary to correct for noisy data caused by low particle density, where small interrogation windows (and thus fewer particles per window) were necessary to try and properly resolve the large velocity gradients near the wall.

The underestimation of the streamwise as well as spanwise velocity fluctuations from LF wall-parallel data sets was due to poor spatial resolution which attenuated small-scale fluctuations, as will become clear in Sections 3.2.4, 3.2.5, and 3.2.7. In addition, the dynamic range of the LF measurements was worse than the SF measurements. For the LF data it was difficult to capture the small spanwise displacement of particles in the flow which were displaced in the spanwise direction by an order of magnitude less than the they were in the streamwise direction per frame.

The wall-normal velocity fluctuations and Reynolds stress profiles are presented in Fig. 3.2. Again, a large attenuation in the profiles was observed for set 1 where the difference was attributed to smoothing of this data. For set 2 there appears to be a slight attenuation in the wall-normal velocity fluctuations near the wall when compared to the data of Erm and Joubert [1991] (each measurement averaged over $17\delta_\nu$), although this does not appear to be the case when comparing to the computations of Wu and Moin [2009], which have better wall-normal resolution (10 points below y^+ = 5 and 18 below y^+ = 10). The difference in the peak location of the Reynolds stress between the data of Wu and Moin [2009] and the data presented here is somewhat unusual given that all of the other fluctuating velocity profiles match well. This could be from a mismatch in Reynolds numbers as well as the higher spatial resolution available in the computations of Wu and Moin [2009] as compared to the present experiments and the hotwire measurements of Erm and Joubert [1991].

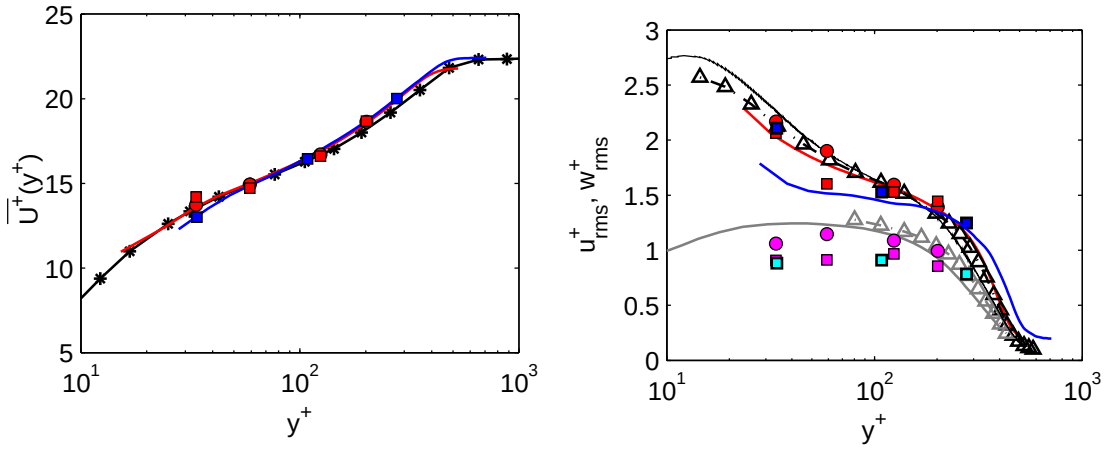

(a) Mean profile

(b) Rms profile

Figure 3.1: (a): Mean streamwise velocity profiles. Blue line and symbols: set 1, red line and symbols: set 2, black line: data from DeGraaff and Eaton [2000] at Re_θ = 1430 for comparison. Solid lines: wall-normal measurements, symbols: wall-parallel measurements where □: LF data and ○: SF data. (b): Rms velocity profiles for streamwise and spanwise velocity fluctuations. Blue line and symbols: set 1 streamwise velocity fluctuations, cyan symbols: set 1 spanwise velocity fluctuations, red line and symbols: set 2 streamwise velocity fluctuations, magenta symbols: set 2 spanwise velocity fluctuations, ○: SF wall-parallel data, □: LF wall-parallel data, and solid lines: wall-normal data. For comparison, solid black and gray lines: data from Wu and Moin [2009] at Re_θ = 900, dashed black and gray lines with △ symbol: data from Erm and Joubert [1991] at Re_θ = 1003, black lines: streamwise velocity fluctuations, gray lines: spanwise velocity fluctuations

Resolution is particularly important in the region of high shear near the wall.

3.2 Velocity spectra

In this section the velocity spectra calculated from the time-resolved PIV data will be presented. First, the definition of the spectrum will be given followed by a discussion of steps taken to best recover spectra from PIV data. Next, the symmetries of the different spectra will be discussed which will be used to determine the best way to present the spectral information. The spectra in 1, 2, and 3 dimensions will then be presented for the data sets investigated and will be followed by a discussion of the possibility of merging spectra from experiments with two different spatial resolutions. This section will conclude with a discussion of scale-based convection velocities and the appropriateness of using the local mean to convert between spatial and temporal domains.

3.2.1 Spectrum definition

The power spectral density (i.e., spectrum) of velocity fluctuations at one wall-normal location is defined as the Fourier transform of the correlation of those velocity fluctuations, where the relevant

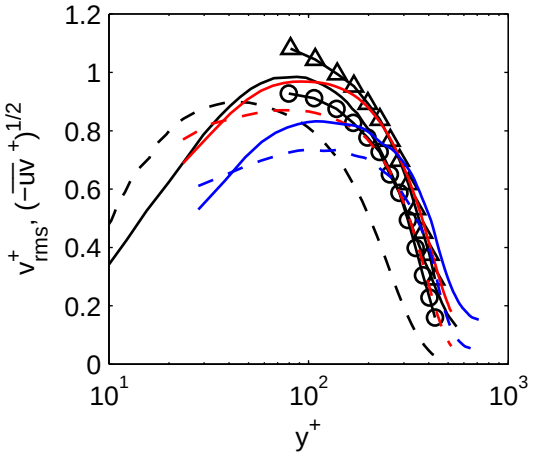

Figure 3.2: The rms wall-normal velocity (solid lines) and Reynolds stress (dashed lines) fluctuations; blue: set 1, red: set 2. △: v^+_{rms} and ○: $\sqrt{-\overline{uv}}^+$ from Erm and Joubert [1991] at $Re_\theta = 1003$, solid black line: v^+_{rms} and dashed black line: $\sqrt{-\overline{uv}}^+$ from the computations of Wu and Moin [2009] at $Re_\theta = 900$ are shown for comparison.

non-normalized 3D correlation function is defined in Eqn. 3.2.

$$R_{ij}(\xi,\zeta,\tau) = \langle u_i(x,z,t)u_j(x+\xi,z+\zeta,t+\tau)\rangle \tag{3.2}$$

In the above equation, ξ and ζ are the separation between points in the streamwise and spanwise directions, respectively, τ is the separation in time, the subscripts i and j represent different velocity components where $\{1,2,3\} \rightarrow \{u,v,w\}$, and the triangle brackets represent an ensemble average. The Fourier transform pair relating the correlation function to the power spectrum ϕ is given in Eqns. 3.3 and 3.4.

$$\phi_{ij}(k_x,k_z,\omega) = \frac{1}{(2\pi)^3}\iiint_{-\infty}^{\infty} R_{ij}(\xi,\zeta,\tau)e^{-i(\xi k_x+\zeta k_z+\tau\omega)}d\xi d\zeta d\tau \tag{3.3}$$

$$R_{ij}(\xi,\zeta,\tau) = \iiint_{-\infty}^{\infty} \phi_{ij}(k_x,k_z,\omega)e^{i(\xi k_x+\zeta k_z+\tau\omega)}dk_x dk_z d\omega \tag{3.4}$$

k_x and k_z are the streamwise and spanwise wavenumbers, respectively, and ω is the angular frequency. The Fourier transform pair is defined as above to allow for proper normalization of the spectrum, where the normalization is defined by combining Eqns. 3.2 and 3.4 at zero shift in time and space as given in Eqn. 3.5.

$$R_{ij}(0,0,0) = \langle u_i u_j\rangle = \iiint_{-\infty}^{\infty} \phi_{ij}(k_x,k_z,\omega)dk_x dk_z d\omega \tag{3.5}$$

In practice, the spectrum is calculated by taking the finite Fourier transform of u_i, multiplying

by the complex conjugate of the finite Fourier transform of u_j, and then normalizing the resulting spectrum using Eqn. 3.5. More discussion on this calculation will be provided in Section 3.2.2

2D spectra can be calculated by integration of the 3D spectrum over one dimension as shown in Eqn. 3.6 (where the limits are finite in practice), or by using the finite Fourier transform method on a 2D subset of the original 3D sample records and taking an ensemble average over all subsets.

$$\phi_{ij}(k_x, k_z) = \int_{-\infty}^{\infty} \phi_{ij}(k_x, k_z, \omega) d\omega \tag{3.6}$$

The above equation can be altered to calculate the spectrum over any two wave components. Similarly, 1D spectra can be calculated as the integral of a 2D spectrum or by using a 1D subset of the original 3D data set and ensemble averaging over all subsets.

3.2.2 Spectrum calculation

When calculating the spectrum from time-resolved PIV, there are several factors that must be taken into account to make sure the results are an accurate representation of the flow in question. These matters will be discussed in depth here.

3.2.2.1 Averaging in space

As discussed by Adrian [1988a], the velocity measured by the PIV algorithm, $\breve{U}_i(x, y, z, t)$, is not the velocity at a single point in the flow, $U_i(x, y, z, t)$, but the velocity signal averaged over the laser sheet thickness (~ 1 mm for the present experiments) and convolved with a rectangular window, $h(x, z)$, which represents the averaging effect of an interrogation window. The relation between the measured and the true velocity is given in Eqn. 3.7, the definition of the convolution integral is presented in Eqn. 3.8, and the measured fluctuating velocity is defined in Eqn. 3.9.

$$\breve{U}_i(x, y, z, t) = \left[\int_{y-l_t/2}^{y+l_t/2} U_i(x, y', z, t) dy' \right] \star h(x, z) = U_i^A(x, y, z, t) \star h(x, z) \tag{3.7}$$

$$f \star g(x, z) = \iint_{-\infty}^{\infty} f(x - \xi, z - \zeta) g(\xi, \zeta) d\xi d\zeta \tag{3.8}$$

$$\breve{u}_i(x, y, z, t) = \breve{U}_i(x, y, z, t) - \overline{\breve{U}}_i(y) \tag{3.9}$$

U is the instantaneous velocity, u is the fluctuating velocity, the star represents convolution, the superscript A represents an integral over the laser thickness, and the over bar indicates an average over all space, time, and experiments that closely approximates the true mean as discussed by Tomkins and Adrian [2005].

The spatial averaging from the interrogation window, h, attenuates fluctuations smaller than two window widths, and will also attenuate scales near this limit to a lesser extent. This, then, leads to an attenuation of the measured mean square fluctuations and the velocity spectrum.

When considering the measured fluctuating velocity signal, $\breve{u}$, given in Eqn. 3.9, a spectrum which differs from the true spectrum will result. The Fourier transform of Eqn. 3.9 multiplied by its complex conjugate is given in Eqn. 3.10, where the convolution theorem has been used to separate out the effects of smoothing from the interrogation window.

$$\begin{aligned} \breve{\phi}_{ij}(k_x, k_z, \omega) &= \phi^A_{ij}(k_x, k_z, \omega)\Xi(k_x, k_z) \\ \Xi(k_x, k_z) &= \mathrm{sinc}^2\left(\frac{W_{I,x}}{2}k_x\right)\mathrm{sinc}^2\left(\frac{W_{I,z}}{2}k_z\right) \end{aligned} \tag{3.10}$$

$\breve{\phi}$ is the 3D power spectrum of the measured velocity signal, ϕ^A is the spectrum of velocity fluctuations averaged over the laser sheet thickness, Ξ is the square magnitude of the Fourier transform of the rectangular window, h, and W_I is the PIV interrogation window size in either x or z as denoted by the subscript. The measured spectrum, $\breve{\phi}$, must be normalized by the measured mean square value of the velocity fluctuations, which is the mean square value of the fluctuations defined in Eqn. 3.9. Note again that ϕ^A is not the true spectrum, ϕ, nor is it the spectrum averaged in the wall-normal direction. Instead it is the spectrum of the velocity fluctuations which have been averaged in the wall-normal direction over the laser sheet thickness, $l_t \approx 1$–1.5 mm and thus $l_t^+ \approx 30$–45. To determine whether the average of the fluctuations over the sheet thickness was representative of the fluctuations at the center of the sheet, one would need to measure the correlation of the instantaneous fluctuations over a small range of y for each wall-normal location. As the velocity gradient is higher near the wall, less coherence is expected in this region, and thus the fluctuating velocity measured in planes near the wall will be more in error.

The effect of Ξ in Eqn. 3.10 is to attenuate the spectrum, particularly at high wavenumbers, where the amplitude of Ξ goes to zero at $k = 2\pi/W_I$. Since Ξ is known, one could recover ϕ^A simply by dividing by Ξ, although, in practice, this does not work where Ξ approaches zero (i.e., for wavenumbers near $2\pi/W_I$ where the function is ill-posed). As noted by Foucaut et al. [2004], the attenuation becomes significant above a wavenumber $k_{cut} = 2.8/W_I$, at which point, the signal is already attenuated by a factor of $\sqrt{2}$.

The effect of this spatial averaging is demonstrated in Fig. 3.3 by artificially smoothing SF data at one wall-normal location with different sized filters and then sub-sampling the data. It is apparent from Fig. 3.3a, that this averaging does indeed cause an attenuation of the small scales, and that even data before k_{cut} is attenuated to some extent, as expected. By dividing by Ξ, the data are brought into agreement up to, and even beyond k_{cut}. The only disagreement is near where Ξ approaches

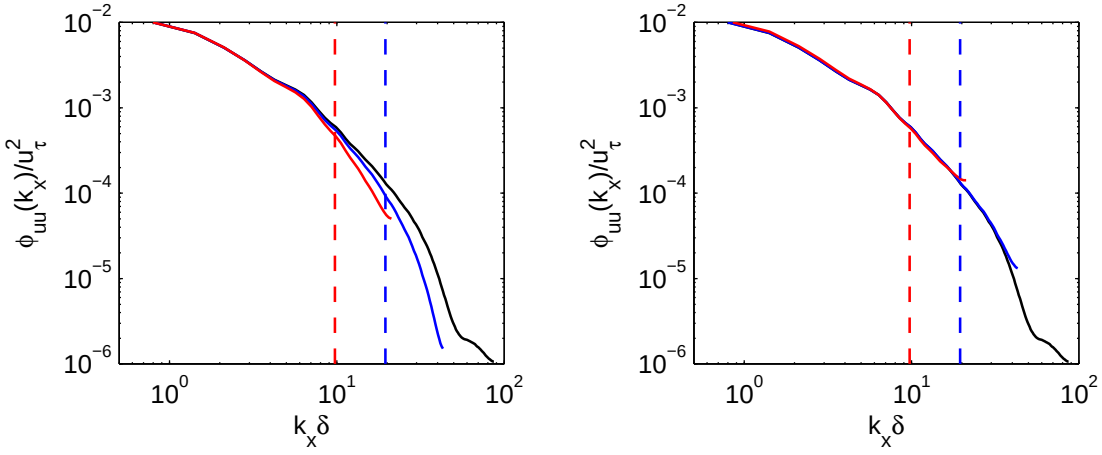

(a) Original (b) Corrected

Figure 3.3: (a): The effect of spatial averaging. Black: base spectrum calculated from data at one wall-normal location, blue: spectrum from data smoothed over 3 vector spacings and every other point sampled, red: spectrum from data smoothed over 5 vector spacings and every fourth point sampled, dashed lines: k_{cut} for the spectra with the corresponding colors. Smoothing was performed in x using a moving average filter (identical to the effect of having a larger interrogation window). (b): The same as (a) but spectra have been corrected by dividing by Ξ.

zero, as expected.

3.2.2.2 Windowing

Since the experimental data was not periodic and of finite length, the data was windowed in both space and time prior to calculating the Fourier transform to reduce spectral leakage. As the data was of finite length, it was naturally windowed by a top-hat function, but this sort of window provides poor side-lobe attenuation when viewed in frequency space, and thus distributes the energy at one frequency to other, much higher frequencies. To prevent much of this leakage to higher frequencies at the cost of expanding the main lobe (i.e., keeping the leakage local in frequency space), a 3D Hann window, an extension of the 2D Hanning window used by Tomkins and Adrian [2005], was applied to subsets of the data. Multiplying the measured velocity signal by the 3D Hanning window, denoted by g_H, provides an estimate of the spectrum as presented in Equation 3.11.

$$\hat{\phi}_{ij}(k_x,k_z,\omega) = \Big[\,[(U_i^A H)\star G_H]\,[((U_j^A)^* H^*)\star G_H^*]\,\Big] \tag{3.11}$$

The hat indicates that this is an estimate of the spectrum since the signal is windowed and of finite length, the capital letters are finite Fourier transforms of the corresponding lower case quantities where $U_i U_j^* = \phi_{ij}$, $HH^* = \Xi$, and the asterisk represents the complex conjugate. Estimates of the 2D and 1D spectra were calculated as before and the mean square fluctuations were the same as for the non-windowed data using a proper weighting of the windowing function (multiplying the signal

by $\sqrt{8/3}$ for each dimension over which the window is applied; see Bendat and Piersol [1986] Section 11.5.2 for an explanation of this factor).

The division of this estimate of the spectrum by Ξ to correct the high wavenumber range gives a reasonable estimate of the true spectrum since the convolution with G in spectral space mainly affects the low frequency/wavenumber range. The same operations were performed by Tomkins and Adrian [2005].

3.2.2.3 Aliasing

To avoid spatial aliasing, interrogation windows with 50% overlap were used which attenuate aliased energy content above the Nyquist frequency. That is, the interrogation window attenuates the spectrum to zero at $k = 2\pi/W_I$ and the maximum measureable frequency given a 50% overlap is $k = 2\pi/2(0.5W_I) = 2\pi/W_I$, the same value. Thus any energy from higher wavenumbers that would be aliased has already been largely attenuated by the spatial averaging created by the interrogation window.

To avoid temporal aliasing, the data was oversampled during recording, low-pass filtered, and then subsampled before calculating the spectrum as discussed by Wernet [2007]. This was necessary as no low-pass filter is naturally applied in time as it is in space, and unlike many techniques where a temporal filter can be applied to a time-series during recording, this is not possible with a camera. The low-pass filter cutoff for the time signal was set so that $\omega_{cut} = \overline{U}(y)k_{cut}$.

3.2.2.4 Additional operations

In addition to the low-pass filter applied to avoid temporal aliasing, the low frequency tunnel vibrations evident in the data from set 1 were filtered out before calculation of the spectrum.

Before performing the finite Fourier transform, each run of a given data set was split into a number of windows to provide more samples to help converge the spectrum. As the focus of the current work was on capturing the largest scales in the flow, data was not split in the streamwise direction. For both the LF and SF data, data was split into 5 windows overlapping by 50% in time given the long recording times. Also, the LF data was split into 3 windows with 50% overlap in the spanwise direction which provided 3 windows that were 2.5δ wide. This smaller domain size was adequate as the peaks in the streamwise and spanwise velocity spectra over spanwise wavelengths were close to $\lambda_z/\delta = 1$, and thus the peaks would be well resolved. Choosing a 50% overlap between interrogation windows was helpful in recovering data lost by the windowing process.

Finally, when calculating the finite Fourier transform, the data was zero padded to twice its original length in all 3 directions. This assured that each transform was performed with an even number of elements and also helped to smooth the appearance of the final spectrum. Note that

this procedure did not add any new information to the spectrum and acted, in some sense, as an interpolation.

3.2.2.5 Summary

To summarize, corrections were made to correct for attenuation of the small-scale features of the flow by the PIV interrogation windows as well as spectral leakage of energy from the most energetic scales to higher frequencies. To account for these issues and prevent aliasing, the data was recorded at a higher sampling rate than necessary and the vector fields were calculated using 50% overlap of the interrogation windows. Before any calculations were performed, the data was low-pass filtered in time to get rid of unwanted noise. Prior to calculation of the spectrum, the signal was split into subsets and windowed using a Hann window to help reduce spectral leakage. Finally, the finite Fourier transform of each subset was calculated (zero padded to twice its original length), all calculations were averaged, and the data was divided by the smoothing function Ξ to get an estimate of the spectrum ϕ^A where data beyond the cutoff in k_x and k_z was ignored. 1D and 2D spectra were calculated by integration of the resulting 3D spectrum.

3.2.3 Spectral symmetry

Here the symmetry of both the auto-spectrum, ϕ_{ii}, and the cross-spectrum, ϕ_{ij} where $i \neq j$, will be discussed.

3.2.3.1 Auto-spectrum symmetries

The 3D auto-spectrum, ϕ_{ii}, is even and real which provides symmetry about any coordinate plane if the spectrum is rotated by 180^o about the origin, and thus only 4 independent octants exist. Similarly, all 2D spectra are even and real with rotational symmetry about the origin, and thus have only 2 independent quadrants each. Therefore, any 2D spectrum can be represented by any half plane and the 3D spectrum by any 4 connected octants. In this half space representation, the magnitude of the spectra are doubled to preserve the normalization. The 2 non-redundant quadrants of each 2D streamwise velocity spectrum are shown in Figs. 3.4a, 3.4b, and 3.4c and the four non-redundant octants (choosing $\omega > 0$) of the 3D streamwise velocity spectrum are shown in Fig. 3.4d for one wall-normal location. As usual, the 1D spectra are symmetric about zero frequency/wavenumber, and thus may be represented in one quadrant by doubling the magnitude of the spectrum.

From Figs. 3.4b and 3.4c, only a slight asymmetry is noted in k_z which arises from poorer resolution in this direction as well as slight tilting of the PIV cameras, although some corrections have been made for the latter. For all practical purposes, these spectra are symmetric in k_z. For $\phi_{ii}(k_z,\omega)$ this symmetry arises since there is no mean spanwise flow and thus no spanwise direc-

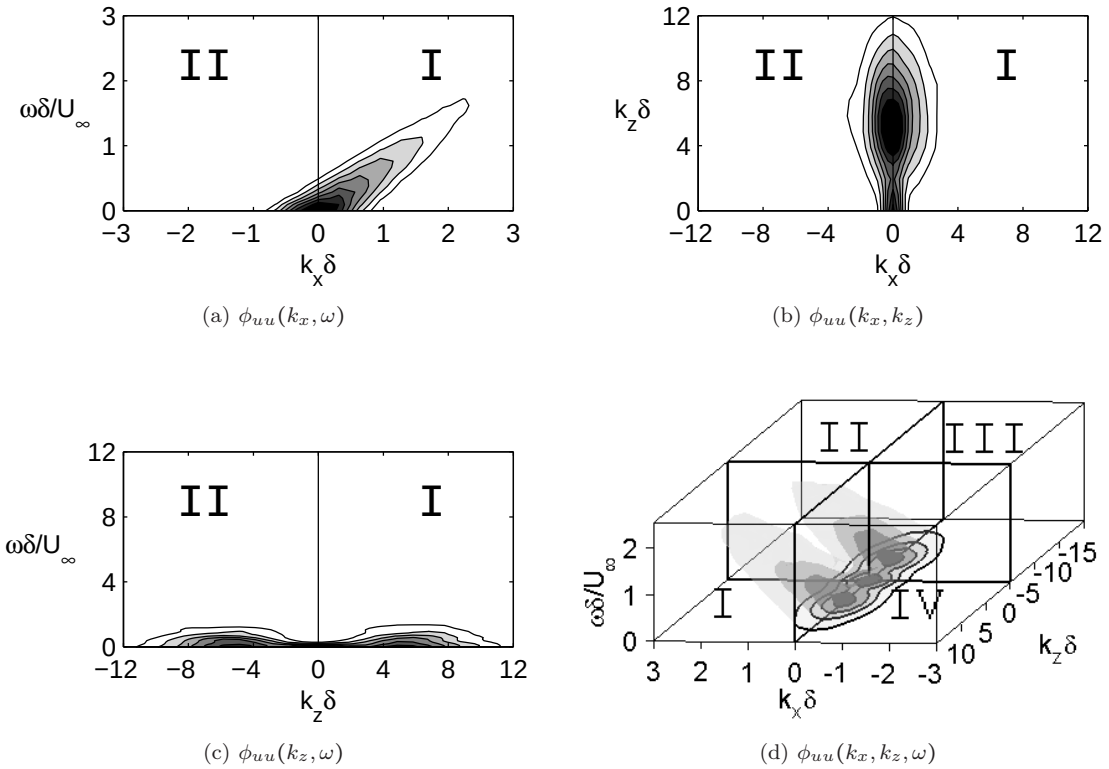

(a) $\phi_{uu}(k_x,\omega)$ (b) $\phi_{uu}(k_x,k_z)$

(c) $\phi_{uu}(k_z,\omega)$ (d) $\phi_{uu}(k_x,k_z,\omega)$

Figure 3.4: Half-space representation of each 2D streamwise velocity spectrum at $y^+ = 108$ (set 1) as well as the 3D spectrum. The spectra at other wall-normal locations are qualitatively similar. For (a), (b), and (c), the levels range from 20% to 80% of the maximum energy in 10% increments moving from light to dark shades. For (d), the levels range from 15% to 75% of the maximum energy in 20% increments moving from light to dark shades. The intersection of the spectrum with $\omega = 0$ is denoted by solid black lines to better illuminate the shape of the spectrum.

tional preference. For $\phi_{ii}(k_x,k_z)$ there should physically be no distinction between the positive and negative wavenumber pairs. Thus, both of these spectra can be represented in one quadrant with the magnitude doubled to preserve the normalization.

For $\phi_{ii}(k_x,\omega)$ the two quadrants are not equivalent, where quadrant I is interpreted as downstream traveling waves and quadrant II as upstream traveling waves. The amount of energy in quadrant II is not negligible (at $y^+ = 108$ quadrant II represents about 12% of the total area under the spectrum), and it is necessary to use both planes when integrating $\phi_{ii}(k_x,\omega)$ to recover $\phi_{ii}(k_x)$, $\phi_{ii}(\omega)$, or any other integral quantities, otherwise a low wavenumber spectral distortion will result.

The energy in quadrant II of $\phi_{ii}(k_x,\omega)$ comes from energy concentrated at two distinct spanwise wavenumbers, which can be observed in Fig. 3.4d. Both the energy at $(k_x,k_z,\omega) = (0,0,0)$ and the energy centered at $(0,\pm 5/\delta,0)$ should be zero since the mean has been subtracted from the data before calculating the spectrum, and thus the spectrum should be zero along any of the coordinate axes. The energy is non-zero, though, due to slight spatial variations of the mean velocity from

the overall mean as well as slight variations of the mean over the entire field of view at a given time from the overall mean. In addition, windowing the velocity signal spreads or leaks energy to nearby frequencies and wavenumbers, and thus energy is spread to the plane where $k_x < 0$ and $\omega > 0$. The peak at $(0,0,0)$ shows the variation of the local mean from the overall mean. The peak at $(0,\pm 5/\delta,0)$ is energy spread from a nearby peak in the spectrum as shown in Fig. 3.7b of Section 3.2.4. In conclusion, it is not expected that energy measured in quadrant II in Fig. 3.4a represents a major contribution of upstream traveling waves, but is instead a local spreading (due to the windowing of the velocity signal) of energy to surrounding frequencies and wavenumbers.

For the 3D spectrum shown in Fig. 3.4d, the same symmetry exists in k_z and the same asymmetry exists in k_x as might be expected from the 2D spectral plots. Thus, the spectrum can be represented by the two octants covering all k_x, positive k_z, and positive ω with the magnitude doubled to preserve the normalization as given in Equation 3.12.

$$\begin{aligned}\overline{u^2} &= \iiint_{-\infty}^{\infty} \phi_{ii}(k_x,k_z,\omega)dk_x dk_z d\omega = 4\iiint_{0}^{\infty} \left[\phi_{ii}(k_x,k_z,\omega)+\phi_{ii}(-k_x,k_z,\omega)\right] dk_x dk_z d\omega \\ &= 4\iiint_{-\infty}^{\infty} k_x k_z \omega \left[\phi_{ii}(k_x,k_z,\omega)+\phi_{ii}(-k_x,k_z,\omega)\right] d\ln k_x \, d\ln k_z \, d\ln\omega\end{aligned} \tag{3.12}$$

While the energy distributed over negative k_x is non-negligible and must be included for proper normalization of $\phi_{ii}(k_x,k_z,\omega)$, only data for positive streamwise wavenumber, k_x, will be shown when these spectra are presented in premultiplied form. First of all, since a majority of this energy is near zero streamwise wavenumber and frequency, which represents the mean flow, its distribution is not of interest in the present study. Secondly, being concentrated near zero streamwise wavenumber and frequency, when premultiplied, the energy density of waves in this quadrant will be very small and will make little contribution to the premultiplied spectrum overall.

3.2.3.2 Cross-spectrum symmetries

While the cross-spectra (ϕ_{ij}, $i \neq j$) do not have symmetries, the real and imaginary parts of these spectra (the co- and quad-spectra, respectively) do, as will be discussed. It should be noted that unlike the auto-spectrum, the cross-spectrum is not positive definite. For the 1D spectra it can be shown that:

$$\phi_{ij}(-\omega) = \phi_{ij}^*(\omega) = \phi_{ji}(\omega) \tag{3.13}$$

Therefore, the negative quadrant is the complex conjugate of the positive quadrant. Thus, the real part of $\phi_{ij}(\omega)$ is even and the imaginary part is odd. Furthermore, M_{ij}, the magnitude is even

and Θ_{ij}, the phase angle, is odd.

$$M_{ij}(\omega) = \sqrt{\Re[\phi_{ij}(\omega)]^2 + \Im[\phi_{ij}(\omega)]^2} \tag{3.14}$$

$$\Theta_{ij}(\omega) = tan^{-1}\left(\frac{\Im[\phi_{ij}(\omega)]}{\Re[\phi_{ij}(\omega)]}\right) \tag{3.15}$$

For the 2D spectra, it follows that:

$$\begin{aligned} \phi_{ij}(-k,-\omega) &= \phi^*_{ij}(k,\omega) = \phi_{ji}(k,\omega) \\ \phi_{ij}(-k,\omega) &= \phi^*_{ij}(k,-\omega) = \phi_{ji}(k,-\omega) \end{aligned} \tag{3.16}$$

Thus the real part of the 1st and 3rd quadrants are identical and the real part of the 2nd and 4th quadrants are identical. The imaginary part is of equal magnitude, but opposite sign in the 1st and 3rd quadrants and also in the 2nd and 4th quadrants. Given these results, the magnitude spectrum has the same properties as the real part and the angle spectrum has the same properties as the imaginary part. To show the amplitude of the spectrum it is sufficient to show any 2 connected quadrants with the amplitude doubled to preserve the normalization. To show the phase angle, any two connected quadrants are sufficient if it is noted that the angles will be of opposite sign when rotated by 180°. For the case of the phase angle spectrum, the amplitude should not be doubled.

Finally, for the 3D case, the relations are:

$$\begin{aligned} \phi_{ij}(-k,-m,-\omega) &= \phi^*_{ij}(k,m,\omega) = \phi_{ji}(k,m,\omega) \\ \phi_{ij}(-k,m,\omega) &= \phi^*_{ij}(k,-m,-\omega) = \phi_{ji}(k,-m,-\omega) \\ \phi_{ij}(-k,-m,\omega) &= \phi^*_{ij}(k,m,-\omega) = \phi_{ji}(k,m,-\omega) \end{aligned} \tag{3.17}$$

As with the auto-spectrum, the real part as well as the magnitude of the cross-spectrum can be represented by any four connected octants with the amplitude doubled. This is the same for the imaginary part and the angle spectrum except that the amplitude should not be doubled for the angle spectrum and it must be noted that the mirror quadrants have the same magnitude, but opposite sign, for both. Also note that the position of the mirrored quadrants flips place if the order of the correlation is reversed.

3.2.4 1D spectra

All spectra presented from here forward are presented over wavelength as opposed to wavenumber and frequency for interpretation purposes. The streamwise and spanwise wavelengths are $\lambda_x = 2\pi/k_x$

and $\lambda_z = 2\pi/k_z$, and the temporal wavelength is $T = 2\pi/\omega$.

Streamwise velocity spectra over streamwise and spanwise wavelength are shown in Fig. 3.5 and spanwise velocity spectra are presented in Fig. 3.6. These spectra were calculated from wall-parallel measurements and are shown for all wall-normal locations. The spectra are presented in premultiplied form (i.e., premultiplied by the streamwise or spanwise wavelength) where equal areas under the spectra have equal energy when plotted in semi-logarithmic coordinates. In this form it is easy to determine the wavelength of the most energetic scales in the flow, or equivalently, the size of the most energetic eddies. In these figures, none of the data have been corrected for attenuation by dividing by Ξ, presented in Eqn. 3.10; the effects of this correction will be presented later.

The streamwise velocity spectra at all wall-normal locations have a peak at $\lambda_x/\delta = 3$, associated with the large-scale motions (LSMs), as shown in Figs. 3.5a and 3.5b. In the spanwise direction, the peak in the streamwise velocity spectrum lies between $\lambda_z/\delta = 0.3$ and 1 as shown in Figs. 3.5c and 3.5d. The spanwise wavelength of this peak increases with distance from the wall (only noticeable in the well-resolved SF data) while the energy level decreases, consistent with the decrease in the mean square streamwise velocity fluctuations. The peak in the spanwise velocity fluctuations is found at $\lambda_x/\delta = \lambda_z/\delta = 1$ and the energy level as well as the location of this peak changes little with distance from the wall as shown in all plots in Fig. 3.6. The major difference between the spanwise velocity spectrum at different wall-normal locations is the reduction of small-scale (short-wavelength) spanwise velocity fluctuations, particularly in the wake region $y/\delta = 0.48$. This is most notable in the well-resolved SF data shown in Fig. 3.6d to the left of the dotted black line.

Viewing these 1D spectra, it is apparent that the LF data does not sufficiently resolve small-scale activity. This results in a lower than average measure of the rms streamwise and spanwise velocity fluctuations, and this resolution issue becomes worse as the wall is approached. Comparing wavelengths to the left of the dotted black line in Figs. 3.5c and 3.5d, it is apparent that the spanwise resolution of the streamwise velocity fluctuations is the major problem. As with hotwire measurements, it is important to have proper resolution of spanwise fluctuations of the streamwise velocity. Generally, it is suggested that a hotwire have a length less than $20\delta_\nu$ (see Ligrani and Bradshaw [1987]), where the effect of a larger measurement volume is to attenuate a large range of streamwise velocity fluctuations, with the attenuation strongest near the wall [Hutchins et al., 2009]. The highest resolution achieved in the PIV measurements was 30 viscous units for the SF data, so even this set of measurements experienced some level of attenuation.

While is it apparent that the SF data is needed to resolve the smallest energetic scales in the flow, the shorter streamwise field of view makes it difficult to capture the largest streamwise wavelengths. In Fig. 3.5b, the SF data just barely catches the energetic peak at $\lambda_x/\delta = 3$. The effect of such a small measurement window is explored using hotwire measurements in Fig. 5.10 of Section 5.4.1. On the other hand, spanwise velocity fluctuations (Fig. 3.6b and 3.6d) as well as the spanwise variation

of streamwise velocity fluctuations (Fig. 3.5d) are adequately resolved using this smaller field of view as the most energetic wavelengths for these spectra are close to 1δ.

Overall, it is apparent that properly recovering the distribution of the streamwise velocity fluctuations in a turbulent flow is quite difficult, requiring an interrogation window less than 20 viscous units in size while simultaneously resolving scales on the order of 10δ or larger. Considering even a moderate Reynolds number, $Re_\tau = 2000$, where the secondary energetic peak at $\lambda_x/\delta = 6$ [Hutchins and Marusic, 2007] would appear, a window size of at least 12δ in the streamwise extent and 2–3δ in spanwise extent would be required. With a set window size of 32 pixels and a high resolution camera (say 4k x 4k pixels), 125 windows of size $20\delta_\nu$ would be available per camera, that is a 1.25δ field of view per camera. To fully resolve the spatial field would require a 10 x 2 array of cameras, an impractical task. In Section 3.2.8 a possible solution to this problem is investigated by using multiple magnifications to try and resolve the entire range of wavelengths of interest.

To show that the spectra recovered from the SF data accurately represent the flow, comparisons are made to the hotwire measurements of Erm and Joubert [1991] at a similar Reynolds number and similar wall-normal locations in Fig. 3.7. In addition, the data are also show when divided by the correction, Ξ, to show the improvement of the spectral shape below the attenuation cutoff. The agreement with the data from Erm and Joubert [1991] is good for the SF data set, but the amplitude is attenuated for the LF data and in many cases the shape is also wrong. The main disagreement between the SF data and the literature is the increased level of streamwise velocity fluctuations at small streamwise wavelengths. Perhaps this is an effect of noise in either the spatial or temporal data. The other discrepancy is the lack of a peak in the spanwise velocity fluctuations around $\lambda_x/\delta = 1.5$. Perhaps this could even be an error in the data from Erm and Joubert [1991] as fluctuations at this scale should be well resolved in both the LF and SF data sets. At planes further from the wall, the SF data shows an even more satisfactory fit to the data from Erm and Joubert [1991].

It is interesting to note that the correction applied affects the streamwise velocity spectrum over a broad range of streamwise wavelengths as shown in Fig. 3.7a. On the other hand, Fig. 3.7c and 3.7d show that for the spanwise velocity spectrum, the correction has the most effect at small streamwise and spanwise wavelengths. This is a matter of the aspect ratio of the fluctuations as will be investigated in Section 3.2.5. While the division by Ξ helps to correct the LF data, the amplitude of the LF 1D spectra are still underestimated. This is simply because there are some small scales that cannot be recovered, even with the correction, due to limited resolution. Thus, when integrating the 3D spectrum to recover the 1D spectrum, there are scales (both spatial and temporal) which will be missing and thus affect the spectral shape over a range of streamwise and spanwise wavelengths.

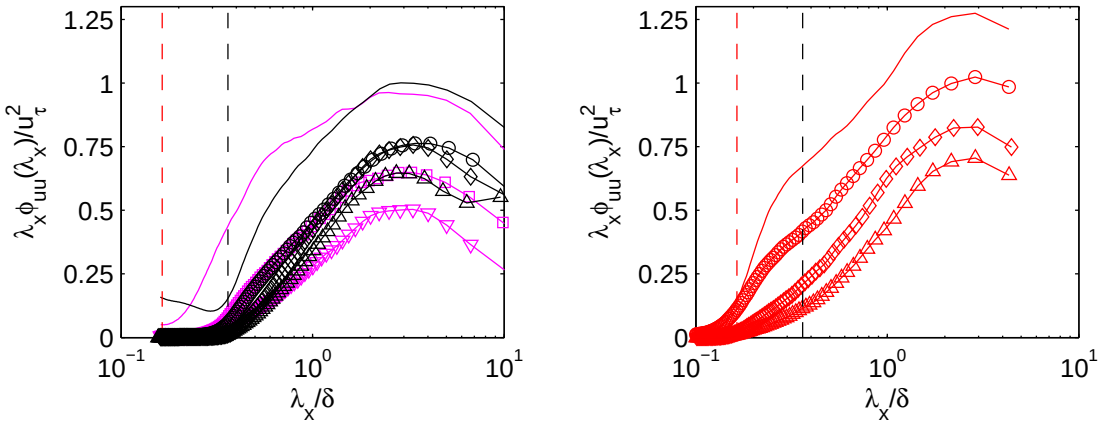

(a) LF $\lambda_x\phi_{uu}(\lambda_x)/u_\tau^2$

(b) SF $\lambda_x\phi_{uu}(\lambda_x)/u_\tau^2$

(c) LF $\lambda_z\phi_{uu}(\lambda_z)/u_\tau^2$

(d) SF $\lambda_z\phi_{uu}(\lambda_z)/u_\tau^2$

Figure 3.5: The streamwise velocity spectra over (a,b): streamwise wavelength and (c,d): spanwise wavelength. (a,c): LF data from set 1 (magenta) and set 2 (black); (b,d): SF data. Solid line: $y/\delta = 0.08$ (0.07 for set 1), ○: $y/\delta = 0.14$, □: $y/\delta = 0.23$, ◊: $y/\delta = 0.30$, △: $y/\delta = 0.48$, ▽: $y/\delta = 0.59$. Dashed vertical lines: wavelength below which spectra are significantly attenuated by the averaging effects of the interrogation spot size; LF: black, SF: red

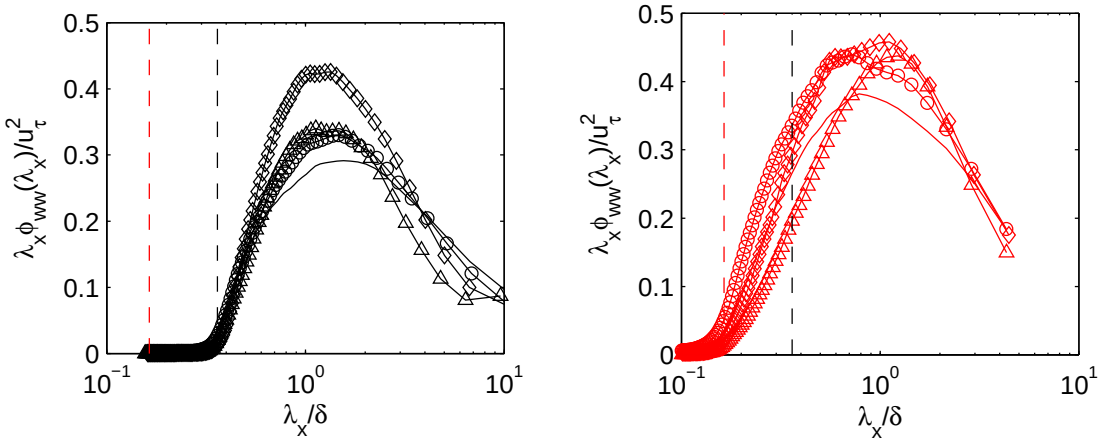

(a) LF $\lambda_x\phi_{ww}(\lambda_x)/u_\tau^2$

(b) SF $\lambda_x\phi_{ww}(\lambda_x)/u_\tau^2$

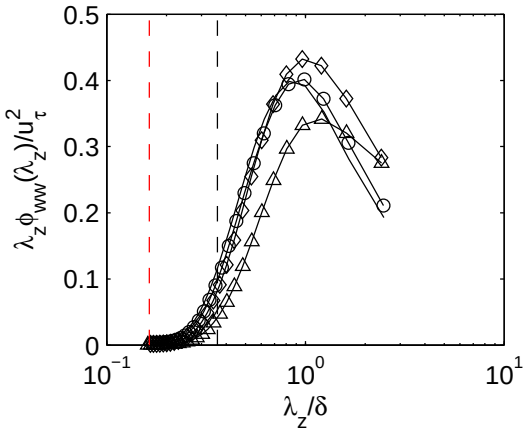

(c) LF $\lambda_z\phi_{ww}(\lambda_z)/u_\tau^2$

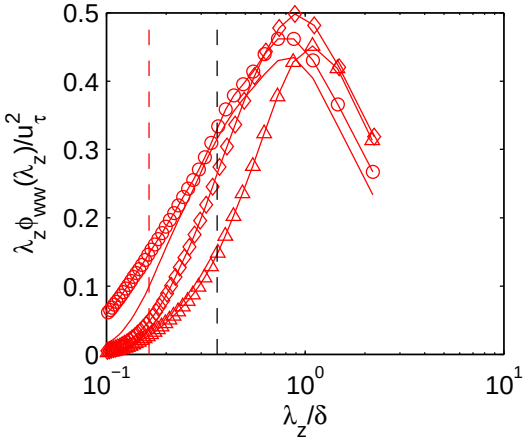

(d) SF $\lambda_z\phi_{ww}(\lambda_z)/u_\tau^2$

Figure 3.6: The spanwise velocity spectra over (a,b): streamwise wavelength and (c,d): spanwise wavelength. (a,c): LF data from set 2; (b,d): SF data. Solid line: y/δ = 0.08, ○: y/δ = 0.14, ◇: y/δ = 0.30, △: y/δ = 0.48. The dashed vertical lines are the same as in Fig. 3.5.

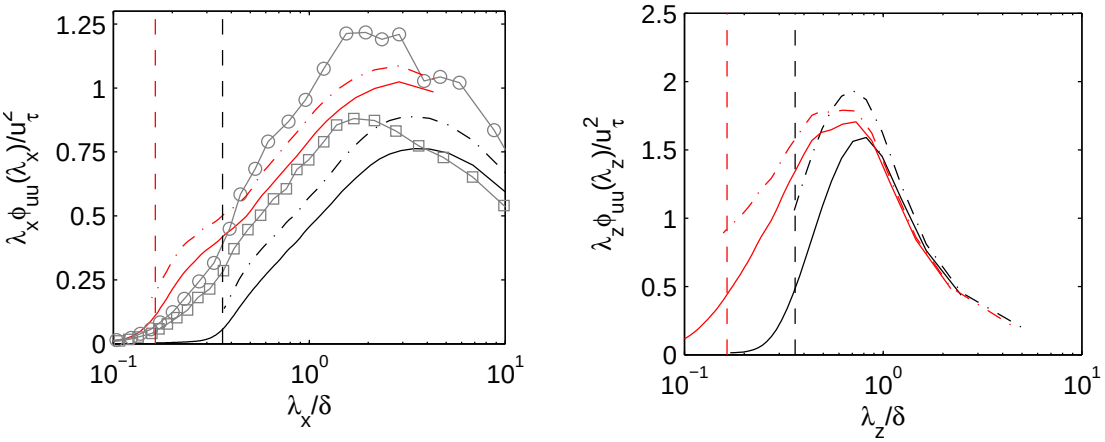

(a) $\lambda_x\phi_{uu}(\lambda_x)/u_\tau^2$ at $y/\delta = 0.14$

(b) $\lambda_z\phi_{uu}(\lambda_z)/u_\tau^2$ at $y/\delta = 0.14$

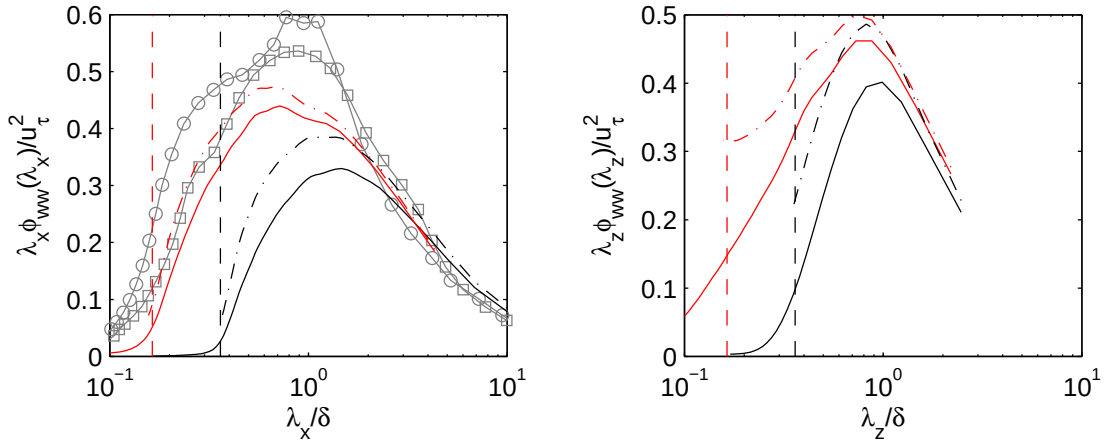

(c) $\lambda_x\phi_{ww}(\lambda_x)/u_\tau^2$ at $y/\delta = 0.14$

(d) $\lambda_z\phi_{ww}(\lambda_z)/u_\tau^2$ at $y/\delta = 0.14$

Figure 3.7: A comparison of streamwise (a,b) and spanwise (c,d) velocity spectra over streamwise (a,c) and spanwise (b,d) wavelengths at $y/\delta = 0.14$; black: LF set 2, red: SF set 2. Solid lines: uncorrected data (already presented in Figs. 3.5 and 3.6), dash-dot lines: data corrected by dividing by Ξ. Gray: data from Erm and Joubert [1991] at $Re_\theta \approx 1020$ at heights of ○: $y/\delta = 0.1$ and □: $y/\delta = 0.2$. The dashed vertical lines are the same as in Fig. 3.6.

3.2.5 2D spatial spectra

Fig. 3.8 shows the 2D streamwise and spanwise velocity spectra over all streamwise and spanwise wavelengths for both the LF and SF data of set 2. Much like in Figs. 3.5 and 3.6, it is apparent that the larger interrogation window for the LF data attenuates small scales in the flow and skews the distribution of energy presented by the spectrum. This is less of an issue further from the wall where the small scales are less energetically significant as shown in Fig. 3.9 presenting the spectra at $y/\delta = 0.48$.

In each figure, the black line denotes wavelength pairs with an aspect ratio (λ_x/λ_z) equal to one. For the streamwise velocity spectrum, the aspect ratio is large, following the red line where $\lambda_x/\lambda_z = 10\lambda_z$, with a preference for streamwise-aligned scales even down to the smallest energetically significant scales. For the spanwise velocity spectrum, though, the aspect ratio is much closer to 1 over a large range of scales (even up to $\lambda_x/\delta = \lambda_z/\delta = 0.65$, a peak not picked up in the LF data). This is comparable to the turbulent channel flow computations of Jiménez et al. [2004] where the streamwise velocity spectrum and streamwise, wall-normal cospectrum had a large aspect ratio (what the authors called anisotropic) compared to the spanwise and wall-normal velocity spectra with an aspect ratio close to, but not quite equal to, 1 (what the authors called isotropic). These authors also found that the energetic peak of the streamwise spectrum closely followed the line $\lambda_z^+ = 13(\lambda_x^+)^{1/3}$, or in terms of outer units, $\lambda_x/\delta = 13/Re_\tau^{2/3}(\lambda_z/\delta)^{1/3}$ at $y^+ = 15$.

For both streamwise and spanwise velocity fluctuations, the attenuation of small scales becomes important near the wall, where spanwise resolution is the main concern for streamwise velocity fluctuations. This is demonstrated in Fig. 3.8 where a strong energetic peak is found in the SF data that lies in a region where the LF data has already become significantly attenuated. For the spanwise velocity fluctuations, the resolution in x and z are equally important, although the peak in the spanwise velocity spectrum is centered at longer wavelengths in both the streamwise and spanwise direction when compared to the peak in the streamwise velocity spectrum.

These trends help to explain the differences in the LF and SF 1D spectra presented in Fig. 3.7. Being that the streamwise velocity spectrum has a peak of nearly constant λ_z for changing λ_x (due to the large aspect ratio mentioned earlier), a change to the spectrum over a single spanwise wavelength will affect the shape of the spectrum over a broad range of streamwise wavelengths as evidenced in Fig. 3.7a. On the other hand, for the spanwise velocity spectrum, the peak in λ_z changes evenly with the change in λ_x (the aspect ratio is near 1), so the effects of attenuation or modification of short streamwise wavelengths only modifies the spectrum over a range of short spanwise wavelengths and likewise for larger scales.

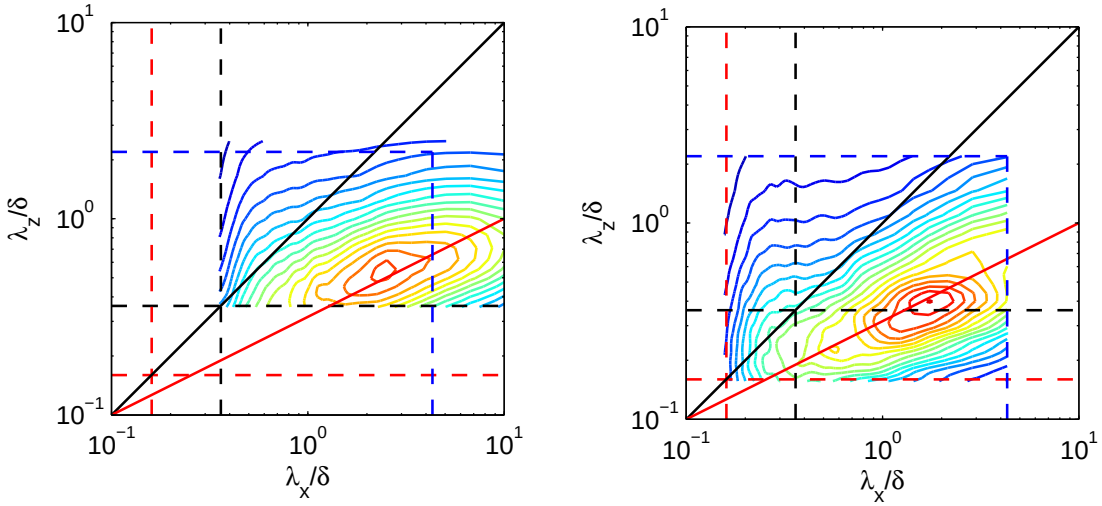

(a) LF $\lambda_x\lambda_z\phi_{uu}(\lambda_x,\lambda_z)/u_\tau^2$

(b) SF $\lambda_x\lambda_z\phi_{uu}(\lambda_x,\lambda_z)/u_\tau^2$

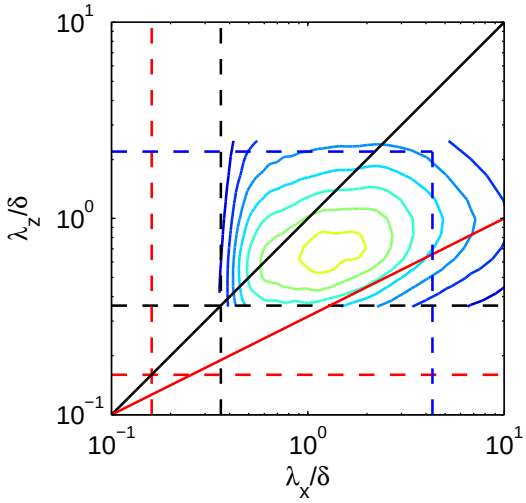

(c) LF $\lambda_x\lambda_z\phi_{ww}(\lambda_x,\lambda_z)/u_\tau^2$

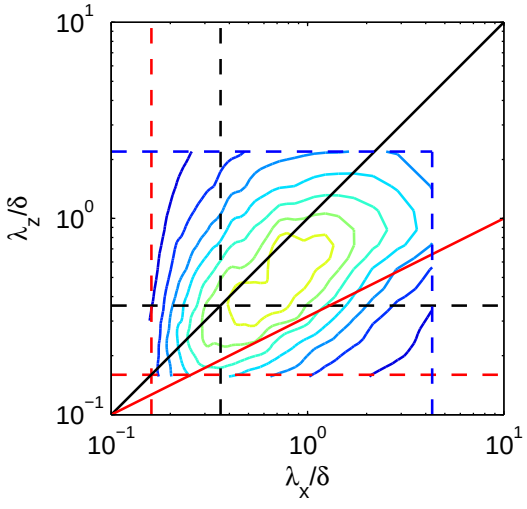

(d) SF $\lambda_x\lambda_z\phi_{ww}(\lambda_x,\lambda_z)/u_\tau^2$

Figure 3.8: The 2D velocity spectrum over all streamwise and spanwise wavelengths at $y/\delta = 0.08$ (calculated from set 2) for LF (a,c) and SF (b,d) data for streamwise (a,b) and spanwise (c,d) velocity fluctuations. The data have been divided by Ξ. The contour levels represent energy with the lowest level being (a,b): 0.05 and (c,d): 0.025, and increasing in steps of (a,b): 0.05 and (c,d): 0.025 between contours; least energetic: blue, most energetic: red. Dashed red and black lines: same as in Fig. 3.5, dashed blue lines: largest resolvable wavelengths for the SF data, solid black line: $\lambda_x = \lambda_z$, solid red line: $\lambda_x/\lambda_z = 10\lambda_z$

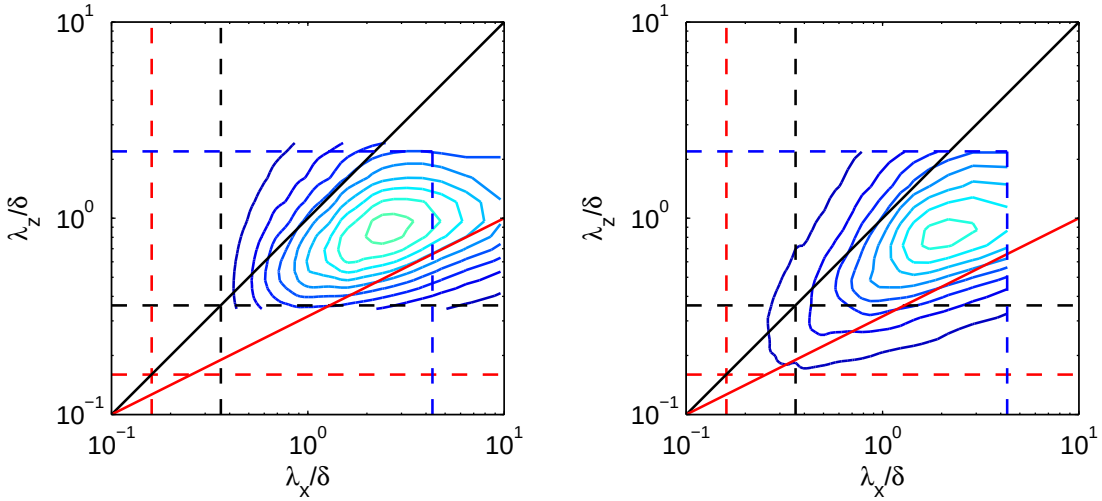

(a) LF $\lambda_x\lambda_z\phi_{uu}(\lambda_x,\lambda_z)/u_\tau^2$

(b) SF $\lambda_x\lambda_z\phi_{uu}(\lambda_x,\lambda_z)/u_\tau^2$

(c) LF $\lambda_x\lambda_z\phi_{ww}(\lambda_x,\lambda_z)/u_\tau^2$

(d) SF $\lambda_x\lambda_z\phi_{ww}(\lambda_x,\lambda_z)/u_\tau^2$

Figure 3.9: Same as Fig. 3.8 except at $y/\delta = 0.48$

3.2.6 2D spatio-temporal spectra

The spectra over streamwise and temporal wavelength are presented in Fig. 3.10 at y/δ = 0.08 and Fig. 3.11 at y/δ = 0.48. These spectra can be used to illustrate the spread of scale convection velocities when considering the flow as a composition of traveling waves. In each figure, the solid black line indicates the local mean. If there were a perfect one-to-one correspondence between streamwise and temporal wavelengths, then these spectra would collapse onto the black line. Nonetheless, if the spectra are symmetric about this line, then Taylor's hypothesis (the hypothesis that a temporal signal can be converted to a spatial signal by multiplying by the local mean velocity) will still hold as the integral of these spectra in either λ_x or T will be identical.

The spread of these spectra for both streamwise and spanwise velocity fluctuations narrows as the free stream is approached. In most cases the spectra are also bounded by the minimum convection velocity, $U^+_{c,min}$ = 8 [Morrison et al., 1971], and the maximum convection velocity, U_∞, shown by the dashed black lines. The lower limit appears to be valid in all cases, except near the wall for a small portion of long wavelength low energy streamwise velocity fluctuations (e.g., Figs. 3.10a and 3.11a). On the other hand, a small portion of large streamwise scales tend to travel faster than the free-stream velocity in all cases except at planes near the wall for spanwise velocity fluctuations.

These spectra show a larger spread in convection velocities for longer wavelength fluctuations, particularly for streamwise velocity fluctuations. For spanwise velocity fluctuations, the spread is more even, especially at y/δ = 0.08, where the spectral contours appear nearly elliptical. In all cases, the peak in the spectrum is usually near the local mean velocity, with the speed being a little slower than the local mean for both streamwise and spanwise velocity fluctuations in plane LF0, although the SF data at the same wall-normal location does not show this trend. The decrease in the spread of convection velocities with distance from the wall already noted would be required if Taylor's hypothesis were to hold and scales were restricted to travel slower than the free-stream velocity. That is, further from the wall, the local mean is closer to the free-stream velocity, and, if the convection velocity is bounded by the free-stream velocity, then the spectrum would have to thin on the high-speed side. Furthermore, to retain symmetry about the local mean velocity line, the low-speed side would have to thinned by an equal amount.

Other interesting features include the plateau of streamwise velocity fluctuations seen in the SF data at y/δ = 0.08 (see Fig. 3.10b). These fluctuations at small wavelength and large time are likely introduced by noise in the measurements (perhaps insufficient particle density) and were seen in plane LF1 for set 1 as well. This region is responsible for the large peak in energy at low streamwise wavelengths shown in the 1D spectra (e.g., the streamwise velocity spectrum at y/δ = 0.08 in Fig. 3.5b). Also, as with the other spanwise velocity spectra for the 2 planes nearest the wall, the LF data shows a different trend than the SF data. For the LF data there is a kink in the spectrum around λ_x/δ = 1, beyond which scales convect faster than the local mean on average, and

below which they convect at the local mean on average. The range of wavelengths where scales travel faster than the local mean in this spectrum matches the region where discrepancies are found between the spatial and temporal spectra as will be shown in Section 3.3.

3.2.7 3D spectra

The 3D premultiplied streamwise and spanwise velocity spectra, $\lambda_x\lambda_z T\phi_{ii}(\lambda_x, \lambda_z, T)$, are presented in Fig. 3.12 for one wall-parallel plane using both LF and SF data, where the data has been corrected by Ξ. The cutoff of each spectrum is clearly shown here, and the effect of this cutoff on all of the spectra presented so far can easily be understood by considering an integration in one or more coordinate directions.

These three-dimensional spectra show not only the energy distribution over all scales, but over all scales traveling at all streamwise velocities, where the streamwise convection velocity of a scale is defined as $U_c = \lambda_x/T$. These convection velocities will be studied further in Section 3.3. In this framework, if the flow were decomposed into traveling waves as in the model of McKeon and Sharma [2010], then the spectra would be the footprints of these waves at particular wall-normal locations. For flow control applications, measurements taken at several wall-normal locations would provide a well characterized response of the boundary layer to a periodic excitation (as studied in Jacobi et al. [2010] and Jacobi and McKeon [2011] using hotwires) and alterations of the spectra would indicate how a particular input restructured the flow. Such information could be used to inform the design of devices for turbulence control.

3.2.8 Merging LF and SF spectra

Merging spectra which have different resolutions in only one dimension can be done without much difficulty. To merge the spectra together, data from the lower resolution spectrum with the larger field of view should be retained from the first data point up until the cutoff at $k_{cut} = 2.8/W_I$. Data for the high-resolution spectrum with a smaller field of view should be ignored for the first several points due to differences in the low-wavelength tail that arise due to leakage from surrounding frequencies. The effect of the window length on the low-wavelength tail is shown using long-time hotwire measurements in Fig. 5.10 of Section 5.4.1. Using this figure as a guide, the exact wavenumber below which the high resolution data can be used depends on the size of the window with respect to the longest wavelength peak in the spectrum. The two partial spectra retained can then be joined together and renormalized so that the area is equal to $\overline{u_i^2}$ for the spectrum with the higher spatial resolution, and thus the more correct measurement of $u_{i,rms}$.

This process becomes much more involved when the resolutions vary in two or more dimensions and the success of such a method is dependent on the shape of the spectrum. For instance, consider

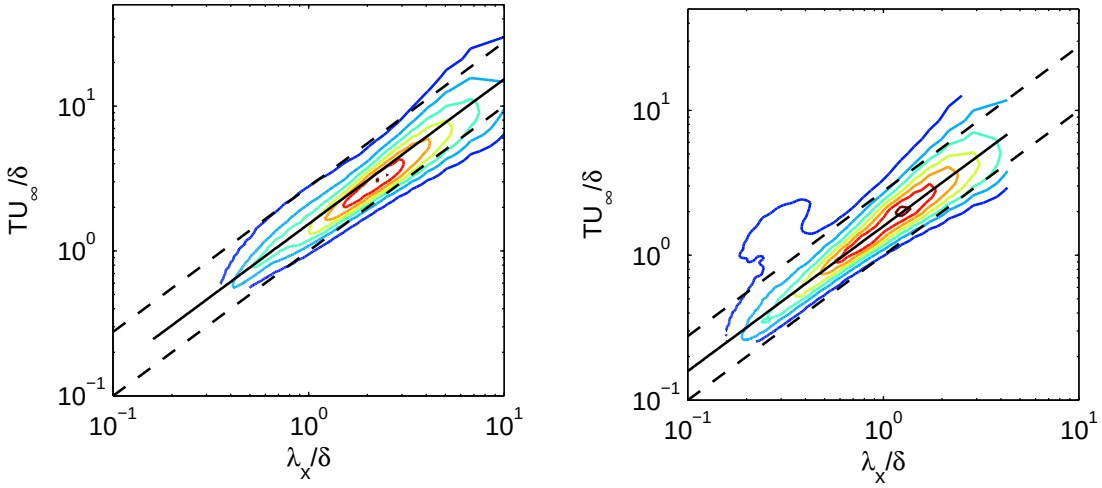

(a) LF $\lambda_x T \phi_{uu}(\lambda_x, T)/u_\tau^2$

(b) SF $\lambda_x T \phi_{uu}(\lambda_x, T)/u_\tau^2$

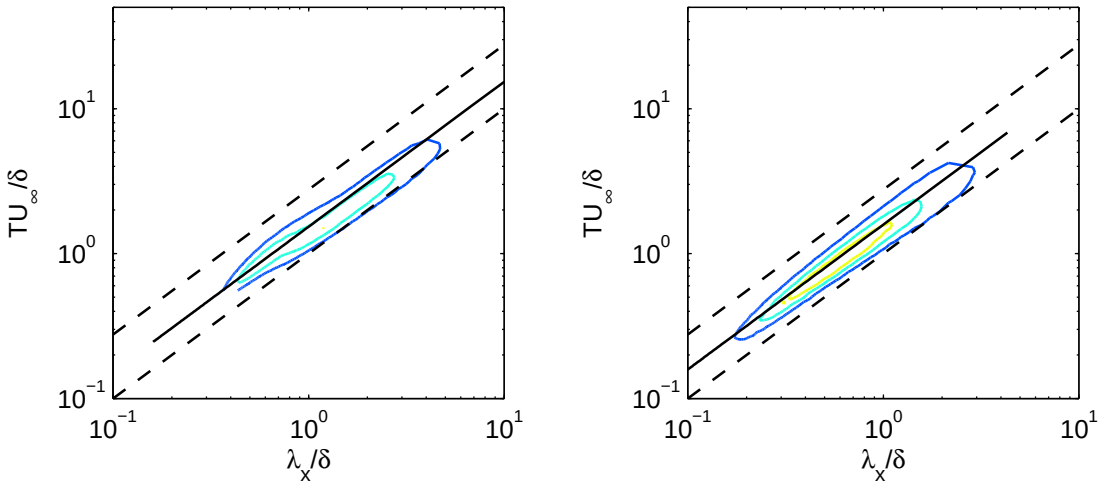

(c) LF $\lambda_x T \phi_{ww}(\lambda_x, T)/u_\tau^2$

(d) SF $\lambda_x T \phi_{ww}(\lambda_x, T)/u_\tau^2$

Figure 3.10: The 2D velocity spectrum over all streamwise and temporal wavelengths at $y/\delta = 0.08$ (calculated from set 2) for both LF (a,c) and SF (b,d) data for streamwise (a,b) and spanwise (c,d) velocity fluctuations. The data have been divided by Ξ. The contour levels represent energy, with the lowest level being 0.2 and increasing in steps of 0.2 between contours for all figures; blue: least energetic, red: most energetic. Solid black line: convection velocity ($U_c = \lambda_x/T$) equal to the local mean, dotted black lines: convection velocities equal to U_∞ (highest velocity) and $8u_\tau$ (lowest velocity)

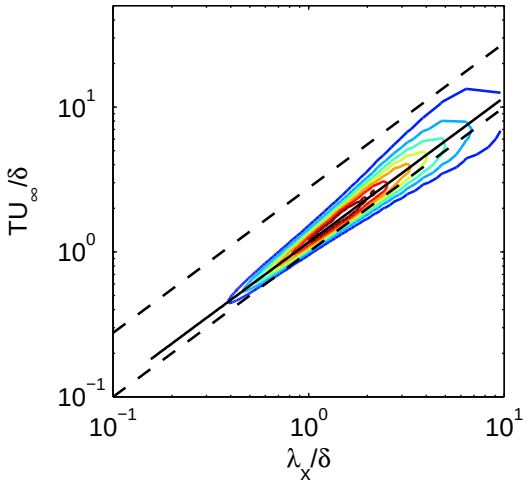

(a) LF $\lambda_x T\phi_{uu}(\lambda_x, T)/u_\tau^2$

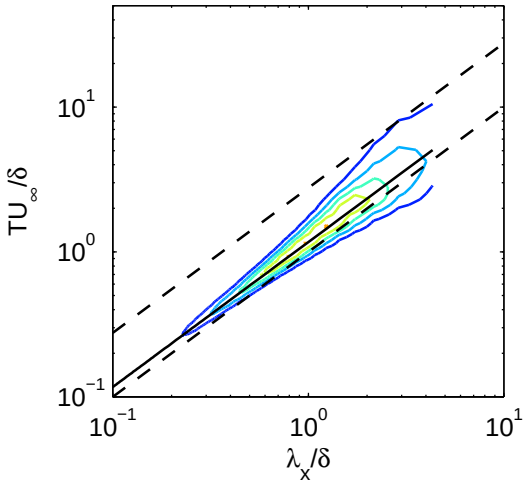

(b) SF $\lambda_x T\phi_{uu}(\lambda_x, T)/u_\tau^2$

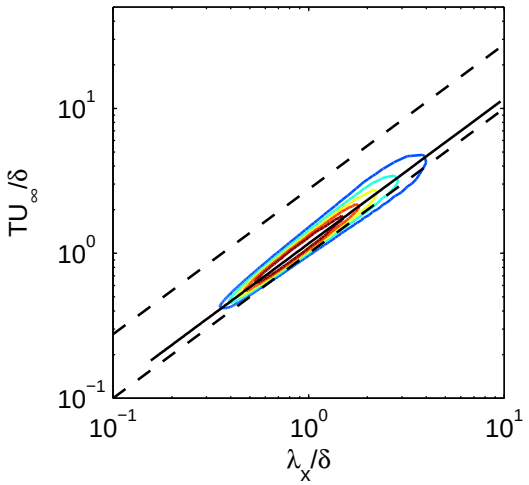

(c) LF $\lambda_x T\phi_{ww}(\lambda_x, T)/u_\tau^2$

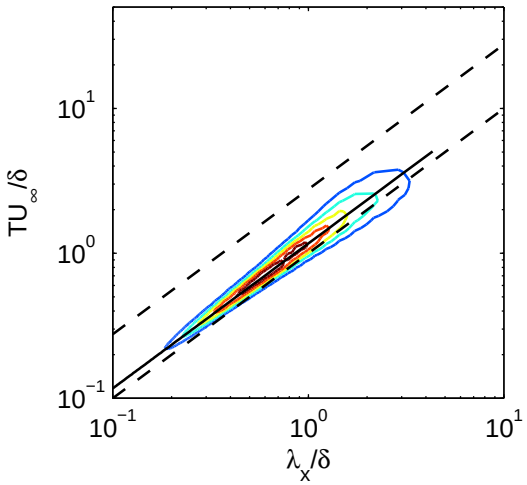

(d) SF $\lambda_x T\phi_{ww}(\lambda_x, T)/u_\tau^2$

Figure 3.11: Same as Fig. 3.10 except at $y/\delta = 0.48$

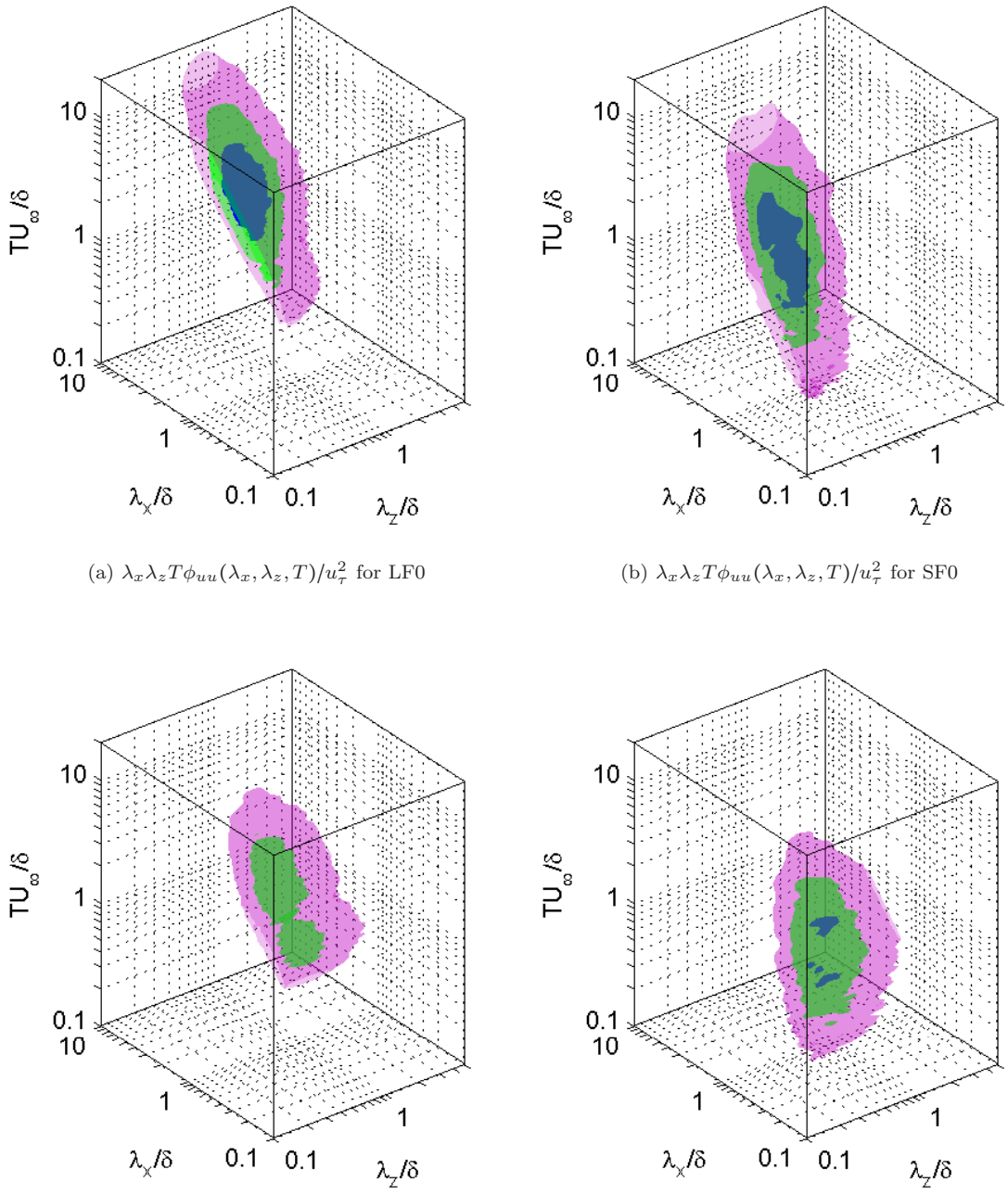

(a) $\lambda_x\lambda_z T\phi_{uu}(\lambda_x,\lambda_z,T)/u_\tau^2$ for LF0

(b) $\lambda_x\lambda_z T\phi_{uu}(\lambda_x,\lambda_z,T)/u_\tau^2$ for SF0

(c) $\lambda_x\lambda_z T\phi_{ww}(\lambda_x,\lambda_z,T)/u_\tau^2$ for LF0

(d) $\lambda_x\lambda_z T\phi_{ww}(\lambda_x,\lambda_z,T)/u_\tau^2$ for SF0

Figure 3.12: The streamwise (a,b) and spanwise (c,d) velocity spectra over all wavelengths at $y/\delta =$ 0.08 using the LF (a,c) and SF (b,d) data from set 2. The data has been corrected by Ξ. The contour levels for the streamwise velocity spectra are purple: 0.25, green: 0.5, and blue: 0.75. For the spanwise velocity spectra, the levels are purple: 0.125, green: 0.25, and blue: 0.375.

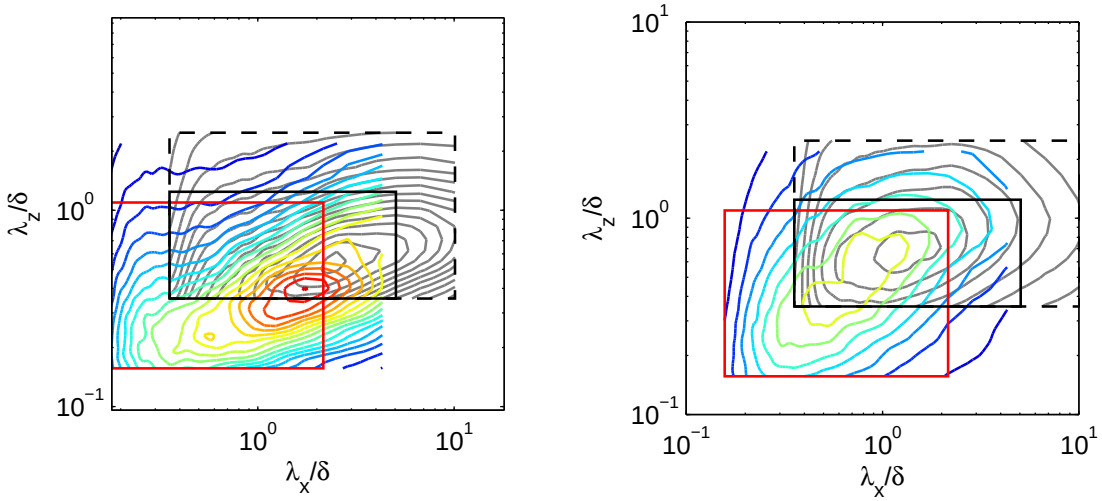

(a) Streamwise velocity spectrum

(b) Spanwise velocity spectrum

Figure 3.13: Merging of the premultiplied 2D spectra of streamwise (a) and spanwise (b) velocity fluctuations over streamwise and spanwise wavelengths, $\lambda_x \lambda_z \phi_{ii}(\lambda_x, \lambda_z)/u_\tau^2$ using the LF (gray lines) and SF (colored lines) data sets at $y/\delta = 0.08$. The limits where each spectrum is valid are outlined by a box; black: LF, red: SF, dotted: region of the LF data that is used even though the data may be distorted in this region. The contours represent energy in steps of 0.1 for the streamwise velocity spectra and 0.025 for the spanwise velocity spectra.

the SF and LF streamwise and spanwise velocity spectra presented in Fig. 3.13. Boxes have been drawn around both the LF and SF data to elucidate the region of validity of the spectra based on the criteria outlined for the 1D merging process. It is apparent that there are regions of the spectrum that will not be readily resolved by either window, that is regions of long streamwise and short spanwise wavelength as well as regions of short streamwise and long spanwise wavelength. Thus, it is not possible to seamlessly join the LF and SF data sets, particularly for the streamwise velocity spectrum. To be able to merge spectra of multiple magnifications in the current case, more cameras would be needed to extend the field of view in both the streamwise and spanwise directions. Potentially a higher resolution CCD could be used instead assuming that a high enough seeding density were possible to retain the same size interrogation windows. Of course, if the goal was only to observe the dominant peak in energy over streamwise and spanwise wavelengths and integration did not need to be performed in either spatial direction, then simply using multiple magnifications of the same area would suffice.

3.3 Convection velocities

Taylor's hypothesis is investigated by directly comparing the spatial and temporal spectra in Fig. 3.14. The corrected data is presented noting that the comparison is similar for the uncorrected data. For

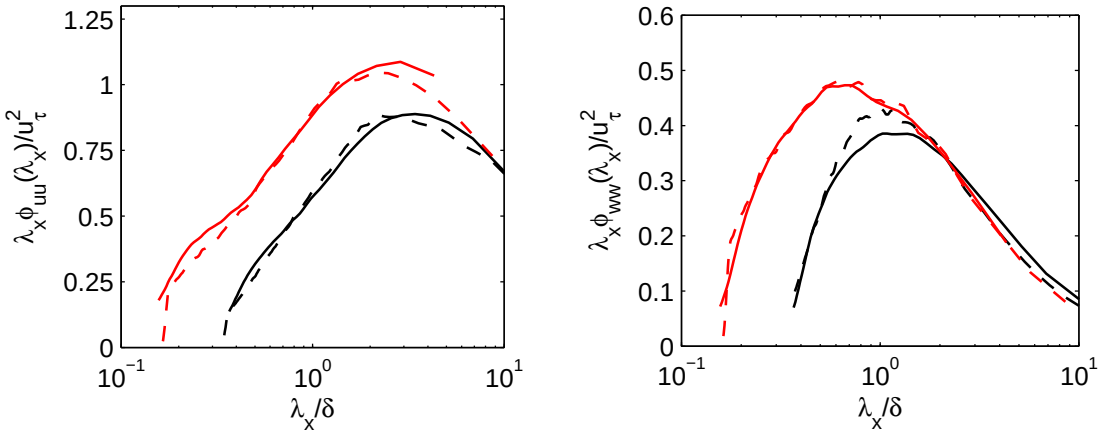

(a) Streamwise velocity spectrum comparison

(b) Spanwise velocity spectrum comparison

Figure 3.14: The streamwise (a) and spanwise (b) velocity spectra are compared at $y/\delta = 0.14$ over streamwise wavelength (solid lines) and over time (dotted lines), converted to space utilizing Taylor's hypothesis. Black: LF, red: SF. The data were corrected by Ξ.

Table 3.1: Taylor-equivalent spatial resolution

Plane	1-LF1	1-LF2	1-LF3	2-LF0 / SF0	2-LF1 / SF1	2-LF2 / SF2	2-LF3 / SF3
Δx_T^+	6.6	8.2	10.1	12.1 / 4.7	12.6 / 5.2	14.1 / 5.8	10.7 / 6.5

the streamwise velocity spectrum, the agreement between the two measures is good with the spectrum over streamwise wavelengths (solid line) having a slightly higher peak at long wavelengths as shown in Fig. 3.14a. As this difference is larger for the SF data where the resolution of large scales is worse, it is expected that this difference may be exaggerated due to poor resolution of the large streamwise wavelength end of the spectrum. A small discrepancy is also noted at short wavelengths which arose from the cutoff applied in frequency space (this cutoff is visible in Fig. 3.10).

For the spanwise velocity spectrum the SF shows good collapse over the whole range of streamwise wavelengths, even at long wavelengths. The difference noted for the LF data where the peak at $\lambda_x/\delta = 1$ is lower for the spatial compared to the temporal wavelength was also noted in the spectrum over streamwise wavelength and time presented in Fig. 3.10c. This is linked to the difference in the two spectra at long wavelengths.

For reference, the temporal spacing between data points has been converted to the spatial domain in Table 3.1 for comparison with the streamwise and spanwise resolution of the flow.

The effect of applying Taylor's hypothesis can also be tested by direct comparison of the 2D spatial streamwise or spanwise velocity spectra to the 2D spatio-temporal streamwise or spanwise velocity spectra. Such a comparison is shown at $y/\delta = 0.08$ in Fig. 3.15. The agreement is quite favorable, even at this point near the wall. One major difference is observed in the peak location of the spanwise velocity spectrum using the LF data as shown in Fig. 3.15c. As noted with all spanwise

velocity spectra, the aspect ratio of the energetic peak is near 1, so the streamwise resolution becomes more important, particularly near the wall. Thus, this difference may be a resolution issue and not a contradiction of Taylor's hypothesis. Another difference is noted, though, in the peak location for the streamwise velocity spectrum using the SF data. This difference may be indicative of a scale-dependent convection velocity since the two spectra match well except over a small wavenumber range. This difference is found over long streamwise wavelengths that may be the footprints of large streamwise structures that reach up further into the boundary layer and travel faster than the local mean. Differences at short streamwise wavelengths for this spectrum, though, are from noise in the flow (see Fig. 3.10b, where the noise plateau is noted in the range $\lambda_x/\delta = 0.18$–0.43 and $TU_\infty/\delta = 0.8$–2.5, which is equivalent to $\lambda_x/\delta = 0.5$–1.6 applying Taylor's hypothesis).

To gain further insight into a potential scale-dependent convection velocity, a single convection velocity can be calculated for each streamwise and spanwise scale pair from the three-dimensional spectrum using Eqn. 3.18, which is a modified form of the equation given by del Álamo and Jiménez [2009] and used in earlier works by Jiménez et al. [2004] and Flores and Jiménez [2006]. The modification was simply to write the convection velocity over wavelength as opposed to wavenumber.

$$U_c(\lambda_x, \lambda_z, y) = \lambda_x \frac{\int_{-\infty}^{\infty} \phi_{ij}(\lambda_x, \lambda_z, T, y) dT}{\int_{-\infty}^{\infty} T \phi_{ij}(\lambda_x, \lambda_z, T, y) dT} \tag{3.18}$$

This convection velocity definition uses a value of T that is weighted by the 3D streamwise velocity spectrum. In this way, it gives the dominant convection velocity for each streamwise-spanwise scale pair. A map of the convection velocity is presented in Fig. 3.16 where lines of constant convection velocity are plotted on top of $\lambda_x \lambda_z \phi_{ii}(\lambda_x, \lambda_z)$ to highlight the convection velocity of the most energetic scales. These maps provide a mapping between the spatial and temporal signal for each streamwise and spanwise scale pair. As demonstrated, the convection velocity does not have a strong dependence on the spanwise scale of the flow, except for some deviations for long streamwise wavelengths. These deviations, along with deviations between the LF and SF data, can be explained by the limited temporal resolution of the data sets.

In Fig. 3.17, slices of the 3D velocity spectrum at constant T (shown in red) are overlaid on the streamwise velocity spectrum over streamwise and spanwise wavelengths for both LF and SF data. These slices are taken at the largest and smallest T resolvable with the present data, that is they are taken from the top and bottom of the spectrum shown in Fig. 3.12a or 3.12b. When calculating the scale based convection velocity using Eqn. 3.18, integration is performed in T between these cuts. Any energy in the flow beyond these limits is not captured by the current measurements and results in an incorrect estimate of the convection velocity, at least over some range of wavelengths. These red contours are included to highlight the region where the convection velocity as well as the shape of the 2D spatial spectrum (also calculated by an integral in T) will likely be incorrect. Note

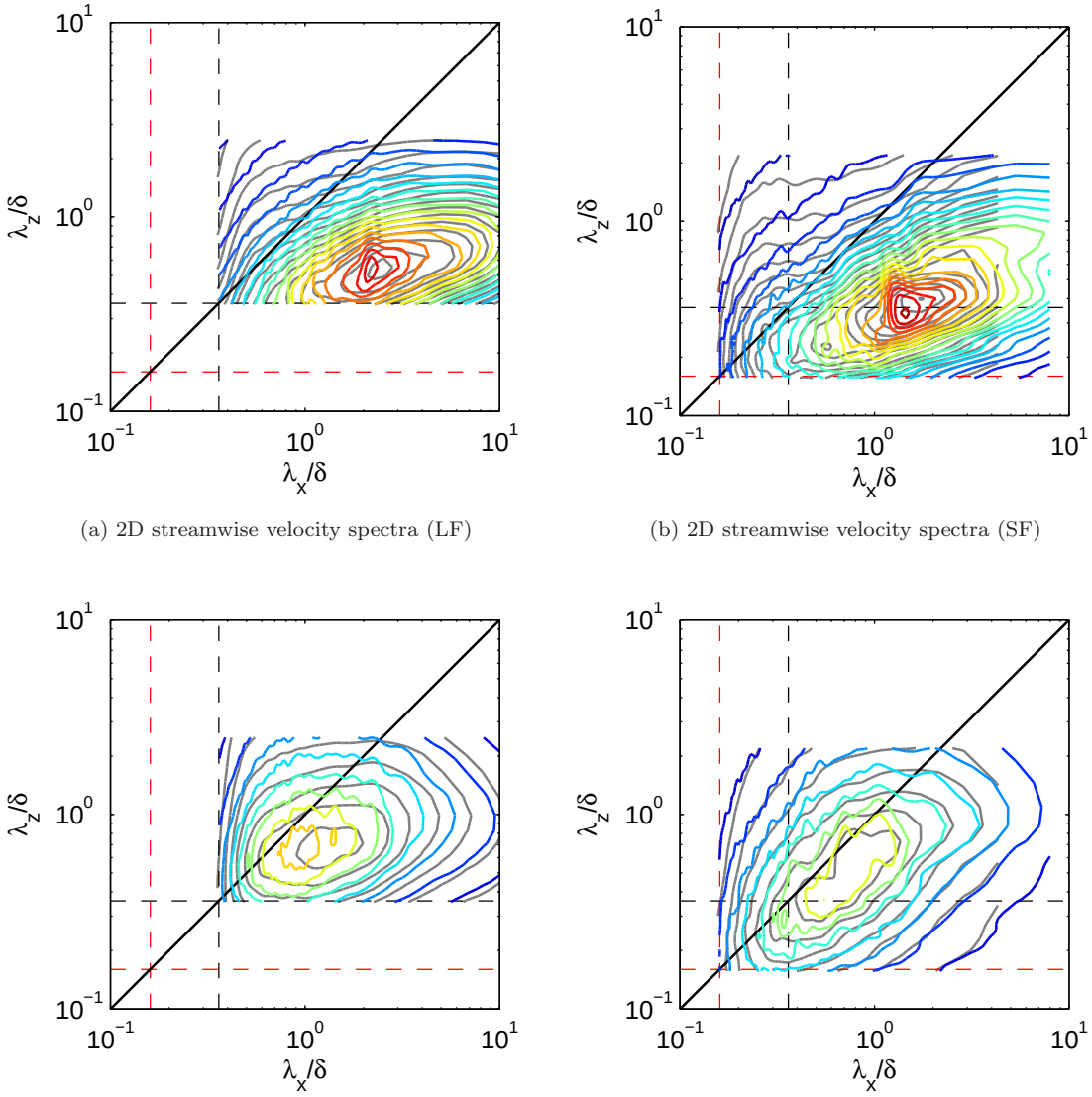

(a) 2D streamwise velocity spectra (LF)

(b) 2D streamwise velocity spectra (SF)

(c) 2D spanwise velocity spectra (LF)

(d) 2D spanwise velocity spectra (SF)

Figure 3.15: A comparison of the streamwise (a,b) and spanwise (c,d) velocity spectra over streamwise and spanwise wavenumber (solid gray lines) with the spectrum over streamwise wavelength and time (colored lines), converted to streamwise and spanwise wavelength using Taylor's hypothesis; (a,c): LF, (b,c): SF. The data have been divided by Ξ. The contours represent energy starting from (a,b): 0.05, (c,d): 0.025 and increasing in steps of (a,b): 0.05, (c,d): 0.025; blue: least energetic, red: most energetic

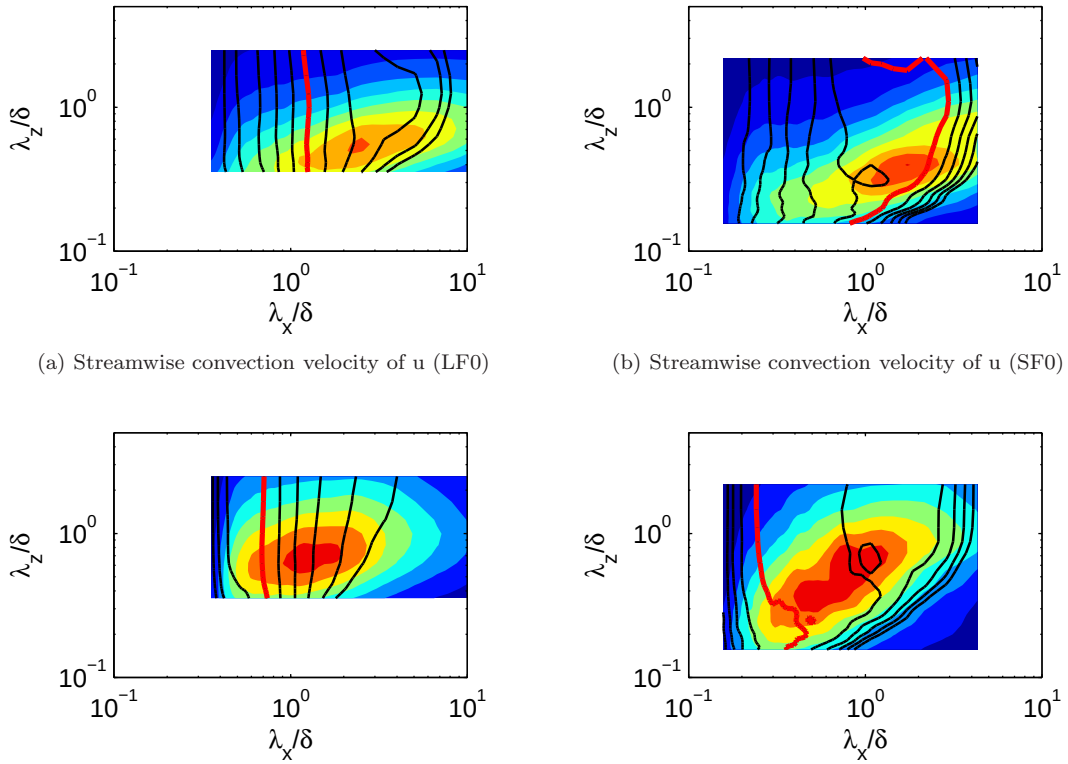

(a) Streamwise convection velocity of u (LF0)

(b) Streamwise convection velocity of u (SF0)

(c) Streamwise convection velocity of w (LF0)

(d) Streamwise convection velocity of w (SF0)

Figure 3.16: The convection velocity maps for streamwise (a,b) and spanwise (c,d) velocity fluctuations over all wavelengths using the LF (a,c) and SF (b,d) data from set 2. The data has been corrected by Ξ. Red line: local mean velocity, solid black lines: convection velocity increasing in increments of $u^+ = 1$ to the right of the local mean and decreasing in increments of $u^+ = 1$ to the left. These contour lines are plotted on top of filled contours of $\lambda_x \lambda_z \phi_{ii}(\lambda_x, \lambda_z)/u_\tau^2$ to highlight the most energetic convection velocities. The contour levels for the streamwise velocity spectra change in steps of 0.2 and those for the spanwise velocity spectra change in steps of 0.025.

that for the calculation of the spectrum, integration is performed up until zero wavenumber (infinite wavelength) and does not stop at the large T cutoff. Nonetheless, the large wavelength portion of the spectrum is distorted slightly due to the lack of information of the spectral shape between the largest resolvable temporal wavelength and infinity.

Now consider the effects of this under-resolution on the calculated convection velocities. On the small-scale end of the spectrum, energy at shorter temporal wavelengths is unresolved and thus there is a bias toward longer wavelengths, or equivalently slower convection velocities. Likewise, for the large-scale end of the spectrum, energy at larger temporal wavelengths is unresolved and thus there is a bias toward shorter wavelengths, or equivalently faster convection velocities.

From this, the deviation of the convection velocity contours from a straight line in λ_z may be due to the variable amount of unresolved energy in λ_z for long streamwise scales indicated by the curved contours in Fig. 3.17 at large λ_x. Comparing the regions over which this long time cutoff extends

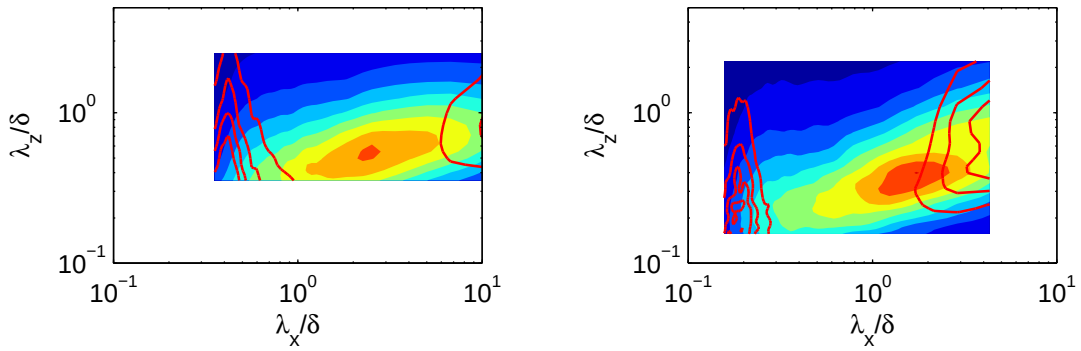

(a) LF $\lambda_x\lambda_z\phi_{uu}(\lambda_x,\lambda_z)/u_\tau^2$ (b) SF $\lambda_x\lambda_z\phi_{uu}(\lambda_x,\lambda_z)/u_\tau^2$

Figure 3.17: Regions affected by temporal cutoffs of the 3D spectrum. Filled contours: premultiplied streamwise velocity spectra over streamwise and spanwise wavelength using the (a) LF and (b) SF data with energy increasing in increments of 0.1 between contours. Red contours: streamwise-spanwise cuts of the 3D velocity spectrum at the maximum and minimum temporal wavelengths obtained with levels starting at 0.05 and increasing in steps of 0.05

for both sets of data, it is also apparent that the SF data feels this effect more strongly, hence why the convection velocity contours are more curved at longer wavelengths in the SF compared to the LF data. On the small wavelength side, this cutoff accounts for the rapid decrease in convection velocity as the smallest resolvable streamwise wavelength is approached.

Using these scale-dependent convection velocities, the conversion between the spatial and temporal domain can be computed as shown in Fig. 3.18 and compared to the case of using a constant convection velocity (see Fig. 3.15). These conversions work well with the exception of scales with long streamwise wavelengths and short spanwise wavelengths. It is already apparent that at long streamwise wavelengths the shape of the spectrum is incorrect due to spectral leakage between surrounding energetic wavelengths in the spectrum. Thus, the integration to find the convection velocity will be distorted. Another exception is noted for all small streamwise scales. This disagreement comes from the low-pass filter applied in time to eliminate temporal aliasing. Due to this filter, there is no information from which to calculate a convection velocity for small streamwise scales. Besides these differences, the scale-based convection velocity does help to bring the peak location of the spectra into agreement better than using a single convection velocity. For instance, compare the agreement between the peak locations in Fig. 3.18b and 3.18c using the variable convection velocity to those in Fig. 3.15b and 3.15c using a fixed convection velocity.

Earlier work by Monty and Chong [2009] also investigated the effect of using a scale-dependent convection velocity for converting 1D streamwise velocity spectra over temporal wavelength to streamwise wavelength and found that the effect is most critical for long temporal wavelengths, particularly for flow near the wall. We also find that convection velocities of scales larger than the boundary layer thickness tend to travel faster than the local mean (see Fig. 3.16), and thus need to

be corrected for.

3.4 Large-scale small-scale interaction

In order to quantify the interaction of large-scale and small-scale motions in the flow, the method of Chung and McKeon [2010] from their computational study of channel flow was used, which is equivalent to methods used by Bandyopadhyay and Hussain [1984] in a turbulent boundary layer and Guala et al. [2011] in the atmospheric surface layer. The moving average filter described in Eqn. 3.19 was used to extract the large-scale signal of the flow, $U_L(t)$, in time for a fixed point in space.

$$U_L(t) = \frac{1}{\tau_L} \int_{t-\tau_L/2}^{t+\tau_L/2} U(t')dt' \tag{3.19}$$

In the equation, τ_L is the length of the window used in the moving average which dampened fluctuations at frequencies higher than $1/\tau$. For all measurements presented here, $\tau_L = \delta/U(y)$. Assuming that Taylor's hypothesis holds and all scales convect at the local mean, this filter will separate scales smaller than and larger than the boundary layer thickness. The small-scale signal was then calculated as $U_S = U - U_L$. As with the analysis of Chung and McKeon [2010], the correlation between the envelope of the small scales, $\tilde{U}_S$ defined in Eqn. 3.20, and the large scales was used to extract information about the interaction of the large and small scales.

$$\tilde{U}_S(t) = \sqrt{\frac{1}{\tau} \int_{t-\tau_L/2}^{t+\tau_L/2} U_s^2(t')dt'} \tag{3.20}$$

The correlation between the large scales and the envelope of the small scales, $R_{u_L,\tilde{u}_S}$, is given in Eqn. 3.21 and provides an indication of the phase difference between the two signals.

$$R_{u_L,\tilde{u}_S}(y) = \frac{\overline{(U_L(y,t) - \overline{U}_L(y)) \cdot \left(\tilde{U}_S(y,t) - \overline{\tilde{U}}_S(y)\right)}}{\sqrt{\overline{(U_L(y,t) - \overline{U}_L(y))^2}\,\overline{\left(\tilde{U}_S(y,t) - \overline{\tilde{U}}_S(y)\right)^2}}} \tag{3.21}$$

The over bar indicates averaging in time (the direction of filtering) and over all statistically independent realizations. In Figs. 3.19 and 3.20, the correlation coefficient is presented at all measured wall-normal location for the correlation between the large streamwise velocity scales and the envelope of the small streamwise (Fig. 3.19), wall-normal (Fig. 3.20a), and spanwise (Fig. 3.20b) velocity scales. Only data from set 2 was used in these calculations. Compared to the results of Mathis et al. [2009b], our data shows fair agreement in the wake region when scaled in outer units. The results differ slightly when compared to Chung and McKeon [2010], but this is expected due to the difference in the wake region between internal and external flows. Compared to either, agreement is

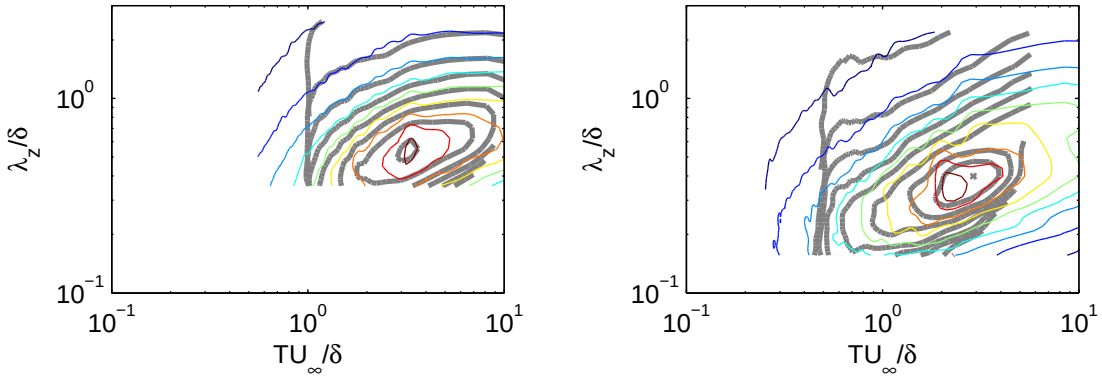

(a) Streamwise velocity spectrum LF0

(b) Streamwise velocity spectrum SF0

(c) Spanwise velocity spectrum LF0

(d) Spanwise velocity spectrum SF0

Figure 3.18: Space-time conversion using convection velocity maps. The streamwise (a,b) and spanwise (c,d) velocity spectra at $y/\delta = 0.08$ are presented over streamwise and spanwise wavelengths ($\lambda_x \lambda_z \phi_{ii}(\lambda_x, \lambda_z)/u_\tau^2$) using the LF (a,c) and SF (b,d) data sets. Colored contours: original spectra over time and spanwise wavelength, gray contours: spatial spectra converted using the convection velocity maps in Fig. 3.16. Contour levels increase in increments of 0.1 for streamwise velocity spectra and 0.025 for spanwise velocity spectra.

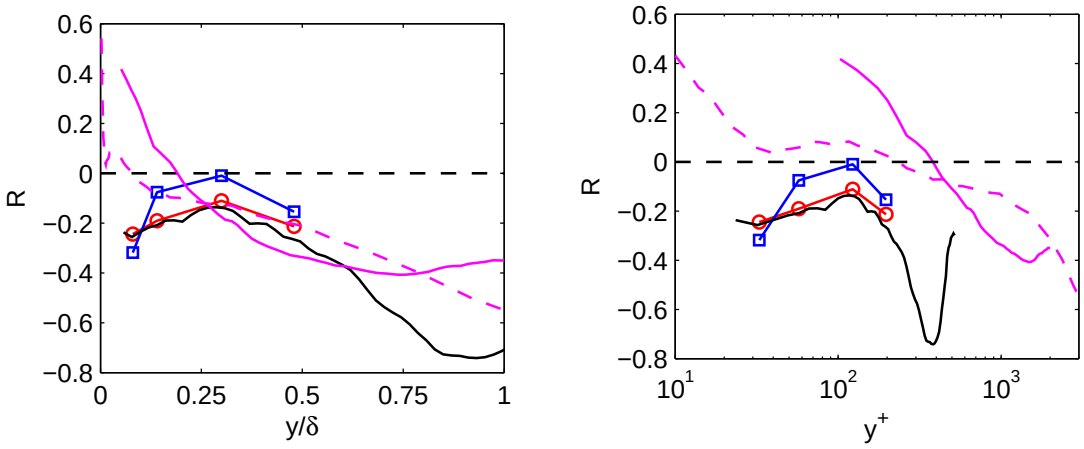

(a) $R_{u_L,\tilde{u}_S}$ Outer units (b) $R_{u_L,\tilde{u}_S}$ Inner units

Figure 3.19: The correlation coefficient between the large-scale streamwise velocity fluctuations, u_L, and the envelope of the small-scale streamwise velocity fluctuations, $\tilde{u}_S$ in inner (a) and outer (b) units. Black line: correlation from wall-normal measurements, symbols: wall-parallel measurements; red ○: SF, blue □: LF data, solid magenta line: data from the large eddy simulation of channel flow by Chung and McKeon [2010] at Re_τ = 2000, dotted magenta line: data from the boundary layer experiments of Mathis et al. [2009b] at Re_τ = 3000

poor in the log layer and below, even when scaled in inner units.

Oddly, the streamwise velocity correlation does not show a positive correlation near the wall as found by Chung and McKeon [2010] in channel flow and by Mathis et al. [2009b] for boundary layers, and even the streamwise-spanwise correlation only shows a slightly positive value near the wall. This would indicate that the large and small scales in all measured planes are more than 90 degrees out of phase, where the signals approach 180 degrees out of phase as the free stream is approached. Of course, care must be taken in comparing these flows due to the difference in Reynolds numbers (the present data is at $Re_\tau \approx 410$ compared to Re_τ = 2000 from Chung and McKeon [2010] and Re_τ = 3000 by Mathis et al. [2009b]). For this reason, the data have been presented in both inner and outer units in Fig. 3.19. The trend appears to be correct when presented in inner units, but the value of the correlation is still less than expected and negative. This negative value may be explained by the limited range of resolution, both missing the largest energetic scales (particularly for the SF data where the streamwise resolution is limited to about 4.5δ) as well as the smallest. This is investigated using well-resolved hotwire measurements in Fig. 5.8 of Section 5.3.3.

It is interesting to note that the correlation between the large streamwise scales and the small streamwise, spanwise, and wall-normal scales is similar beyond approximately 0.3δ, which is near the edge of the log region. Thus, the effect of the large scales on the small scales may be more uniform in the wake region of the flow.

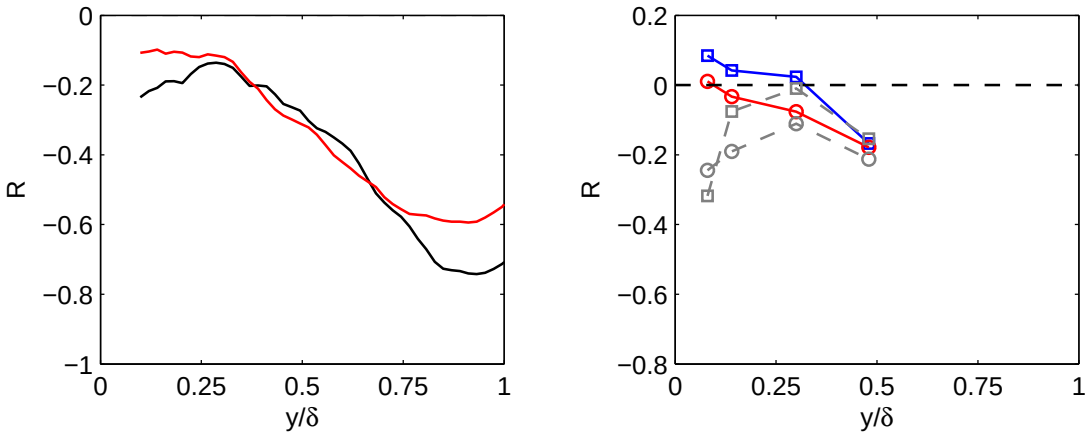

(a) $R_{u_L,\tilde{v}_S}$ (b) $R_{u_L,\tilde{w}_S}$

Figure 3.20: (a): Correlation between the large-scale streamwise velocity signal and small-scale envelope of black: streamwise and red: spanwise velocity fluctuations using wall-normal measurements. Note the similarity in the correlation coefficients between y/δ = 0.3 and 0.75. (b): Correlation between the large-scale streamwise velocity signal and the small-scale envelope of spanwise velocity fluctuations using red: SF, and blue: LF wall-parallel data. $R_{u_L,\tilde{u}_s}$ is shown in gray with corresponding symbols for comparison. Note the similarity beyond y/δ = 0.3.

3.5 Summary

In this chapter, the statistics associated with time-resolved PIV measurements were discussed and a velocity spectrum over streamwise, spanwise, and temporal wavelengths was calculated. Methods were outlined to correct for spectral leakage, attenuation of small scales, and spatial and temporal aliasing for this calculation. The calculation of this spectrum using a high resolution small field of view (SF) and low resolution large field of view (LF) clearly demonstrated the effects of spatial resolution on the spectrum. For measurements of streamwise velocity fluctuations, the attenuation of small spanwise scales by the PIV interrogation window size affected the shape of the spectrum over all streamwise and temporal wavelengths. On the other hand, for spanwise velocity fluctuations, this effect was more concentrated toward the small-scale end of the spectrum over streamwise and temporal wavelengths. From this, it is clear why a resolution of $20\delta_\nu$ would be necessary for accurate analysis of the turbulent statistics. Similar effects can be expected using Large Eddy Simulation (LES) for boundary layer computations and these effects need to be accounted for by the sub-grid scale model.

Upon comparison to the literature, it was shown that the SF data set with a spatial resolution of $30\delta_\nu$ resolved the flow well while the LF data set did not. While most SF statistics matched well with data from the literature, the measurement of the amplitude modulation near the wall did not. This could be an effect of the low Reynolds number of these measurements, but this hypothesis would need to be tested by using the same setup at a higher Reynolds number, or equivalently,

taking well-resolved hotwire measurements at a lower Reynolds number for comparison.

The effect of applying Taylor's hypothesis was investigated at each wall-normal location, and, for the 1D spectra, the agreement was reasonable, particularly above y/δ = 0.14. Comparing the 2D velocity spectra over streamwise and spanwise wavelengths to those over temporal and spanwise wavelengths showed some difference in the peak location of the streamwise velocity spectrum. By computing a map of convection velocities for each streamwise and spanwise velocity scale pair using the 3D spectrum, these differences were rectified. These convection velocity maps showed that there was little variation in the convection velocity with the spanwise size of a scale. Most of the variation was with the streamwise wavelength of the scales.

Considering the convection velocity of both streamwise and spanwise velocity fluctuations, it was interesting to note that the spread in the convection velocities of spanwise velocity fluctuations was nearly equal for scales of all streamwise wavelengths as opposed to the spread in the convection velocity of streamwise velocity fluctuations, where the spread increased with the streamwise wavelength of the scale. This was particularly notable near the wall where convection velocities for some streamwise velocity fluctuations exceeded the free-stream velocity, but appeared to be bounded by this limit for spanwise velocity fluctuations.

Finally, it was investigated whether two spectra calculated with varying spatial resolution and fields of view could be merged together so that a total picture of the velocity spectrum could be obtained using a small number of cameras (maybe even one) at multiple magnifications. Considering the streamwise velocity spectrum over streamwise and spanwise wavelengths, it became apparent that this would not be possible as, even with the 2-camera setup, the field of view was not long enough to capture structures which were streamwise elongated and narrow in the spanwise extent, and vice versa, with the former being the region of most concern. This was less of an issue for the spanwise velocity spectrum, although it was apparent that not all energy could be captured with the current setup. Even with a larger field of view and finer resolution the merging process would be difficult and would have similar requirements to resolving all of the scales in the flow at one magnification. On the other hand, if only the peak of the spectrum is to be analyzed, it would be possible to use multiple magnifications to map out this region.

Chapter 4

Coherent Structures

This chapter presents an investigation of the evolution of coherent structures in wall-parallel planes. In particular, structures associated with the dynamically significant hairpin vortex packets discussed by Adrian et al. [2000] were studied which leave a signature in the form of swirling coherent structures (SCS) and low- and high-momentum regions in wall-parallel planes. A cartoon of these structures is provided in Fig. 4.1 where the green line/plane illustrates the laser sheet used for PIV measurements. This chapter begins with a discussion of the methods for extracting these flow features as well as presenting their average sizes and shapes. Next, a method for tracking these structures is introduced, from which the trajectories, convection velocities, and lifetimes of these various structures were extracted. Finally, using the large amount of data available, swirling coherent structures are classified as attached or detached from the wall and the features of these different types of structures are presented.

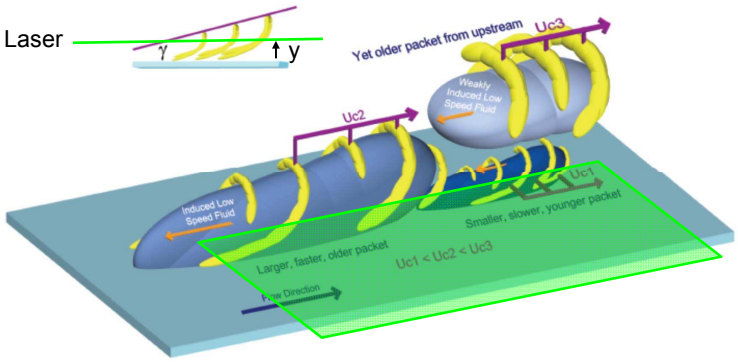

Figure 4.1: A diagram illustrating the hairpin packet paradigm from Adrian et al. [2000]. The green plane and line illustrate where the laser sheet would cut these structures when performing wall-parallel PIV measurements.

4.1 Swirling coherent structure (SCS) identification

In this section we discuss the identification of swirling coherent structures (SCS), that is, coherent structures identified by regions of swirling flow in wall-parallel planes. These structures will be interpreted as cuts of coherent vortices throughout this chapter although it is not guaranteed that these swirling structures always coincide with vortices in the flow. In the literature there are many methods proposed for identifying vortices, and subsequently SCS, but as discussed by Jeong and Hussain [1995], most intuitive measures fail to identify vortex cores. For example, the requirement that pathlines are closed or, at least, form a tight spiral, fails in that the particle traced may not complete a spiral about the core in the lifetime of the vortex. Furthermore, this method is not Galilean invariant, and thus it is difficult to identify all vortex cores in the flow as they tend to travel at a range of convection velocities. Simply using the vorticity magnitude may also fail if the background shear is comparable to the vorticity magnitude within the vortex core. Furthermore, the cutoff to identify individual vortex cores is flow dependent, and may not detect weak, yet dynamically significant vortices. Finally, the existence of a local pressure minimum which could be argued to be formed from the centrifugal force created by swirling motions in the flow is neither a sufficient nor a necessary condition for the presence of a vortex core [Jeong and Hussain, 1995].

In order to better identify vortex cores in a Galilean invariant setting, several methods have been proposed and can be found in the review of Jeong and Hussain [1995] as well as a more recent review by Chakraborty et al. [2005]. These methods include the Δ [Chong et al., 1990], Q [Hunt et al., 1988], λ_2 [Jeong and Hussain, 1995], and swirling strength ($\lambda_{c,i}$) [Zhou et al., 1999], criteria. While these methods generally provide different results in a 3D flow field, in a 2D plane, as studied here, all of the criteria are identical. Nonetheless, each method will be discussed briefly and the equivalence in a 2D field demonstrated.

4.1.1 Δ criterion

The Δ criterion developed by Chong et al. [1990] defines a vortex as a region where the velocity gradient tensor, ∇u, has complex eigenvalues, λ. These complex eigenvalues indicate that the instantaneous streamlines in a reference frame translating with a fluid particle are closed or spiraling. To determine if complex eigenvalues exist, first consider the characteristic equation for ∇u in Eqn. 4.1.

$$\lambda^3 + P\lambda^2 + Q\lambda + R = 0 \tag{4.1}$$

The three invariants are defined as $P = -\nabla \cdot u$, $Q = \frac{1}{2}\left((\nabla \cdot u)^2 - tr((\nabla u)^2)\right)$, and $R = -Det(\nabla u)$. If the discriminant of this characteristic polynomial, Δ, is positive, then complex eigenvalues will exist. For the case of an incompressible flow, $P = 0$ and the discriminant simplifies to the form of Eqn. 4.2.

$$\Delta = \left(\frac{1}{2}R\right)^2 + \left(\frac{1}{3}Q\right)^3 \tag{4.2}$$

4.1.2 Q criterion

The Q criterion introduced by Hunt et al. [1988] identifies a vortex as a region of positive Q (the invariant discussed in Section 4.1.1) where there is a local pressure minimum. Considering an incompressible flow, Q can be written in the form of Eqn. 4.3 which shows Q as a measure of the balance between the vorticity magnitude and the shear strain rate in the flow. In this equation, S and Ω are the symmetric and anti-symmetric parts of the velocity gradient tensor, respectively, and are defined as $S = \frac{1}{2}\left(\nabla u + (\nabla u)^T\right)$ and $\Omega = \frac{1}{2}\left(\nabla u - (\nabla u)^T\right)$. Thus, a region with positive Q can be interpreted as a region where the vorticity dominates.

$$Q = \frac{1}{2}\left(||\Omega||^2 - ||S||^2\right) \tag{4.3}$$

As noted by Jeong and Hussain [1995], a region of positive Q does not imply that a pressure minimum will exist in that region, although this is generally the case.

4.1.3 λ_2 criterion

This identification method proposed by Jeong and Hussain [1995] helps to eliminate regions where pressure minima exist and swirling motions do not, and vice versa, by eliminating the unsteady straining and viscous effects that create these regions in the flow. By taking the gradient of the incompressible Navier-Stokes equation and omitting the unsteady and viscous terms from the symmetric part (the anti-symmetric part is the vorticity transport equation), one will recover Eqn. 4.4

$$S^2 + \Omega^2 = -\frac{1}{\rho}\nabla(\nabla p) \tag{4.4}$$

Since the unsteady and viscous terms have been neglected, all identified pressure minima should align with swirling motions. A pressure minimum will occur in a plane with two positive eigenvalues of the pressure Hessian, or according to Eqn. 4.4, a plane where at least two of the eigenvalues of the symmetric tensor, $S^2 + \Omega^2$, are negative. If the eigenvalues of $S^2 + \Omega^2$ are ordered as $\lambda_1 \geq \lambda_2 \geq \lambda_3$, then this reduces to the requirement that $\lambda_2 < 0$. As discussed by Jeong and Hussain [1995], while the Q criterion measures the excess in rotation rate over the strain rate magnitude in all directions, the λ_2 criterion looks for this excess on a specific plane.

4.1.4 Swirling strength

This method introduced by Zhou et al. [1999], as with the Δ criterion, uses the knowledge that the existence of a pair of complex conjugate eigenvalues of the velocity gradient tensor at a point in the flow indicates spiraling streamlines. These complex eigenvalues can be written in the form $\lambda = \lambda_{c,r} \pm i\lambda_{c,i}$, where $\lambda_{c,r}$ is the real part of the complex eigenvalue and $\lambda_{c,i}$ is the imaginary part of the complex eigenvalue, also called the swirling strength. Eqn. 4.5 gives the swirling strength for a 2D measurement. The larger the value of $\lambda_{c,i}$, the higher the local swirling rate and the stronger the vortex. To better identify individual vortex cores, a threshold is often placed on the square of the swirling strength. Although $\Delta = 0$ and $\lambda_{c,i} = 0$ are equivalent, in the case of a non-zero threshold, the interpretations are much different as discussed by Chakraborty et al. [2005].

$$\lambda_{c,i}(x,z) = \left| Im\left[\sqrt{(u_x + w_z)^2 + 4(u_x w_z - u_z w_z)}\right]\right| \tag{4.5}$$

A signed swirling strength defined in Eqn. 4.6 can be used to identify the direction of rotation, as in Natrajan et al. [2007], where ω_y is the wall-normal vorticity.

$$\Lambda_{c,i}(x,z) = \|\lambda_{c,i}(x,z)\| \frac{\omega_y(x,z)}{\|\omega_y(x,z)\|} \tag{4.6}$$

4.1.5 Equivalence of methods for incompressible 2D flow

For 2D incompressible flow, the velocity gradient tensor reduces to the form of Eqn. 4.7.

$$\nabla u = \begin{bmatrix} a & b \\ c & -a \end{bmatrix} \tag{4.7}$$

The discriminant is $\Delta = a^2 + bc$, the eigenvalues are $\lambda = \pm\sqrt{a^2 + bc}$, the complex part of the eigenvalues is $\lambda_{c,i}^2 = a^2 + bc$, and $Q = -a^2 - bc$. Thus, the Δ, Q, and swirling strength criteria all require that $a^2 + bc < 0$. Furthermore, the symmetric part of the velocity gradient tensor is given in Eqn. 4.8.

$$S^2 + \Omega^2 = \begin{bmatrix} a^2 + bc & 0 \\ 0 & a^2 + bc \end{bmatrix} \tag{4.8}$$

whose eigenvalues are $\lambda = a^2 + bc$, and thus $a^2 + bc < 0$ must be satisfied for the λ_2 criterion as well.

Note that while these statements are true for incompressible flow, these four methods will provide varying results when considering 2D compressible flow. For an incompressible flow, the invariant P in Eqn. 4.1 is no longer zero, Eqn. 4.3 is no longer true, and the simplification in the velocity gradient that $\frac{\partial u}{\partial x} = -\frac{\partial v}{\partial y}$ cannot be made.

For SCS identification in the 2D incompressible boundary layer studied here, the swirling strength criterion was chosen. The threshold for extracting SCS was set such that $\lambda_{c,i} > \lambda_{rms}$, separating the swirling regions from background noise. This threshold was also considered by Wu and Christensen [2006], although they found a more stringent threshold of $\lambda_{c,i} > 1.5\lambda_{rms}$ was better for their measurements in the wall-normal plane.

4.1.6 Effect of $\lambda_{c,r}$

As discussed by Chakraborty et al. [2005], all of the methods discussed, except the λ_2 method, can be related directly to the real and imaginary parts of the complex eigenvalues of the velocity gradient tensor (i.e., $\lambda_{c,r}$ and $\lambda_{c,i}$). From the thorough analysis of these authors, it was proposed that the main differences between the four vortex identification methods can be rectified by choosing an appropriate ratio of $\lambda_{c,r}/\lambda_{c,i}$, termed the "inverse spiraling compactness", in addition to a cutoff in $\lambda_{c,i}$. The argument is that while $\lambda_{c,i}$ is a measure of the local swirling rate, $\lambda_{c,r}$ measures the strength of stretching (negative) or compression (positive) of the vortex. A negative ratio would indicate that the vortex has a tendency to remain coherent in time. A slightly positive value would also be acceptable as the spreading rate of the vortex would still be low compared to its spiraling rate and the lifetime of the vortex. For the present data set, the use of this metric showed little difference in SCS identification so it was not used, but this criterion is worth noting for future studies.

4.1.7 Calculation methods for swirling strength

To calculating the swirling strength, derivatives of the streamwise and spanwise velocities must be taken. Given the inherent noisiness of numerical derivatives of PIV data, the velocity field was convolved with a smoothing kernel before differentiation. Three different types of smoothing were investigated including:

1. A moving average filter with no weighting
2. A moving average filter with Gaussian weighting, $w_g(n) = exp\left(-\frac{1}{2}\left(\frac{2.5n}{N/2}\right)^2\right)$, where N is the number of data points per window (an odd integer) and $-N/2 \leq n \leq N/2$.
3. The Savitzky-Golay (SG) filter. The calculation of this filter and the smoothing kernels used are documented in Savitzky and Golay [1964].

After smoothing, numerical differentiation was performed using a central difference method (on the edges of the domain forward and backward difference methods were used where appropriate), except in the case of the SG filter where a differentiation kernel was calculated and convolved with the velocity field instead. To compare the filters and also chose the best filter size, the three methods were compared using 5 x 5, 7 x 7, and 9 x 9 smoothing kernels on a subsection of the flow field as

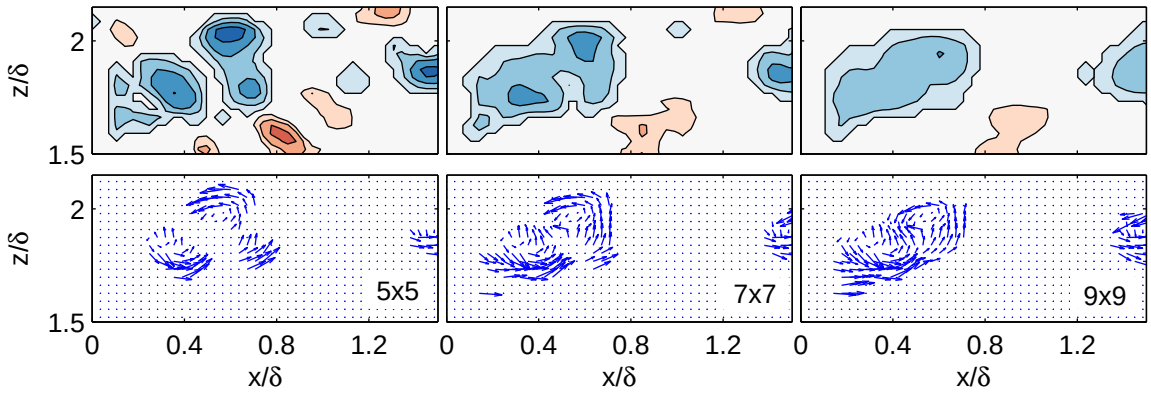

Figure 4.2: Signed swirl using a moving average filter. Top three panels: signed swirl field (red: positive, blue: negative, white: zero) with smoothing kernels of size 5 x 5, 7 x 7, and 9 x 9, moving from left to right. Contours range from -50 to 50 m/s in steps of 10 m/s. Bottom three panels: sections of the velocity field associated with negative swirl satisfying $\Lambda_{c,i} \leq 1.5\lambda_{rms}$. The data shown is a portion of the velocity field at one instant in time for plane SF1.

shown in Figs. 4.2, 4.3, and 4.4. In each figure, the top row of panels shows the signed swirl field and the bottom row of panels shows velocity vectors associated with negative swirling events satisfying $\Lambda_{c,i} \leq 1.5\lambda_{rms}$. Note that this is more strict that the cutoff value of $1\lambda_{rms}$ used for SCS extraction in all subsequent measurements. The improved differentiation and detection of SCS using smoothing is apparent when considering the swirl field calculated without the use of any smoothing filter as shown in Fig. 4.5.

While the moving average tends to blur surrounding cores together, the Gaussian weighted average as well as the SG filter tend to keep nearby cores separate. Of the three filtering methods, the SG filter was chosen with a 7 x 7 kernel size, although the Gaussian weighted filtering should perform similarly. This choice provides a good balance between providing enough smoothing to eliminate noise yet not enough to blur nearby structures together. Different polynomial orders for the SG filter were tested and it was found that increasing the polynomial order acts similarly to decreasing the filter width for the the present data. Thus, a quadratic polynomial order was retained as a higher polynomial order would require a larger smoothing kernel for the same results.

Little difference was noted in extracting SCS using 1 or 1.5 times the rms swirling strength (below this limit cores were no longer well separated), so a cutoff of $\lambda_{c,i} \geq \lambda_{rms}$ was chosen for extracting SCS, where the rms of the swirl can be considered a measure of the background noise. For the sake of tracking SCS (to be described in Section 4.4), cores bounded by a box of size less than 2 vector spacings in the streamwise or spanwise direction were not analyzed. These small swirling regions were generally found to be energetically insignificant and would often disappear from one timestep to the next, which indicates that they likely arose from noise in the vector fields.

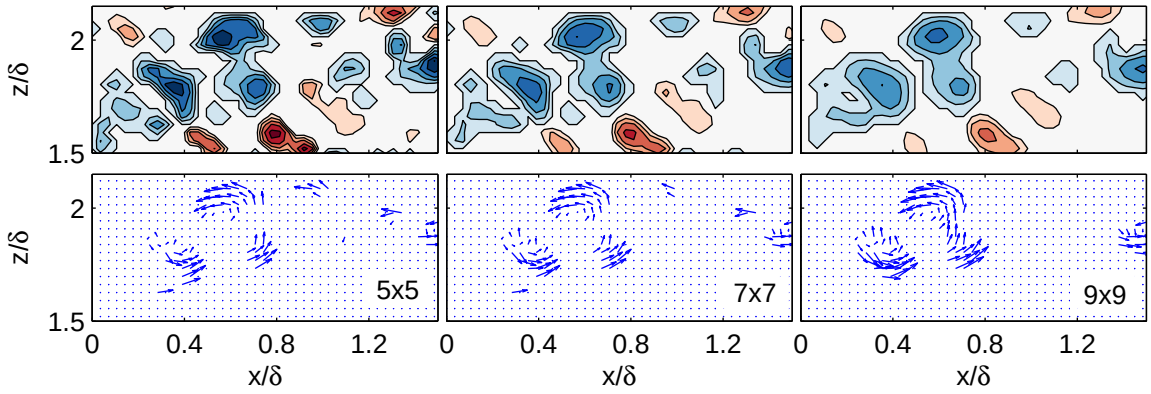

Figure 4.3: Same as Fig. 4.2 except a Gaussian weighted moving average filter was used for smoothing.

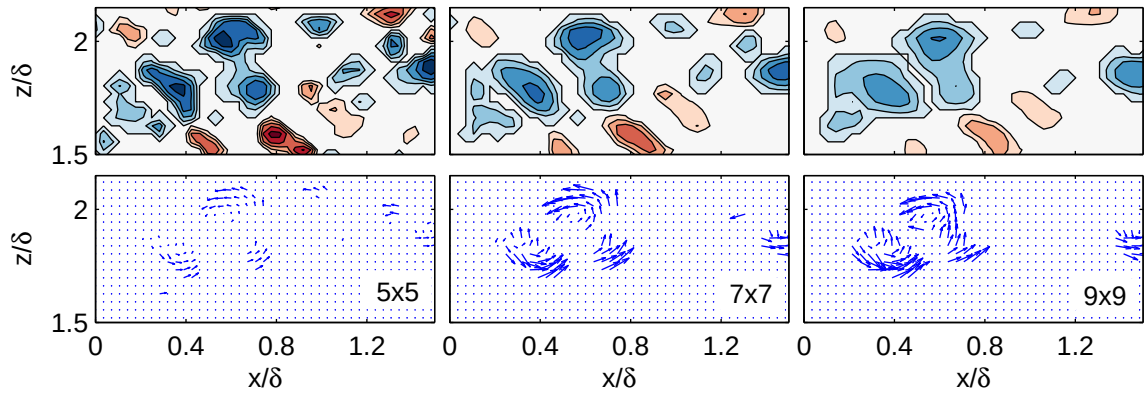

Figure 4.4: Same as Fig. 4.2 except a quadratic SG filter was used for smoothing.

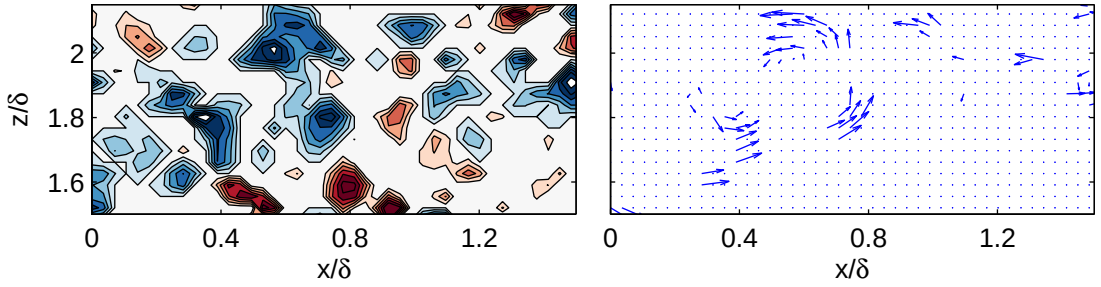

Figure 4.5: Signed swirl field with no filtering. Left panel: signed swirl field (red: positive, blue: negative, white: zero). Contours range from -50 to 50 m/s in steps of 10 m/s. Right panel: sections of the velocity field associated with negative swirl satisfying $\Lambda_{c,i} \leq 1.5\lambda_{rms}$. The data shown is a portion of the velocity field at one instant in time for plane SF1.

4.2 SCS properties

Properties of the identified SCS, such as their radius or eccentricity, can be extracted directly from the shape of regions identified using the cutoff in $\lambda_{c,i}$ discussed in Section 4.1.7 or by using the method of Carlier and Stanislas [2005] and fitting the velocity field of an idealized vortex to the velocity field in the vicinity of an identified SCS. In addition, the average size, spacing, and arrangement of SCS in the flow can be captured using linear stochastic estimation (LSE). These three methods will be discussed in the following sections.

While both LF and SF data sets were obtained for all wall-normal locations, only SF data was used for SCS identification as the LF data was too coarse to accurately detect SCS. For the LF data, the vector spacing was $35\delta_\nu$ (see Table 2.2), which means the PIV interrogation spot size was $70\delta_\nu$ (interrogation was performed with 50% overlap between windows). For the SF data, the interrogation spot size was only $30\delta_\nu$. Carlier and Stanislas [2005], in agreement with other investigators, found that the average vortex core diameter was about $50\delta_\nu$, smaller than the interrogation spot size for the LF data.

To illustrate the effect of a large interrogation window on the detection and measurement of the radius of a SCS a model problem is studied. In this model, the radial velocity field about a SCS is modeled by a Gaussian with a radius[1] of 1 as illustrated in Fig. 4.6. Given that the radius of a vortex core should be around 25 viscous units [Carlier and Stanislas, 2005] smoothing filters with a width of 1.4 and 2.8 times the radius of the Gaussian were applied to illustrate the effect of the size of the interrogation windows for the SF and LF data, respectively. After smoothing, the data was normalized by the velocity amplitude at the center to show the effect of a cutoff relative to the measured data (This illustrates the cutoff $\lambda_{c,i} \geq \lambda_{rms}$ where λ_{rms} is calculated from data that has already been smoothed by the interrogation window size). As shown, the LF data would increase the effective radius and not accurately represent the shape of the vortex. For the SF data the difference is more reasonable with the radius 1.4 times larger than the model velocity field.

4.2.1 SCS properties from extracted swirling regions

As discussed in Section 4.1.7, SCS were identified by looking for regions of either positive or negative signed swirl where $\lambda_{c,i} \geq \lambda_{rms}$ and where the regions were no less than 2 vectors in size in either the streamwise or spanwise direction. From each of these regions, the area, A, eccentricity, ϵ, yaw angle, θ_y, swirling strength weighted centroid, and average core velocity, u_{core}, were measured. From these measurements it was also possible to infer the equivalent radius of the SCS, r_{eq}, and the inclination angle, α, as will be discussed. To determine which SCS properties could be extracted with confidence, results were compared to the literature. The density of SCS was compared to Wu and

[1] The radius of a Gaussian is defined as two standard deviations from the mean.

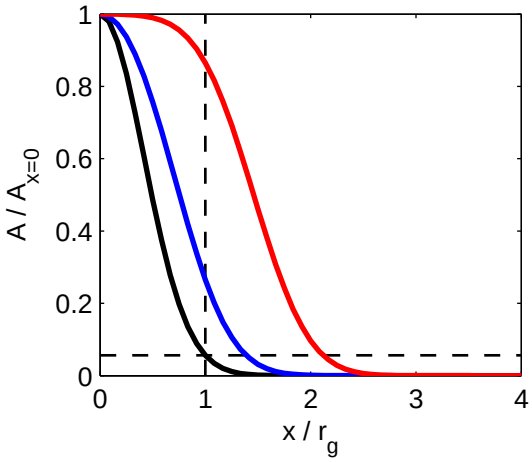

Figure 4.6: The positive half of a Gaussian velocity distribution is shown in black. The blue and red lines represent the velocity distribution when a moving average filter of size 1.4 r_g and 2.8 r_g has been applied, respectively, where these distributions have been renormalized to be 1 at $x/r_g = 0$. The vertical dotted line is at r_g and the horizontal dotted line indicates the radius of the other distributions.

Christensen [2006], the SCS radius distribution was compared to Carlier and Stanislas [2005], and the distribution of inclination and yaw angles was compared to Ganapathisubramani et al. [2006]. For each plane, the SCS properties in 500 statistically independent snapshots were analyzed.

4.2.1.1 SCS density and centroid calculation

The average number of cores identified in each snapshot for each plane is shown in Fig. 4.7. The number of SCS captured was normalized to be a density per $\delta \times \delta$ region. As with the measurement of spanwise vortex heads by Wu and Christensen [2006], the current data shows a decrease in the number of SCS with wall-normal distance.

The centroids of the identified SCS were calculated by weighting the geometric centroids of these structures with the local swirling strength. Calculating a weighted centroid prevented bias caused by noise or weak swirling events next to a SCS. In addition, this measure allows the determination of the centroid location to sub-vector spacing and was thus more suitable for extracting the SCS velocity from consecutive images as discussed in Section 4.4.

4.2.1.2 Equivalent radius

From the area, A, an equivalent radius was defined as $r_{eq} = \sqrt{A/\pi}$. This is the most appropriate measure of the SCS radius as it was expected that many of the SCS in the flow were cuts of vortex structures tilted at some angle with respect to the wall, and thus cuts through these vortex tubes in wall-parallel planes were likely elliptical (see Tomkins and Adrian [2003] for example), not perfectly circular.

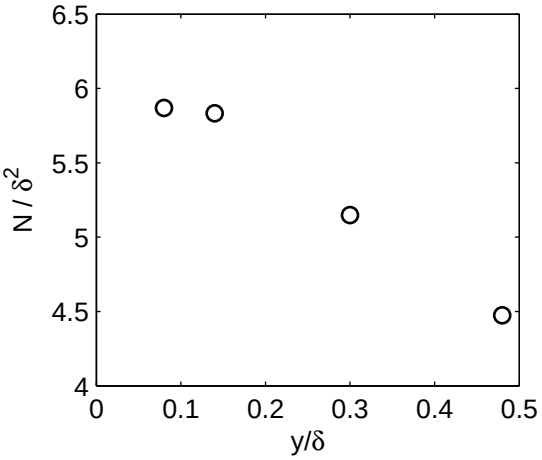

Figure 4.7: The number of SCS found per $\delta \times \delta$ area for each wall-normal location

Fig. 4.8a shows the distribution of the radii of SCS binned to the nearest $7.2\delta_\nu$ and Fig. 4.8b shows the change in the mean radius with wall-normal location. Note that the pdf presented in Fig. 4.8a, as well as all subsequent pdfs, was normalized such that the area under the pdf was equal to 1. Recall that the PIV spatial resolution was $15\delta_\nu$ so the diameter was only accurate to this value, and the radius was accurate to half this value, close to the bin width in the radius histogram in Fig. 4.8a. While the two planes near the wall share an almost identical radius distribution, as the free stream is approached, the distribution begins to skew towards larger core radii consistent with Townsend's attached eddy hypothesis. Carlier and Stanislas [2005] showed the same radius trend with a mean radius between 20 and $30\delta_\nu$ moving from the wall to the wake region. In any case, the calculated values in Fig. 4.8 are outside this range.

This difference can be rectified in two ways. First, considering Fig. 4.6, it should be expected that the PIV interrogation window increases the SCS radius, and dividing by a factor of 1.4, by which the radius was expected to increase in the model problem, improves the agreement with Carlier and Stanislas [2005] as shown by the square symbols in Fig. 4.8b. Alternatively, a correction can be applied to calculate the actual core radius as was measured by Carlier and Stanislas [2005] as opposed to the equivalent radius measured here. This is done by inferring the radius of the tilted SCS from the inclination angle and the aspect ratio of the elliptical SCS measured. Given that $r_{eq} = \sqrt{A/\pi}$, the area of an ellipse $A = \pi ab$ (a and b are the major and minor axes of the ellipse, respectively), $a = b/sin(\alpha)$ assuming a tilted circular vortex tube, and the core radius, $r = b$, then:

$$r = r_{eq}\sqrt{sin(\alpha)} \tag{4.9}$$

By applying this correction, the radii also fall within the expected range of sizes as shown by the triangle symbols in Fig. 4.8b.

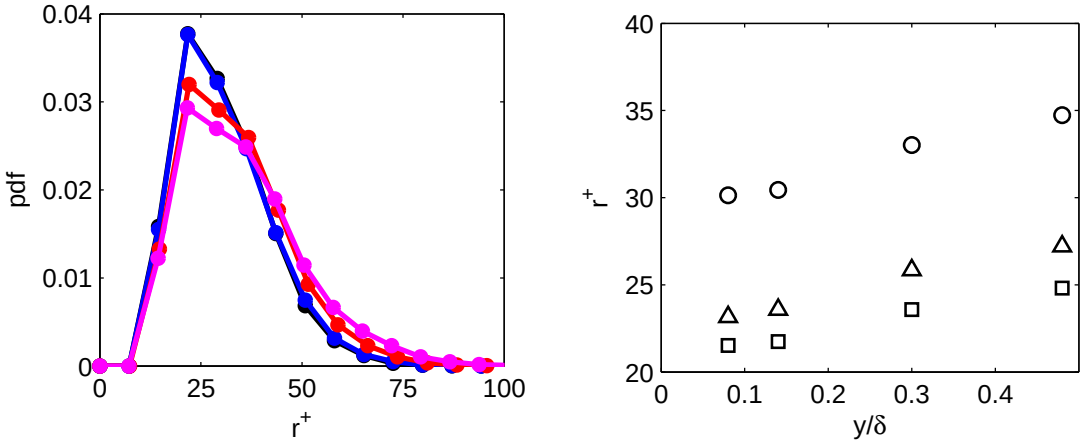

(a) Core radius distribution

(b) Mean core radius

Figure 4.8: (a): Distribution of the SCS equivalent radii for plane SF0: black, SF1: blue, SF2: red, SF3: magenta. Note that the black and blue lines overlap. (b): Wall-normal variation ○: mean equivalent radius, □: mean equivalent radius divided by 1.4, and △: mean core radius (calculated from r_{eq} using Eqn. 4.9)

4.2.1.3 Inclination and yaw angles

From the eccentricity, $\epsilon = \sqrt{1-(b/a)^2}$, where a and b are the major and minor axes of an ellipse, respectively, the inclination angle, α, of the vortex tube cutting a wall-parallel plane was inferred using Eqn. 4.10 assuming that the vortex tube was circular.

$$\alpha = \sin^{-1}\left(\sqrt{1-\epsilon^2}\right) \tag{4.10}$$

To calculate the eccentricity, an ellipse with the same second moments of area as the identified swirling region was constructed and the ratio of the major to minor axis was recorded. In addition to measuring eccentricity, the angle the major axis forms with respect to the free stream was extracted, the yaw angle, θ_y. The definition of α and θ_y are shown in Fig. 4.9.

The distribution of the inclination angles binned to the nearest 5° and the variation of the mean inclination angle with wall-normal distance are shown in Fig. 4.10. As observed in Fig. 4.10a, the distribution of the inclination angles does not vary significantly with wall-normal distance. This is in agreement with the findings of Ganapathisubramani et al. [2006] whose data is included in Fig. 4.10a for comparison.

Fig. 4.11a shows that the error in the inferred inclination angle changes both with the aspect ratio of the SCS (b/a) and the length of the major axis, a. This error was calculated assuming that the maximum error in the measurement of any axis was within half a vector spacing, $7.5\delta_\nu$. Points along the lines in Fig. 4.11a mark the length of the minor axis ranging from $b = 0.5$ up to $b = a - 0.5$ vector spacings to show measurable aspect ratios. The error is particularly high near an aspect ratio

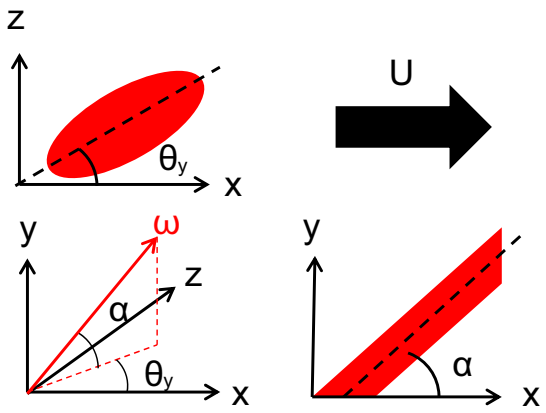

Figure 4.9: The angles α and θ_y are defined with respect to the vorticity vector in red in the bottom-left panel. The 2D views show the inclined structure of a vortex tube with an inclination angle α in the x-y plane (bottom right) and an elliptical cut of the vortex tube with a yaw angle θ_y in the x-z plane (top right).

of one as any small error in measurement in one of the axes of the ellipse will result in a drastically different inclination angle. Overall, though, the error changes little with (b/a) below (b/a) = 0.5, decreases with increasing a, and is usually below about 20° over a wide range of a and b. For a major axis larger than 3 vector spacings, the error falls to about 8°.

There are three main differences between the distribution of angles inferred from the present data and the data of Ganapathisubramani et al. [2006]. First, an angle of 0° cannot be inferred from the present 2D-2C PIV measurements, hence why the histograms do not match near 0° in Fig. 4.10a. The deficit of counts at angles beyond 50° as well as the spike at 90° can be explained by the difficulty in inferring the tilting angle given the limited size of the SCS identified. Fig. 4.11b is the same as Fig. 4.11a except the aspect ratio is converted to an angle. This shows that for all core sizes considered, there were generally 2 or fewer points that could be inferred between α = 50° and α = 90°, and there were no points in between when a = 2. Thus the inferred angle will have a tendency to be binned either at 50° or 90° degrees, but not in between. Finally, the double peak in the pdf near 30° and 40° is a combined effect of binning to the nearest 5° as well as the limited resolution of the inclination angle already discussed and shown by the solid circles in Fig. 4.11a.

The pdf showing the distribution of yaw angles is shown in Fig. 4.12. The limited resolution shows up in the form of peakiness in this pdf (likely caused by the limited yaw angles that can be extracted from regions of 5 x 5 vectors on average). This data is compared to yaw angle, θ_{yx}, from Ganapathisubramani et al. [2006] which ranges from −180° to 180°. A comparison to the present measurements is made by summing together the region $-180° \leq \theta_{xy} \leq -90°$ with $0° \leq \theta_{xy} \leq 90°$, noting symmetry about 0°, and taking into account the origin of their data is on the spanwise as opposed to the streamwise axis. Ignoring the peak values, the pdf of θ_y actually fits well with data from Ganapathisubramani et al. [2006] at y/δ = 0.09 and also shows almost no variation in the

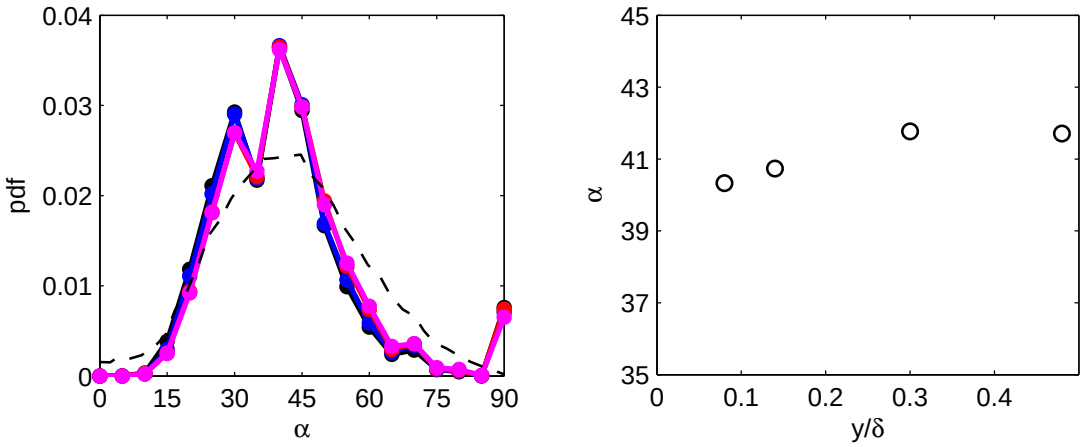

(a) Inclination angle distribution

(b) Mean inclination angle

Figure 4.10: (a): Distribution of the inclination angles of SCS for plane SF0: black, SF1: blue, SF2: red, and SF3: magenta. Dashed black line: elevation angle distribution from Ganapathisubramani et al. [2006] at $y/\delta = 0.09$. (b): The mean inclination angle variation with wall-normal distance

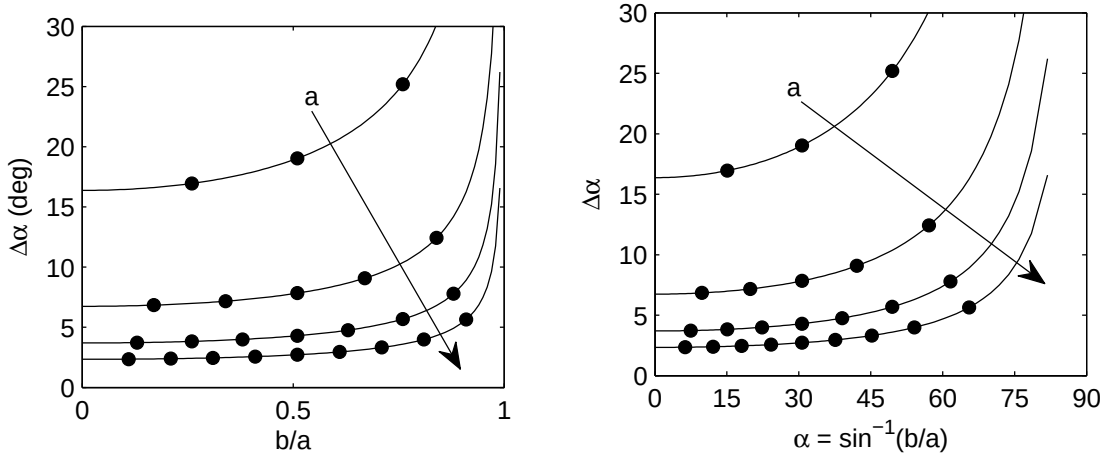

(a) Error in angle with aspect ratio

(b) Error in angle with angle

Figure 4.11: (a): Error in the inferred inclination angle, $\Delta\alpha$, with varying aspect ratio for an elliptical SCS with a major axis, a. The length, a, changes from 3 to 6 vector spacings, increasing in the direction of the arrow. (b): Same as (a) except that the ratio has been replaced by the inferred inclination angle.

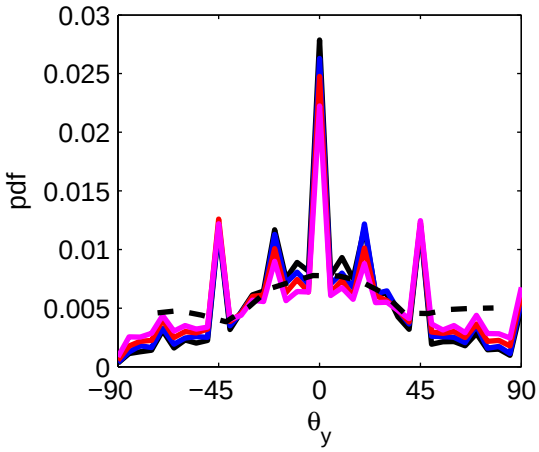

Figure 4.12: The pdf of the yaw angle for planes SF0: black, SF1: blue, SF2: red, and SF3: magenta. Dashed black line: distribution of θ_y converted from θ_{yx} data from Ganapathisubramani et al. [2006]

distribution with wall-normal distance which is also consistent.

4.2.1.4 SCS convection velocity

The average velocity in each SCS, u_{core}, was also calculated as this is a measure of the SCS convection velocity. This is a useful calculation method when time-resolved data is not available. It is equivalent to the convection velocity that, when subtracted from the instantaneous velocity, would produce a set of closed, circular streamlines about the SCS.

The variation of the pdf of the SCS convection velocity with respect to the local mean is shown in Fig. 4.13 along with the variation of the mean convection velocity with wall-normal distance. As shown, the mean value is not that different from the local mean velocity with a value slightly higher than the local mean near the wall and slower than the local mean far from the wall. The change in the histograms is most notable in plane SF3 at y/δ = 0.48. Here there is a definite thinning of the pdf on the high-velocity end. This is an effect of the upper limit on the convection velocity set by the free-stream velocity. This is readily observable in the pdf of the absolute convection velocity in Fig. 4.14. Here it is apparent that no SCS traveled at speeds above the free-stream velocity (U_∞/u_τ = 22.5) and none were observed below u^+ = 8, which is the lower bound on the convection velocity of disturbances in the boundary layer as found by Morrison et al. [1971].

While the agreement is not perfect, the distribution of both the SCS radii and SCS inclination angles match well with the literature and thus using the shape of the extracted swirling regions should be a useful way to extract information about the evolution of the SCS in time. It should be noted, though, that the small size of most of the SCS will make it difficult to pick up small changes in the properties of the SCS.

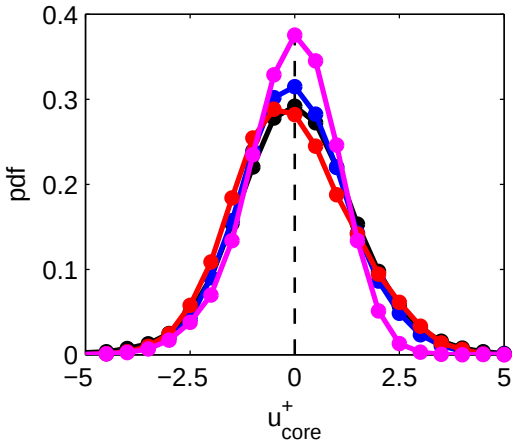

(a) SCS velocity distribution about $\overline{U}(y)$

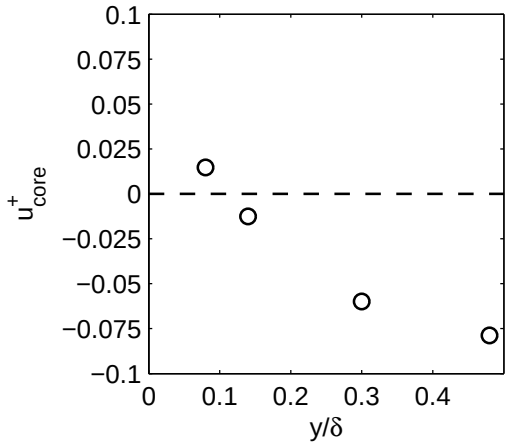

(b) Mean SCS velocity with respect to $\overline{U}(y)$

Figure 4.13: (a): Distribution of the SCS core velocity for plane SF0: black, SF1: blue, SF2: red, and SF3: magenta. (b): Mean SCS velocity variation with wall-normal distance

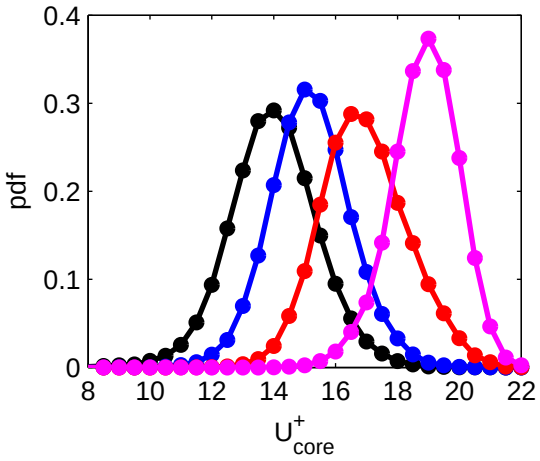

Figure 4.14: Distribution of the absolute SCS core velocity for plane SF0: black, SF1: blue, SF2: red, and SF3: magenta

4.2.2 SCS properties from a fit to a model vortex

SCS properties can also be extracted by fitting the velocity field of a model vortex to the velocity field in the vicinity of an identified swirling region, where the identification of swirling regions was discussed in Section 4.1.7. This method can extract SCS properties based on the velocity field in the vicinity of a SCS and does not depend on the shape of the extracted SCS. In addition, an error between the model and the actual velocity field is provided and can be used to determine the goodness of the fit. To calculate the SCS properties, non-linear least-squares regression was used to fit a velocity field prescribed by the Lamb-Oseen vortex, given in Eqn. 4.11, to the velocity field in the neighborhood of a local maximum of swirling strength.

$$u\hat{\imath} + w\hat{k} = u_c\hat{\imath} + \frac{\Gamma}{2\pi}\left[\frac{-(z-z_c)\hat{\imath} + (x-x_c)\hat{k}}{r^2}\right]\left[1 - e^{-(r/r_c)^2}\right] \tag{4.11}$$

The fit parameters in Eqn. 4.11 are u_c, the streamwise convection velocity of the SCS, Γ, the SCS strength, (x_c, z_c), the SCS centroid, and r_c, the radius of the SCS. A spanwise convection velocity could also be prescribed, but the inclusion of this parameter in the non-linear least-squares fitting gave poor results.

As discussed in Section 4.2.1, SCS can intersect the viewing plane at various angles and the actual in-plane SCS shapes will likely not be circular like the Lamb-Oseen vortex, but elliptical. By prescribing two more free parameters, the inclination angle, α, and the yaw angle, θ_y, a non-linear least-squares fit can be performed between the measured velocity field and a projection of the Lamb-Oseen vortex velocity field from a plane at some angle with respect to the measurement plane. To do this, the in-plane velocities are calculated as in Eqn. 4.11 except using the stretched and tilted coordinates (denoted by an accent mark) defined in Eqn. 4.12. The velocity must also be transformed back from the tilted plane using Eqn. 4.13.

$$\begin{aligned} \acute{x} &= \cos(\pi/2 - \alpha)[x\cos(\theta_y) + z\sin(\theta_y)] \\ \acute{z} &= z\cos(\theta_y) - x\sin(\theta_y) \end{aligned} \tag{4.12}$$

$$\begin{aligned} u &= \sin(\alpha)[\acute{u}\cos(\theta_y) - \acute{w}\sin(\theta_y)] \\ w &= \sin(\alpha)[\acute{w}\cos(\theta_y) + \acute{u}\sin(\theta_y)] \end{aligned} \tag{4.13}$$

When performing non-linear least-squares regression using these equations, the variables were normalized such that they were of similar amplitude during minimization resulting in a more accurate measure of the SCS parameters. In addition, this helped to set the necessary accuracy of the minimization and lowered the computational cost. The normalization was chosen as follows:

* An accuracy of $1^\circ = 1.75 \times 10^{-2}$ rad was desired for angle measurements, which required an accuracy $O(10^{-2})$. This was the the accuracy set for the least-squares fit. The value of α ranged from 0 to $\pi/2$ and θ from $-\pi/2$ to $\pi/2$.

* Sub-vector accuracy was desired in the measurement of the centroid and radius of the SCS so for a vector spacing of $\approx 4 \times 10^{-4}$ m, scaling r, x_0, and z_0 by 200 provided an accuracy of $0.125\Delta x$.

* Multiplying the convection velocity by 4 gives an accuracy of the velocity within $\approx 0.1u_\tau$. The rescaled convection velocity ranges from 0 and 2.

* Γ ranged from $10^{-3} - 10^{-4}$ m^2/s^2 so multiplying by 1000 provided a range between 0 and 1 along with reasonable accuracy.

Upon normalization, minimization was performed using the MATLAB function *lsqnonlin* with upper and lower bounds set so that:

* $-\overline{U}(y) \leq u_c \leq U_\infty - \overline{U}(y)$

* $0.5 \leq r_c/\Delta x \leq 5$

* $-0.01\ m^2/s^2 \leq \Gamma \leq 0.01\ m^2/s^2$

* $0 \leq \alpha \leq 90$

* $-90 \leq \theta_y \leq 90$

* Centroid located within a bounding box enclosing the identified SCS

A first guess at each parameter was as follows:

* Centroid at the location of maximum swirl

* $r_{c,0} = \sqrt{A/\pi}$, where A was the enclosed area of the SCS

* $\Gamma_0 = \pi r_{c,0}^2 \omega_{max}^2$

* $u_{c,0} = 0$,

* $\alpha_0 = \pi/4$

* $\theta_{y,0} = 0$.

Minimization was performed twice. The first time, minimization was performed without the angles included (matching to a circular vortex) to obtain a second guess at the initial centroid

location, $r_{c,0}$, Γ_0, and $u_{c,0}$. The second time, minimization was performed with all of the listed parameters and the new guesses at the centroid location, etc.

Unfortunately, unlike the marginal effects of the limited spatial resolution on the results in Section 4.2.1, the least-squares fit did not work well with this limited information as shown by the radius, inclination angle, yaw angle, and convection velocity histograms in Fig. 4.15. Although the shift to a larger radius with wall-normal distance is apparent in Fig. 4.15a, the radius in each plane is overestimated relative to measurements using the SCS shape as well as data from Carlier and Stanislas [2005]. For the two angles shown in Figs. 4.15b and 4.15c, the calculated values do not agree well with the data from Ganapathisubramani et al. [2006] and appear to lock on to the initial guess of these parameters (α = 45° and θ_y = 0°). It was verified that changing the initial guess changed the dominant angle in these pdfs.

The only parameter that appears to be readily extracted using this method is the convection velocity which again shows the expected shape change for plane SF3 where the free-stream velocity limitation becomes important. This was also the only parameter which had a strong one to one correspondence between the value calculated using the shape of the SCS (in this case the mean core velocity) and the vortex velocity field fit. All of the other parameters show limited or no correspondence between the two calculation methods.

Due to the difficulty in obtaining accurate values with the resolution of these experiments and the increased computational costs of performing the least-squares regression, SCS properties were analyzed using the parameters based on the shape of the SCS as presented in Section 4.2.1.

4.2.3 SCS properties using linear stochastic estimation

4.2.3.1 Method

Linear stochastic estimation (LSE), introduced by Adrian [1977] (see also Adrian [1979]), can be used to easily and efficiently estimate a conditionally averaged field, and thus can be useful in describing the dominant structures in the flow discussed in Sections 4.2 and 4.3. In order to understand LSE, first consider the conditional average $< \underline{g}', \underline{E} >$, that is, the conditional average of some quantity g given the occurrence of some event E, where the prime indicates a shift in either time or space away from the location where E in detected. Both g and E are vectors and may contain an arbitrary number of dimensions. From Adrian [1988b], assuming "that both g and the random variables defining each event component have zero mean value and that they involve N points $(x_1, x_2, \cdots, x_N)$", the stochastic estimate can be expanded in terms of the event data, E, and truncated to first order (hence the use of the word linear in linear stochastic estimation), as in Eqn. 4.14.

$$\hat{g}_i' = L_{ij} E_j \tag{4.14}$$

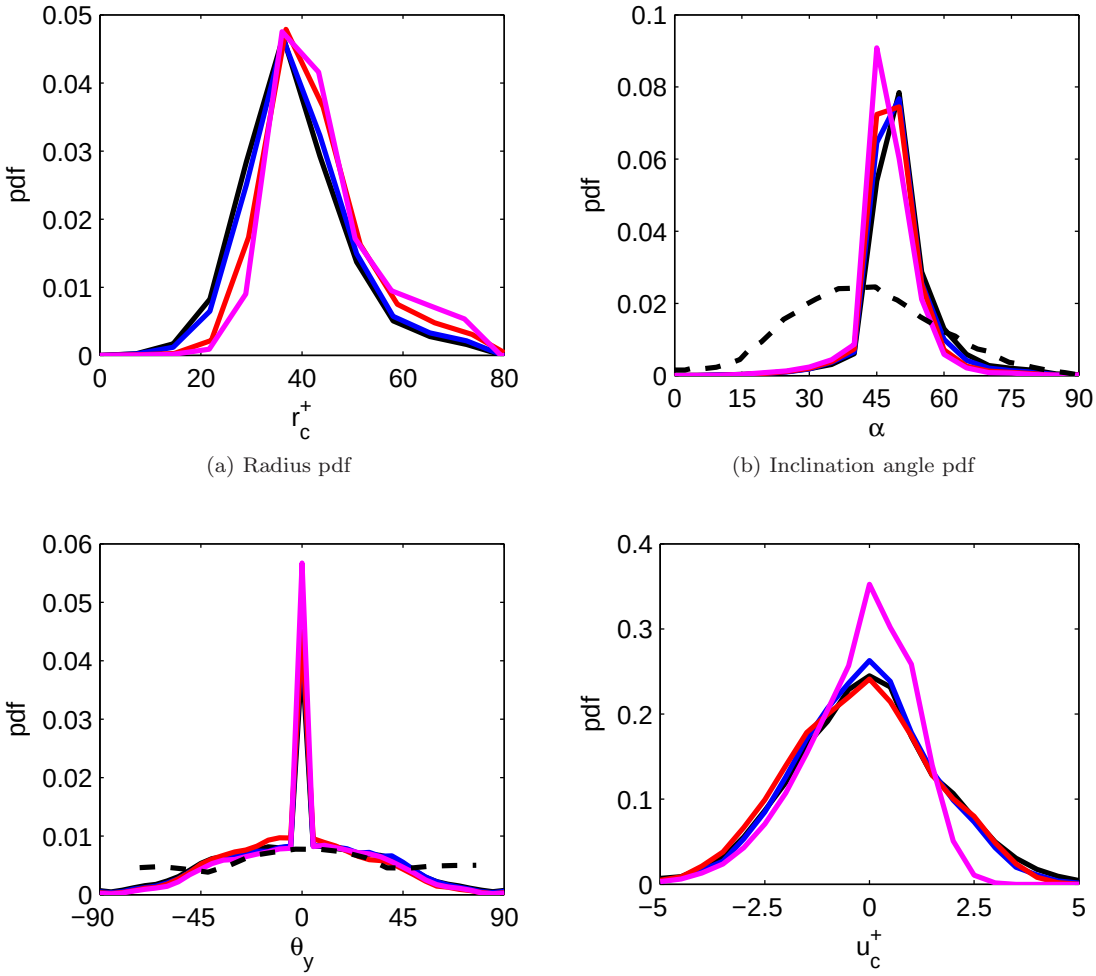

(a) Radius pdf

(b) Inclination angle pdf

(c) Yaw angle pdf

(d) Convection velocity pdf

Figure 4.15: Pdfs of fit parameters. (a): Pdf of the SCS core radii. (b): Pdf of the SCS inclination angle. (c): Pdf of the SCS yaw angle. (d): Pdf of the SCS convection velocity. The solid lines are for planes SF0: black, SF1: blue, SF2: red, and SF3: magenta. Dotted black lines: data from Ganapathisubramani et al. [2006], as shown in Figs. 4.11 and 4.12

where $i = 1, \cdots, n$, $j = 1, \cdots, m$, and the hat indicates an estimate of the true value. To determine the unknown coupling coefficients, L_{ij}, that link the event vector to the desired vector field, least-squares minimization is performed yielding the set of linear algebraic equations given in Eqn. 4.15.

$$L_{ij} = < E_j E_k >^{-1} < g_i' E_k > \tag{4.15}$$

The field g can then be estimated from the ratio of the correlation amongst the data to the correlation between the data and the variable being estimated as given in Eqn. 4.16.

$$\hat{g}_i' = < E_j E_k >^{-1} < g_i' E_k > E_j \tag{4.16}$$

This method is particularly useful in that the structure of the estimated event is the same regardless of the value of the event chosen. Thus, unlike a regular conditional average, the exact value of the event does not need to be accurately determined a priori and the calculation is much more efficient as no conditional averaging is actually performed.

4.2.3.2 Results

The LSE of the velocity field conditioned on the existence of a positive swirling event, λ_{pos}, as given in Eqn. 4.17 is shown for plane SF1 in Fig. 4.16a.

$$\hat{u}_i' = \frac{< u_i', \lambda_{c,i} >}{< \lambda_{c,i} \lambda_{rms} >} \lambda_{pos} \tag{4.17}$$

The elliptical swirling field is identified as expected. The variation in the SCS shape with wall-normal distance is demonstrated in Fig. 4.17 with the SCS becoming more circular (and thus less inclined) further from the wall. By normalizing each vector by its velocity magnitude as done by Christensen and Adrian [2001], the existence of spanwise aligned counter-rotating SCS pairs flanking low- and high-momentum regions are observed as shown in Fig. 4.16b. As this pattern of low- and high-momentum regions and SCS was not observed for all positive swirling events, averaging over many instances, as done with the LSE, would tend to obscure this pattern, and hence why it was not visible without normalization. Note that the counter-rotating SCS next to the high-momentum region is less prominent than the one next to the low-momentum region. This may indicate that counter-rotating SCS pairs about low-momentum regions are more common than those about high-momentum regions. Also note that the spacing of counter-rotating SCS pairs is between 0.2 and 0.4δ, similar to the size of low-momentum regions shown Fig. 4.21b.

The strong presence of counter-rotating SCS pairs is confirmed by presenting the LSE of a negative swirling region conditioned on the existence of a positive swirling region as shown for all planes in Fig. 4.18. From these figures, the average spacing between the spanwise aligned SCS can

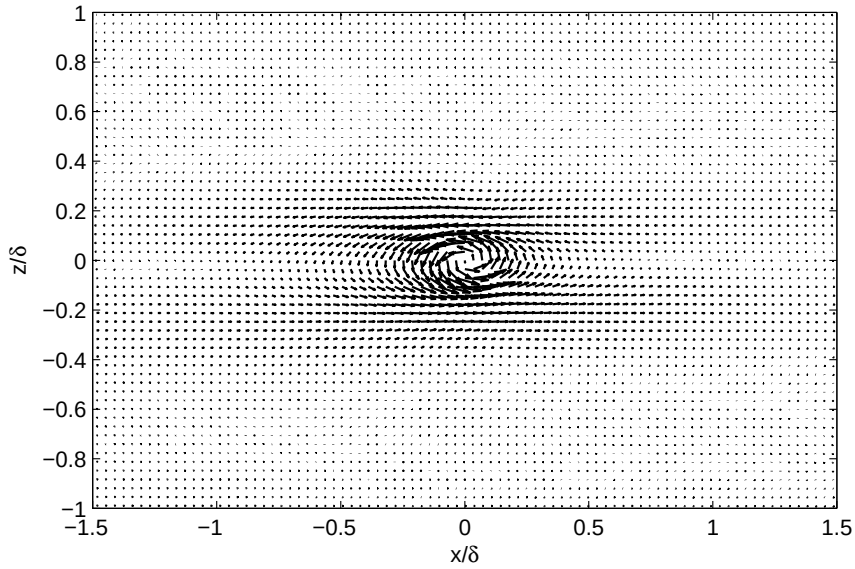

(a) Velocity field conditioned on positive swirl for SF1

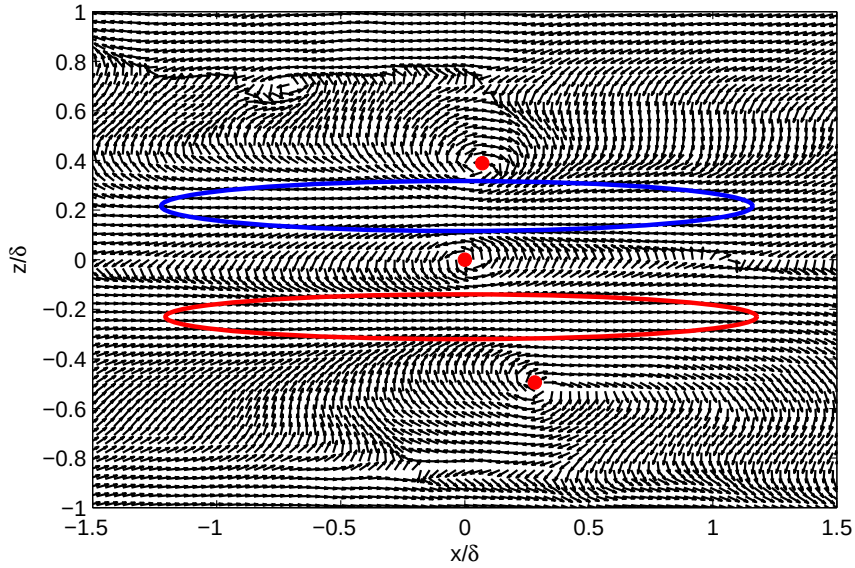

(b) Velocity field normalized by the velocity magnitude

Figure 4.16: (a): LSE of the velocity field conditioned on the existence of a positive swirling event, $< u_i', \lambda_{c,i} > / \lambda_{rms}$ for plane SF1. (b): Same as (a) except each vector is normalized by its magnitude. Identified SCS cores are marked by red dots and regions of high and low momentum are circled in red and blue, respectively.

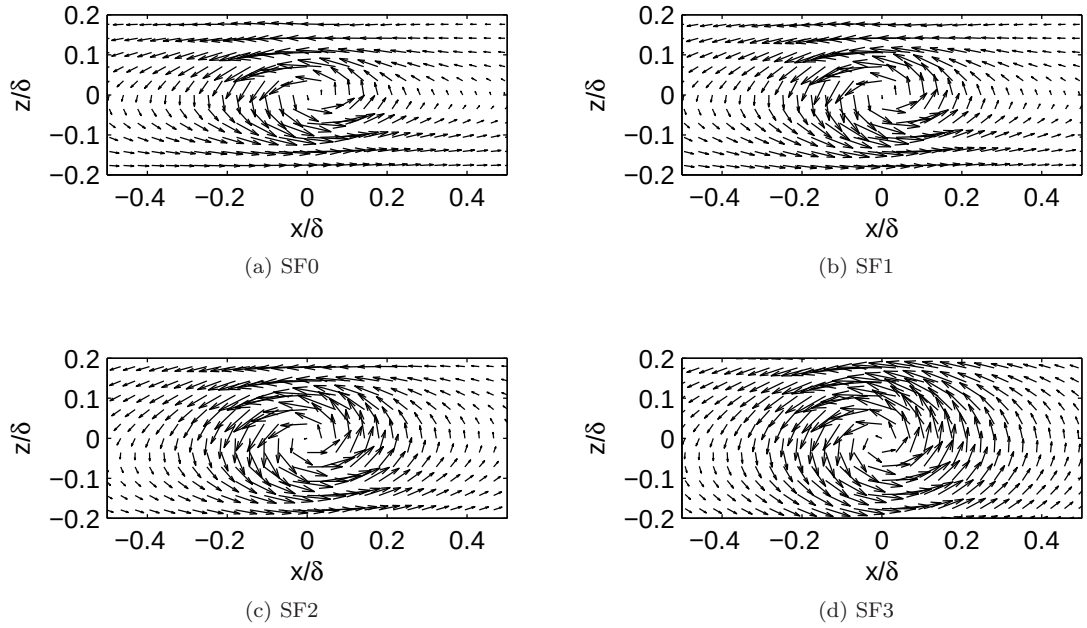

(a) SF0 (b) SF1

(c) SF2 (d) SF3

Figure 4.17: LSE of the velocity field conditioned on the existence of a positive swirling event for all four wall-parallel planes

Table 4.1: SCS spacing inferred from Fig. 4.18

Plane	SF0	SF1	SF2	SF3
$\|z_{ccw} - z_{cw}\|/\delta$	0.21	0.21	0.22	0.28
$\|z^+_{ccw} - z^+_{cw}\|$	86	86	90	115

be extracted to the nearest vector spacing ($15\delta_\nu$) as presented in Table 4.1. In all cases, the most probable spacing is around 100 viscous units or 0.2δ with the spacing increasing with wall-normal distance. This value is smaller than the spacing inferred from the LSE of the velocity field shown in Fig. 4.16b, but is similar to the width of the low-momentum regions as shown in Fig. 4.21b. In the plots in Fig. 4.18 the zero value (blue contours) centered at (0,0) indicate the region of the smallest recorded swirling structures. Also, note that, as mentioned with the LSE of the velocity fields, the presence of a counter-rotating SCS is less probable on the positive z side, the side where the counter-rotating pair would flank a high-momentum region. The signature of the counter-rotating SCS on positive z side also become weaker as the free stream is approached, and hence the asymmetry in Fig. 4.18.

4.3 Low- and high-momentum region identification

The identification of low or high momentum regions relative to the mean is easy to understand, but the cutoff used to separate these regions is subjective. In this section, direct and average methods

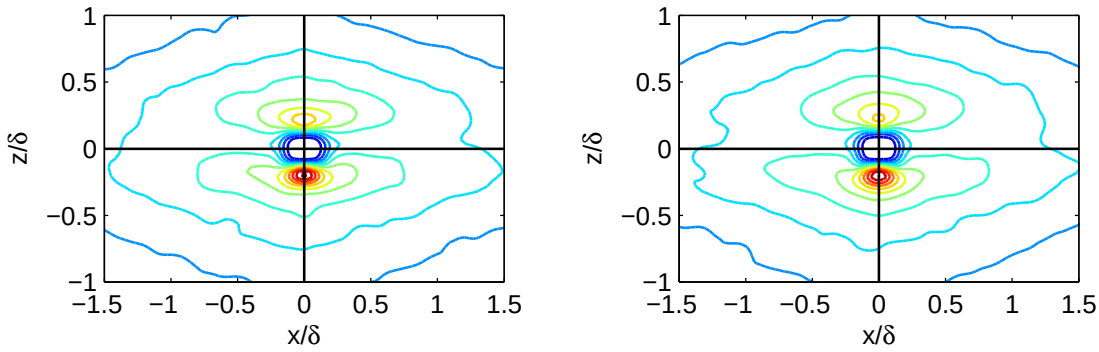

(a) SF0

(b) SF1

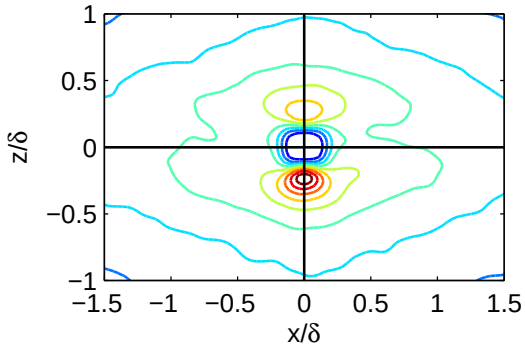

(c) SF2

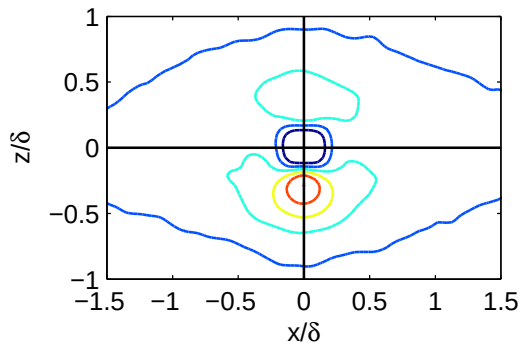

(d) SF3

Figure 4.18: LSE of a negative swirling region conditioned on the existence of a positive swirling region. The levels are identical in each figure with red being the highest and blue being 0.

are used to identify these regions and the results are compared.

4.3.1 Direct identification of low- and high-momentum regions

In order to find low-momentum regions, some sort of threshold must be defined. Ganapathisubramani et al. [2003] used a threshold based on the Reynolds shear stress, $\overline{uv}$, which makes sense given that these regions are collocated with hairpin packets that produce significant Reynolds stress. This information is not available for 2D2C wall-parallel velocity measurements so Tomkins and Adrian [2003] chose a threshold based on the deviation of the instantaneous streamwise velocity from the local mean by a fixed percentage, 10%. While this is one way to choose a threshold based on the streamwise velocity, there are (at least) three choices for an appropriate cutoff:

1. A fixed deviation from the local mean velocity (i.e., $u = \pm\beta_f$)
2. A deviation from the local mean velocity by a fixed percentage of the local mean velocity (i.e., $u = \pm\beta_m\overline{U}(y)$) as used by Tomkins and Adrian [2003]
3. A deviation from the local mean velocity by a fixed percentage of the local rms velocity (i.e., $u = \pm\beta_r u_{rms}$)

where the plus is for high-momentum regions and the minus for low-momentum regions. It is apparent that conditions (2) and (3) introduce a threshold that varies with wall-normal distance. The threshold increases with wall-normal distance for condition (2) as the mean velocity increases and the threshold decreases with wall-normal distance for condition (3) as the turbulence intensity decreases away from the wall. There are reasons for considering all of these methods, and a discussion and comparison will be provided here.

Regardless of the cutoff method used, the cutoff coefficients (β_f, β_m, or β_r) must be chosen to adequately extract the structures of interest. If the cutoff is too high, only a small portion of the flow will be extracted which will not be representative of low-momentum regions. If the cutoff is too low, the entire flow may appear as one connected region and the identified regions would contain velocities near the local mean (definitely not low-momentum regions).

The cutoffs chosen were $\beta_f = 0.03m/s$, $\beta_m = 0.1$, and $\beta_r = 0.67$. The value of β_m was chosen to match the cutoff used by Tomkins and Adrian [2003]. The value of β_r was chosen so that only 50% of the fluid, on average, would be contained in the low- and high-momentum regions (about 25% in low- and 25% in high-momentum regions), which appeared to reproduce the desired results from visual inspections of the velocity fields. The value of β_f was chosen to produce similar results to the other two methods keeping the value the same for all planes investigated.

The streamwise length, L_x, of the identified structures is defined as the length of the smallest box which completely encloses the identified structure. Since some of these structures were shown to not

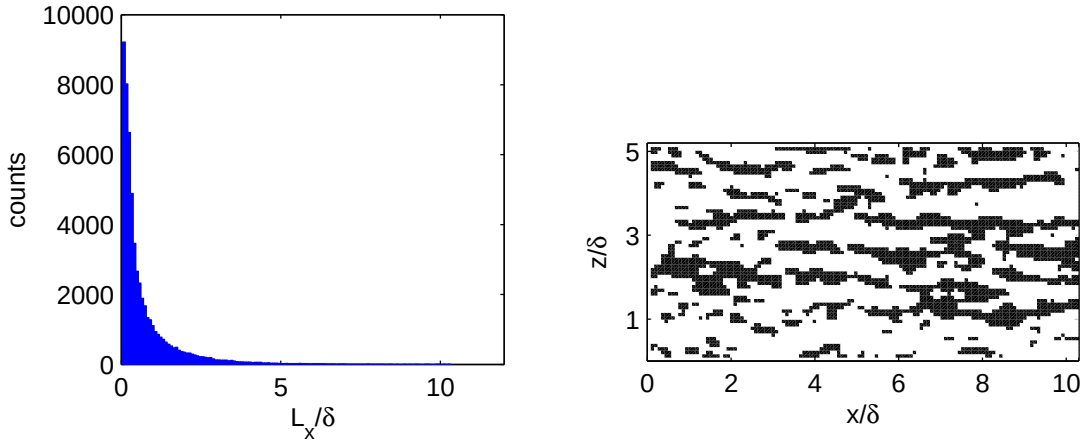

(a) Histogram

(b) Instantaneous velocity field

Figure 4.19: (a) Histogram of the length of low-momentum zones for plane LF1 of set 2 using a cutoff of $\beta_r = -0.67u_{rms}$, and (b) these zones at one instant in time.

be completely streamwise aligned and/or fork in the spanwise direction, such a bounding box is not appropriate for measuring the spanwise width, L_z. In this case, the width of an identified structure was measured at each streamwise location along the bounding box and this value was averaged over the length of the box. For forked structures, the width was the combined width of both prongs of the fork.

With this method of measuring low-momentum regions, meandering low-momentum regions were identified as a single entity. Recent work by McKeon and Sharma [2010] as well as Dennis and Nickels [2011] suggests that this meandering may simply be the identification of several smaller large-scale structures that are close in the spanwise direction. Thus, whether the suggested method is the correct way to measure the length of low-momentum regions is up for debate.

Using any of the three cutoffs presented, a range of structures can be found as shown in the streamwise length histogram in Fig. 4.19a as well as the instantaneous field in Fig. 4.19b.

Even though low-momentum regions are know to be quite long [Dennis and Nickels, 2011], a large number of small structures are noted in the velocity fields as shown in Fig. 4.19. Regardless of the cutoff selected small regions always appear either as noise when the cutoff is set too low or as fragments of longer structures when the cutoff is set too high. To make a comparison between the structures extracted using the different cutoff methods and between different planes, it would be best to have a single metric. A weighted mean was employed to help highlight the presence of the most energetically significant long structures in the flow. The weighting was done such that the measured lengths and widths of the structures were weighted by the velocity in the region providing a meaningful mean structure size. The weighting is presented in Eqn. 4.18, where A_{LM} is the area of a low-momentum region, N is the total number of low-momentum regions found and M is the

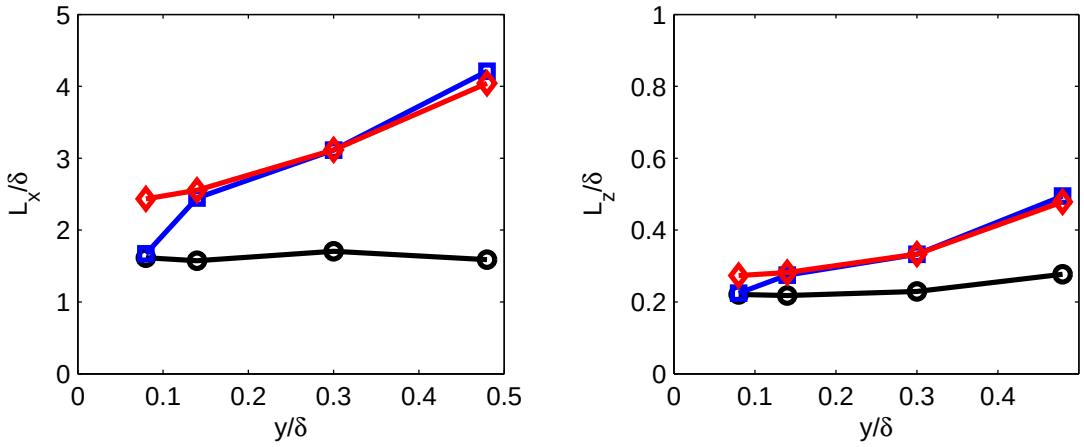

(a) Streamwise length (b) Spanwise length

Figure 4.20: Velocity-weighted average (a) streamwise, and (b) spanwise length of low-momentum regions from LF, set 2 data using a cutoff of $\beta_m = 0.1\overline{U}(y)$: black ○, $\beta_r = 0.67u_{rms}$: blue □, and $\beta_f = 0.03m/s$: red ◊

number of vectors in a particular low-momentum region. The equation can be simplified noting that the flow is incompressible and that the vectors are uniformly spaced.

$$L_x = \frac{\sum_{i=1}^{N}\left[\int_{A_{LM}} \rho u dA\right] L_x(i)}{\sum_{i=1}^{N}\int_{A_{LM}} \rho u dA} = \frac{\sum_{i=1}^{N}\left(L_x(i)\sum_{j=1}^{M(i)} u\right)}{\sum_{i=1}^{N}\left(\sum_{j=1}^{M(i)} u\right)} \tag{4.18}$$

A comparison of the effect of the three different cutoffs is shown in Figs. 4.20. This figure shows a growth in both the streamwise and spanwise extent of structures identified using the fixed velocity cutoff or the cutoff based on a percentage of the rms velocity, similar to the findings of Tomkins and Adrian [2003]. Little change was observed for the cutoff based on a fixed deviation from the mean velocity, so this method was not used. The cutoff based on the rms velocity was chosen to identify low-momentum regions as it had a more meaningful interpretation than a fixed deviation from the local mean.

As shown in Figs. 4.21, all planes show an increasing streamwise and spanwise length scale of low-momentum regions with wall-normal distance, although the SF data tends to show less increase in planes far from the wall. There is also a large overshoot in these measurements for plane LF3 of set 2. Very similar findings in terms of the trends in the mean lengths and widths were found when studying high-momentum regions. Of course, some differences must exist between the high- and low-momentum regions given that the skewness of velocity fluctuations is non-zero near the wall.

The spanwise growth of low-momentum regions with wall-normal distance was linear over the range $y/\delta = 0.08$–0.59 ($y^+ = 33$–278) with widths increasing from $L_z/\delta = 0.2$–0.4 ($L_z^+ \approx 80$–160). In

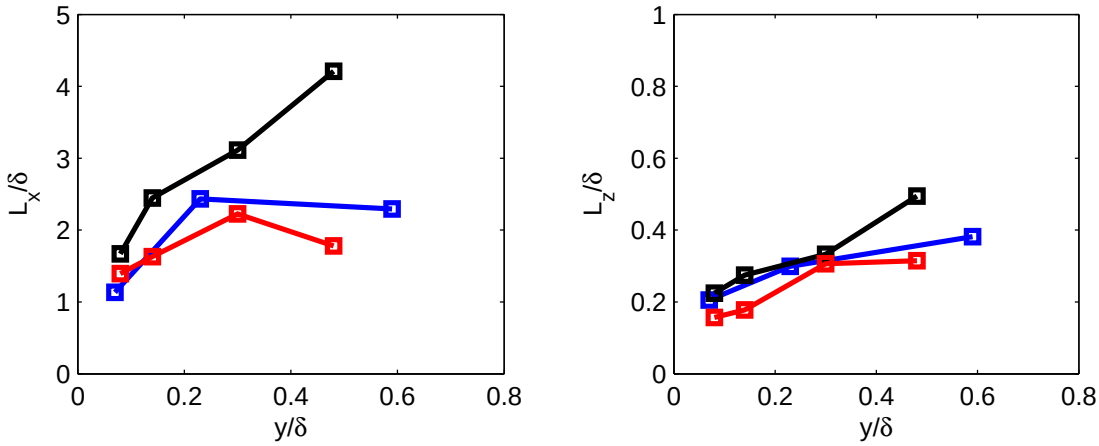

(a) Streamwise length

(b) Spanwise length

Figure 4.21: Velocity-weighted average (a) streamwise, and (b) spanwise length of low-momentum regions using data from LF set 1: blue line, LF set 2: black line, and SF set 2: red line with a cutoff of $\beta_r = 0.67 u_{rms}$

the $Re_\tau = 2230$ experiments of Tomkins and Adrian [2003], they found an increase of $L_z^+ = 250$–500 from $y^+ = 100$–440, or $L_z/\delta = 0.11$–0.22 over a range of $y/\delta = .045$–0.2, where these values were measured directly (using a threshold 10% lower than the local mean velocity) as well as using linear stochastic estimation. The match to the present data is best in outer scaling, although values are higher. This likely arises from the difference in threshold between the two cases (see Fig. 4.20b) as well as a difference in Reynolds number leading to different structure sizes.

Fig. 4.21a shows that the streamwise length of the structures increases rapidly with wall-normal distance ranging from about $1 - 3\delta$ ($L_x^+ \approx 400$–1200). Tomkins and Adrian [2003] found that $L_x^+ = 1500$–2100 ($L_x/\delta = 0.67$–0.94) from $y^+ = 100$–440 ($y/\delta = 0.045$–0.2) using linear stochastic estimation (direct measurement was not possible due to the limited field of view). In outer units, this is shorter than the sizes inferred from the present data. This discrepancy may be expected as LSE was used to calculate this value, which is not necessarily a good measure of the streamwise extent of a structure as will be discussed in Section 4.3.2. In addition, their limited streamwise field of view precludes the detection of structures longer than 1.4δ in streamwise extent.

These streamwise lengths can also be compared to lengths inferred from the streamwise velocity spectra presented by Kim and Adrian [1999] and Monty et al. [2009]. From the pipe flow experiments of Kim and Adrian [1999], the energetic peak at the low wavenumber (long wavelength) end of the spectrum was shown to increase rapidly with wall-normal distance up to lengths of nearly 12δ. For the lowest Reynolds number measurement ($Re_\tau = 1058$), this increase stopped at $y/\delta = 0.25$, while it continued up to $y/\delta = 0.45$ for the higher Reynolds number measurements ($Re_\tau = 1984$ and 3175), after which the length quickly decreased to 2δ. Monty et al. [2009] found that the quick change in

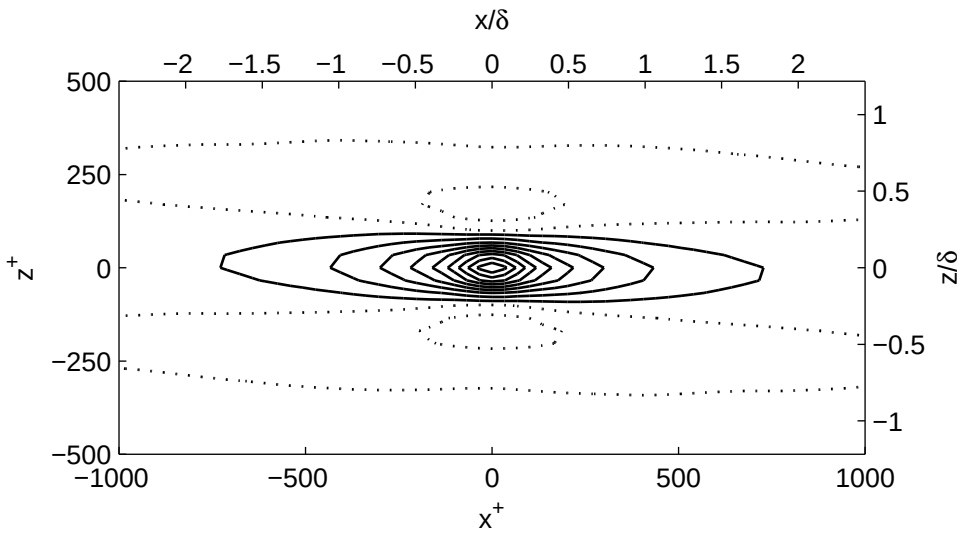

Figure 4.22: Coupling coefficient for the LSE of the conditional average of the streamwise velocity field given a low-speed event. Solid contours range from -1.0 to -0.1 and the dotted contours range from 0 to 0.1 with a difference of 0.1 between successive contours.

structure size at a certain wall-normal distance was a switch from the dominance of the VLSM or superstructure peak to the LSM peak. While the VLSM peak was dominant in internal flows out to arguably $y/\delta = 0.7$, the superstructure peak in the boundary layer quickly died out beyond the log layer, and the LSM peak became dominant. In the present data, no superstructure peak was noted in the spectrum, so it is likely that at the present Reynolds number of $Re_\tau = 410$, the structures captured are related to the LSM peak in the streamwise velocity spectrum and thus should be around 3δ at all distances from the wall, consistent with measurements in Fig. 4.21a which also show an increase in streamwise length with wall normal distance.

4.3.2 Linear stochastic estimation of low- and high-momentum regions

The LSE of the streamwise velocity field conditioned on the occurrence of a low-speed event[2] ($g' = u'(x+\xi, z+\zeta)$ and $E = -u(x,z)$) is shown in Fig. 4.22 for one wall-normal location. The streamwise elongated LSE of a low-speed event shown in Fig. 4.22 is qualitatively similar to the LSE calculated in other wall-parallel planes and for other data sets.

Although it is tempting to conclude that the length or width of the contours of the LSE are the average size of low-momentum regions in the flow, this is not the case. The LSE of this event is simply the autocorrelation of the streamwise velocity field normalized by the mean square streamwise velocity according to Eqn. 4.16. The LSE gives the average velocity field around the occurrence of

[2]This is not actually the LSE, but the coupling term, L_{ij}. The actual velocity field will be recovered by multiplying by the velocity of interest for the conditional average.

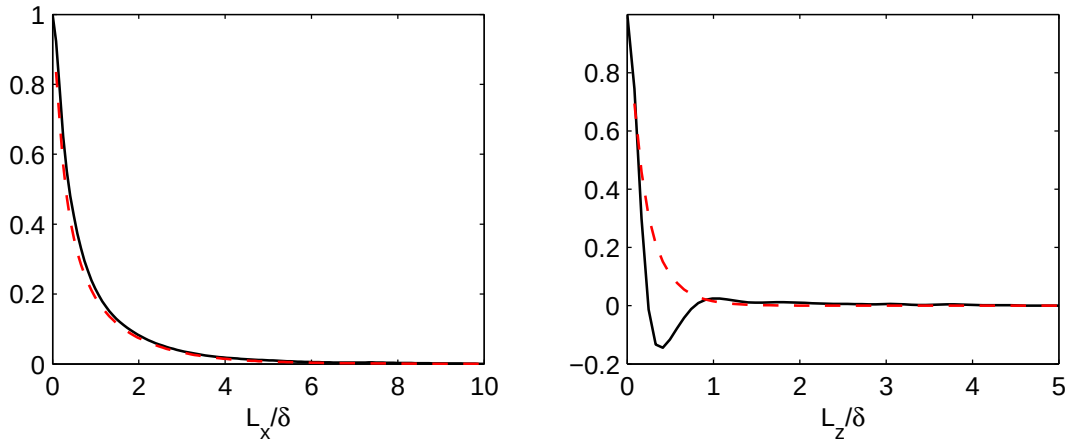

(a) Streamwise length

(b) Spanwise width

Figure 4.23: The streamwise velocity autocorrelation is shown in black for LF1 set 2; (a): $R_{uu}(x,0)$, (b): $R_{uu}(0,z)$. The dotted red line is $\int_x^\infty p(x')dx' / \int_0^\infty p(x)dx$, where $p(x)$ is the pdf of the streamwise (spanwise for (b)) length of low-momentum regions (i.e., Fig. 4.19a).

a particular velocity (or a small range of velocities), and the shape that is extracted simply shows that the low-momentum regions, for the case of a negative velocity, tend to be elongated in the streamwise direction. While a good correlation is found between the width of the LSE and the measured lengths from the present data as well as the investigations of Tomkins and Adrian [2003], the range of widths identified by different contour levels is quite small, so a selection of any level may give a good estimate. It is difficult, though, to determine a streamwise length as the variation of lengths with contour level is large and the relationship between the contour levels, which are normalized by $\overline{u^2}$, and the low-momentum regions identified from the velocity fields using a cutoff in u_{rms} is not immediately clear.

A relationship between the coupling coefficient of the LSE and the cumulative sum of the structure length pdfs does exist as shown in Fig. 4.23. In this figure, slices at zero shift and x and z are compared to the cumulative sum, $\int_x^\infty p(x')dx' / \int_0^\infty p(x)dx$, of the pdf of streamwise or spanwise lengths of low-momentum regions, p(x) (i.e., Fig. 4.19a). From this relationship, it appears that the peak in the correlation at zero shift includes the energy of all low-momentum structures, while lower levels of the correlation correspond to a range of scales beyond a certain minimum size. By considering both functions, a particular level of the LSE could be linked to an average over all regions with some size $L_x > \delta$, for example.

4.4 SCS tracking

In order to analyze SCS trajectories as well as to investigate the average lifetime and property change of SCS in time, SCS were tracked in time using the time-resolved data. Tracking is performed on Eulerian structures; that is structures are identified in each frame independent of one another as opposed to tracking the evolution of Lagrangian tracers in time as performed by Yang and Pullin [2011]. The data was subsampled in time so that, on average, a SCS would travel forward at least one vector spacing between frames; $\Delta t_{new} = \frac{\Delta x}{\overline{U}(y)}$. Before tracking, SCS were identified using the swirling strength and cores which were too small were ignored as discussed in Section 4.1.7. The swirl weighted centroids of the remaining SCS in each frame were then calculated. Due to limited resolution, sometimes two or more nearby SCS were identified as a single swirling region. These could be broken into individual cores by looking for all cores which had 2 or more local swirling maxima. While breaking up cores in this way was potentially useful, it was found that the tracking statistics were not noticeably changed when this was done, so it was not used for the results presented.

The centroids in consecutive frames were then compared to determine the SCS trajectories. For each SCS in the first frame, a nearest neighbor was identified in the second frame. If the nearest neighbor was within a "reasonable" distance of the original SCS, then the two cores were labeled as the same SCS. If this criterion was not met, then the trace for that particular SCS was ended and the SCS was assumed to have dissipated or left the field of view. The criteria for a valid nearest neighbor requires that the SCS either does not move in the streamwise direction (for any convection slower than the local mean, the SCS will not move a whole vector spacing) or that it does not move more than a SCS traveling at the free-stream velocity. This range defined as $0 \leq (x_1 - x_0) \leq U_\infty/\overline{U}(y)\Delta x$ was widened to account for inaccuracies in determining the SCS centroid by Δx on both ends. In addition, spanwise motion was restricted such that $|z_2 - z_1| \leq 2\Delta z$. This constraint was applied as the main direction of flow was in the streamwise direction and the spanwise motion was expected to be only a small fraction of this.

After identifying all SCS trajectories, at the end of each SCS trajectory (i.e., where there were no valid nearest neighbors in the next frame), the SCS position was projected forward at the local mean velocity for the next two time steps to see if any SCS trajectories that started in these two time steps were potential extensions to the terminated SCS trajectory. If so, the two trajectories were merged together. This process was performed as it was noted that sometimes a SCS would seem to disappear in one frame but then return in the next. This disappearance of SCS traces could occur for several reasons. One such case is illustrated in Fig. 4.24. In the first panel, two nearby SCS of the same sign are illustrated by blue circles with the x marking the centroid. In the second panel, the SCS are wrongly marked as a single core and thus only one centroid is found. The circled SCS in the first frame has now lost its trace as only one of the two SCS can be linked with this

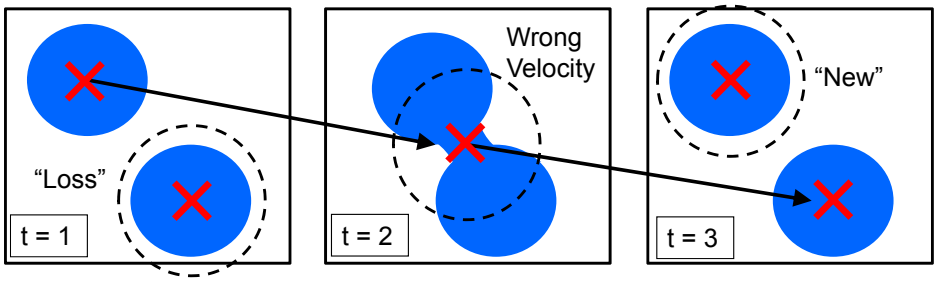

Figure 4.24: Cartoon showing how a SCS trace can be lost due to poor resolution. SCS are represented by blue regions and the SCS centroids are marked with red x's.

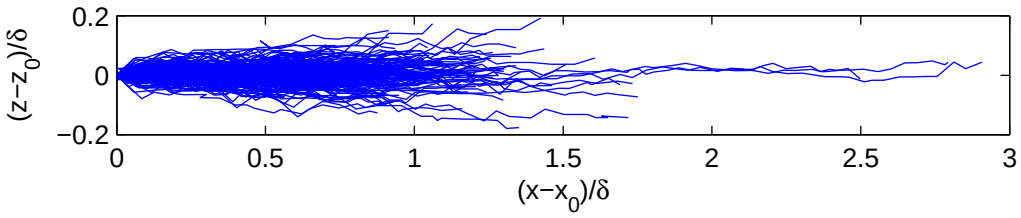

Figure 4.25: SCS trajectories from one run on plane SF1 that persist for more than one eddy turnover time (δ/U_∞)

new structure. In the final frame, the SCS are again correctly identified, but the circled SCS is incorrectly marked as a new SCS as there was no distinct nearest neighbor in the previous frame.

4.4.1 SCS trajectories

Overall, the SCS trajectories were found to be streamwise aligned with limited motion in the spanwise direction as shown in Fig. 4.25. The trajectory angle, θ_t, was calculated by fitting a straight line between the first and last point of a trajectory which was accurate given that the trajectories were, in general, close to straight lines. A histogram of the trajectory angles is shown in Fig. 4.26a showing that the spanwise motion was indeed small and was observed equally in both directions. It was noted that both positive and negative SCS were biased towards positive angles in plane SF2 (and to a lesser extent in plane SF0), which was likely caused by a slight misalignment of the camera by 2 degrees or so with respect to the streamwise direction. By applying a linear shift to the histograms as shown in Fig. 4.26b, the histograms become nearly symmetric about zero. Once fixed, this group of histograms clearly shows that the width, and thus the spanwise motion, decreases with wall-normal distance.

The relatively small, and sometimes non-present, spreading of the SCS, along with observations from the time-resolved velocity fields, supports the claim that vortex packets do not grow self-similarly in the spanwise direction, but instead must grow through some other discrete mechanism such as the packet merging mechanism discussed by [Tomkins and Adrian, 2003]. In any case, as the

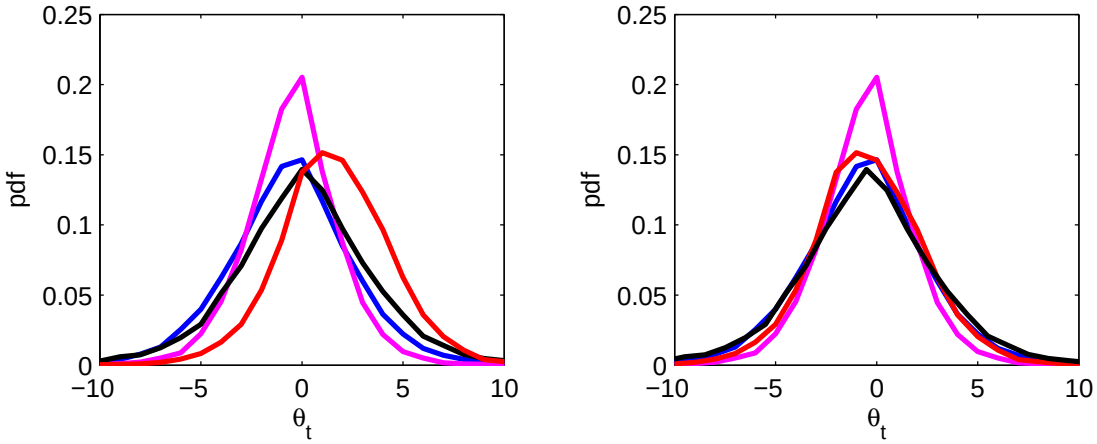

(a) SCS trajectory angle histogram

(b) SCS trajectory angle histogram

Figure 4.26: (a): Histogram of the SCS trajectory angles for planes SF0: black, SF1: blue, SF2: red and SF3: magenta. Data is compiled from both CW and CCW swirling motions and for all runs recorded. (b): Same as (a) except histograms have been corrected by subtracting 0.5° from the SF0 histogram and 2° from the SF2 histogram.

increase in spanwise length scales with wall-normal distance appears to support a self-similar growth on average, there must be some alternative mechanism or explanation for this spanwise growth.

4.4.2 Measured SCS convection velocities

From the SCS trajectories, the SCS convection velocity can be extracted. Between individual time steps, the measured convection velocity can fluctuate dramatically due to issues in finding the SCS centroid as shown in Fig. 4.27a. Over a number of time steps, though, the average convection velocity quickly converges to a mean value as shown in Fig. 4.27b. For this reason, the average convection velocity over a trajectory is reported as opposed to the instantaneous values.

The pdf of the convection velocities at each wall-normal location for SCS which persist for more than 1 eddy turnover time are shown in Fig. 4.28a. The mean values are shown in Fig. 4.28b and compared to the mean values calculated from the average core velocity as presented in Fig. 4.13b.

By comparing the histograms using the mean trajectory velocity and the mean core velocity as shown in Fig. 4.29a it becomes apparent that while the trend in the mean convection velocity is similar between the two calculation methods, the convection velocities are shifted towards values below the local mean when using the mean trajectory velocity. The differences in the pdfs are similar for all planes investigated where the positive tail of the pdfs are nearly identical for the two methods, but the negative tails are longer and the central peaks lower for the mean trajectory velocity calculation.

In some cases, the mean core velocity matches up quite well with the average trajectory velocity

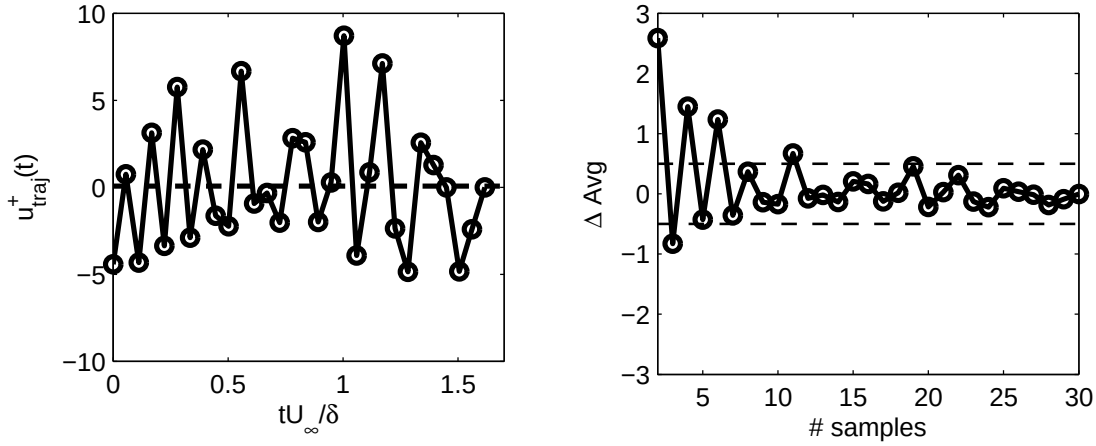

(a) SCS trajectory velocity variation

(b) Mean velocity convergence

Figure 4.27: (a): Instantaneous velocity from one SCS trajectory. (b): Change in the running average velocity for the same SCS trajectory as in (a). The value quickly converges and is within 0.5 u_τ (denoted by the dotted lines) of the mean by about 11 samples (more than half an eddy turnover).

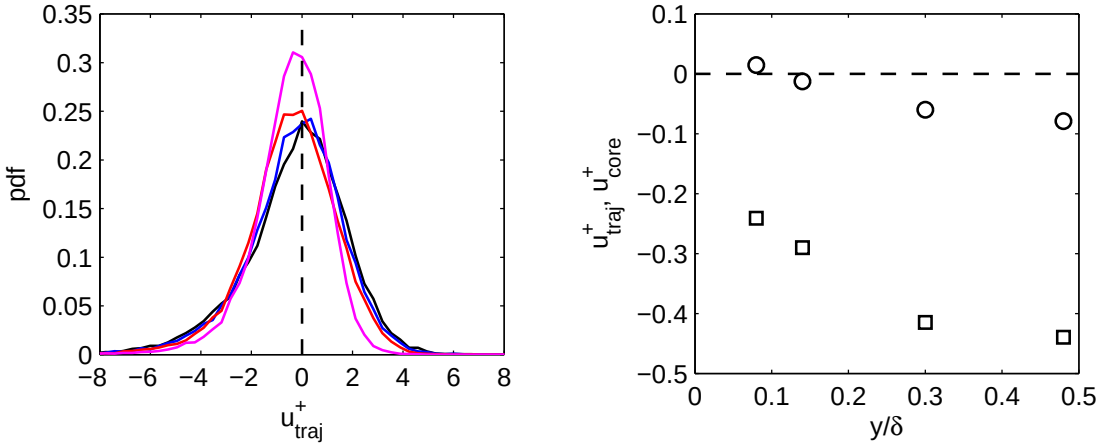

(a) SCS convection velocity pdf

(b) Mean convection velocity

Figure 4.28: (a): Pdf of the mean trajectory velocity for planes SF0: black, SF1: blue, SF2: red, and SF3: magenta. (b): Mean convection velocity for each plane with □: mean trajectory velocity from (a), ○: mean core velocity shown in Fig. 4.13b

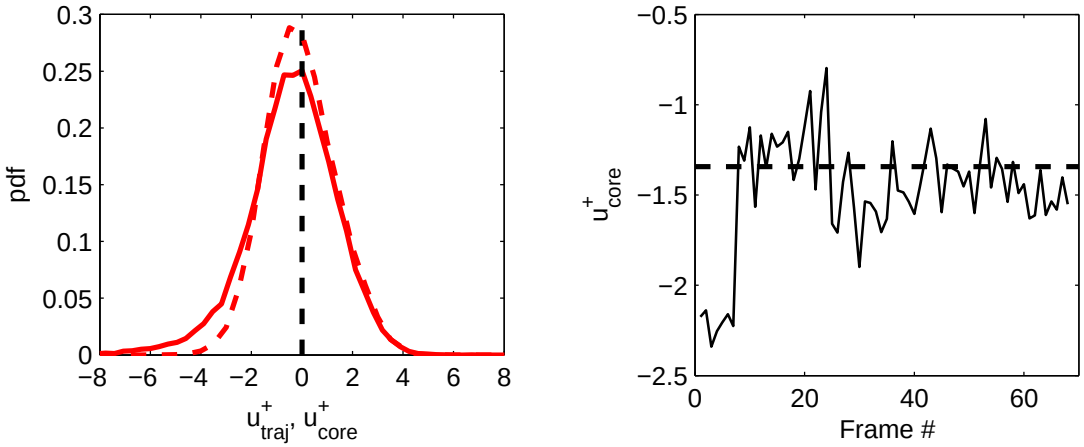

(a) Velocity pdf comparison

(b) Single trajectory velocity comparison

Figure 4.29: (a): Comparison of convection velocity pdfs for plane SF2. Dotted line: u_{core}, solid line: u_{traj}. (b): Comparison of the core velocity and the mean trajectory velocity for one trajectory. Dotted line: mean trajectory velocity, solid line: core velocity calculated at each timestep along the trajectory

as shown in Fig. 4.29b, but there are many cases where the match is not quite as good. In Fig. 4.30a, a cloud of points shows the mean trajectory velocity plotted against the mean core velocity averaged over the trajectory for each SCS trajectory. The appearance of the longer low-speed tail is apparent here. Also, a pdf of the difference between these two calculated quantities, as in Fig. 4.30b, shows that around 50% of the SCS trajectories have a difference of more than u_τ between the two measures.

Either method of calculating the convection velocity give similar results in terms of the distribution of convection velocities. On the other hand, for individual structures, there is usually some discrepancy between the two methods so when investigating a single structure, it is best to be able to directly measure the convection velocity.

4.4.3 SCS lifetimes

Using the time-resolved data, the average SCS lifetime can be measured. The lifetime is defined as the amount of time that a SCS in one of the wall-parallel planes can be tracked in time. Of course, this will be skewed slightly due to SCS which leave the field of view (so there is a limit to the amount of time a SCS can be tracked). Also, it is possible for a SCS to travel up or down in the wall-normal direction as time progresses or to grow away from the wall with the boundary layer, which grows by about 10% over the field of view. A pdf of the SCS lifetimes for each plane is shown in Fig. 4.31.

It would appear that a majority of the SCS exist less than 1 eddy turnover time, but a majority of these counts are likely due to issues with tracking a particular SCS in time, for example, the problem illustrated in Fig. 4.24. As the free stream is approached, SCS tend to live for longer periods of time

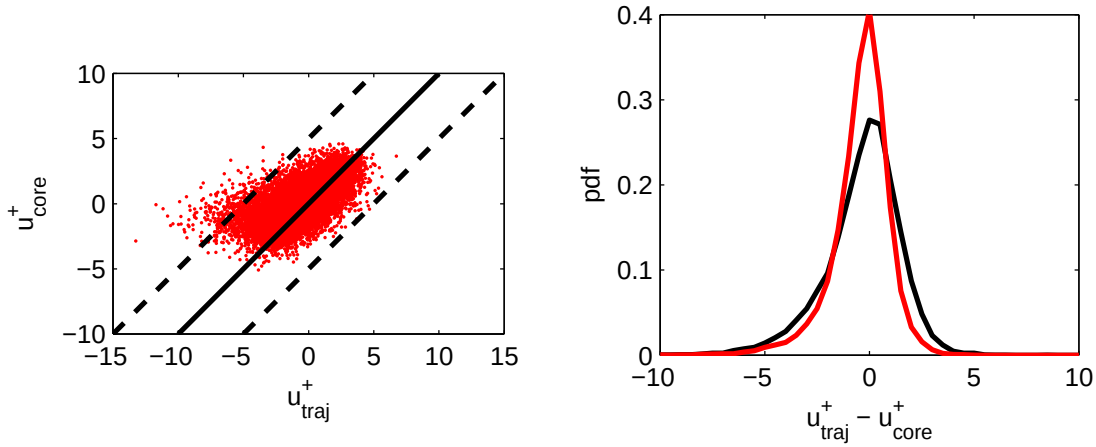

(a) Velocity measurement point cloud for plane SF2

(b) Velocity measurement difference pdf

Figure 4.30: (a): Point cloud of the average trajectory velocity vs. the mean core velocity averaged over the trajectory. Solid black line: a one-to-one relationship between velocities, dashed lines: differences of $\pm 5u_c^+$ between velocities. (b): Histogram of the difference between the two velocity measures for plane SF0: black and SF2: red

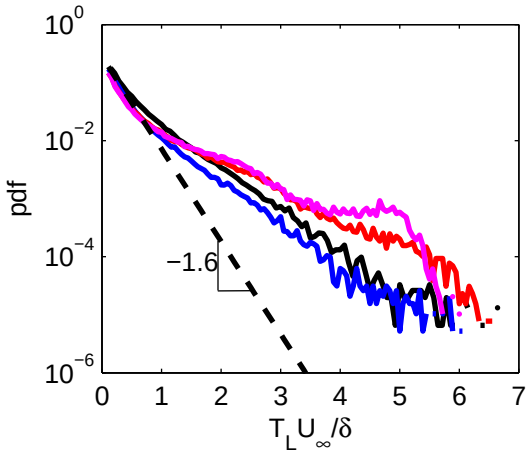

Figure 4.31: Pdf of SCS lifetimes for planes SF0: black, SF1: blue, SF2: red, and SF3: magenta. Dashed black line: the slope of all pdfs before $0.5\delta/U_\infty$

which is postulated to be an effect of the reduction of turbulent stresses deforming and possibly destroying these structures. The buildup of the pdf at long times in plane SF3 is an effect of the limited observation time (limited by the size of the domain) as will be shown in Section 4.5.

4.5 Statistically inferred SCS structures

In this section a method for inferring the SCS structure, in particular whether the SCS is attached or detached from the wall, from the wall-parallel plane data will be discussed. First, the assumptions made will be stated, the calculation method will be presented, and finally, conclusions about the SCS structure lifetimes and convection velocities will be presented.

4.5.1 Assumptions

In each wall-parallel plane a number of SCS were tracked in time and these SCS convected at a range of velocities as presented in Section 4.4.2. The SCS identified in these wall-parallel planes were simply slices of SCS passing through the plane. For such a SCS to remain coherent in a 3D sense, all parts of the SCS must travel at, or near, a single convection velocity. From this assumption, it may be concluded that SCS signatures in two different planes that travel at the same convection velocity have the potential to be part of the same SCS. Although all four planes were measured separately, and thus a direct connection cannot be made, the large amount of data available allows statistical inferences about the SCS.

It is proposed, then, that by comparing the convection velocity histograms between two planes, one can infer a relationship amongst SCS in them. Fig. 4.32 illustrates how this works. Regions where the convection velocity histograms for the two planes overlap, region B in Fig. 4.32, are inferred to be from structures connected between the two planes. Regions of the histograms that do not overlap, regions A and C, are assumed to be from structures that exist in only one of the two planes. By analyzing these charts for all combinations of the four measured planes, 10 different structures can be inferred as shown in Fig. 4.33. The method for identifying these different structures is described in Appendix B. In addition, a better terminology for naming the various SCS is introduced where $\Psi(i,j)$ denotes the structure that is connected between planes y_i and y_j, but does not extend beyond either. For example, structure 3 from Fig. 4.33 would be called $\Psi(1,3)$. By counting the number of structures of each type, the percentage of each type of structure in the flow can be inferred. These percentages are given in Fig. 4.34.

From Fig. 4.34 it is apparent that the most prevalent SCS is an "attached" structure [3] that does not reach beyond the log layer. The taller attached structures are less common than the ones

[3] Here "attached" refers to SCS which reach down to plane SF0 which is close to the wall ($y^+ = 38$), and thus SCS reaching down this far likely extend down into the laminar sublayer.

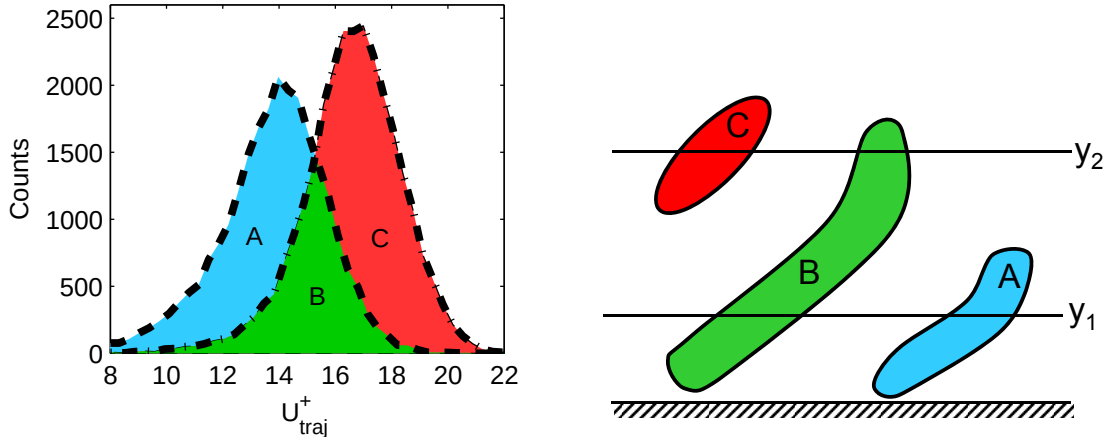

(a) Histogram comparison

(b) Cartoon of inferred structures

Figure 4.32: In (a) three regions are identified by comparing the convection velocity histograms at y/δ = 0.08 and y/δ = 0.30. The labeled regions are referenced in (b) showing the structure shapes inferred from the histogram comparison in (a).

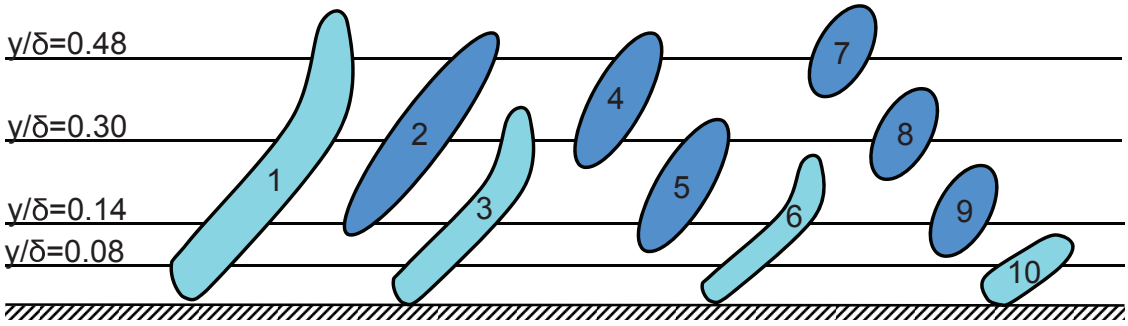

Figure 4.33: All possible SCS connections inferred from the convection velocity histograms and enumerated. SCS which reach down to plane SF0 are in light blue and are called "attached" structures.

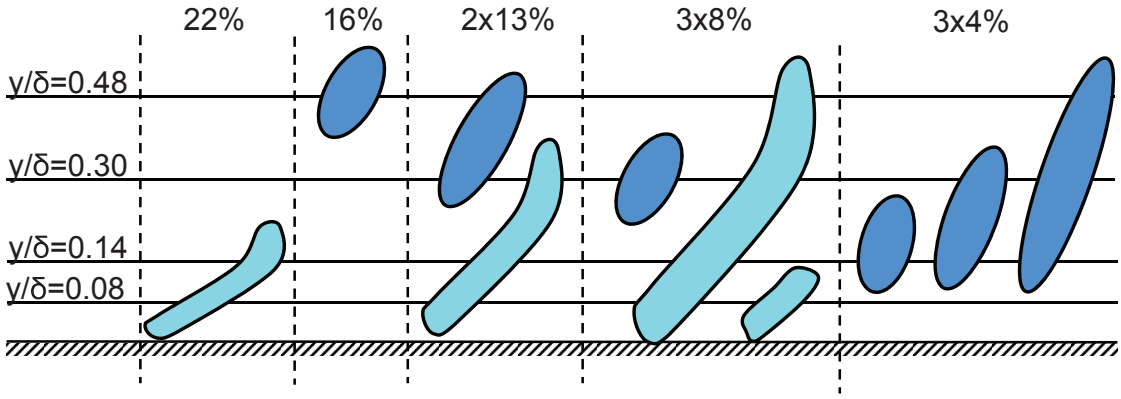

Figure 4.34: The SCS shown in Fig. 4.33 are shown in order of their prevalence in the boundary layer. The percentage given is rounded to the nearest percent and SCS with similar percentages are grouped together.

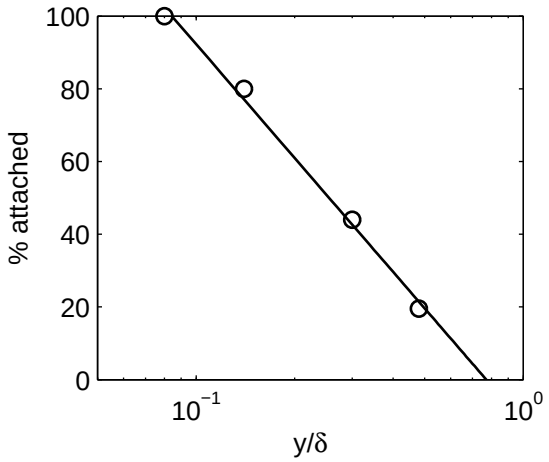

Figure 4.35: The percentage of SCS at a given wall-normal distance that are "attached" to the plane nearest the wall

spanning planes SF0 and SF1. As shown in Fig. 4.35, the number of attached structures detected in each plane appears to decrease logarithmically with wall-normal distance; the calculation of this quantity is described in detail in Appendix B. This is in agreement with the observation that the majority of spanwise hairpin heads are found in the log layer [Wu and Christensen, 2006].

4.5.2 Joint convection velocity, lifetime histograms

Joint pdfs or histograms of the SCS convection velocity and SCS lifetime can be constructed for each wall-parallel plane. An example is shown in Fig. 4.36 which shows the integral relationship between the joint pdf and the pdfs of convection velocity and SCS lifetime. The jpdf for each of the wall-parallel planes is presented in Fig. 4.37.

The red line in Fig. 4.37 indicates the edge of the domain. This edge is the time at which a SCS would leave the field of view if the SCS started at the most upstream end of the field of view and was traveling at a given velocity, U_c^+. While almost no SCS reach this time limit near the wall, further from the wall, as in Figs. 4.37c and 4.37d, a larger percentage of SCS reach this point. In particular, a large buildup of counts is found at this limit in Fig. 4.37d. Thus, in this plane, the lifetime of a reasonable portion of SCS actually persist for longer than 5 eddy turnover times. This buildup of counts was previously identified in the SCS lifetime histograms shown in Fig. 4.31. Noting that there is little buildup of counts at the edge of the domain for plane SF2, though, the change in slope between planes SF1 and SF2 in Fig. 4.31 was due to a difference in the overall lifetime as opposed to an artifact of this buildup of counts.

As with the convection velocity histograms discussed in Section 4.5.1, jpdfs can also be constructed for each of the inferred SCS types providing information about the distribution of convection velocities and lifetimes for each of these structures. By integrating over the lifetime, the velocity

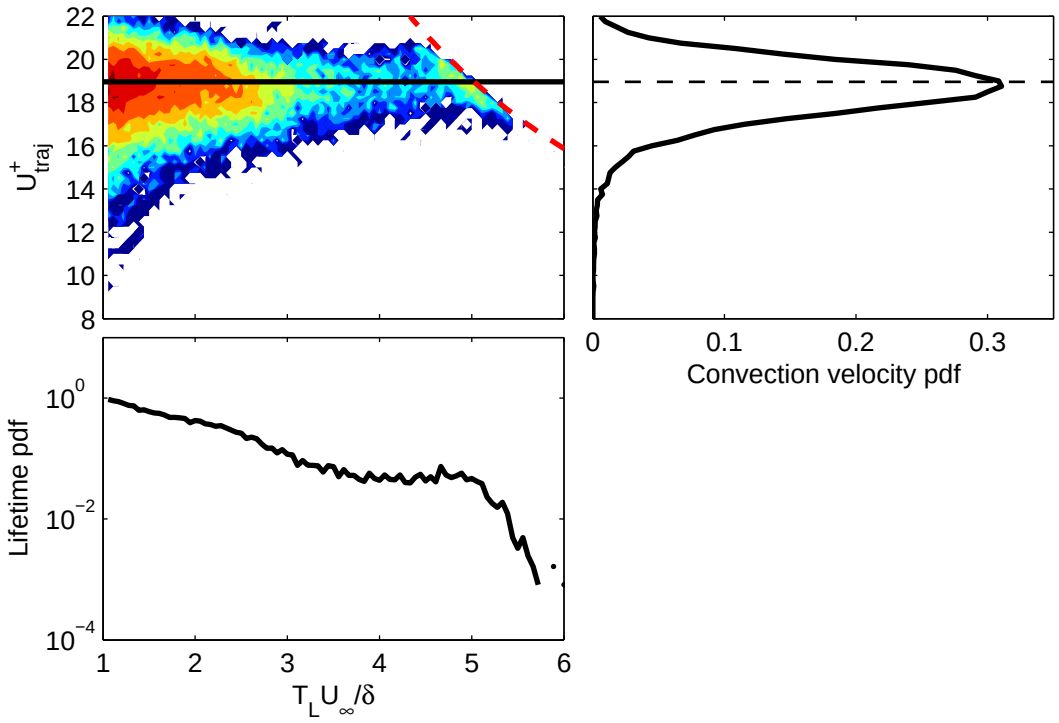

Figure 4.36: Top-left panel: joint pdf of SCS convection velocity and SCS lifetime; red line: edge of the domain, black line: local mean velocity. Top-right panel: convection velocity pdf calculated by integrating over the lifetime. Bottom-left panel: lifetime pdf calculated by integrating over the convection velocities. These pdfs are for SCS where $T_L \geq T_E$.

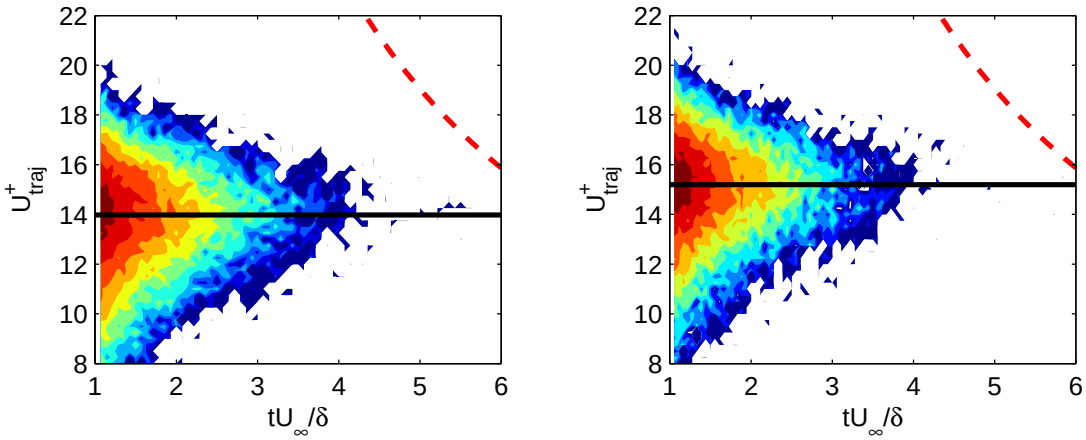

(a) SF0

(b) SF1

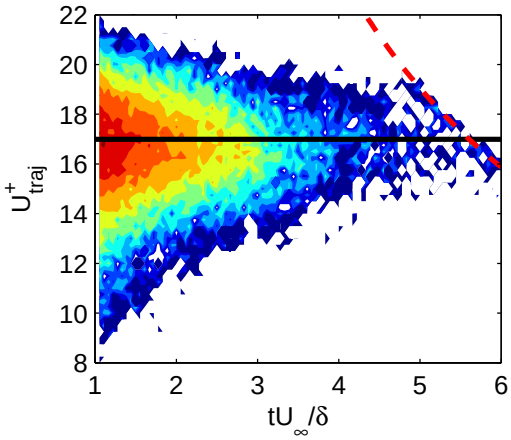

(c) SF2

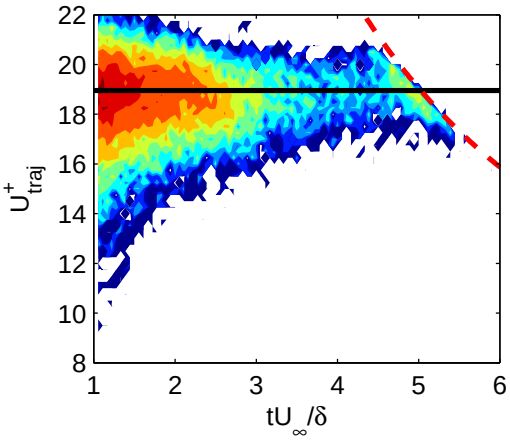

(d) SF3

Figure 4.37: The joint pdfs of SCS convection velocity and SCS lifetime for (a): SF0,(b): SF1, (c): SF2, and (d): SF3. The color indicates the log of the number of counts per bin. Black line: local mean velocity, dashed red line: edge of the domain

pdfs associated with each type of structure can be calculated as shown in Figs. 4.38 and 4.39. Among these, Fig. 4.38a shows the pdfs for all attached structures, Fig. 4.38b shows all detached structures that reside only in one plane, and Fig. 4.39a shows the remaining detached structures. Finally, Fig. 4.39b shows the pdf of all attached vs. all detached structures. Each figure shows the local mean velocity of each measured plane by dotted vertical lines for reference, and the mean value is marked by a circle on each pdf (as opposed to the mode value which is the peak in the pdf).

From Fig. 4.38a it is found that all attached structures have a long low-speed tail unlike the detached structures in Fig. 4.38b and Fig. 4.39a, leading to a mean convection velocity less than the mode value for all attached structures. In addition, for each attached structure, both the mode and mean values of convection velocity are below the local mean velocity of the "upper plane". For example, $\Psi(1,3)$ (red line in Fig. 4.38a) is an attached structure whose mean and mode convection velocity are well below the local mean of plane 3 (SF2), the "upper plane" for this structure (dotted red line). This makes sense considering that each structure must convect at one convection velocity, and this convection velocity is likely between the two extremes; the convection velocity immediately next to the wall and the convection velocity of the final plane that the SCS passes through. The structure's convection velocity is different than the local mean velocity over most of its height and is not being stretched up and growing away from the wall, but simply traveling downstream.

To investigate this point further, a comparison is made between the local mean velocity of the "upper plane", the minimum convection velocity in the boundary layer, $U^+_{c,min} = 8$ [Morrison et al., 1971], and the mean convection velocity for an attached structure using the parameter γ in Eqn. 4.19.

$$\gamma = \frac{(\overline{U}_{traj} - U_{c,min})}{(\overline{U}(y) - U_{c,min})} \tag{4.19}$$

The value of γ ranges from 0.72–0.74 for all attached structures. This shows that all attached SCS, in a mean sense, convect at a speed 3/4s of the way between the minimum convection velocity and the local mean of the "upper plane".

For the detached structures shown in Fig. 4.38b and Fig. 4.39a, the mode and mean convection velocity are much closer to one another due to the lack of the low-velocity tail. For structures that are only present in one plane (Fig. 4.38b), the convection velocity is generally between the plane above and below as might be expected for a detached structure being convected by the flow. The mode convection velocity and the local mean coincide well, and the parameter γ from Eqn. 4.19 is above 0.88 in all cases, that is the convection velocity is close to the local mean velocity of the plane that these structures cut through.

For the other detached structures in Fig. 4.39a the convection velocity pdfs generally rest between the local mean velocity of the "lower" and "upper" planes for each of these structures. This is similar to the findings for the detached structures in Fig. 4.38b and the same conclusions can be drawn.

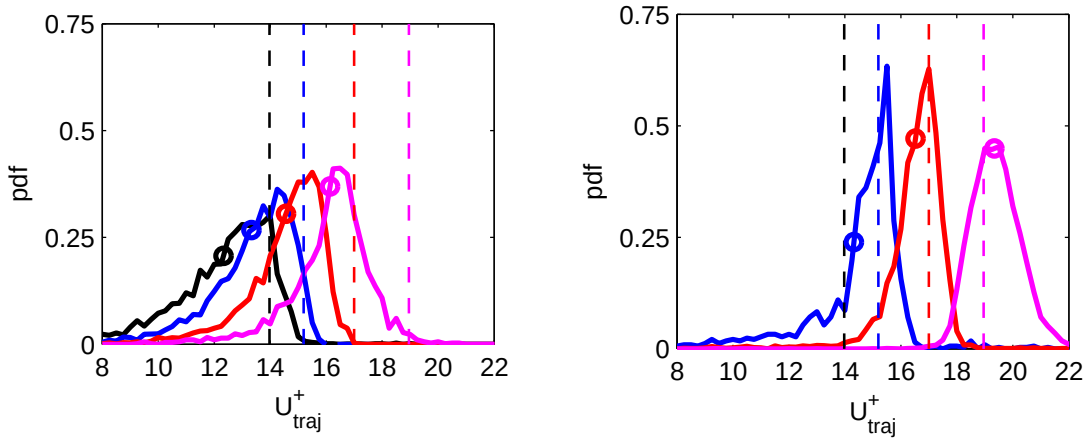

(a) Attached structures

(b) Single plane structures

Figure 4.38: (a): Convection velocity histograms for all attached structures; $\Psi(1,1)$: black, $\Psi(1,2)$: blue, $\Psi(1,3)$: red, and $\Psi(1,4)$: magenta. (b): Convection velocity of structures that exist only in one plane; $\Psi(2,2)$: blue, $\Psi(3,3)$: red, and $\Psi(4,4)$: magenta. In both figures, circles: mean convection velocity calculated from the histogram, vertical dashed lines: local mean velocity from planes SF0 (black), SF1 (blue), SF2 (red), and SF3 (magenta)

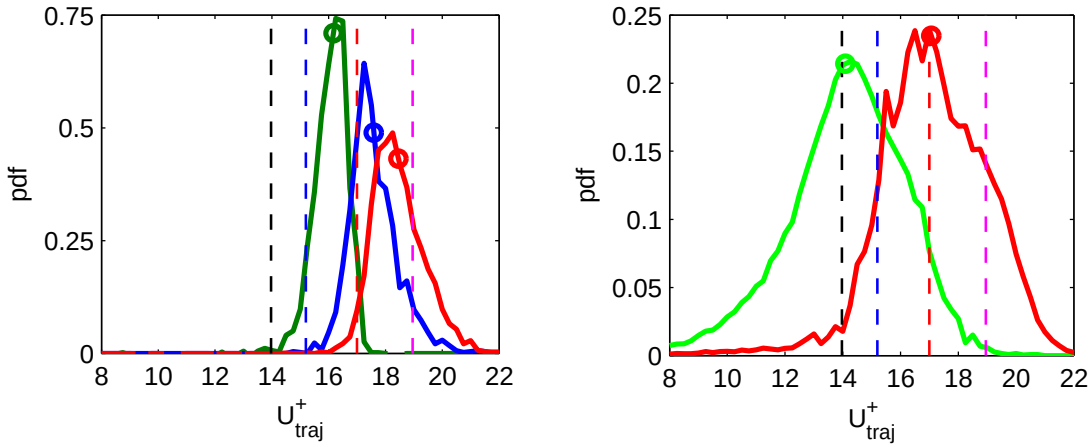

(a) Remaining detached structures

(b) Attached and detached

Figure 4.39: (a): Convection velocity pdfs of the remaining structures; $\Psi(2,3)$: dark green, $\Psi(2,4)$: blue, and $\Psi(3,4)$: red. (b): Convection velocity pdfs for all attached structures (green) and all detached structures (red). In both figures, circles: mean convection velocity, vertical dashed lines: local mean velocity from planes SF0 (black), SF1 (blue), SF2 (red), and SF3 (magenta)

The combined effect of all attached and all detached structures on the shape of the convection velocity pdf is shown in Fig. 4.39b. Again, the long low-velocity tail of the attached structure pdf is notable. Now, though, the mean and mode convection velocity are similar and are both near the local mean at plane SF0. It is also noted that the velocity almost never exceeds the local mean in plane SF3, that is these structures rarely reach beyond 50% of the boundary layer height. For the detached structures, the pdf has a slight bias toward the high-velocity tail and the mean and mode convection velocity are near the local mean for plane SF2. The slowest of these structures never travels slower than the local mean of plane SF0 and nowhere near the expected minimum convection velocity, as might be expected of structures that are not connected to the near-wall region.

The lifetime pdfs for these same structures are shown in Figs. 4.40 and 4.41. The faster decay rate of the attached structures in Fig. 4.40a compared to the detached structures in Figs. 4.40b and 4.41a is notable as is the similarity in the decay rate amongst different attached and different detached structures. In general it appears that the probability of having a SCS exist for an additional eddy turnover time drops by less than half a decade (0.4) for detached structures, but drops by nearly a full decade for attached structures as verified by the average attached and detached structure lifetimes in Fig. 4.41b. The noise at large times for the attached SCS lifetimes is due to the small number of counts at lifetimes beyond about 4 eddy turnover times and the decay at large times for the detached structures is due to the limited field of view beyond about 4–5 eddy turnover times as noted earlier.

Joint SCS lifetime, SCS convection velocity histograms were also analyzed using the mean core velocity as opposed to the mean trajectory velocity. All findings were similar with the main difference being the lack of the elongated low-speed tail for the attached SCS. As noted previously, this tail was the main difference between the convection velocity histograms using the two different calculation methods. Whether this tail is actually a signature of attached structures or from poor tracking of SCS is debatable.

4.6 Summary

In this chapter, SCS and low- and high-momentum regions were investigated in wall-parallel planes. Using a threshold on the swirling strength, individual SCS were identified in the flow and were also tracked in time. SCS properties were evaluated using the properties of the extracted swirling regions. From these, the distribution of the SCS radius, inclination angle, and yaw angle were found to be similar to results in the literature. The resolution of all of these properties was low due to the moderate spatial resolution available. Generally SCS were only 3 or 4 vectors wide, which reduced the resolution of both the inclination angle and yaw angle to around 10° and 20°, respectively. This also made it difficult to track the instantaneous change of properties along a SCS trajectory, and

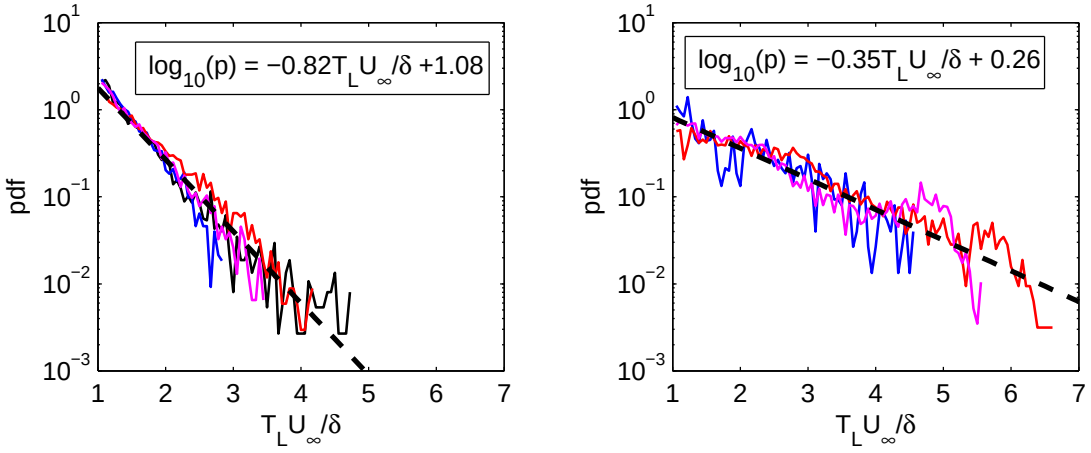

(a) Attached structures

(b) Single plane structures

Figure 4.40: (a): Lifetime pdfs for all attached structures; $\Psi(1,1)$: black, $\Psi(1,2)$: blue, $\Psi(1,3)$: red, and $\Psi(1,4)$: magenta. (b): Lifetime pdfs of the detached structures that exist only in one plane; $\Psi(2,2)$: blue, $\Psi(3,3)$: red, and $\Psi(4,4)$: magenta. In both figures, dashed black lines: log fit to the lifetime decay for all structures in the figure

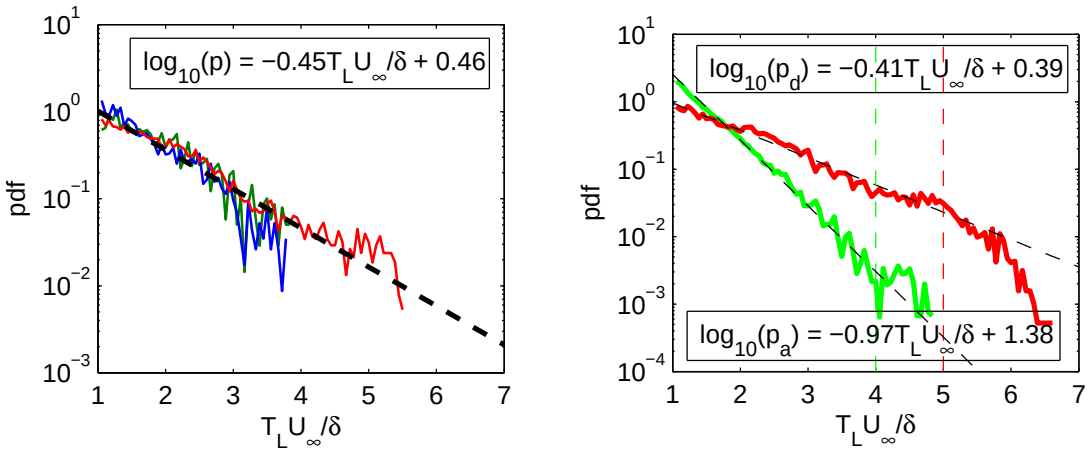

(a) Remaining detached structures

(b) Attached and detached

Figure 4.41: (a): Lifetime pdfs of the remaining structures; $\Psi(2,3)$: dark green, $\Psi(2,4)$: blue, and $\Psi(3,4)$: red. Dashed black line: log fit to the lifetime decay for all structures. (b): Lifetime pdfs for all attached structures (green) and all detached structures (red). Dashed black lines: the log fit to the lifetime decay for the attached structures up to the dashed green line and detached structures up to the dashed red line

thus the properties of a SCS could only be found in an average sense over its trajectory.

Histograms of the SCS convection velocity were measured by tracking trajectories in time as well as from an average of the velocity within each SCS. The pdfs of both of these were similar, with the difference being the appearance of a low-speed tail when SCS were tracked in time. On the other hand, there was not a one-to-one correspondence between the two calculation methods. In both cases, the convection velocity histogram in the plane furthest from the wall showed an asymmetry on the high-speed end, which was from the influence of the free stream (i.e., structures in the flow could not travel faster than the free stream).

The size of low-momentum regions ranged from 0.2–0.4δ in spanwise extent and about 1–2.5δ or 1–4δ in streamwise extent, with the lengths increasing away from the wall. This growth was also found in the literature. Given that the Reynolds number was low Re_τ = 410, VLSMs, and thus longer streamwise structures, were not expected in the flow. Low-momentum regions were also investigated using linear stochastic estimation (LSE), from which similar spanwise lengths were inferred, but from which streamwise lengths were shorter than measured earlier. It was expected that while the LSE showed the general shape of low-momentum regions, the LSE itself was an average over structures of multiple lengths, and must be interpreted as such. Applying LSE to the swirl fields, SCS spacings similar to the width of the low-momentum regions was found.

Analyzing the lifetime of SCS trajectories, it was found that the lifetime increased with distance from the wall, likely linked with the lower levels of shear stress in this region. In addition, convection velocity pdfs allowed the statistical inference of attached and detached structures. Of all the inferred structure types, near-wall-attached structures were most prevalent. Reanalyzing the lifetime pdfs for attached and detached structures, it was found that detached structures have a tendency to live longer with the pdf dropping by a decade over 1 eddy turnover time for attached structures but only 40% of a decade for detached structures. While detached structures appeared to be convected by the flow with velocities similar to the planes through which they cut, attached structures convected at speeds between the velocity in the plane nearest the wall and the uppermost plane through which the attached structure was detected (generally a speed 3/4s of the way between $8u_\tau$ and the local mean of the topmost plane through with the SCS cut). This could explain the increase in scales traveling faster than the local mean near the wall as noted by Krogstad et al. [1998].

Chapter 5

Measurements Over a Spatially Periodic Roughness

In this chapter, the flow over the periodic roughness described in Section 2.2.2.2 is analyzed. This chapter begins with a discussion of the method for determining the friction velocity and other fundamental quantities to characterize the rough-wall turbulent boundary layer. The drag measured over the rough surface is also presented and compared to the drag over a smooth surface. This is followed by a discussion of the flow development downstream of the start of the roughness as well as the variation of the turbulent statistics at different points between roughness elements, called stations. Finally, the variation in the streamwise velocity spectrum at different stations will be studied as well as the differences between the smooth-wall and rough-wall spectra. As the slope of the downstream side of the roughness elements was small (14°), only mild separation would be expected and thus hotwire measurements downstream of a roughness element should provide useful information about the flow.

5.1 Measurement and definition of fundamental quantities

One of the major difficulties in scaling the measured velocity profiles and spectra over the rough-wall was the determination of the friction velocity and the virtual origin of the roughness, e, discussed in Section 1.2.2. For a smooth wall, the location of the origin (in this case, the wall) is known, so the friction velocity can be calculated by optimizing the fit between the measured mean velocity profile and the log law (i.e., Clauser's method). For a rough wall, both the virtual origin (the location below the roughness peaks at which the mean velocity profile would extrapolate to zero velocity) and the friction velocity must be fit simultaneously. To do so, the modified Clauser method was used [Perry and Li, 1990].

Using the Clauser method as described in Section 3.1 with the smooth wall mean velocity profiles, a value of u_τ = 0.97 m/s was calculated where the value of u_τ could be determined to the nearest

Location	u_τ (m/s)	δ (mm)	ΔU^+	k_s^+	k_s/k	δ/k_s
5-Profile	1.12	40.6	4.5	26.9	0.47	112
6-Profile	1.14	42.5	5.1	34.3	0.58	97
7-Profile	1.10	43.3	4.3	24.3	0.43	130
7-Spectrum	1.11	44.2	4.5	27.4	0.48	122

Table 5.1: Parameters for the rough-wall boundary layer. Measurements are averaged over all stations for a given location.

0.01 m/s, although the actual accuracy of the method is expected to be less.

The modified Clauser method was derived by Perry and Li [1990] using the equation for the composite velocity profile in Eqn. 1.5 with a velocity defect, ΔU^+, added in to account for the roughness induced downward shift of the mean velocity profile. This profile is given in Eqn. 5.1, is equivalent to Eqn. 1.7, and, after some algebra, can be transformed into the more useful form in Eqn. 5.2 as shown in Appendix C.

$$\frac{\overline{U}(y)}{u_\tau} = \frac{1}{\kappa}\ln\left(\frac{yu_\tau}{\nu}\right) + B - \frac{\Delta U}{u_\tau} + \frac{\Pi}{\kappa}W_c\left(\frac{y}{\delta}\right) \tag{5.1}$$

$$\frac{\overline{U}(y)}{U_\infty} = 1 + \frac{u_\tau}{U_\infty}\frac{1}{\kappa}\ln\left(\frac{y'}{\delta^*}\right) + \frac{u_\tau}{U_\infty}\frac{1}{\kappa}\ln\left(\frac{u_\tau}{U_\infty}\right) + \frac{u_\tau}{U_\infty}\frac{1}{\kappa}\left(\ln(1+\Pi) - 2\Pi - \ln(\kappa) + \Pi W_c\left(\frac{y}{\delta}\right)\right) \tag{5.2}$$

δ^* is the displacement thickness defined in Eqn. 5.3 and $y' = y + e$, where e is the offset of the virtual origin.

$$\delta^* = \int_0^\delta \left(1 - \frac{\overline{U}(y)}{U_\infty}\right) dy \tag{5.3}$$

Plotting the measured mean velocity profiles in the form $\overline{U}(y)/U_\infty$ vs. y/δ^*, the offset, e, and friction velocity ratio, u_τ/U_∞, were varied to find the best fit between the mean velocity profiles and Eqn. 5.2 in a least-squares sense. This fit was performed over the range $100 < y^+ < 0.12\delta$. Once u_τ and e were calculated, the velocity defect, ΔU^+, was measured by comparing the rough and smooth wall profiles. The equation for this offset is given in Eqn. 5.4.

$$\Delta U^+ = \overline{U}(y)^+ - \left(\frac{1}{\kappa}\ln(y^+) + B\right) \tag{5.4}$$

The variation of u_τ, ΔU^+, k_s (using Eqn. 1.8), as well as other related properties, are documented in Appendix D. A summary of the average values (averaged over all stations) at locations 5-7 are provided in Table 5.1 showing a slight decrease in u_τ and increase in δ moving downstream.

At location 7, the roughness height was $k/\delta = 0.019$ or, in inner scaling, $k^+ = 56$ and the equivalent sand grain roughness was $k_s/\delta = 0.008$ or $k_s^+ = 25$, found using Eqn. 1.8. According to the criteria

discussed in Section 1.2.2 the boundary layer approximation was preserved over this roughness, but the flow was only transitionally rough, and thus the effect of the roughness shape was important. While the roughness height was large in physical units, the equivalent sand grain roughness was about half the size of the actual roughness, meaning that the roughness only input a weak perturbation to the flow. This makes sense given the sparsity (in both streamwise and spanwise extent) as well as the shallow incline and decline of the roughness elements. It is interesting to note that compared to the rms roughness height, k_{rms} = 0.25 mm, k_s is 1.3 times larger. Perhaps k_s is more strongly correlated with k_{rms} than the peak roughness height, k, in general.

From the modified Clauser calculations, it was also noted that the inferred u_τ varied quite dramatically at different stations along the roughness; that is within one period of the roughness. For smooth, and even most studies of rough-wall turbulent boundary layers, u_τ is nearly constant with streamwise variation. For the smooth-wall measurements, u_τ varied by less than 1% over a length of $8.8\delta_0$, where δ_0 is the boundary layer thickness just upstream of the plate. For the fully developed rough-wall boundary layer (stations 5–7 as will be discussed in Section 5.3.2), though, within one period of the roughness ($0.55\delta_0$), the value of u_τ varied by 3.2% on average (± 0.035 m/s) with a maximum variation of 5.8% (± 0.064 m/s). This variation also produced a variation in k_s by 20–30% along one period of the roughness. Regardless of this large change along the roughness, it was decided that the local value of u_τ should be used to normalize the turbulent quantities; a mean value was not used. It was expected that the local value would allow a proper comparison between statistics at different stations along the roughness.

The variation of δ (calculated as the wall-normal location where the velocity reaches 99% of the free-stream velocity) was also calculated and values are presented in Fig. 5.1. Fitting a slope to this data, the change in the boundary layer thickness with streamwise location was found to be 1:54; that is the boundary layer thickness would double in height over a length of $54\delta_0$. Along one period of the roughness for locations 5-7, the average variation in δ was 1.2% (± 0.55 mm) and the maximum variation was 4.5% (± 2 mm).

Other important smooth- and rough-wall parameters at location 7 were summarized earlier in Table 2.5 of Section 2.2. For the rough-wall data, the values recorded were averaged over all stations at location 7. It is interesting to note that while Re_τ and u_τ were larger for the rough wall measurements, the value of δ was almost identical for both.

5.2 Drag measurements

The drag was measured with both smooth and rough plates using the setup shown in Fig. 2.10. The average shear stress at the wall was calculated by taking the total force imparted on the surface, F, and dividing by the area, A, as given in Eqn. 5.5. From this, the coefficient of friction, C_f was

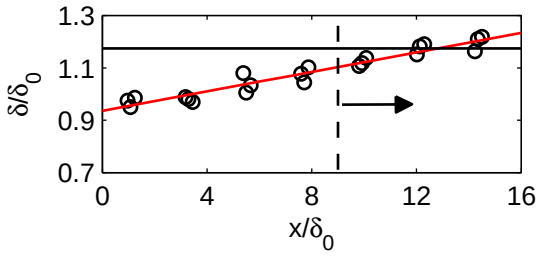

Figure 5.1: The variation of δ along the rough plate. The vertical axis is stretched by a factor of 10 to better show the streamwise variation. Red line: linear fit to the data with a slope of 0.0186, a ratio of 1:54, solid black line: δ measured at location 7 over the smooth wall, dotted black line: location beyond which the rough-wall boundary layer has reached a self-similar or fully developed state

calculated as defined in Eqn. 5.6. The measurements are summarized in Table 5.2.

$$\tau_w = \frac{F}{A} \tag{5.5}$$

$$C_f = \frac{\tau_w}{1/2\rho U_\infty^2} \tag{5.6}$$

Surface	C_f	$u_\tau(m/s)$	u_τ Clauser (m/s)	% diff u_τ
Smooth	0.0027	0.8911	0.969	8.0
Rough	0.0036	1.0305	1.140	9.6

Table 5.2: Drag measurements with $U_\infty = 25.3m/s$

The drag force was higher over the rough wall than the smooth wall. It should be noted that unlike the smooth wall case, the rough-wall boundary layer was adjusting to the new rough-wall boundary condition for the first few δ_0 along the plate. Thus, the drag measured over the rough wall was not necessarily representative of the fully developed rough -wall boundary layer.

The values of u_τ calculated from the drag measurements (a value of u_τ averaged over the entire plate) were within 10% of the values calculated using the Clauser method at the most downstream location. In both cases, the Clauser method provided a higher estimate of u_τ. Since u_τ should be lower at the downstream end of the plate, one would expect the value of u_τ from the Clauser method to be lower, which was not the case, so this 10% difference indicates the percent error between the two methods.

5.3 Mean and rms velocity profiles

In this section, the smooth wall profiles are compared to the literature to assure that the facility was capable of producing a canonical zero-pressure-gradient boundary layer. Next, the variation

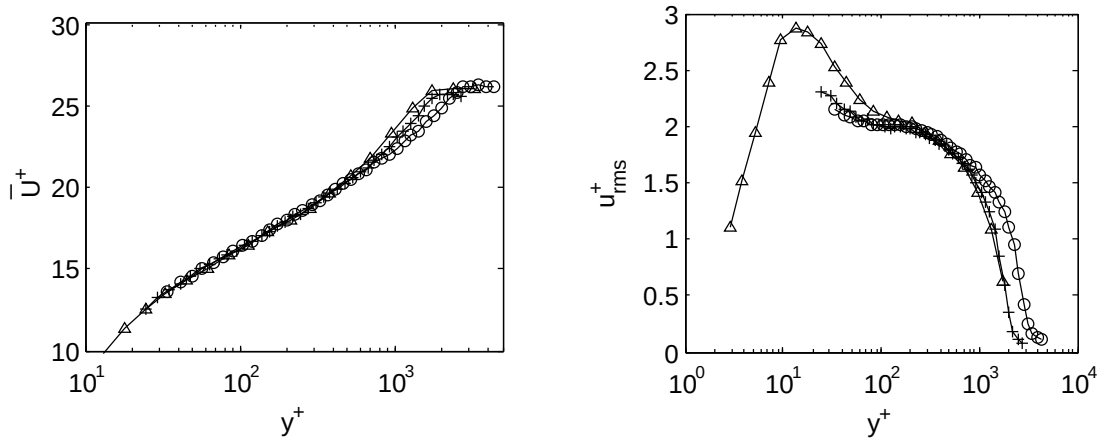

(a) Smooth wall mean velocity profile

(b) Smooth wall rms streamwise velocity profile

Figure 5.2: (a): The mean streamwise velocity profile. (b): The rms streamwise velocity fluctuation profile. (+): measurements at location 3 with Re_θ = 5150, (△): data from DeGraaff and Eaton [2000] at Re_θ = 5200, (○): Data at location 7 at the operating Reynolds number of Re_θ = 7300

in the mean and rms profiles are compared at all locations along the roughness to infer when the boundary layer reached a fully developed state (that is when it had fully adjusted to the rough-wall boundary condition). Finally, the variation of the statistics at different stations along the roughness is investigated for stations where the flow is fully developed, and these measurements are compared to the smooth wall measurements.

5.3.1 Smooth-wall profiles

The mean and rms velocity profiles for measurements over the smooth surface are shown in Fig. 5.2 for two different Reynolds numbers. These profiles compare well with the data of DeGraaff and Eaton [2000] (compare the plus and triangle symbols). For Re_θ = 7300, the late departure of the mean velocity profile from the log layer and the extra extent of the rms profile beyond the Re_θ = 5200 profiles were expected due to the increase in scale separation with Reynolds number. The mean velocity in the wake region was slightly lower than the data of DeGraaff and Eaton [2000], likely due to the slight variation in the free-stream velocity between the location of the measurement probe and the Pitot tube used for calibrating the measurement probe (see Fig. 2.7a). This skewed the calibration at the highest velocities, where the maximum error was U^+_{er} = −0.37 for Re_θ = 7300. The error decreased for lower calibration velocities, and hence there is no difference in the profiles closer to the wall. The low value of the rms velocity fluctuations up to, and possibly beyond, y^+ = 100 was expected due to the long viscous length of the hotwire, l^+ = 77, as described in Section 2.2.2.1.

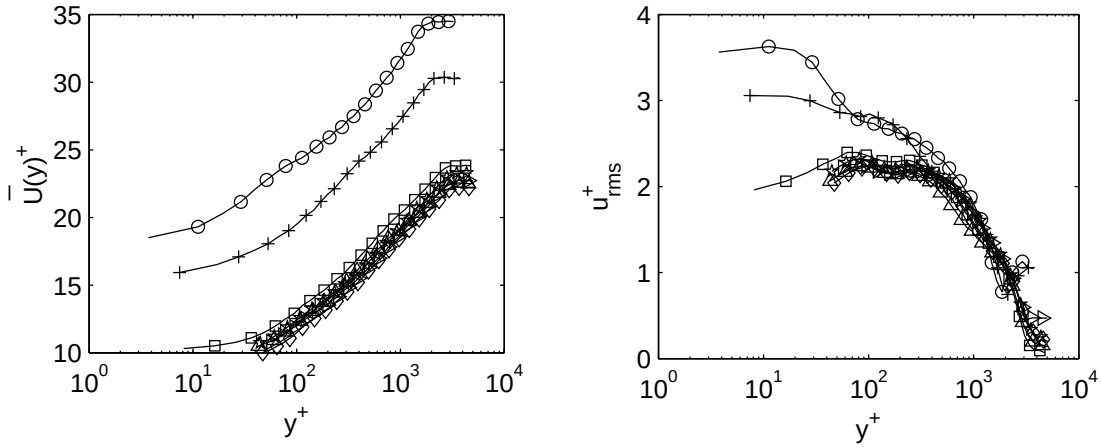

(a) Mean Velocity (b) RMS Fluctuations

Figure 5.3: The (a): mean and (b): rms streamwise velocity profiles at station 1 of location 1: ○, 2:+ , 3:△, 4:□, 5:◊, 6:▷, and 7:☆ in inner scaling

5.3.2 Streamwise development of the flow over the rough test plate

In order to assure that the boundary layer had reached a fully developed state by the main measurement location (location 7, $14.2\delta_0$ downstream) and to understand what was happening to the flow as it developed, the streamwise velocity statistics and the amplitude modulation coefficient were investigated at different locations along the plate at station 1.

5.3.2.1 Variation of the velocity statistics

The comparison of the mean and rms streamwise velocity profiles at different locations are presented in inner units in Fig. 5.3 and in outer units in Fig. 5.4. The level of the free-stream velocity fluctuations is noted in Fig. 5.4b to show that these fluctuations were indeed low.

As shown, all rough-wall profiles are surely collapsed by location 5, and are nearly collapsed as early as location 3. Comparing the statistics at the other two stations (see Appendix D), it appears that the data collapses by location 5 at station 2 and by location 4 at station 3. The same collapse was found for higher order moments of the streamwise velocity (the skewness and flatness; see Appendix D). Thus the boundary layer had reached a fully developed state over any point along the roughness by location 5, or $9.8\delta_0$ downstream. This development length was shorter than the value of $20\delta_0$ suggested by Andreopoulos and Wood [1982] and also the more recent value of $15\delta_0$ suggested by Efros and Krogstad [2011], and it may be expected that this was because the roughness was 3D and sparse, and thus presented less of an obstacle to the flow than the 2D bar roughness studied by these authors.

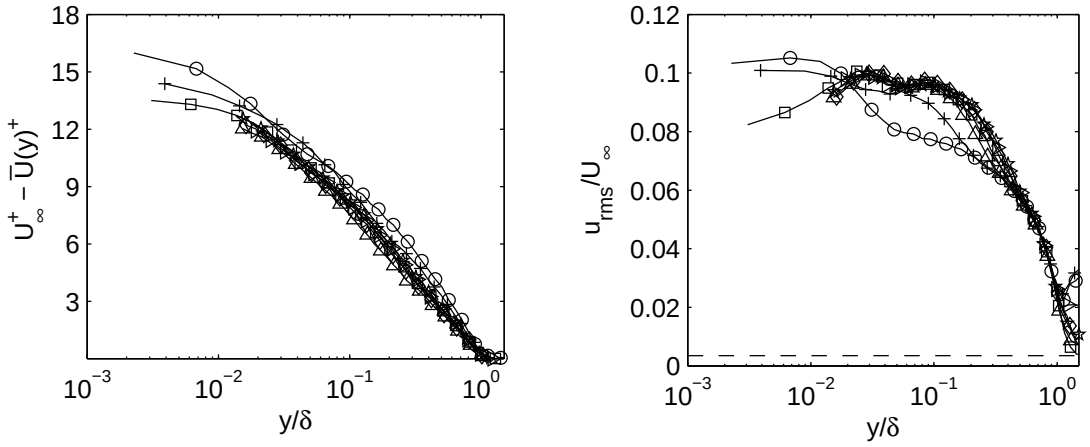

(a) Mean Velocity

(b) RMS Fluctuations

Figure 5.4: The (a): mean and (b): rms streamwise velocity profiles at station 1 of location 1: ○, 2:+ , 3:△, 4:□, 5:◊, 6:▷, and 7:☆ in outer scaling. The dashed black line in (b) shows the maximum value of the free-stream velocity fluctuations measured over the smooth plate from Fig. 2.7b.

5.3.2.2 Variation of the amplitude modulation

Fig. 5.5 shows the variation of the amplitude modulation with streamwise distance and also shows collapse by location 5, $9.8\delta_0$ downstream. The development itself is also interesting. It is clear that right after the start of the roughness the structure of the flow is disrupted near the wall leading to a near zero correlation coefficient. Meanwhile, the organization further from the wall is retained as indicated by a correlation coefficient identical to the smooth wall case. Further downstream, this disruption moves to the wake region, but the structure near the wall develops to a state similar to that of the smooth wall.

5.3.3 Statistics for the fully developed rough-wall boundary layer

This section discusses the variation of statistics for locations 5–7 where the flow is considered fully developed. The discussion starts with a comparison of the mean and rms streamwise velocity profiles at different stations along the roughness. This is followed by a comparison to the smooth wall mean and rms profiles. Finally, the amplitude modulation for the rough wall is discussed and compared to the smooth wall to infer differences in the flow structure.

5.3.3.1 Comparison of rough-wall profiles

Variations of the mean and rms statistics at different stations along the roughness are presented in outer units in Fig. 5.6 for the fully developed flow at location 7. It was observed that the variation along the roughness was limited to a thin region near the wall, which, for all locations and all stations analyzed, was limited to about 5k (5 roughness heights) from the virtual origin. This is similar to

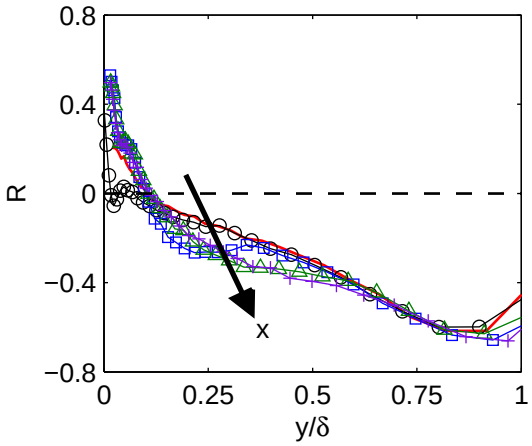

Figure 5.5: Amplitude modulation correlation at station 1 of several locations. Red line: location 0, black ○: location 1, blue □: location 3, green △: location 5, purple +: location 7

the findings of Hong et al. [2011] who observed that spatial variations over a periodic roughness died out about 2k above the roughness peaks.

5.3.3.2 Comparison of rough- and smooth-wall profiles

The smooth wall mean and rms streamwise velocity profiles are compared to the rough-wall profiles at station 1 of locations 5–7 in Fig. 5.7. While variations along the roughness were constrained to a few k above the roughness, the deviation of the rough-wall profiles from the smooth-wall profile persist out to about $y/\delta = 0.3$ or 17k, outside the log layer. This is quite interesting as the differences between smooth- and rough-wall profiles are generally contained within a few roughness heights of the wall [Flack et al., 2007]. Even recent work by Monty et al. [2011] where changes were observed well beyond 5k, no variation was observed beyond the log layer. The present measurements also show a near-wall hump around $y/\delta = 0.03$ in the rms statistics.

Beyond $y/\delta = 0.5$, well into the wake region, differences also exist between the rough and smooth wall mean and rms profiles. The smooth wall profiles show a higher mean velocity as well as a higher level of turbulent fluctuations than the rough wall in this region. To assure this was not an issue with the determination of u_τ for the rough-wall measurements, various combinations of u_τ and e were tested. With these changes, even if the wake region could be brought into agreement between rough and smooth wall cases, this was at the expense of agreement near the wall, pushing the region of overlap out from $y/\delta = 0.3$ to 0.5. It is interesting that such a small perturbation created a large change in the mean and rms profiles, even extending into the wake region of the flow. Furthermore, the effect in the wake region is a decrease in the turbulence intensity. If this were simply a Reynolds number effect, it should be expected that the turbulence intensity of the rough-wall flow would be higher given the higher friction Reynolds number of this flow.

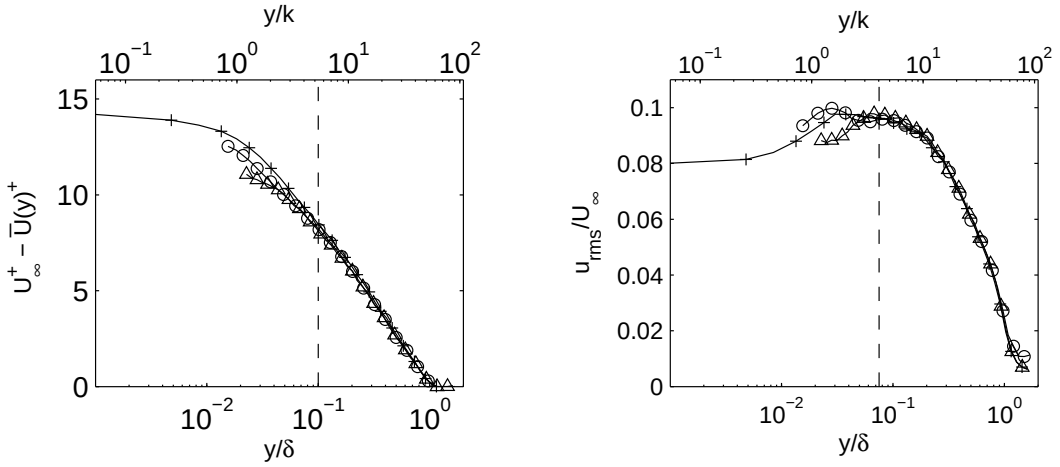

(a) Mean profiles at Location 7

(b) RMS profiles at Location 7

Figure 5.6: The (a): mean and (b): rms streamwise velocity profiles for stations ○: 1, +: 2, and △: 3 at location 7 (14.2 δ_0 downstream). Dashed vertical line: the wall-normal position beyond which the various profiles collapse

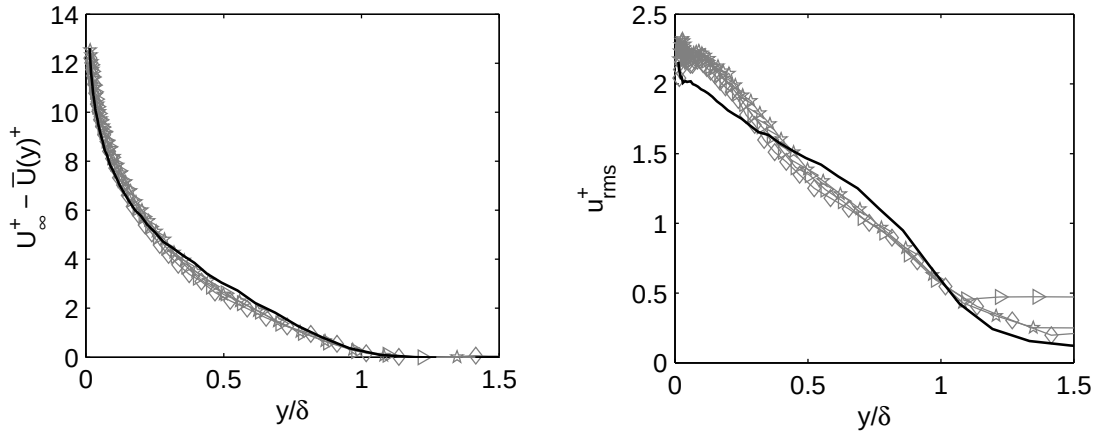

(a) Smooth and rough mean profiles

(b) Smooth and rough rms profiles

Figure 5.7: The (a): mean and (b): rms streamwise velocity profiles are compared between the smooth wall data (solid black line) and the rough-wall results at station 1 of locations 5:◊, 6:▷, and 7:☆

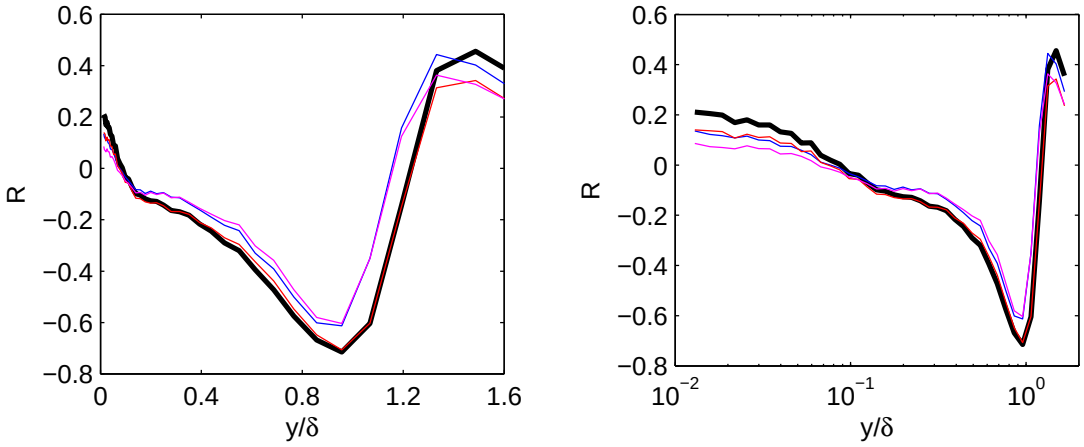

(a) Linear scaling

(b) Logarithmic scaling

Figure 5.8: The amplitude modulation correlation in linear (a) and logarithmic (b) scaling. Black: original correlation (solid red line in Fig. 5.9), blue: correlation where the window size was reduced by 10 (change from TU_∞/δ = 116 to TU_∞/δ = 11.6), red: correlation where the data was smoothed over 5 time steps (change from T^+ = 1.48 to T^+ = 7.38), magenta: correlation with smoothing and reduced window size

5.3.3.3 Comparison of the amplitude modulation over rough and smooth walls

In addition to changes in the mean and rms statistics, the roughness also had an effect on the interaction between large and small scales in the flow as observed from the amplitude modulation correlation described in Section 3.4. Data from the hotwire measurements show results in line with the results of Chung and McKeon [2010] and Mathis et al. [2009b]. It should be noted that while the Reynolds number of the present experiments was similar to Mathis et al. [2009b] ($Re_\tau \approx 3000$ for both), the length of the hotwire probe, l^+ = 77, dampened out some small-scale contributions to the correlation.

Before discussing the differences between the amplitude modulation over rough and smooth walls, the effect of resolution and window size on the calculation of the amplitude modulation was tested to assure results were robust. This test is also useful for determining the effects of resolution on the PIV data studied earlier. Fig. 5.8 shows the effect of resolution changes in linear and logarithmic scaling to focus on effects in the wake and near wall regions, respectively. Both decreasing the window size and filtering out high frequency information causes a decrease in the correlation coefficient below y/δ = 0.12. Both also cause an increase in the correlation further from the wall, although the increase is much more pronounced when reducing the window size. Performing both of these operations has an effect equal to the sum of the two operations.

From this analysis, the effect of choosing a smaller window size, and thus eliminating the possibility of observing the modulating effects of some of the longest oscillations of the streamwise velocity, is to push the correlation toward zero at all wall-normal locations. This can be interpreted

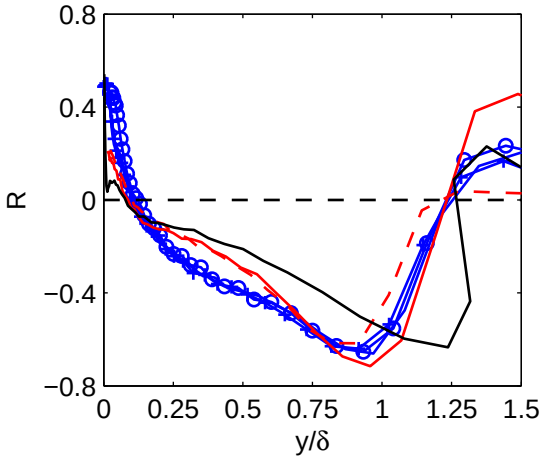

Figure 5.9: The amplitude modulation correlation. Solid red line: smooth-wall measurement at location 7, dashed red line: smooth-wall measurement at location 0, solid blue lines and symbols: rough-wall measurements at location 7 and station 1 (solid line), 2 (+), and 3 (○), black: data from Mathis et al. [2009b]

as the large and small scales being more in phase, or as a decrease in the modulation effect. The later explanation suggests that the largest scales contribute significantly to the modulation and it is suspected that this is the proper interpretation of this shift. This resolution effect is similar to the decrease in amplitude modulation calculated from the PIV data in comparison to the literature values shown in Fig. 3.19a

The amplitude modulation correlation is shown as a function of wall-normal distance for the smooth wall measurements in Fig. 5.9 along with rough-wall measurements at location 7. From Fig. 5.9 it is apparent that the large-scale small-scale modulation is unchanged at different stations along the roughness. This indicates that the interaction between the large and small scales is unaffected by the location along the roughness once the flow is fully developed. That is, although the small-scale fluctuations will change near the wall due to the local geometry of the wall, the way in which they interact with large scales is unchanged. The difference between the rough and the smooth wall profiles is confined to a region between y/δ = 0.25 and 0.75, the wake region. This is the region where similarity was previously shown in the correlation coefficient between the large streamwise velocity scales and the small-scale envelope of the streamwise, spanwise, and wall-normal velocity fluctuations in Figs. 3.20a and 3.20b of Section 3.4. The change in the correlation is to a more negative value, increasing the amplitude of the correlation, or, when interpreted as a phase relationship, the roughness appears to have pushed the large and small scales further out of phase in the wake region.

5.3.3.4 Summary of findings from fully developed turbulent statistics

Usually variations in turbulent statistics are confined to the log layer and below following Townsend's hypothesis (see Flack et al. [2005] and Flack et al. [2007] for example), but here differences were observed much further from the wall in the mean and rms statistics as well as the amplitude modulation effect. From the above comparisons, it was found that roughness affected both the mean and rms profiles up to $y/\delta = 0.3$ showing higher values of u_{rms} and $\overline{U}$ near the wall as might be expected with the increase in the friction velocity. Also, a hump in the rms statistics was observed near the wall at $y/\delta = 0.03$. In the wake region from $y/\delta = 0.5$ to 0.75, the mean and rms statistics show values lower than the smooth wall case, and the amplitude modulation correlation shows a more negative correlation which was unexpected.

Considering these changes, it may be hypothesized that the sparsity and periodicity of the roughness may help flow structures developed over the roughness elements to grow into the wake region unimpeded and thus change the statistics in the wake both in a mean and rms sense. This will be investigated by studying the streamwise velocity spectrum over the rough wall in the following section.

The appearance of a hump in the streamwise velocity rms profile is also interesting and indicative of an alternative mechanism for generation of turbulent energy near the wall. This mechanism will also be studied using the streamwise velocity spectrum in Section 5.4.

5.4 Streamwise velocity spectra

In this section, the streamwise velocity spectrum is presented for both rough and smooth wall boundary layers. This section begins with a discussion of the method for calculating the spectrum from the measurements. Next, the variation of the spectrum at different stations along the roughness is discussed. Finally, comparisons are made to the smooth wall spectrum and possible mechanisms for differences are discussed.

5.4.1 Calculation

To gain insight into the mechanisms responsible for the change in the structure of the boundary layer, the streamwise velocity spectrum, normalized as in Eqn. 5.7, was analyzed. In order to produce a converged spectrum, each of the 64 blocks of data recorded were split into 50 windows with 50% overlap and, as with the PIV data, each window was multiplied by a Hanning window to prevent spectral leakage and then zero padded to twice its original length. The frequency spectrum was converted to a spectrum over streamwise wavelength by employing Taylor's frozen turbulence hypothesis ($\lambda_x = 2\pi\overline{U}(y)/\omega$). This allows the interpretation of the spectrum as the distribution of

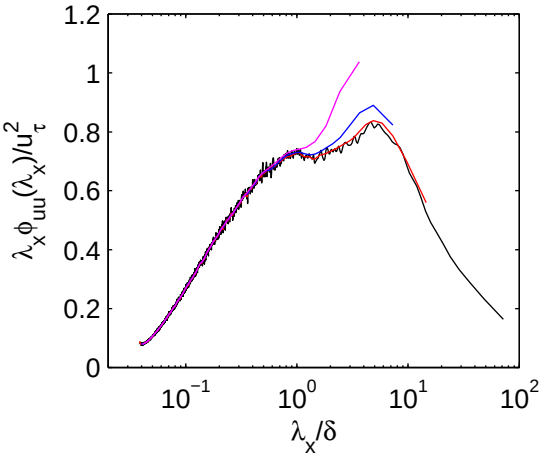

Figure 5.10: The streamwise velocity spectrum at $y^+ = 120$ over location 7. The colors indicate window sizes of $\lambda_x/\delta = 72$: black, 14.6: red, 7.3: blue, and 3.6: magenta

energy in the flow over eddies of various streamwise lengths.

$$\int \phi_{uu}(\omega)d\omega = \overline{u^2} \tag{5.7}$$

The effect of increasing the number of windows, and thus decreasing the longest scales resolvable, was investigated in Fig. 5.10 at $y^+ = 120$. It is shown that while splitting a long time series into many shorter windows and averaging helps to smooth the spectrum, if the window size becomes too small, the shape of the spectrum will be distorted due to spectral leakage. This distortion becomes prominent when the window size approaches the long wavelength peak of the spectrum. This is important when considering the comparison between the LF and SF spectra discussed in Chapter 3, where the long wavelength end of the SF data is likely distorted similar to the blue line in Fig. 5.10. Given the agreement of the spectra using a window size of $\lambda_x/\delta = 72$, which was used with to calculate the spectra in this chapter, and the smaller window size of $\lambda_x/\delta = 14.6$, the hotwire data could actually have been split into more windows without affecting the shape of the spectrum.

By compiling the spectra at all wall-normal locations as in Fig. 5.11b a composite spectrum can be formed and viewed as a contour plot as in Fig. 5.11c, where the color indicates the amount of energy at a given wavenumber and wall-normal location. While data near the wall was not recovered, peaks in energy were observed in the range $\lambda_x/\delta = 0.5$–3 and $\lambda_x/\delta = 5$–6 near the wall, while beyond about $y/\delta = 0.2$, only the peak at $\lambda_x/\delta = 3$ was discernible. This is similar to the findings of Monty and Chong [2009]. The $\lambda_x/\delta = 3$ peak was associated with the large-scale motions (LSMs) and the $\lambda_x/\delta = 6$ peak was associated with the very large scale motions (VLSMs) or super structures. The location of both of these peaks can be seen clearly in the 1D spectrum near the wall in Fig. 5.11a.

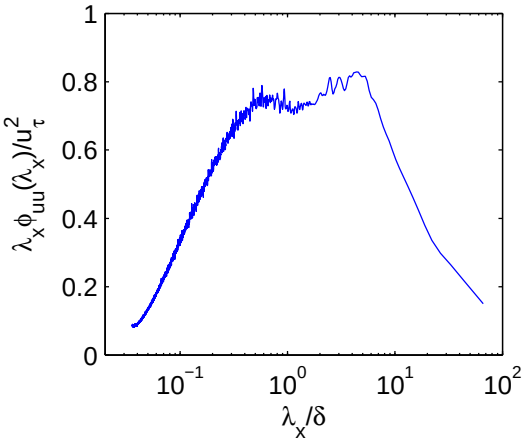

(a) Smooth wall spectrum at $y/\delta = 0.025$

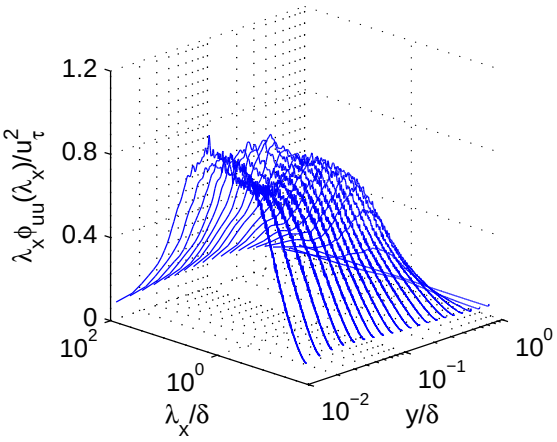

(b) Smooth wall spectrum at all wall-normal locations

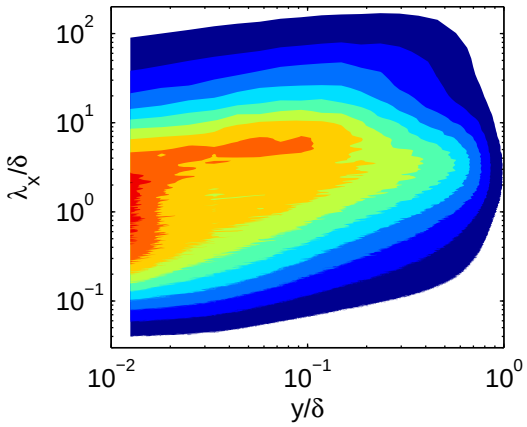

(c) Smooth wall composite spectrum

Figure 5.11: (a): The smooth-wall streamwise velocity spectrum at $y/\delta = 0.025$. (b): The spectra are compiled to show all wall-normal heights at once. (c): The composite spectrum, $\lambda_x\phi_{uu}(\lambda_x, y)/u_\tau^2$, as a contour plot where the levels range from 0.1 to 1.0 in increments of 0.1

5.4.2 Comparison of rough-wall spectra

The effect of the roughness on the turbulent spectrum is shown in Fig. 5.12 for stations A-D and Fig. 5.13 for stations E and F with the top two panels presenting the data with the same levels as A-D and the bottom two panels with more levels to better show activity in the near-wall region. One striking feature of all of these spectra is the formation of a broad energetic peak in the range $1 \leq \lambda_x/\delta \leq 6$ with a maximum between $0.03 \leq y/\delta \leq 0.08$. The distribution of energy covers a broader range of wavelengths than observed in the smooth-wall spectrum at the same distance from the wall. The spectrum at location D in Fig. 5.12e appears representative of this feature common to the rough-wall spectra. In addition to this feature, Figs. 5.13c and 5.13d clearly show a sharp peak at a wavelength of $\lambda_x/\delta = 0.3$ ($\lambda_x^+ \approx 1000$) near the wall.

By plotting consecutive spectra on top of each other, as in Figs. 5.14, the change in the spectra can be observed as the flow evolves near the wall. From station A to B and B to D, an energetic region covering a large range of scales near the wall gradually moves outward and its intensity weakens; this is especially true of scales in the range $0.5 < \lambda_x/\delta < 3$. Then, after passing over a roughness element (moving from station D to E), another large energetic region forms close to the wall with a peak around $\lambda_x/\delta = 0.3$ while retaining the "common part" from station D (i.e., the outer flow is unchanged). From Fig. 5.14d, it then appears that this region propagates outward and starts the process over.

The arrangement of energy below the virtual origin is made apparent when viewing the spectra at particular wall-normal locations in Fig. 5.15. Just at the virtual origin (magenta and cyan lines), a large portion of energy is centered at $\lambda_x/\delta = 0.12$. Immediately behind the roughness (station E), the energy level increases drastically and the peak moves to shorter wavelengths as the wall is approached. Further downstream (station F) the peak broadens and the energy decreases under the virtual origin. Above the virtual origin, this peak moves to slightly longer wavelengths (i.e., $\lambda_x/\delta = 0.3$) as was already noted in Fig. 5.13. To gain an understanding of this change in the peak location, the data is next viewed in frequency space.

The energy content below the crest is best viewed in frequency space as it is likely that Taylor's hypothesis does not apply near the wall where the mean velocity is low and the amount of mixing is high. Composite streamwise velocity spectra from the two stations immediately behind the roughness elements (E and F) are presented in Fig. 5.16. Immediately behind the roughness there are actually two peaks, one below and one above the virtual origin. Further downstream, only the peak above the virtual origin is observed. The peak above the virtual origin at both stations is centered around $\omega\delta/U_\infty = 11$, which, when normalized by the more relevant parameters k and u_τ is $fk/u_\tau = 0.8$, where f is the frequency, $\omega = 2\pi f$. The peak nearer the wall found at station E starts at $fk/u_\tau = 1.5$ and lowers further from the wall to 0.67. Thus, while the wavelength appears to change with distance beneath the origin, the actual frequency of oscillation is nearly constant. For both peaks

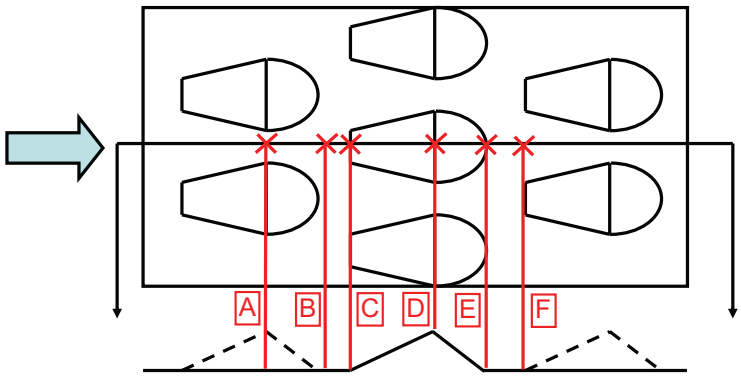

(a) Station diagram

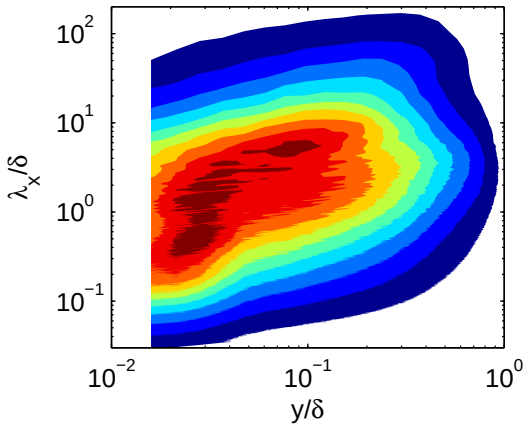

(b) Station A

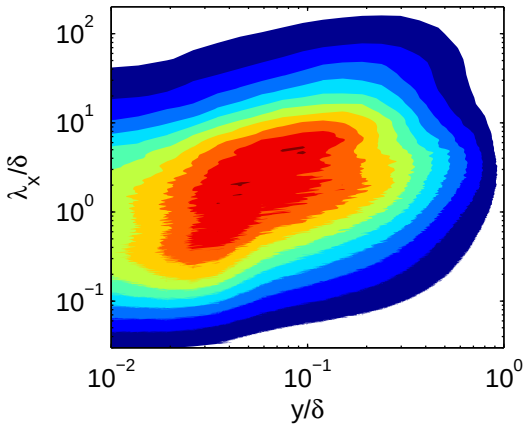

(c) Station B

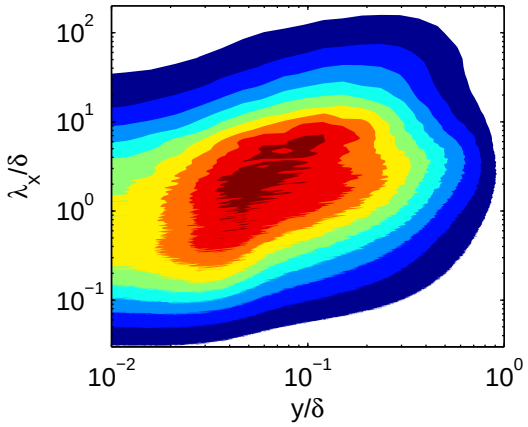

(d) Station C

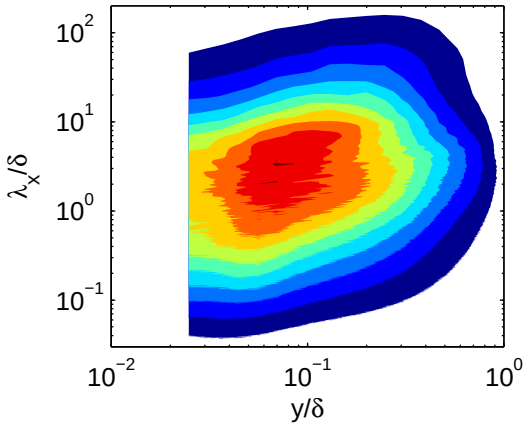

(e) Station D

Figure 5.12: (a) Diagram of the relative position of all of the stations at location 7. (b–e): The composite streamwise velocity spectra, $\lambda_x \phi_{uu}(\lambda_x, y)/u_\tau^2$, for the rough-wall data at stations A–D of location 7. Contour levels range from 0.1 to 1.0 in increments of 0.1. Only data above the roughness peaks is shown for ease of comparison.

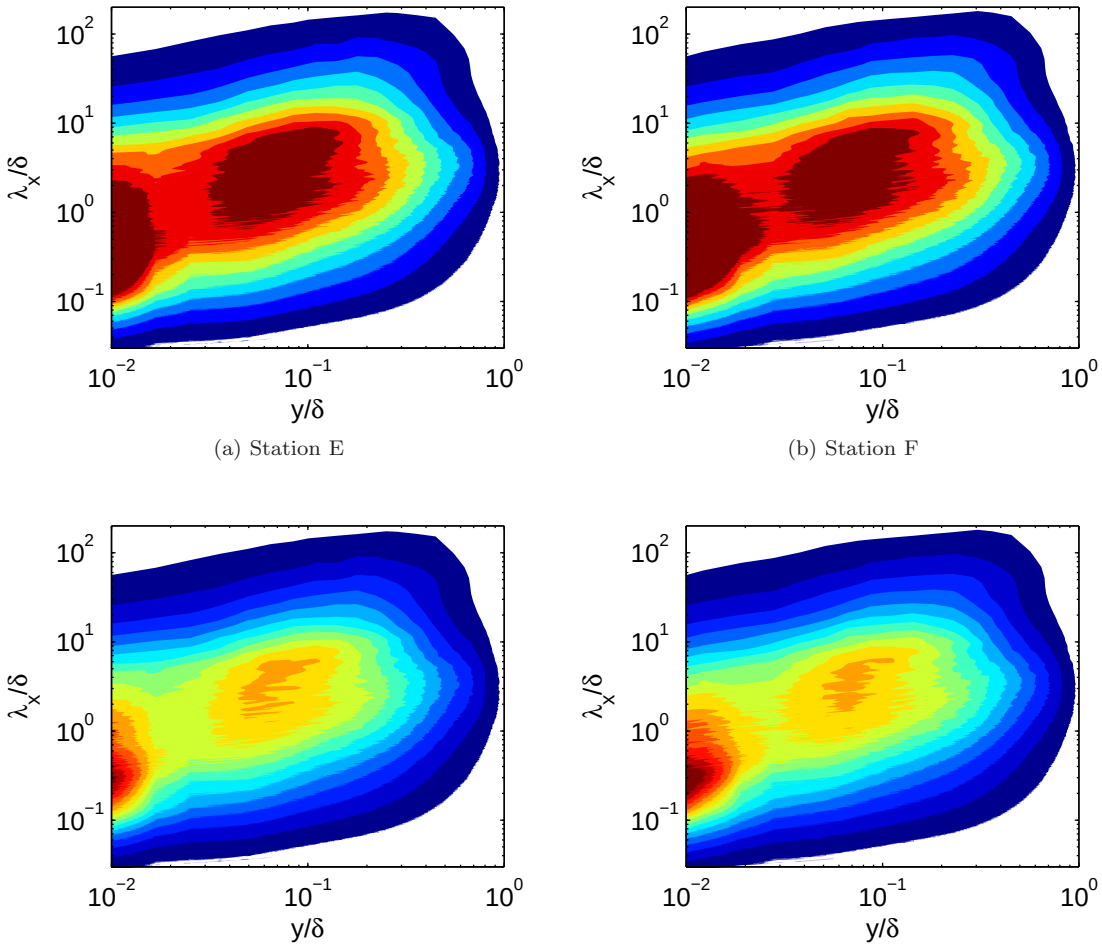

(a) Station E

(b) Station F

(c) Station E (more levels)

(d) Station F (more levels)

Figure 5.13: The composite streamwise velocity spectra, $\lambda_x \phi_{uu}(\lambda_x, y)/u_\tau^2$, for the rough-wall data at stations (a,c): E and (b,d): F of location 7. (a,b): contour levels range from 0.1 to 1.0 in increments of 0.1. (c,d): contour levels range from 0.1 to 1.5 in increments of 0.1 to better show details near the wall. Only data above the roughness peaks is shown for ease of comparison.

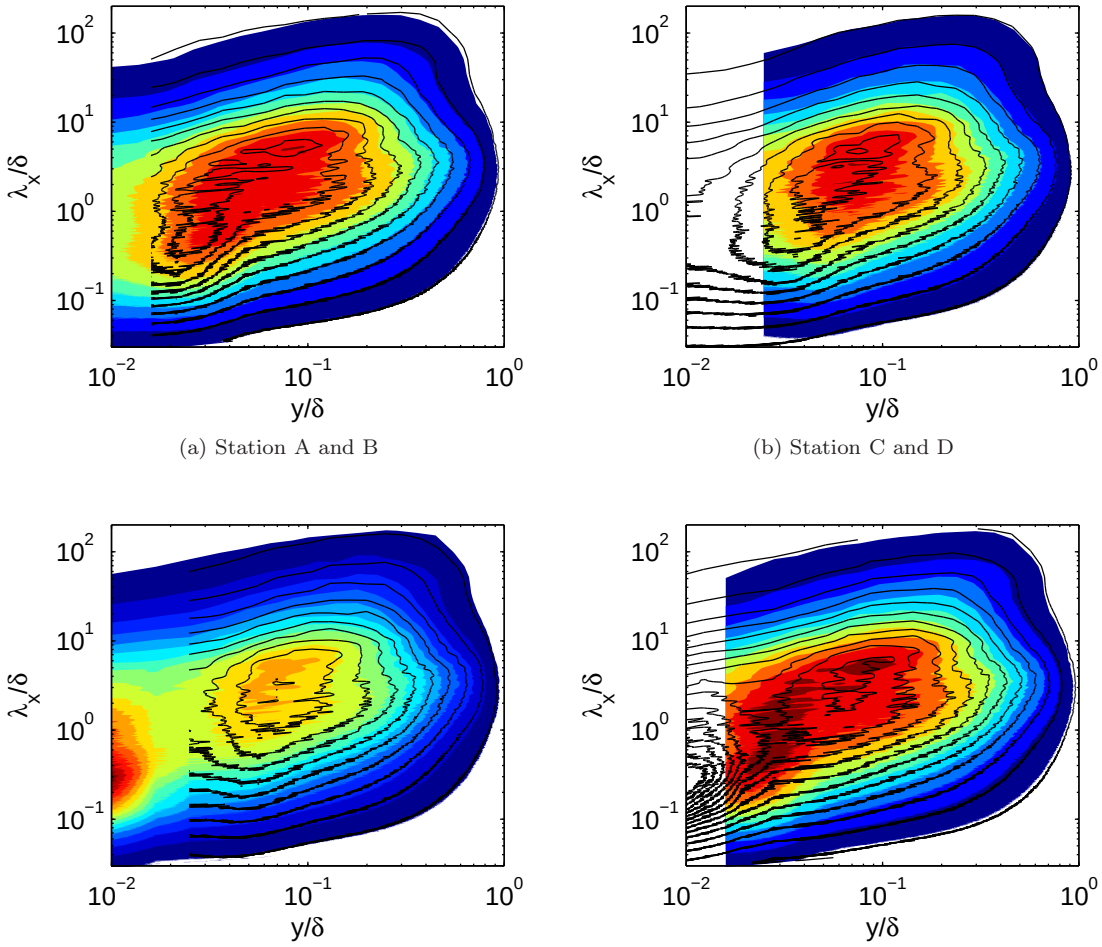

(a) Station A and B

(b) Station C and D

(c) Station D and E

(d) Station F and A

Figure 5.14: Composite spectra, $\lambda_x \phi_{uu}(\lambda_x, y)/u_\tau^2$, at consecutive stations for cases where large changes were noted in the spectral shape. The upstream spectrum is shown by solid black lines and the downstream one by filled contours. For example, in (a), the spectrum for location B is shown with the filled contours while the spectrum for location A is indicated by black lines. In all cases, the step between contours is 0.1.

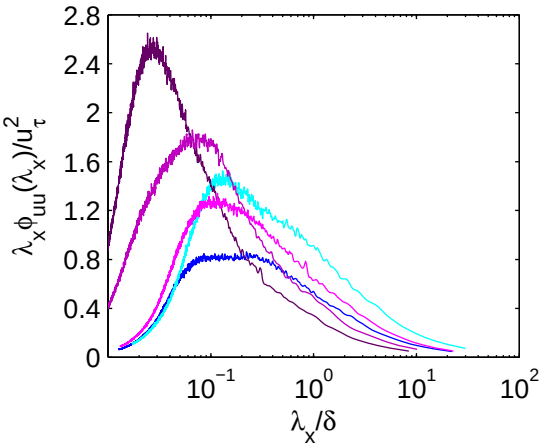

Figure 5.15: Spectra immediately below the virtual origin at $y/\delta = -0.001$ for station E (magenta) and station F (cyan), as well as further below the crests at $y/\delta = -0.01$ (purple) and $y/\delta = -0.014$ (dark purple) for station E and $y/\delta = -0.007$ for station F (blue)

the "roughness Strouhal number" is about 1 meaning that the frequency and viscous time scales are of similar order.

5.4.3 Comparison of rough- and smooth-wall spectra

Comparisons of the rough-wall and smooth-wall composite spectra are shown in Fig. 5.17 with dotted lines drawn at heights k and 2k above the smooth wall. If it were expected that the roughness simply displaced the near-wall activity above the roughness elements, then the energy near the wall would be displaced to a region between these two lines. This does not appear to be the case immediately above a roughness element as shown in Fig. 5.17a. On the other hand, this does appear to be the case in Fig. 5.17b, which is a measurement above the spanwise trough between two roughness elements. Furthermore, the wavelength range of this energetic portion of the spectrum is similar to the range seen in the near-wall activity (around $\lambda_x^+ = 1000$ [Jiménez et al., 2004]) for the smooth wall case.

To investigate this similarity further, Fig. 5.18 shows smooth wall spectra at particular wall-normal locations (red lines) compared to rough-wall spectra at distances one roughness height further from the wall at station A (black lines). It is found that the shape of the spectra are similar as noted from the composite spectra. By multiplying the smooth wall spectra by 1.1 and 1.3, respectively (magenta lines), good agreement is found over a large range of wavelengths, where some discrepancies are found in the plane nearer the wall. In particular, the $\lambda_x/\delta = 0.3$ or $\lambda_x^+ = 1000$ peak is not present in the smooth wall case. This gives a hint that this peak at $\lambda_x/\delta = 0.3$ is due to roughness effects and not just a displacement of near-wall activity that might be suggested when looking at Fig. 5.17b.

Some of the differences between the rough and smooth wall spectra can be seen more clearly when comparing the 1D spectra at comparable distances from the wall. In Fig. 5.19, spectra are

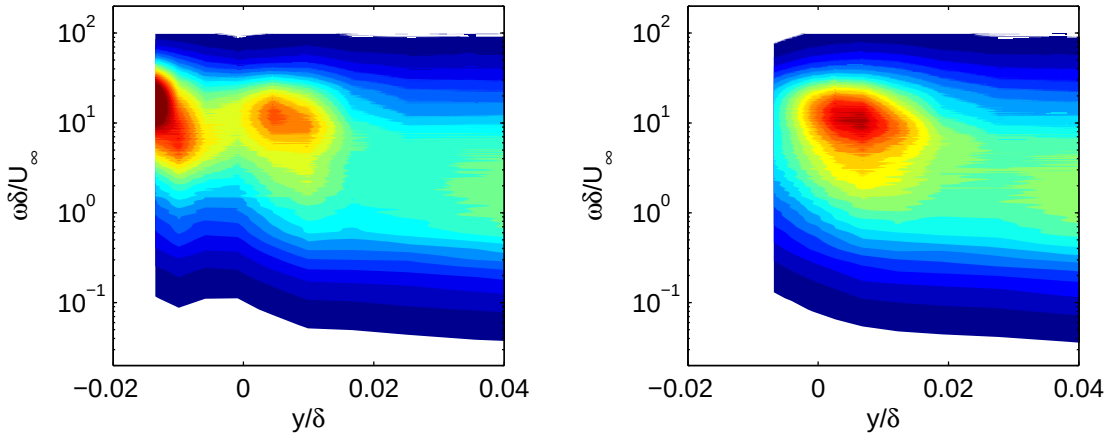

(a) Station E

(b) Station F

Figure 5.16: The composite streamwise velocity spectrum, $\lambda_x\phi_{uu}(\lambda_x, y)/u_\tau^2$, at station (a) E and (b) F near the virtual origin. The levels range from 0.1 to 2.0 in increments of 0.1.

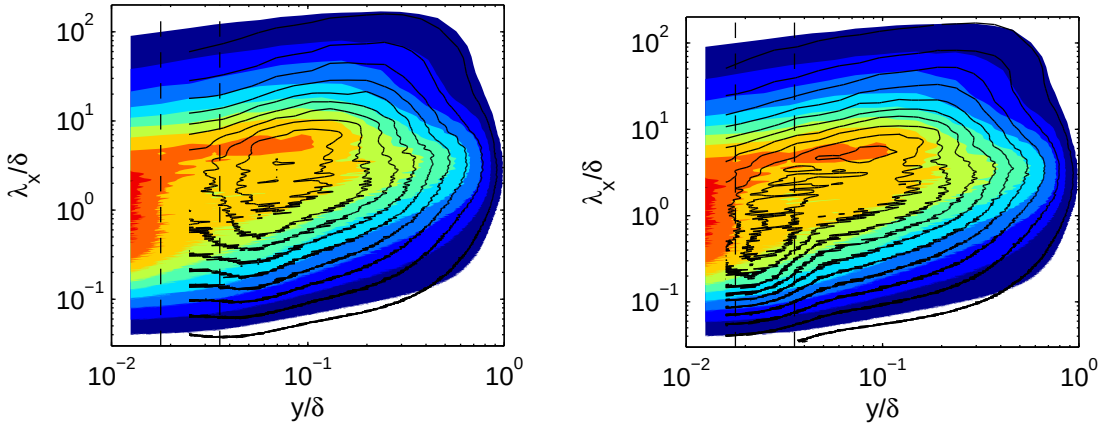

(a) Comparing Smooth and Station D

(b) Comparing Smooth and Station A

Figure 5.17: Smooth-wall, rough-wall composite spectrum, $\lambda_x\phi_{uu}(\lambda_x, y)/u_\tau^2$, comparison. Filled contours: smooth-wall composite streamwise velocity spectrum, solid black lines: rough-wall spectrum, dashed black lines: heights k and 2k above the smooth wall. The step between contours is 0.1.

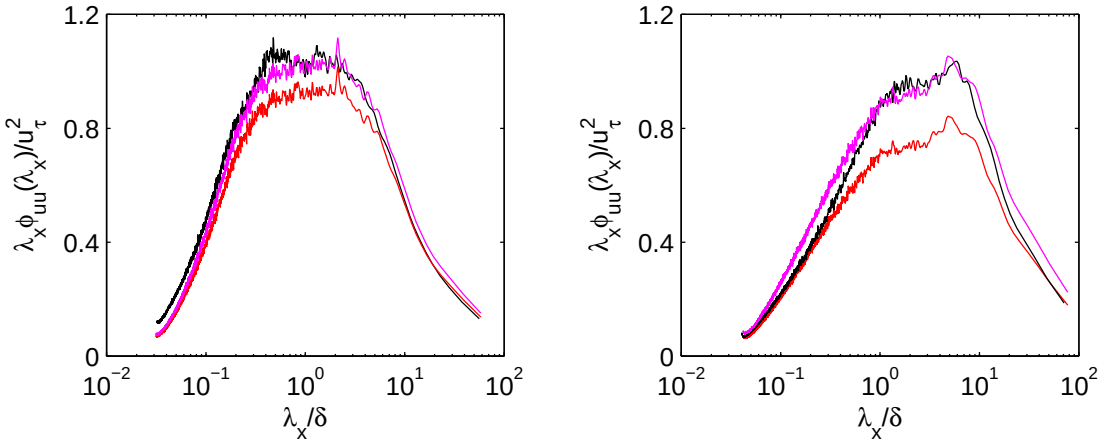

(a) Smooth: y/δ = 0.012, Rough: y/δ = 0.028

(b) Smooth: y/δ = 0.073, Rough: y/δ = 0.096

Figure 5.18: Smooth-wall and rough-wall spectra at station A are compared at wall-normal distances separated by one roughness height (k/δ = 0.018). Red: smooth-wall spectra, black: rough-wall spectra, magenta: smooth-wall spectrum multiplied by a constant factor of (a) 1.1 and (b) 1.25

compared in the buffer layer, log layer, and wake region of the boundary layer to take a closer look at the differences in the energy distribution. Comparing spectra in the buffer layer in Fig. 5.19a, downstream of the roughness elements (station F), the strong energetic peak at $\lambda_x/\delta = 0.3$ is present which appear to persist at all locations along the roughness, although with varying strength. This peak is still quite apparent in the region between the two roughness elements downstream (station A), and even has a slight signature upstream of the next roughness element (station C), which can be seen when comparing this spectrum to the smooth wall case.

Moving to a region just inside the log layer in Fig. 5.19b, spectra at all points along the roughness have a similar shape with a plateau of energy in the range $0.5 \leq \lambda_x/\delta \leq 3$, much like the smooth wall spectrum in the buffer region. When comparing all rough-wall spectra at this wall-normal location to the smooth wall, the major difference, besides the energy level, is that the rough-wall spectra do not show the bimodal shape of the smooth wall spectrum with distinct peaks around $\lambda_x/\delta = 1$ and 5.

Moving even further into the log layer in Fig. 5.19c, little discrepancy is observed between the rough and smooth wall spectra in terms of the energy distribution. The major difference is the energy level which is higher for the rough wall flow. Both show a peak at $\lambda_x/\delta = 6$ and a plateau in energy starting around $\lambda_x/\delta = 1$. For the rough wall, though, the energy distribution is a little bit less peaky around $\lambda_x/\delta = 6$.

Finally, in the wake region shown in Fig. 5.19d, there is almost no difference in the distribution nor level of the energy between the rough and smooth wall flow. Differences at station F (cyan line) are due to difficulties in obtaining the value of u_τ at this station (along with station E) in the

wake of the roughness elements. Further into the wake where differences were noted in the mean and rms velocity profiles, the energy distribution is identical between the smooth- and rough-wall flows although the energy level is lower. This points out that the differences in the wake are not due to a redistribution in energy, just a decrease in energy. While this could still be a roughness effect, it seems likely that changes in the wake region are caused by a measurement error (due to the difference in Reynolds number and viscous wire length or differences in calibration between the rough and smooth wall measurements) as the energy is reduces over the entire range of wavelengths.

5.4.4 Summary of findings from analysis of turbulent spectra

From comparisons of the rough-wall spectra, it is apparent that there is generation of energy right above and below the roughness elements at a dimensionless frequency of $fk/u_\tau \approx 1$. Above the roughness crests, this appear as a peak at $\lambda_x/\delta = 0.3$ or $\lambda_x^+ = 1000$. This peak is seen at all locations along the roughness, but is strongest within 0.25δ of the peak of the roughness. In inner units this peak is similar to that expected due to the near-wall cycle in turbulence over a smooth wall. When looking at the spectra near the rough wall, though, the distribution of energy over the entire range of wavelengths is not similar to the distribution of energy near a smooth wall, so it is suspected that this peak is more closely related to the roughness spacing 0.5δ as opposed to the preservation of the near-wall turbulent cycle with a peak at $\lambda_x^+ = 1000$.

Comparing spectra further from the wall, the distribution of energy for all rough-wall cases seems similar above $y/\delta = 0.06$. At $y/\delta = 0.1$, the rough and smooth wall spectra appear to have similar energy distributions, both showing peaks near $\lambda_x/\delta = 1$ and 6, although the energy level is different. At $y/\delta = 0.3$, both the energy distribution and levels are similar. Beyond this point, even though differences are noted in energy level, the distribution of energy is similar, and thus the dynamics in the wake appear to not be affected by the roughness.

5.5 Summary

The present study investigated the effect of a sparse and shallowly inclined periodic roughness, inspired by the spacing and size of the scales of a sailfish, on the turbulent boundary layer. Due to the sparsity and 3D nature of the roughness, the boundary layer reached a fully developed state quite early, only $9.8\delta_0$ downstream of the start of the roughness. In addition, measurements over a smooth plate produced a canonical zero-pressure-gradient boundary layer, and thus, well-controlled measurements over the roughness were possible. For the particular roughness chosen, the drag on the surface was increased by about 33% over the smooth wall value. Measurements of the mean friction velocity over the entire plate calculated from the drag measurements were within 10% or less of the values inferred using the Clauser method, where values from the Clauser method were always

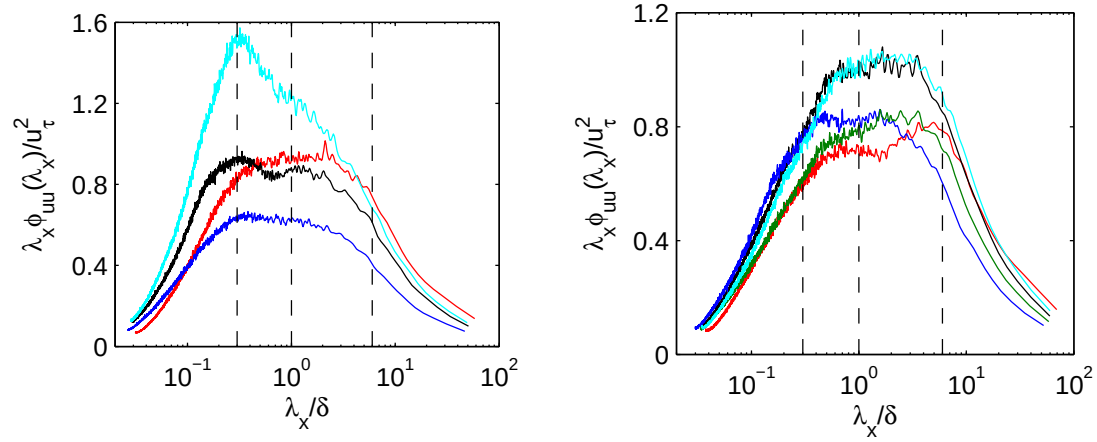

(a) $y/\delta \approx 0.012$, $y^+ \approx 36$

(b) $y/\delta \approx 0.035$, $y^+ \approx 105$

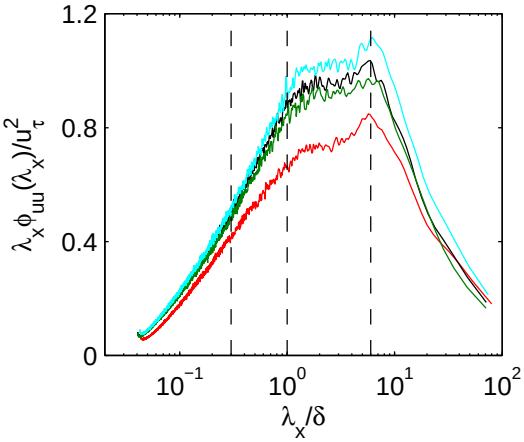

(c) $y/\delta \approx 0.1$, $y^+ \approx 300$

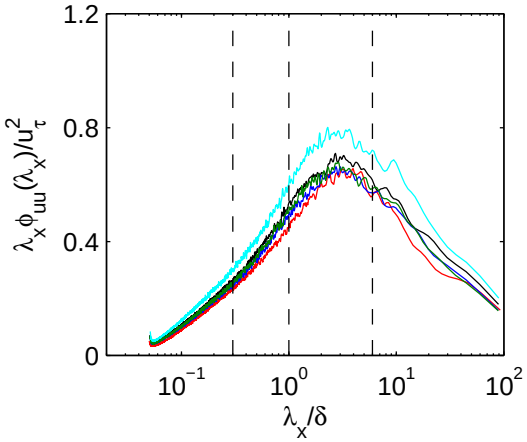

(d) $y/\delta \approx 0.3$, $y^+ \approx 900$

Figure 5.19: The smooth- and rough-wall spectra are compared at near equal distances from the wall or virtual origin, respectively. Red: smooth-wall spectrum. Rough-wall spectra are shown at stations A: black, C: blue, D: green, and F: cyan. Dotted vertical lines are located at $\lambda_x/\delta = 0.3$, 1, and 6 for reference.

higher. For future studies, placing a $10\delta_0$ fetch of roughness upstream of the measurement plate would provide a more accurate measurement of the actual drag increase and friction velocity for the rough-wall flow. In this situation, the flow would be in a fully developed state over the measurement plate and thus the measurement would not be biased by the development region.

While the roughness was small, it changed the mean and fluctuating statistics from the smooth wall values through a substantial portion of the boundary layer when normalizing the velocity differences by the friction velocity. This normalization was necessary to account for the difference in the boundary conditions between the two cases, where the rough wall had increased shear and thus production of turbulence near the wall. Differences in the mean and rms statistics between the rough and smooth wall boundary layers were noted clearly out to about $y/\delta = 0.3$, or 17 roughness heights from the surface. Differences were also noted in the wake beyond $y/\delta = 0.5$. On the other hand, the variation among the rough-wall profiles measured at different stations along the roughness was confined to a region within about 5 roughness heights of the wall, the roughness sublayer.

From investigation of the turbulent spectra it appears that in the wakes of the roughness elements, fluctuations on the order of the streamwise roughness spacing (the peak appeared at $\lambda_x/\delta = 0.3$ or $\lambda_x^+ \approx 1000$) were created and propagated away from the wall. Considering the frequency spectrum, this peak was located at $fk/u_\tau = 0.8$ and a peak below the virtual origin was also present at $fk/u_\tau = 1.5$. This near-wall peak, and thus differences between the rough-wall spectra at different stations, was contained below $y/\delta = 0.06$, right near the limit of differences noted in the mean and rms statistics. Beyond this point, the range of energetic scales was much broader and similar at all stations along the roughness.

Beyond 0.25δ downstream of a roughness element, the energetic peak near the wall appeared to merge into a broad peak in the spectrum covering a range $0.5 < \lambda_x/\delta < 6$ as opposed to the two peaks seen in the smooth wall case; one around $\lambda_x/\delta = 1$ associated with large δ-scaled motions and another around $\lambda_x/\delta = 5 - 6$ associated with the very large scale motions (VLSMs). Differences between the shape of the smooth- and rough-wall spectra were noted up to $y/\delta = 0.075$ approximately. Beyond this point, the spectral shape was similar between rough- and smooth-wall spectra. At $y/\delta = 0.3$, the rough and smooth wall spectra reach a point where both the shape and amplitude are similar. Beyond this point, there is only a small difference between the rough- and smooth-wall spectra in terms of amplitude, but the distribution of energy over different wavelengths was nearly identical. While is was initially hypothesized that the sparsity of the roughness allowed structures produced by the roughness to grow into and modify the outer region of the flow, the nearly identical distribution of energy would lead one to expect that this may be an effect of some measurement error.

Overall, these results show that even a small roughness can produce a large change to the flow, where modifications were observed well into the log layer for the present set of experiments. Such modifications may have useful implementations as either active or passive flow control devices. In

addition, it is recommended that more types of well-controlled (i.e., periodic) "transitional roughnesses" be studied as these flows are geometry-dependent, and thus tuning the geometry could have interesting effects on the flow. Perhaps this less intrusive roughness type could be used to periodically produce structures to modify the features of the turbulent boundary layer in a useful way. Even more importantly, the use of a dynamic roughness, that is a roughness whose height varies periodically in time as well as space, may be useful for introducing a particular spatial as well as temporal frequency to the flow that could potentially perturb a very specific region of the 3D velocity spectrum presented in Chapter 3. An initial investigation of producing such a surface is discussed in Appendix E.

Chapter 6

Conclusions

Time-resolved 2D PIV measurements were made in wall-normal and wall-parallel planes of a canonical zero pressure gradient boundary layer at Re_τ = 410 – 470. These measurements were used to study the distribution of turbulent energy in a 3-dimensional spectrum over streamwise, spanwise, and temporal wavelengths for the first time. This decomposition allowed the study of a scale-dependent convection velocity for both streamwise and spanwise velocity fluctuations. In addition, these measurements were used to study the time evolution of coherent structures in the turbulent boundary layer.

A second set of measurements were made using hotwire anemometry to study the effect of a 3D periodic roughness on the turbulent boundary layer at Re_τ = 3000. The roughness had elements spaced 0.5δ in streamwise extent and 0.25δ in spanwise extent to mimic the scale spacing on a sailfish at its maximum velocity. The alteration of the mean and rms statistics, along with the change in the streamwise velocity spectrum, was studied to analyze the effect of this sparse roughness on the boundary layer.

6.1 Summary and major findings

Choosing the correct spatial and temporal resolution played a major role in correctly presenting the energetic features of turbulent spectra, resolving swirling motions in the flow, as well as measuring the amplitude modulation effect using PIV. As with hotwire experiments, experiments showed that an inner scaled interrogation window size of $\Delta x^+ = \Delta z^+ = 20$ was required. From an analysis of the spatial spectra, it became clear that poor spanwise resolution was particularly vexing for the measurement of streamwise velocity fluctuations where attenuation was noted up to the longest measurable streamwise wavelengths. In addition, in order to capture the large scales properly, the field of needed to be at least twice as long as the long wavelength peak of the velocity spectrum, confirmed by hotwire experiments. While the longest peak was found at $\lambda_x/\delta = 3$ for the streamwise velocity spectrum (and thus a field of view 6δ long was necessary), for higher Reynolds number

flows, the streamwise velocity peak will move to 6δ for external flows and up to 10δ for internal flows, so a much longer field of view would be required for higher Reynolds numbers. For the current measurements, the LF data provided a large enough field of view while the SF provided sufficient spatial resolution.

The convection velocity of energetic scales in the flow appeared to be independent of the spanwise wavelength of the scale, but did have a dependence on the streamwise wavelength, particularly near the wall. Longer wavelength features tended to convect faster than the local mean consistent with the idea that these scales are tall in the wall-normal direction. Considering the spectra over streamwise wavelength and time, the spread of the convection velocities for spanwise velocity fluctuations was less dramatic and was bounded by the free-stream velocity near the wall unlike streamwise velocity scales. In all cases, the application of Taylor's hypothesis produced reasonable agreement between the spatial and temporal spectra although some slight differences were noted near the wall consistent with other researchers. Differences noted in the plane nearest the wall should be taken with caution, though, as the velocity gradient across the laser thickness was high at this location.

Vortices in the flow were found to travel on straight, streamwise-aligned trajectories at a range of speeds. The spread of convection velocities was symmetric about the local mean with major deviations only noted in the wake region where the limiting speed of the free-stream velocity biased the distribution toward lower convection velocities. This is consistent with the idea of the vortex signatures being cuts of coherent structures that extend over a range of wall-normal distances convecting at a single convection velocity, not necessarily equal to the local mean where the structure is cut. Using this idea, the lifetimes and convection velocities of attached and detached structures was statistically inferred. It was found that vortex structures attached to the wall traveled slower and had shorter lifetimes than detached structures. In general vortex signatures measured further from the wall persisted for longer periods of time, sometimes exceeding 5 eddy turnover times. The shorter lifetime near the wall was expected to be caused by the larger velocity gradients near the wall promoting a faster decay of structures in this region.

Low-momentum regions in the flow were identified using both direct measurements and linear stochastic estimation. In the mean, the streamwise length of these structures was found to range from 1–4δ in streamwise extent and 0.2–0.4δ in spanwise extent, with lengths increasing moving away from the wall. The streamwise extent was consistent with the LSM peak at $\lambda_x/\delta = 3$ in the streamwise velocity spectrum. Superstructures with lengths near 6δ were not expected due to the low Reynolds number of the current experiments.

From measurements over a 3D sparse periodic roughness, the flow reached a fully developed state (collapse in statistics up to the 4th order) less than $10\delta_0$ downstream of the start of the roughness. For the fully developed flow, differences in turbulent statistics between different stations along the roughness were limited to about 5k from the wall, the roughness sublayer. Interestingly, variations

between the rough and smooth wall statistics were seen well above this region. Differences near the wall were seen in all statistics and even the distribution of turbulent energy in the streamwise velocity spectrum up to about $y/\delta = 0.3$, into the wake region. Beyond this region, the distribution of energy was the same in all cases, and any differences were rectified by inaccuracies in determining u_τ. The mean and rms statistics, though, showed variation regardless of this modification of u_τ throughout the wake region. The same was true for the amplitude modulation. The reason for this difference was unknown, but may have been problem with calibration for high velocities.

In addition to these general changes, the periodic roughness was shown to input a scale at $\lambda_x/\delta = 0.3$ or $\lambda_x^+ \approx 1000$ which was observed throughout the roughness sublayer. It was concluded that this scale was created by the roughness and not simply the appearance of the near-wall activity associated with flow over the smooth surface behind the roughness elements. It is interesting to note that this wavelength is on the order of the streamwise spacing of the roughness elements and not their height.

6.2 Future work

It would be of interest to apply the time-resolved PIV analysis to flow over a rough-wall, or perhaps a wall with a time-varying roughness, to view whether or not a periodic roughness can be used to perturb a particular region of the 3D velocity spectrum. It would also be interesting to investigate the convection velocity of different scales near the roughness elements to see exactly how Taylor's hypothesis would be altered by the presence of roughness.

In addition, it would be important to use a computational database to verify the claims made concerning the statistically inferred vortex structures. From a full 3D spatial field, connected vortex structures could be identified and the method outlined in this thesis could be used to calculate the inferred structures from 2D wall-parallel slices of the full 3D field. This could be done using a number of snapshots of the flow, where the convection velocity would be found using the mean velocity in the vortex core, or by saving a series of time-resolved images. The latter would be more computationally costly, but could also be used to observe the time evolution of these 3D structures.

For measurements over the sparse roughness, streamwise and spanwise velocity correlations performed using two hotwire probes would help to further elucidate the structure of the flow, in particular if a spanwise periodicity on the order of the spanwise roughness element spacing is also observed. In addition, if space-time spectra could be calculated, then results could also be analyzed as modifications to traveling waves. For the sake of accuracy, it would also be of interest to recheck the differences in the streamwise velocity statistics between the rough and smooth wall flows which were observed in the wake region to see if this really was caused by the roughness, and if so, if this is an effect of the sparsity or roughness shape.

Appendix A

PIV processing parameters

The vector processing parameters for all planes of all PIV data sets are recorded here. The processing parameters common to all wall-parallel planes of set 1 are given in Table A.1 and the parameters for set 2 are given in Tables A.2 and A.3. The differences between the various planes are noted in Tables A.4 and A.5 for sets 1 and 2, respectively. Tables A.6 and A.7 give the processing parameters for the wall-normal plane of set 1, while Tables A.8 and A.9 provide this information for set 2. Before processing, vector fields were cropped to ensure that the centers of the interrogation windows, and thus the vectors calculated, would overlap. The cropped regions for the wall-parallel planes of set 1 are listed in Table A.10 and the cropped regions for all planes of set 2 are listed in Table A.11. Table A.10 also includes the camera tilt angle for set 1 since the image correction option was not used, and thus this value was needed to correct the velocity fields after vector calculation. For set 2, since image correction was used, some extra rows and columns were created in some cases and needed to be eliminated to get the fields to overlap. Notes on these row and column corrections are recorded in Table A.12.

After correction, the vector fields calculated from adjacent cameras were merged providing vector fields of the size indicated in Tables A.13 and A.14 for sets 1 and 2, respectively. These tables also indicate the number of overlapping rows between cameras. Since the edges of the original images are ignored (the first and last rows and columns of each image are removed), when the images from adjacent cameras do not overlap or only overlap by one vector, vectors are inserted using an interpolation between camera 1 and 2. If the number of overlapping vectors exceeds 1, any excess rows are averaged between camera 1 and 2. Note that for the wall-normal plane of set 2, two additional columns near the plate were also removed due to poor data quality there (a combination of laser reflections and steep velocity gradients).

Vector calculation parameter	
Correlation mode	Cross correlation, frame 0 x frame 1
Multipass	Constant size
Window size	32 x 32
Window shape	1:1 rectangular
Overlap	50%
Number of passes	2
Usage of masked out pixels	
Use pixel masking on images	yes
Condition for disabling vectors by pixel masking:	
1st pass	0.1
Later passes	0.2
Condition to switch to direct calculation:	
1st pass	1
Later passes	0.1
Initial reference vector field	
Restrictions implied by reference vector fields:	
Relative vector range restriction	reference $\pm\frac{windowsize}{4}$
Absolute vector range restriction	reference ±4 pixel
Vector position	Symmetrical
Correlation function (final passes)	
Correlation function	Normalized
High accuracy mode	Yes
Correlation peak validation	
Quantity stored in "peak ratio"	$\frac{correlation\ ratio}{peak}$
Multipass post processing	
Median filter:	
Type	Remove & Replace
Remove/replace if diff to avg	> 2× rms of neighbors
Remove groups with	< 5 vectors
Fill up empty space	Yes
Fill up all	Yes
Smoothing	1 x Smooth 3 x 3
Vector post processing	
Median filter:	
Type	Remove & Replace
Remove/replace if diff to avg	> 2× rms of neighbors
Remove groups with	< 5 vectors
Fill up empty space	Yes
Fill up all	Yes
Apply allowable vector range again	Yes

Table A.1: Standard options for all wall-parallel planes of set 1

Image preprocessing	
Particle intensity normalization scale length	10
Vector calculation parameter	
Correlation mode	Sequential cross correlation
Multipass	Decreasing size
Window size	64 x 64 → 32 x 32
Window shape	1:1 rectangular → 2:1 elliptical
Overlap	50%
Use image correction	yes
Usage of masked out pixels	
Use pixel masking on images	yes
Condition for disabling vectors by pixel masking:	
1st pass	0.3
Later passes	0.6
Condition to switch to direct calculation:	
1st pass	1
Later passes	0.1
Initial reference vector field	
Initial interrogation window shift:	
Type	Constant
dx	See Table A.5
dy	0 pix
Restrictions implied by reference vector fields:	
Relative vector range restriction	reference $\pm \frac{windowsize}{2}$
Absolute vector range restriction	See Table A.5
Vector position	Symmetrical
Correlation function	
Correlation function (initial passes)	Standard
Second order correlation	Yes
Correlation function (final passes)	Standard
High accuracy mode	Yes
Correlation peak validation	
Only accept correlation peaks in a defined range:	
Vx (pixel)	See Table A.5
Vy (pixel)	0 ± 3
Quantity stored in "peak ratio"	$\frac{correlation\ ratio}{peak}$
Multipass post processing	
Delete vector if peak ratio Q	< 1.3
Median filter:	
Type	Strongly remove & Iteratively replace
Remove if diff to avg	$> 2\times$ rms of neighbors
Reinsert if diff to avg	$< 3\times$ rms of neighbors
Remove groups with	< 5 vectors
Fill up empty space	Yes
Fill up all	Yes
Smoothing	1 x Smooth 3 x 3

Table A.2: Wall-parallel plane processing parameters for set 2 (part 1 of 2)

Vector post processing	
Allowable vector range:	
Vx (pixel)	See Table A.5
Vy (pixel)	0 ± 3
Vz (pixel)	0 ± 20
Delete vector if peak ratio Q	< 1.1
Median filter:	
Type	Strongly remove & Iteratively replace
Remove/replace if diff to avg	$> 2\times$ rms of neighbors
Reinsert if diff to avg	$< 2.5\times$ rms of neighbors
Remove groups with	< 5 vectors
Fill up empty space	Yes
Apply allowable vector range again	Yes

Table A.3: Wall-parallel plane processing parameters for set 2 (part 2 of 2)

Image preprocessing			
Subtract sliding background	10	10	10
Particle intensity normalization scale length	5	3	4
Initial reference vector field			
Initial interrogation window shift:			
dx (pixel)	-3	-3.5	-4.25
dy (pixel)	0	0	0
Correlation peak validation:			
Only accept correlation peaks in a defined range:			
Vx (pixel)	-3 ± 2	-3.5 ± 2	-4.25 ± 2
Vy (pixel)	0 ± 2	0 ± 2	0 ± 2
Vector post processing			
Allowable vector range:			
Vx (pixel)	-3 ± 2	-3.5 ± 2	-4.25 ± 2
Vy (pixel)	0 ± 2	0 ± 2	0 ± 2
Vz (pixel)	0 ± 20	0 ± 20	0 ± 20

Table A.4: Options that differ between the three wall-parallel planes of set 1

Plane	range (pix)
SF0	6 ± 5
LF0	6 ± 5
SF1	6 ± 5
LF1	6 ± 5
SF2	6 ± 5
LF2	7 ± 5
SF3	7 ± 5
LF3	6 ± 5

Table A.5: Range of allowable vectors for set 2

Image preprocessing	
Subtract sliding background	10
Particle intensity normalization scale length	5
Vector calculation parameter	
Correlation mode	Sequential cross correlation, 0+1, 2+3, 4+5,...
Multipass	Decrease size
Window size	32 x 32 to 16 x 16
Window shape	1:1 rectangular
Overlap	50%
Number of passes	2
Usage of masked out pixels	
Use pixel masking on images	yes
Condition for disabling vectors by pixel masking:	
1st pass	0.1
Later passes	0.2
Condition to switch to direct calculation:	
1st pass	1
Later passes	0.1
Initial reference vector field	
Initial interrogation window shift:	
dx (pixel)	-3
dy (pixel)	0
Restrictions implied by reference vector fields:	
Relative vector range restriction	reference $\pm\frac{windowsize}{4}$
Absolute vector range restriction	reference ±5 pixel
Vector position	Symmetrical
Correlation function	
Initial pass:	
Correlation function	Standard
Second order correlation	Yes
Final pass:	
Correlation function	Standard
High accuracy mode	Yes
Correlation peak validation	
Only accept correlation peaks in a defined range:	
Vx (pixel)	-3 ± 2
Vy (pixel)	0 ± 2
Quantity stored in “peak ratio”	$\frac{correlation\ ratio}{peak}$
Multipass post processing	
Median filter:	
Type	Remove & Replace
Remove/replace if diff to avg	> 2× rms of neighbors
Remove groups with	< 5 vectors
Fill up empty space	Yes
Fill up all	Yes
Smoothing	1 x Smooth 3 x 3

Table A.6: Wall-normal processing options for set 1 (part 1 of 2)

Vector post processing	
Allowable vector range:	
Vx (pixel)	-3 ± 2
Vy (pixel)	0 ± 2
Vz (pixel)	0 ± 20
Median filter:	
Type	Remove & Replace
Remove/replace if diff to avg	$> 2\times$ rms of neighbors
Remove groups with	< 5 vectors
Fill up empty space	Yes
Fill up all	Yes
Smoothing	2 x Smooth 3 x 3
Apply allowable vector range again	Yes

Table A.7: Wall-normal processing options for set 1 (part 2 of 2)

Image preprocessing	
Particle intensity normalization scale length	8
Vector calculation parameter	
Correlation mode	Sequential cross correlation, 0+1, 2+3, 4+5,...
Multipass	Decrease size
Window size	32 x 32 to 16 x 16
Window shape	1:1 rectangular to 2:1 elliptical
Overlap	50%
Number of passes	2
Use image correction	Yes
Usage of masked out pixels	
Use pixel masking on images	yes
Condition for disabling vectors by pixel masking:	
1st pass	0.5
Later passes	0.3
Condition to switch to direct calculation:	
1st pass	1
Later passes	0.3
Initial reference vector field	
Initial interrogation window shift:	
dx (pixel)	-5
dy (pixel)	0
Restrictions implied by reference vector fields:	
Relative vector range restriction	reference $\pm\frac{windowsize}{2}$
Absolute vector range restriction	reference ±5 pixel
Vector position	Symmetrical
Correlation function	
Initial pass:	
Correlation function	Standard
Second order correlation	Yes
Final pass:	
Correlation function	Standard
High accuracy mode	Yes
Correlation peak validation	
Only accept correlation peaks in a defined range:	
Vx (pixel)	-5 ± 4.5
Vy (pixel)	0 ± 3
Quantity stored in "peak ratio"	$\frac{correlation\,ratio}{peak}$
Multipass post processing	
Delete vector if peak ratio Q	< 1.5
Median filter:	
Type	Remove & Replace
Remove/replace if diff to avg	$> 2\times$ rms of neighbors
Remove groups with	< 5 vectors
Fill up empty space	Yes
Fill up all	Yes
Smoothing	1 x Smooth 3 x 3

Table A.8: Wall-normal processing options for set 2 (part 1 of 2)

Vector post processing	
Allowable vector range:	
Vx (pixel)	-5 ± 4.5
Vy (pixel)	0 ± 3
Vz (pixel)	0 ± 20
Delete vector if peak ratio Q ¡	1.1
Median filter:	
Type	Strongly remove & Iteratively replace
Remove/replace if diff to avg	$> 2\times$ rms of neighbors
Reinsert if diff to avg	$< 2.5\times$ rms of neighbors
Remove groups with	< 5 vectors
Fill up empty space	Yes
Fill up all	No
Smoothing	None
Apply allowable vector range again	Yes
Apply currently active mask	Yes

Table A.9: Wall-normal processing options for set 2 (part 2 of 2)

Plane	Cam 1 range			Cam 1 tilt	Cam 2 range			Cam 2 tilt
LF1	(1,0)	→	(1024,1022)	0.22° = 4 pix	(0,2)	→	(1024,1024)	0.56° = 10 pix
LF2	(0,0)	→	(1024,1023)	0.06° = 1 pix	(0,1)	→	(1024,1024)	0.34° = 6 pix
LF3	(7,0)	→	(1024,1024)	−0.06° = −1 pix	(0,0)	→	(1024,1024)	0.22° = 4 pix

Table A.10: Crop rectangle for each camera of set 1

Plane	Cam 1			Cam 2		
WN	(2,0)	→	(1023,510)	(0,1)	→	(1023,511)
SF0	(0,4)	→	(1023,1023)	(1,0)	→	(1023,1013)
LF0	(0,3)	→	(1023,1023)	(13,0)	→	(1023,1020)
SF1	(0,4)	→	(1023,1023)	(1,0)	→	(1023,1013)
LF1	(0,0)	→	(1023,1019)	(0,2)	→	(1023,1023)
SF2	(0,0)	→	(1023,1023)	(5,3)	→	(1023,1018)
LF2	(0,0)	→	(1023,1023)	(11,1)	→	(1023,1020)
SF3	(0,2)	→	(1023,1016)	(4,0)	→	(1023,1023)
LF3	(0,0)	→	(1023,1017)	(3,1)	→	(1023,1023)

Table A.11: Crop rectangle for each camera of set 2

Plane	Comment
WN	-
SF0	-
LF0	Ignore 1st row of Cam 1
SF1	-
LF1	Ignore last column of Cam 2
SF2	-
LF2	Ignore 1st row and 1st column of cam 1
SF3	Ignore last column of Cam 2
LF3	-

Table A.12: Merging comments for set 2

Plane	rows/cam	cols/cam	overlap	total rows	total cols
LF1	64	64	2	125	62
LF2	64	64	2	125	62
LF2	64	64	1	126	62

Table A.13: Specifications of frame size for each plane of set 1

Plane	rows/cam	cols/cam	overlap	total rows	total cols
WN	128	64	8	236	60
SF0	64	64	4	122	62
LF0	64	65	0	126	63
SF1	64	64	4	122	62
LF1	64	64	1	125	62
SF2	64	64	2	124	62
LF2	64	64	1	125	62
SF2	64	64	3	123	62
LF2	64	65	3	123	63

Table A.14: Specifications of frame size for each plane of set 2

Appendix B

Inferred SCS calculation

Here a generalized framework for analyzing different types of SCS inferred from data in any number of wall-parallel planes is presented. For any two planes, the structure types A, B, and C as presented in Fig. 4.32b, can be extracted. Defining the convection velocity histogram for plane y_i as $H(i)$, regions between plane y_i and y_j are described by:

$$\begin{aligned} A(i,j) &= H(i) - H(j) && \text{if } H(i) - H(j) \geq 0 \\ B(i,j) &= \begin{cases} H(j) & \text{if } H(i) - H(j) \geq 0 \\ H(i) & \text{if } H(i) - H(j) < 0 \end{cases} \\ C(i,j) &= H(j) - H(i) && \text{if } H(i) - H(j) < 0 \end{aligned} \tag{B.1}$$

where A are structures that are only found at y_i, C are structures that are only found at y_j, and B are structures that are found in both y_i and y_j. With N planes, where $N > 1$, there will be $\sum_{i=1}^{N} i$ different structure types, where $\Psi(i,j)$ denotes a structure that is connected between planes y_i and y_j, but does not extend beyond either. For example, structure 3 from Fig. 4.33 would be called $\Psi(1,3)$. For structures that are connected between two different planes, the histograms for the structures are calculated as follows:

$$\Psi(i,j) = \begin{cases} B(i,j) - B(i,j+1) - B(i+1,j) + B(i-1,j+1) & \text{if } y_i \neq y_0, y_j \neq N \\ B(i,j) - B(i+1,j) & \text{if } y_i \neq y_0, y_j = N \\ B(i,j) - B(i,j+1) & \text{if } y_i = y_0, y_j \neq N \\ B(i,j) & \text{if } y_i = y_0, y_j = N \end{cases} \tag{B.2}$$

The physical intuition for the first case is that the part of the histogram that contributes to structures starting at plane y_i and ending at plane y_j is the region common to these planes less the regions which extend beyond these planes (a portion of the histogram shared between y_i and the plane above y_j as well as between the plane below y_i and plane y_j). The addition of $B(i-1,j+1)$ is to account for structures which extend both above and below the planes of interest which have

Structure #	1	2	3	4	5	6	7	8	9	10
Ψ	(1,4)	(2,4)	(1,3)	(3,4)	(2,3)	(1,2)	(4,4)	(3,3)	(2,2)	(1,1)
% data	8	4	14	13	4	22	16	7	3	9
% model (scaled)	6	6	12	12	5	19	16	5	4	15
% model (unscaled)	6	6	11	14	5	16	20	5	3	14

Table B.1: The percentage of each structure pictured in Fig. 4.33 is presented for the data in the row labeled "% data". Data from the model using Gaussian histograms with equal standard deviations (u^+_{rms} = 1.67) are presented in the next two rows. Unscaled means the area under each histogram is the same, and scaled means the histograms have been scaled to reflect the relative number of structures in each plane, as indicated in Fig. 4.7.

been subtracted out twice by the previously mentioned subtractions. The other cases are simply specializations of this line of thought. Finally, structures which exist in only one plane and do not extend to any others (i.e., $\Psi(i,i)$) are calculated as follows:

$$\Psi(i,i) = \begin{cases} A(i,i+1) - \sum_{n=1}^{i-1} \Psi(n,i) & \text{if } i \leq N/2, i \neq 1 \\ C(i-1,i) - \sum_{n=i+1}^{N} \Psi(i,n) & \text{if } i > N/2, i \neq N \\ A(i,i+1) & \text{if } i = 1 \\ C(i-1,i) & \text{if } i = N \end{cases} \tag{B.3}$$

Noting that the distribution of convection velocities about the local mean has a similar shape for all planes (see Figs. 4.13a and 4.28a, for example), one could build a model histogram at each wall-normal location and calculate the types of SCS that would be present in the flow. In Fig. B.1a a Gaussian curve is fit to the data by eye with a standard deviation of u^+_{rms} = 1.67. This matches all of the profiles well except for plane SF3 where the effect of the free stream is evident by a shortening of the high-velocity tail. Fig. B.1b shows the same curve fit but in absolute velocity to help show the major differences at different wall-normal locations. First, far from the wall, the high-velocity tail of the Gaussian is longer than the measured data. Secondly, for all planes considered, except SF3, the low-velocity tail is too short. Recall, that this elongated low-velocity tail is the major difference between the mean trajectory velocity and the mean core velocity (see Fig. 4.29a). For reference, a standard deviation of u^+_{rms} = 1.33 fits the mean core velocity histograms the best and the shape of these histograms is close to Gaussian, particularly near the wall.

To compare this Gaussian fit to the actual data, the SCS counts measured previously can be used to scale the Gaussian pdfs into Gaussian histograms to highlight the major differences in SCS counts caused by the change in shape. In other words the effect of the non-Gaussian nature of the convection velocity pdfs can be investigated in terms of its effect on the inferred SCS shapes. Table B.1 tabulates the percentage of structures of each type using the actual data as well as the Gaussian convection velocity profiles both scaled and unscaled.

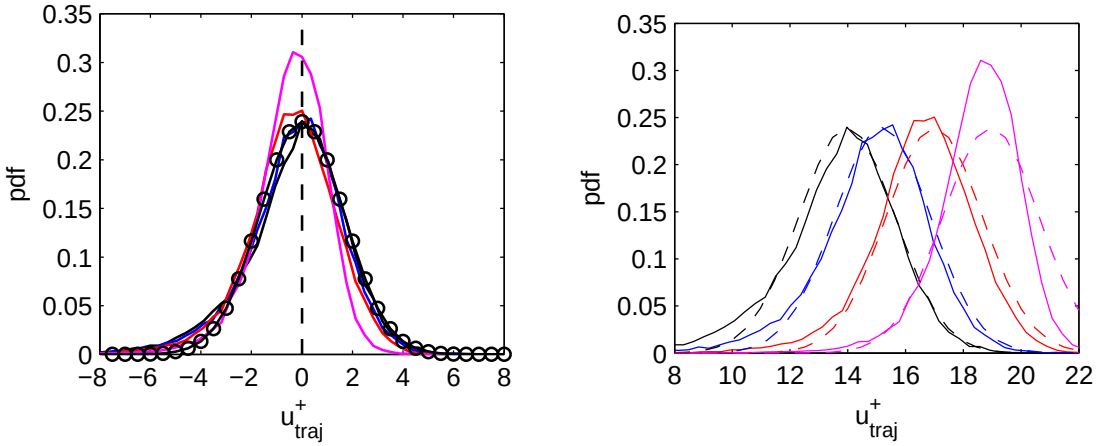

(a) Local convection velocity pdf and Gaussian fit

(b) Convection velocity pdf and Gaussian fit

Figure B.1: (a): A Gaussian with $u^+_{rms} = 1.67$ (○) fits all of the local convection velocity pdfs well in both amplitude and width. (b): Convection velocity pdfs (solid lines) are shown where the local mean has not been subtracted off to better show the Gaussian fit (dashed lines) in each plane. The planes shown are SF0: black, SF1: blue, SF2: red, and SF3: magenta.

It appears that the major difference arises due to the change in the shape of the low-velocity tail. This is indicated by the large increase in the number of structures that do not extend beyond plane 1 and a decrease in all structures connected to plane 1. Regardless of the change of the shape of the high-velocity tail in SF3, there is little change to the percentage of structures attached to this plane. This is because the difference in the shape of this histogram is really only important for regions which do not overlap any other of the histograms (see Fig. B.1b). From Table B.1 one finds that a little over 50% of the SCS identified in these planes are attached to the first plane (this includes SCS that only exist in this first plane).

If the histograms are not scaled (i.e., assuming all planes have equal counts), a further deviation between the model and the actual data is observed with a major decrease in the percentage of SCS near the wall (i.e., $\Psi(1,2)$) and an increase in the number found far from the wall (i.e., $\Psi(4,4)$), as might be expected from such a change.

Appendix C

Modified Clauser method

In order to infer the friction velocity, u_τ, from the mean velocity profile for flow over a rough wall, the modified Clauser method of Perry and Li [1990] was used. Much like the Clauser method, the friction velocity was varied to find a best fit, in a least-squares sense, between the data and the log law. Perry and Li [1990] used the composite profile covering the log layer and wake regions of a rough wall turbulent boundary layer to perform this fit. The profile is presented in Eqn. C.1 as well as in Eqn. 8 or Perry and Li [1990].

$$\frac{U(y)}{u_\tau} = \frac{1}{\kappa}\ln\left(\frac{yu_\tau}{\nu}\right) + B - \frac{\Delta U}{u_\tau} + \frac{\Pi}{\kappa}W_c\left(\frac{y}{\delta}\right) \tag{C.1}$$

Unlike the smooth wall case where the only unknown is u_τ, for the rough wall case there are three unknowns that are linked together by the roughness: the friction velocity, u_τ, the Hama roughness function, ΔU^+, and the offset of the virtual origin, e, where $y = y' + e$, and y' is the wall-normal distance measured from the crests of the roughness elements. Perry and Li [1990], using relations from Coles [1956], found a relationship between ΔU^+ and Π, the wake strength, and thus only two of the three variables needed to be varied, making the fit easier to perform. With the relationship between ΔU^+ and Π, Eqn. C.1 can be simplified to Eqn. C.2 for $\Pi = 0.55$, $\kappa = 0.41$, and $B = 5.0$ (Eqn. 19 in Perry and Li [1990]).

$$\frac{\overline{U}}{U_\infty} = 1 + \frac{1}{\kappa}\frac{u_\tau}{U_\infty}\ln\left(\frac{y}{\delta^*}\right) + \frac{1}{\kappa}\frac{u_\tau}{U_\infty}\ln\left(\frac{u_\tau}{U_\infty}\right) + 0.493\frac{u_\tau}{U_\infty} \tag{C.2}$$

While this functional form is presented for one value of Π, it is not apparent from the work of Perry and Li [1990] how this will change with differences in Π or any of the other log law constants. For that reason, a derivation is provided here. The first step is to derive a relationship between Π and ΔU^+, similar to Eqn. 18 of Coles [1956] for the smooth wall TBL, in order to eliminate ΔU^+ from the equation. This relationship will involve the displacement thickness δ^*.

$$\delta^* = \int_0^\delta \left(1 - \frac{U(y)}{U_\infty}\right) dy \tag{C.3}$$

The value of $U(y)/U_\infty$ in Eqn. C.3 can be found by rearranging Eqn. C.1 into Eqn. C.4.

$$\frac{U(y)}{U_\infty} = \frac{u_\tau}{U_\infty}\frac{1}{\kappa}\ln\left(\frac{yu_\tau}{\nu}\right) + \frac{u_\tau}{U_\infty}\left(B - \frac{\Delta U}{u_\tau}\right) + \frac{u_\tau}{U_\infty}\frac{\Pi}{\kappa}W_c\left(\frac{y}{\delta}\right) \tag{C.4}$$

Neglecting the departure of the velocity profile from the composite form (Eqn. C.1) in the sublayer and buffer layer, Eqn. C.4 is placed into Eqn. C.3 to recover Eqn. C.5.

$$\delta^* = \delta - \frac{u_\tau}{U_\infty}\frac{1}{\kappa}\int_0^\delta \ln(y)dy - \frac{u_\tau}{U_\infty}\frac{\delta}{\kappa}\ln\left(\frac{u_\tau}{\nu}\right) - \frac{u_\tau}{U_\infty}\delta\left(B - \frac{\Delta U}{u_\tau}\right) - \delta\frac{u_\tau}{U_\infty}\frac{\Pi}{\kappa}\int_0^1 W_c\left(\frac{y}{\delta}\right)d\left(\frac{y}{\delta}\right) \tag{C.5}$$

The last integral in Eqn. C.5 is solved by switching the integration over y/δ to an integration over W_c by realizing that W_c is a monotonically increasing function of y up to $y = \delta$.

$$\int_0^1 W_c\left(\frac{y}{\delta}\right)d\left(\frac{y}{\delta}\right) = W_{c,max} - \int_0^{W_{c,max}} \frac{y}{\delta}dW_c \tag{C.6}$$

For normalization, Coles [1956] chose, for convenience, that the integral in Eqn. C.6 should be 1 (see Coles [1956] Eqn. 16). Furthermore, since the wake function appears to be nearly anti-symmetric when measured in experiments, Coles [1956] chose $W_{c,max} = W_c(1) = 2$ (see Coles [1956] Eqn. 17) such that a maximum value would occur close to or at $y/\delta = 1$. Thus Eqn. C.6 is equal to 1.

The other integral in Eqn. C.5 is calculated in Eqn. C.7.

$$\int_0^\delta \ln(y)dy = y\ln(y)\|_0^\delta - \int_0^\delta dy = \delta\ln(\delta) - \delta \tag{C.7}$$

Thus Eqn. C.5 simplifies to:

$$\delta^* = \delta + \frac{u_\tau}{U_\infty}\frac{\delta}{\kappa} - \frac{u_\tau}{U_\infty}\delta\left(\frac{1}{\kappa}\ln\left(\frac{\delta u_\tau}{\nu}\right) + B - \frac{\Delta U}{u_\tau}\right) - \delta\frac{u_\tau}{U_\infty}\frac{\Pi}{\kappa} \tag{C.8}$$

The section in parenthesis in Eqn. C.8 is the value of the composite profile at $y = \delta$ given in Eqn. C.9 minus the wake term.

$$\frac{U_\infty}{u_\tau} = \frac{1}{\kappa}\ln\left(\frac{\delta u_\tau}{\nu}\right) + B - \frac{\Delta U}{u_\tau} + \frac{2\Pi}{\kappa} \tag{C.9}$$

Substituting Eqn. C.9 into Eqn. C.8 provides the relationship in Eqn. C.10.

$$\delta^* = \frac{u_\tau}{U_\infty}\frac{\delta}{\kappa}(1 + \Pi) \tag{C.10}$$

Using Eqn. C.10 to replace δ by δ^* in Eqn. C.9, Eqn. C.11 results providing the desired tran-

scendental equation for Π.

$$2\Pi - \ln(1+\Pi) = \kappa\frac{U_\infty}{u_\tau} - \ln\left(\frac{\delta^* U_\infty}{\nu}\right) - \kappa\left(B - \frac{\Delta U}{u_\tau}\right) - \ln(\kappa) \tag{C.11}$$

To get an equation to perform the modified Clauser fit, the first term on the RHS of Equation C.4 is rewritten to isolate u_τ/U_∞ and also include δ^* in the logarithm to have terms similar to those in Eqn. C.11. This modification is presented in Eqn. C.12.

$$\frac{U(y)}{U_\infty} = \frac{u_\tau}{U_\infty}\frac{1}{\kappa}\ln\left(\frac{y}{\delta^*}\right) + \frac{u_\tau}{U_\infty}\frac{1}{\kappa}\ln\left(\frac{\delta^* U_\infty}{\nu}\right) + \frac{u_\tau}{U_\infty}\frac{1}{\kappa}\ln\left(\frac{u_\tau}{U_\infty}\right) + \frac{u_\tau}{U_\infty}\left(B - \frac{\Delta U}{u_\tau}\right) + \frac{u_\tau}{U_\infty}\frac{\Pi}{\kappa}W_c\left(\frac{y}{\delta}\right) \tag{C.12}$$

Several of the terms in Eqn. C.12 appear in the relationship in Eqn. C.11. Making substitutions, Eqn. C.13 is produced.

$$\frac{U(y)}{U_\infty} = \frac{u_\tau}{U_\infty}\frac{1}{\kappa}\ln\left(\frac{y}{\delta^*}\right) + \frac{u_\tau}{U_\infty}\frac{1}{\kappa}\ln\left(\frac{u_\tau}{U_\infty}\right) + \frac{u_\tau}{U_\infty}\frac{1}{\kappa}\left(\ln(1+\Pi) - 2\Pi + \kappa\frac{U_\infty}{u_\tau} - \ln(\kappa) + \Pi W_c\left(\frac{y}{\delta}\right)\right) \tag{C.13}$$

With additional simplifications, Eqn. C.14 results, which is similar in form to Eqn. 19 of Perry and Li [1990], Eqn. C.2 here, with the constant coefficient of the rightmost term replaced by the terms in parentheses in Eqn. C.14.

$$\frac{U(y)}{U_\infty} = 1 + \frac{u_\tau}{U_\infty}\frac{1}{\kappa}\ln\left(\frac{y}{\delta^*}\right) + \frac{u_\tau}{U_\infty}\frac{1}{\kappa}\ln\left(\frac{u_\tau}{U_\infty}\right) + \frac{u_\tau}{U_\infty}\frac{1}{\kappa}\left(\ln(1+\Pi) - 2\Pi - \ln(\kappa) + \Pi W_c\left(\frac{y}{\delta}\right)\right) \tag{C.14}$$

In order to compare to Perry and Li [1990], we will compare the coefficient of the rightmost term of Eqn. 19 or Perry and Li [1990], which we will call "the coefficient" to the evaluation of the rightmost term in parenthesis of Eqn. C.14. First of all, for the rightmost term in parenthesis to be constant, the variable term with the wake function must be neglected. Note that at $y/\delta = 0.15$, Coles [1956] gives a value of the wake function equal to 0.084, which produces a term an order of magnitude lower than the other terms used to determine "the coefficient". Since the modified Clauser fit is to be performed in the log layer, below $y/\delta = 0.12$, neglecting this term seems reasonable.

Perry and Li [1990] state that they used a value of $\kappa = 0.41$ and $\Pi = 0.55$. Neglecting the variable term with the wake function of the rightmost quantity in Eqn. C.14, a constant value of "the coefficient" equal to 0.561 is obtained, which is fairly close to the value of 0.493 from Perry and Li [1990]. A value of "the coefficient" equal to 0.494 can be obtained with a slightly increased wake strength, $\Pi = 0.57$.

The modified Clauser fit is performed as follows. The value of u_τ/U_∞ as well as e are varied to find

the best fit, in a least squares sense, between the data and Eqn. C.2 in the range $100 < y^+ < 0.12\delta^+$. Note that the outer limit in terms of δ^* varies with u_τ/U_∞ as indicated in Eqn. C.10. Using these results, a fit is then performed to find the value of Π that minimizes the error, in a least squares sense, between the wake function calculated from the data, as in Eqn. C.15, and a $\sin^2$ fit to the Coles wake function given in Eqn. C.16.

$$\frac{\Pi}{\kappa} W_c\left(\frac{y}{\delta}\right) = U^+ - \left[\frac{1}{\kappa}\ln(y^+) + B - \Delta U^+\right] \tag{C.15}$$

$$\frac{\Pi}{\kappa} W_c\left(\frac{y}{\delta}\right) = \frac{2\pi}{\kappa}\sin^2\left(\frac{\pi}{2}\frac{y}{\delta}\right) \tag{C.16}$$

This value of Π is then used in Eqn. C.14 to find the best fit between this equation and the data in the range $100 < y^+ < 0.12\delta^+$ with varying u_τ/U_∞ and e. From these best fit values, a new value of Π is calculated and the process is iterated until the values of u_τ, e, and Π converge.

Appendix D

Roughness parameter variation and statistical convergence along the roughness

The variation of the roughness parameters along the rough plate are presented in Table D.1 for stations 1–3 of locations 1–7 (see Fig. 2.8 and 2.9a). Data for stations A–F where spectral measurements were taken are recorded in Table D.2. Instead of the shift in the virtual origin, e, the y offset of the point nearest the wall from the virtual origin is recorded for each station. δ is measured with respect to the virtual origin. Information provided for locations 1–4 is likely in error as the evaluation of u_τ and other roughness related parameters is dependent on the existence of the log layer, which would be altered at these locations where the flow is still adjusting to the new boundary condition.

Data for the convergence of the mean and rms statistics along the roughness at stations 2 and 3 is provided in Fig. D.1. In addition, the convergence of the skewness and flatness at all 3 stations is presented in Fig. D.2. Finally, the similarity between the skewness and flatness profiles at location 7 at all stations is confirmed in Fig. D.3 and comparisons to the smooth wall profile for the fully developed rough-wall profiles (locations 5–7) are presented in Fig. D.4

Location-Station	u_τ (m/s)	y offset (mm)	δ (mm)	ΔU^+	k_s^+	k_s/k	δ/k_s
0-0	0.96	0.80	36.2	-	-	-	-
1-1	0.74	-0.30	35.3	-7.9	0.2	0.00	10245
1-2	0.73	-1.40	34.4	-8.0	0.2	0.00	10374
1-3	0.76	-0.30	35.7	-7.1	0.2	0.01	7688
2-1	0.84	-0.40	35.8	-3.6	0.9	0.02	2030
2-2	0.71	-2.40	35.5	-8.8	0.1	0.00	14375
2-3	0.86	-0.50	35.1	-2.9	1.3	0.03	1531
3-1	1.13	0.60	39.1	4.0	21.2	0.37	132
3-2	0.76	-2.40	36.4	-6.0	0.4	0.01	5019
3-3	0.91	-0.70	37.4	-0.9	2.8	0.06	763
4-1	1.06	0.00	39.0	3.1	14.7	0.27	180
4-2	0.76	-2.50	37.8	-5.6	0.4	0.01	4418
4-3	1.19	0.70	39.9	5.4	37.7	0.62	80
5-1	1.14	0.65	40.1	4.7	28.3	0.49	103
5-2	1.08	-1.00	40.5	3.9	20.4	0.37	137
5-3	1.15	0.70	41.2	5.0	32.0	0.54	95
6-1	1.11	0.80	41.7	4.3	24.0	0.42	123
6-2	1.11	-0.25	42.8	4.9	30.7	0.54	99
6-3	1.21	1.00	43.1	6.0	48.2	0.78	69
7-1	1.08	0.65	42.1	3.9	20.4	0.37	142
7-2	1.07	-0.35	43.8	3.9	20.4	0.37	147
7-3	1.14	1.00	44.1	5.0	32.0	0.55	100

Table D.1: Variation of parameters along the roughness

Location-Station	u_τ (m/s)	y offset (mm)	δ (mm)	ΔU^+	k_s^+	k_s/k	δ/k_s
Smooth	0.969	0.55	44.1	-	-	-	-
7A	1.10	0.7	44.0	4.4	25.0	0.45	123
7B	1.12	0.1	43.7	4.9	30.7	0.54	102
7C	1.16	0.1	44.5	5.6	40.9	0.69	80
7D	1.12	1.1	44.3	4.9	30.7	0.54	103
7E	1.07	-0.6	44.4	3.6	18.0	0.33	167
7F	1.06	-0.3	44.1	3.7	18.8	0.35	159

Table D.2: Variation of parameters along stations at location 7

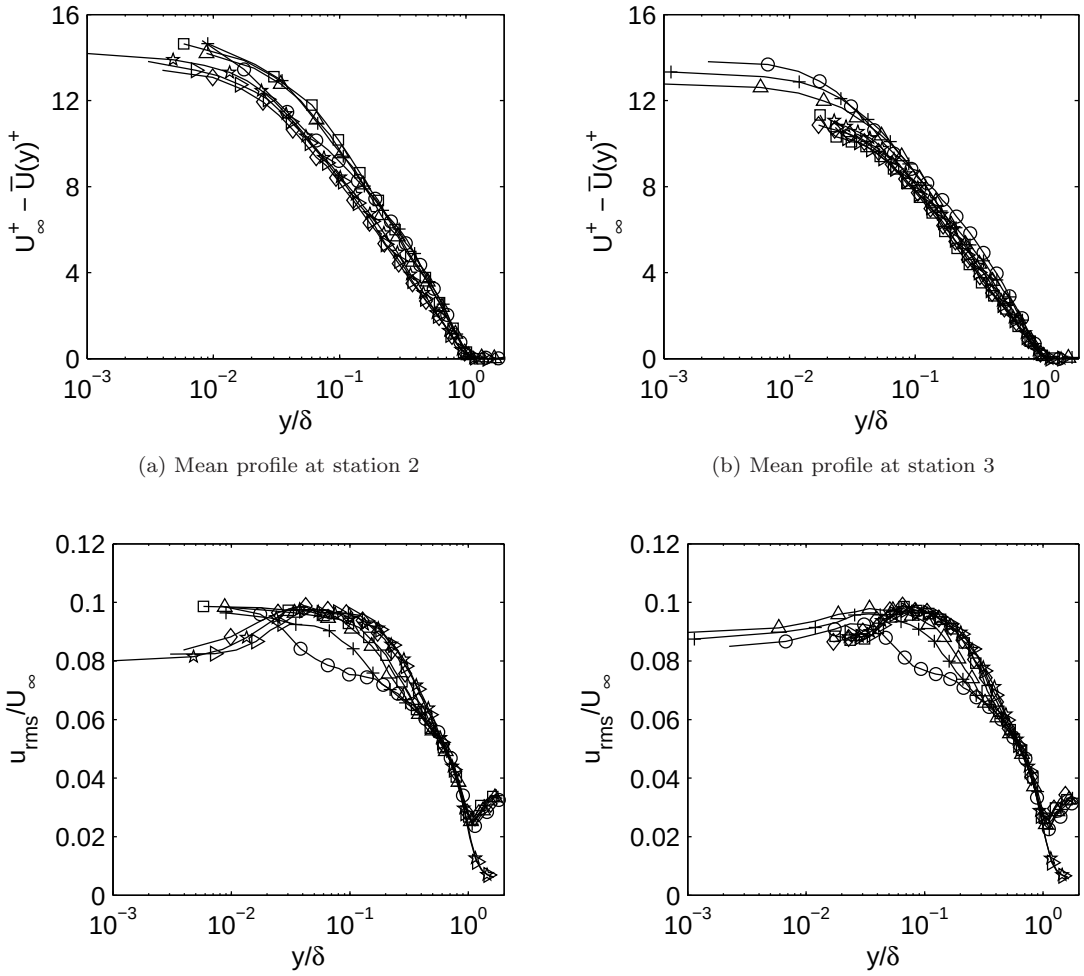

(a) Mean profile at station 2

(b) Mean profile at station 3

(c) Rms profile at station 2

(d) Rms profile at station 3

Figure D.1: Mean (a,b) and rms (c,d) streamwise velocity profiles at stations 1 (a,c) and 2 (b,d) of location 1: ○, 2:+ , 3:△, 4:□, 5:◊, 6:▷, and 7:☆ in outer scaling

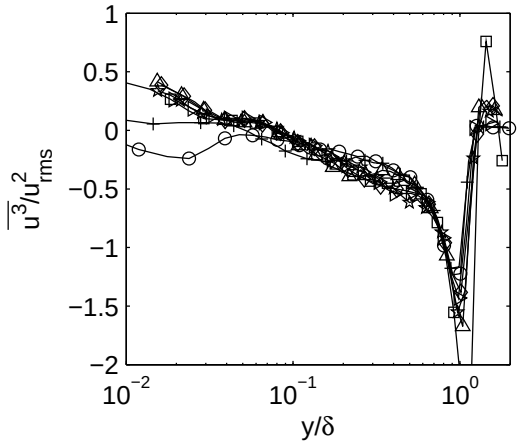

(a) Skewness profiles at station 1

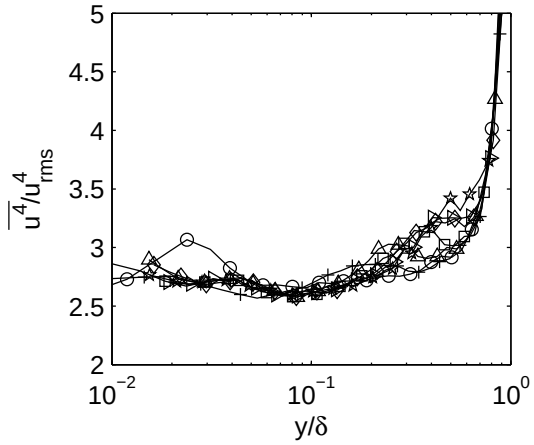

(b) Flatness profiles at station 1

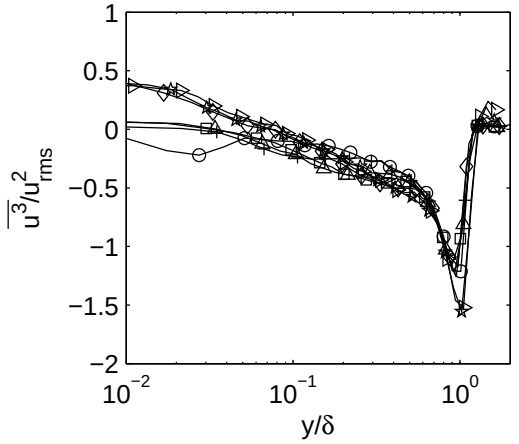

(c) Skewness profiles at station 2

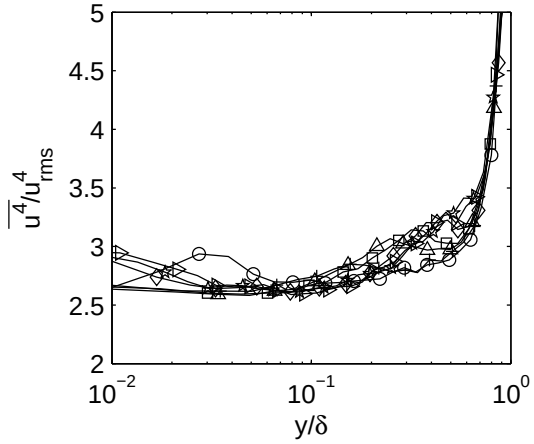

(d) Flatness profiles at station 3

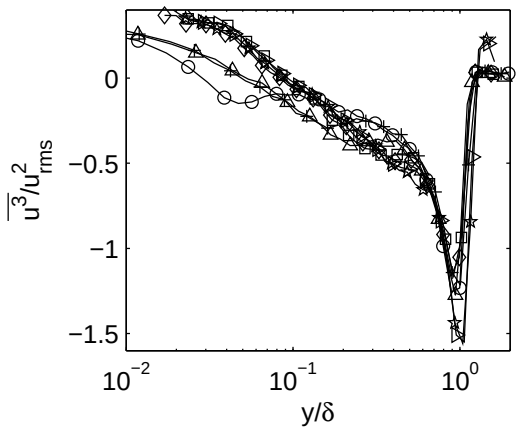

(e) Skewness profiles at station 2

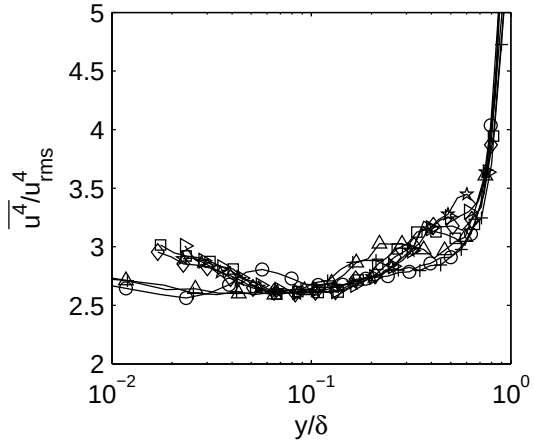

(f) Flatness profiles at station 3

Figure D.2: Profiles of skewness (a,c,e) and flatness (b,d,e) of the streamwise velocity fluctuations for stations 1 (a,b), 2 (c,d), and 3 (e,f) of location 1: ○, 2:+ , 3:△, 4:□, 5:◊, 6:▷, and 7:☆ in outer scaling

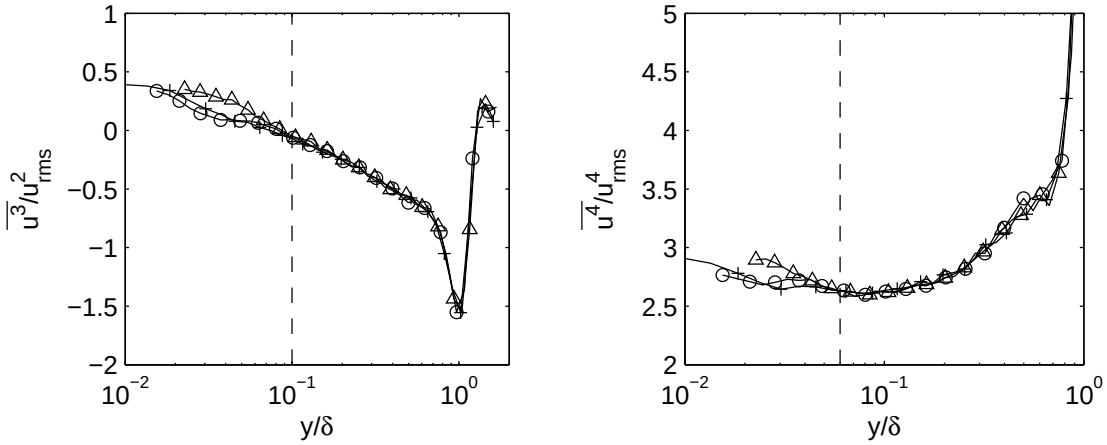

(a) Skewness variation along roughness

(b) Flatness variation along roughness

Figure D.3: Profiles of the (a): skewness and (b): flatness of the streamwise velocity fluctuations at stations 1: ○, 2: +, and 3: △ of location 7

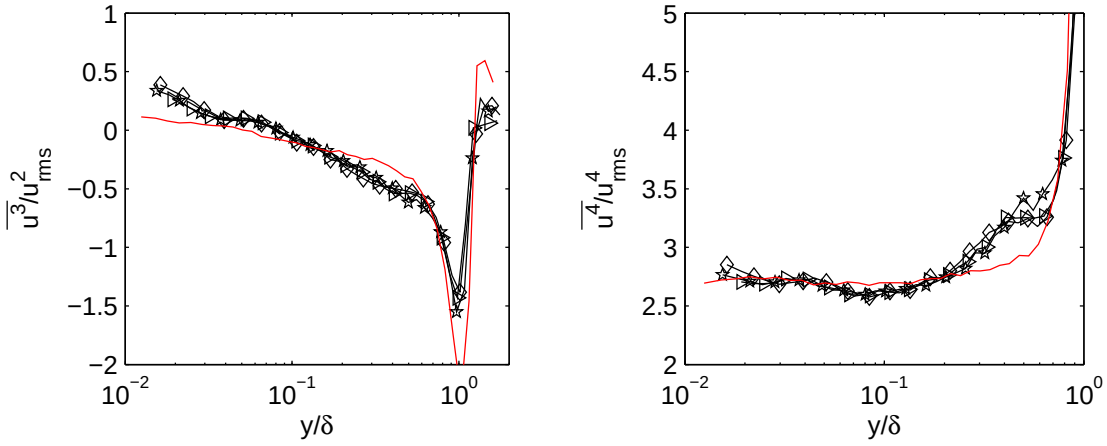

(a) Skewness for fully-developed flow

(b) Flatness for fully-developed flow

Figure D.4: Profiles of the (a): skewness and (b): flatness of the streamwise velocity fluctuations at station 1 of locations 5: ◊, 6: ▷, and 7: ☆. Red line: smooth-wall profile at location 7

Appendix E

Ionic polymer-metal composite (IPMC) dynamic roughness

In this appendix, the suitability of using ionic polymer-metal composites (IPMCs) to create a dynamic roughness, that is a roughness whose amplitude varies in time, is evaluated. IPMCs were investigated for their use in producing a dynamic roughness as they were thin, light weight, electrically actuated, and only required a low voltage to actuate.

Section E.1 provides an introduction to these materials, their actuation mechanism, and a brief review of the literature on IPMCs. The experimental systems used to study these materials are then reviewed in Section E.2. This is followed by the results of a number of experiments. In Section E.3, IPMC samples were actuated in a cantilevered configuration, similar to tests performed in the literature. This was done to understand the repeatability of actuation, hydration requirements, and the response of the IPMC to different voltage inputs. Next, two different methods were used to try and create a dynamic roughness. Section E.4 describes the first setup where a portion of an IPMC surface was rigidly bonded to a base electrode while a small portion was left free to actuate. This sort of actuation was limited to low frequencies, much like the cantilever configuration, but was capable of producing a large peak-to-peak roughness amplitude. In order to try and achieve higher actuation frequencies, the IPMC surface was fully adhered to the base electrode using a conductive gel as described in Section E.5. Here the mechanism for actuation was expected to be a wrinkling or buckling of the surface as described in Section E.1 as opposed to bending, as was the case for the rigidly bonded IPMC in Section E.4. In the end, this second method was only capable of producing small (several micron) variations in the roughness amplitude for frequencies under 10Hz.

E.1 Introduction to ionic polymer-metal composites

Ionic polymer-metal composites (IPMCs) are specially treated ion-exchange membranes that are capable of producing a bending motion under an applied electric field or can produce an electric field

when they are bent. They find use as soft actuators and artificial muscles [Shahinpoor et al., 1998] as well as sensors and energy harvesters [Bar-Cohen, 2004]. IPMCs consist of polymer ion-exchange membranes that have been plated with metal (usually platinum) electrodes. The underlying polymer ion-exchange membranes are porous cross-linked polymers that are permeable to water and either cations or anions [Shahinpoor and Kim, 2001]. For example, Nafion, produced by DuPont, is permeable to water and cations, but impermeable to anions. These materials are supported by a polymer backbone that forms a 3D matrix. Side chains are regularly spaced along the backbone and are terminated by ionic groups that tend to aggregate into clusters. While the backbone is hydrophobic, these ionic clusters are hydrophilic and form a pathway through which water can be transported [Nemat-Nasser and Li, 2000]. Platinum is deposited on the surface from the inside out by soaking the membrane in a platinum solution followed by a reducing process that creates a layer of platinum a few microns thick along the surfaces. The platinum layer is thus fully integrated into the structure of the IPMC [Takenaka et al., 1982].

The modeling of IPMC actuation under an applied voltage is complex and a number of different theories have been proposed. One of the first rigorous micro-mechanical models was developed by Nemat-Nasser and Li [2000] which modeled both the ion and water transport within the ion-exchange membrane. In this model, the deformation was proposed to be caused by an electrical repulsive force between the cations which were transported to the cathode along with a local swelling of the polymer due to water dragged along with the cations. It was proposed that the effect of the electrical charge was dominant at short times due to the longer time required for water transport. In a cantilevered configuration, the swelling at the cathode causes the IPMC specimen to bend toward the anode. Nemat-Nasser [2002] used this model to further evaluate the effects of various parameters. Work by Shahinpoor and Kim [2004] also provides insights into the deformation and relaxation occurring within the polymer. Finally, the model of Enikov and Seo [2005] extends these models to deal with voltages above the equilibrium potential targeting high-voltage operation associated with significant mass transfer. In this case, not only is the water transport important, but so are electrochemical reactions.

Based on concepts from these models a number of studies have been done to improve the performance of IPMC actuators both in terms of maximum displacement and force output. This is usually tested with a strip of IPMC in a cantilever configuration. One of the key parameters for improving actuations is the choice of the mobile cation in the membrane. Under AC actuation at 1.2 V and 0.5 Hz, Kim and Shahinpoor [2003] found that lithium ions produced the highest force output. This performance increase was likely due to the large hydrated volume of lithium which allowed it to drag more water along with it and thus create more swelling at the surface of the IPMC than the other cations tested. Unlike cation choice, the choice of the ion-exchange membrane makes little difference in AC actuation, although under a DC voltage, Nemat-Nasser and Wu [2003] found that

Flemion substrates showed no back-relaxation under an applied voltage, while the standard Nafion substrates do. Additional increases in force generation were achieved by coating the platinum surface with metals such as copper and silver by Shahinpoor and Kim [2000]. A 10–20% increase in the force was realized, which was due to a decrease in the surface resistance, and thus a higher potential across the IPMC, even far from the electrodes.

When operating in air, the hydration of the IPMC is of importance. Water is lost due to leakage of water through the surface as well as loss of liquid water due to hydrolysis when a large voltage (above 1.2 V) is applied. Nemat-Nasser and Wu [2003] found that wet IPMCs are about 10 times more compliant than dry ones, and thus the force generated by a wet IPMC will result in a displacement that is 10 times larger as well. To try and improve the water retention, Kim et al. [2006] tried various surface coatings. It was found that a thin (2–3 nm) parylene coating increased the useful lifetime of the IPMC by nearly 16 times when operating at 3V and 0.5Hz, where the useful lifetime was defined as the time over which the IPMC maintained a peak-to-peak amplitude that was 60% or more of its maximum amplitude.

Finally, while ion-exchange membranes are only manufactured in certain thicknesses, various techniques [Kim et al., 2006, Kim and Shahinpoor, 2002] exist for increasing the thickness to any desired size. This increase in thickness improves the force density, as discussed by Kim and Shahinpoor [2002].

While most tests have been done in cantilevered configurations for applications such as grippers for soft materials, linear actuators, or swimming and flying devices [Shahinpoor et al., 1998], the goal of the present study was to create a rough surface by constraining one surface of the IPMC and allowing the other to deform. The mechanism behind such a deformation is the wrinkle pattern created by the compression and buckling of a stiff, thin film on a thick compliant substrate as described by Chen and Hutchinson [2004] and Huang et al. [2004]. The deformation can be thought of as the buckling of a thin film bound to a viscous layer as used in the model of Huang and Suo [2002] and Huang et al. [2005]. Other surface pattens are realized when the buckled surface delaminates from the substrate as extensively reviewed by Gioia and Ortiz [1997], which is also of interest as a possible actuation mechanism.

E.2 IPMC experiments

This section discusses the IPMC samples used to produce a dynamic roughness as well as the instruments used to measure the surface deformation.

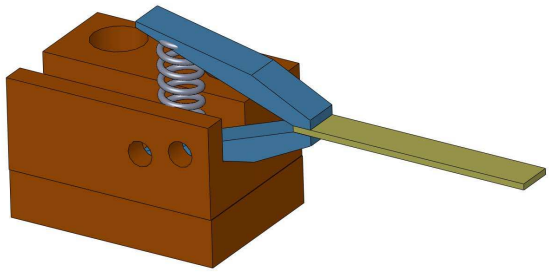

Figure E.1: A drawing of the cantilever setup where the strip of IPMC (yellow) is cantilevered from the electrode clamp (blue)

E.2.1 IPMC samples

The IPMC samples used in all experiments were provided by Environmental Robots Inc. They consisted of a 170 or 300 μm Nafion substrate with sodium cations coated with a platinum electrode with a thickness of 5, 10, 18, or 30 μm. As discussed in Section E.1, an ion-exchange membrane with lithium ions would provide the largest possible displacement of the IPMC, but sodium ions also work well as described by Kim and Shahinpoor [2003]. For these tests, no surface treatments were performed to improve the surface conductivity nor the retention of water although these would be obvious improvements to make in future experiments.

E.2.2 IPMC handling and storage

The IPMC samples were transported and stored in distilled water when not being tested to keep them in a controlled state and assure the same performance between all tests. If the surfaces needed to be hydrated during tests, only distilled water was used to eliminate the introduction of any contaminants to the surfaces. For the same reason, latex gloves were used when handling these materials. If necessary, IPMC specimens would be cleaned with distilled water and non-abrasive cloths or tissues after testing before returning them to storage. A utility knife and straight edge were used to cut the samples to size for the various tests performed.

E.2.3 Cantilevered actuation system

The first set of IPMC experiments used thin IPMC strips, 50 mm long, 13 mm wide, and 0.3 mm thick, in a cantilevered configuration similar to tests often performed in the literature. Tests were performed using the setup shown in Fig. E.1. The tip displacement of the IPMC strip was measured using the Keyenece LK-G32 CCD laser displacement sensor discussed in Section E.2.6. In order to position the cantilevered strip an appropriate distance from the sensor, the setup in Fig. E.1 was attached to the Thor Labs L490 Lab Jack.

Frequency (Hz)	0.02	0.05	0.1	0.5	1	2	10
Measured Voltage (V)	1.98	1.95	1.8	1	0.75	0.6	0.4

Table E.1: Voltage drop across the IPMC with frequency. The input voltage was a 2V sine wave when no load was applied.

The impedance of the IPMC samples decreased with increasing frequency of actuation (see [Shahinpoor and Kim, 2001]), requiring more current at higher frequencies to maintain the same voltage drop across the sample. The voltage signal for these experiments was supplied by a National Instruments PCI-6014 DAQ board with a maximum current output of 5 mA. This limited current output lead to a decrease in voltage drop across the IPMC with increasing frequency as noted in Table E.1 for a 2 V no-load input. A current boosting circuit was built to correct this as described in Section E.2.5, although these cantilever experiments were performed without this circuit. Thus, Table E.1 can be used as a guide for the actual voltage drop across the IPMC at a given frequency.

E.2.4 Dynamic roughness constraint and actuation system 1

One dynamic roughness surface was created by rigidly bonding a 10×10 cm square of IPMC to a rigid copper electrode using Resin Technology Group TIGA 901 silver conductive epoxy. Before applying the epoxy, the IPMC was heated in the CascadeTek curing oven at 65°C for 30 min to remove moisture from the sample in order to prevent debonding when applying the epoxy and curing in the oven. Next, tape was placed around the edges of the IPMC to prevent epoxy from forming a bridge between the upper and lower surfaces. Finally, epoxy was applied between the IPMC and a rigid copper electrode, the two surfaces were clamped together with a rubber sheet and an aluminum plate stacked on top of the IPMC to evenly distribute the load, and the epoxy was cured in the oven at 65°C for 4 hrs.

Upon cooling, distilled water was applied to the surface which caused a portion of the surface to delaminate. This allowed the study of a "selectively adhered" roughness, which could also have been studied by selectively adhering certain portions of the IPMC and allowing other parts to be free to deform. For actuation, the base electrode was placed on top of a rubber sheet and was attached to the optics table using nylon screws for electrical insulation. Bar electrodes were clamped to the top surface to complete the circuit and the voltage input was supplied through the National Instruments PCI-6014 DAQ board. The setup is shown in Fig. E.2. The setup was later moved onto the Lab Jack for dynamic roughness measurements using the Keyence laser displacement sensor.

E.2.5 Dynamic roughness constraint and actuation system 2

A constraint and actuation system was built to firmly hold an IPMC down to a base electrode while keeping the top surface free to deform in order to try and create a dynamic roughness via

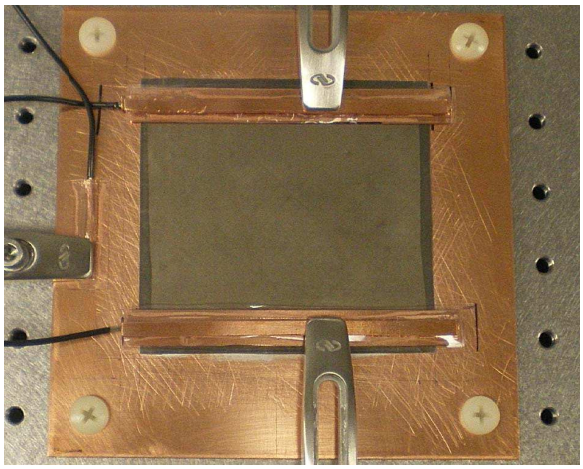

Figure E.2: The setup used to actuate the "selectively adhered" IPMC dynamic roughness

the wrinkling or buckling method described at the end of Section E.1. In this scenario, buckling of either the IPMC on a viscous conductive gel or the buckling of the platinum layer on top of the ion-exchange membrane was expected. To test these different cases, the total thickness as well as the substrate and electrode thicknesses were varied by different amounts. In all, six different combinations were tested as documented in Table E.3 or Section E.5.1.

A drawing of the system used for constraining and actuating the IPMC samples is shown in Fig. E.3a. The whole setup rests on an electrically insulating base (black in Fig. E.3a) which was connected to a Thor Labs L490 Lab Jack using nylon screws (again for electrical insulation) in order to adjust the distance between the sample and the displacement sensor (Section E.2.6) or microscope (Section E.2.7). Samples were sandwiched between the base electrode (red) and ring electrode (tan) to provide a voltage across the sample's thickness. Copper wire was connected to the base electrode through the slit in the bottom surface and held in place by conductive copper tape. The same conductive tape was used to attach copper wire along the perimeter of the ring electrode. In order to improve electrical contact between the electrodes and IPMC specimens, the electrode surfaces were cleaned with steel wool and wiped clean with isopropyl alcohol before use. In addition, conductive gel was used to improve contact while providing a non-rigid connection between the IPMC and base electrode. Both "Lectron II" and "Bodytronics" conductive gels were tested, of which the latter was preferred due to the ability to achieve consistent actuation. The IPMC specimens were cut approximately 1cm longer and wider than the electrodes to prevent any gel that may leak out during setup from forming a bridge between the top and bottom surfaces of the IPMC.

In order to provide a flat surface and even contact, a spacer (blue in Fig. E.3a) was attached flush to the ring electrode via screws along each side of the ring electrode (see the holes on the side of the ring electrode in Fig. E.3a). Once pressed flat, toggle clamps were used to hold down the ring electrode (these rest on the green mounts in Fig. E.3a) and the spacer was removed. A photograph

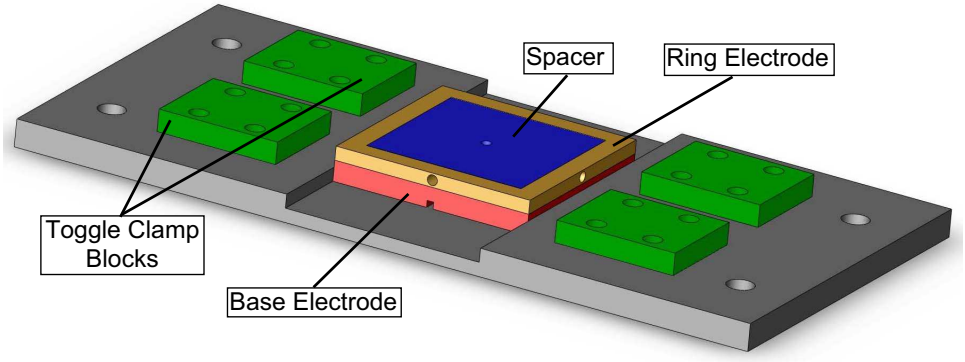

(a) IPMC holder drawing

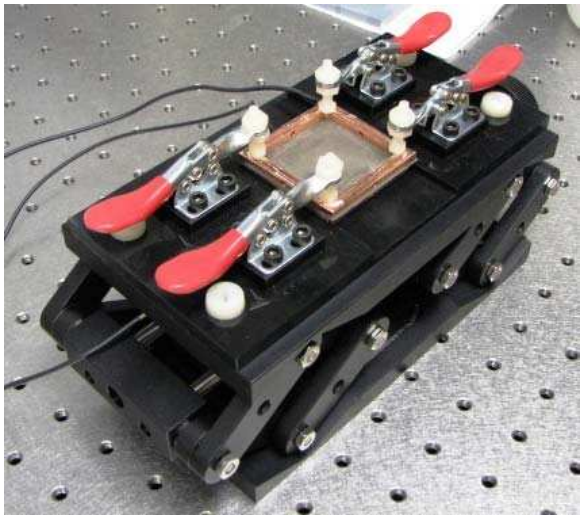

(b) IPMC holder final setup

Figure E.3: (a): A drawing of the holder assembly consisting of an electrically insulating base (black), a base electrode (red), a ring electrode (tan), a spacer (blue), and toggle clamp attachment blocks (green). (b): The final setup with the spacer removed, the toggle clamps engaged, and the base attached to the Lab Jack

of a specimen after setup is shown in Fig. E.3b.

The routine used to ensure that there was a strong bond between the base electrode and the bottom of the IPMC is as follows:

1. Remove the IPMC specimen from storage (see Section E.2.2) and allow to dry.
2. Coat the base electrode and one side of the IPMC with the conductive gel and press these parts together. If the IPMC surface curls up after step 1, the side of the IPMC which the specimen is curling away from is the side which should be coated with the conductive gel.
3. Use a wet foam brush to hydrate the top surface of the IPMC
4. Press the ring electrode with spacer attached onto the top surface of the IPMC. Smooth the IPMC surface and then engage the toggle clamps to hold down the ring electrode.

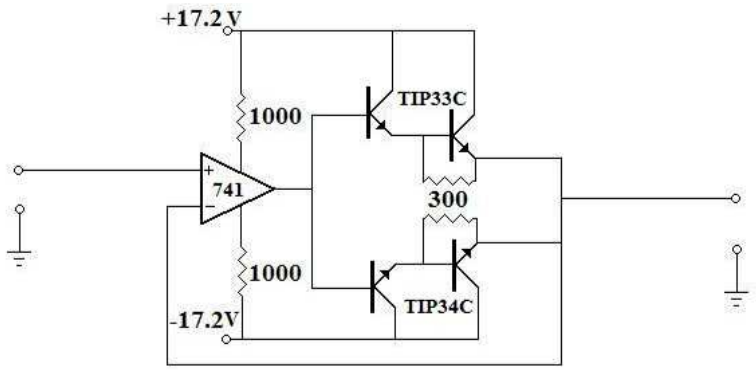

Figure E.4: Current amplifying circuit

5. Once clamped firmly, remove the spacer.

6. Check that the IPMC surface is flat and well bonded to the base electrode. If not, remove and clean the sample and electrode, then go back to step 2.

Actuation of the IPMC specimens was controlled through LabVIEW. Due to the low current output of the data acquisition (DAQ) board (National Instruments PCI-6014), a current amplification circuit was constructed and placed between the DAQ output and the electrodes; the circuit is shown in Figure E.4. Power was supplied to this circuit via a Tek Power bi-polar power supply with a maximum current output of 10 A.

E.2.6 Scanning laser displacement sensor

In order to obtain a quantitative measurement of the static and dynamic surface roughness, a scanning laser displacement sensor was used. A cartoon of the side view of the entire setup along with the IPMC sample holder (discussed in Section E.2.5) is shown in Fig. E.5a and a photograph of the actual system with the sample holder removed is shown in Fig. E.5b. Displacement measurements were made with a Keyence LK-G32 CCD Laser Displacement Sensor controlled through a Keyence LKG-3001 Controller. This sensor was capable of reading out-of-plane displacements with a repeatability of 50 nm and was linear within +/-0.05% over the full measurement range (+/-5 mm). The laser spot size was approximately 30 μm in diameter, which lead to some spatial averaging of the measured out-of-plane displacements.

Several other methods were considered for measuring both static and dynamic roughnesses including several different types of interferometers (white light, electronic speckle, and temporal speckle pattern interferometry) and digital image correlation (DIC). The goals of the surface measurement were to obtain a full field dynamic measurement of the roughness that could be performed both on the bench and in the wind tunnel. DIC has the advantage of providing a full field measurement that

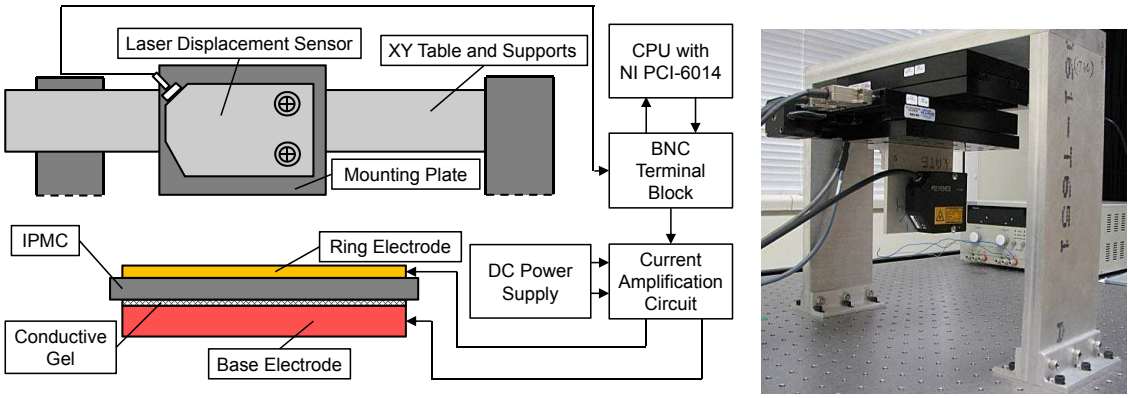

(a) Displacement measurement schematic (b) Displacement sensor

Figure E.5: (a): A cartoon of the IPMC holder, laser displacement sensor, and electrical connections. (b): A photograph of the scanning displacement sensor system

could be used on dull or diffuse surfaces such as the IPMC. The disadvantage is that to measure the expected small deformations of the surface (expected to be on the order of 10s to 100s of microns), images would need to be taken using microscope objectives with working distances on the order of several centimeters. This would not be feasible for in situ measurements in the wind tunnel.

While many interferometers require surfaces to be highly reflective, which the IPMC was not, even interferometers that do not require such a surface would have difficulty in tracking the deformation of the IPMC surfaces. While interferometers can perform both a full field measurement and measure accurately, the large out-of-plane displacement and sharp gradients expected on the IPMC surface would make it difficult to simultaneously record a large field of view while still being able to resolve the fringe patterns developed over individual roughness elements.

The advantage of the scanning laser displacement sensor was that it could measure the surface deformation accurately (down to 50 nm) and had a reasonable working distance so that it could be used in situ. The disadvantage is that it provides a point-wise measurement, but assuming the roughness deformation is stationary in time, the full surface deformation could then be reconstructed by scanning the surface.

In order to scan the laser displacement sensor along the surface, it was mounted to two Griffin Motion LNS-BS linear stages mounted in an x-y table configuration and controlled through two separate PMD Ion Motion Controllers in order to position the sensor. The stages had a total travel of 100 mm and could take steps as small as 100 nm with repeatability ensured within 300 nm by the stage's linear encoder. Over the full length of travel, the position was accurate to within 3 μm, travel was straight within 2 μm and flat within 3 μm. The stage was suspended from a rigid mounting bracket attached to a Newport 4 in thick RG series breadboard supported by a Newport VH workstation with floating supports for breadboard/frame isolation as shown in Fig. E.5b. This table isolated the specimen holder and measurement system from both low and high frequency

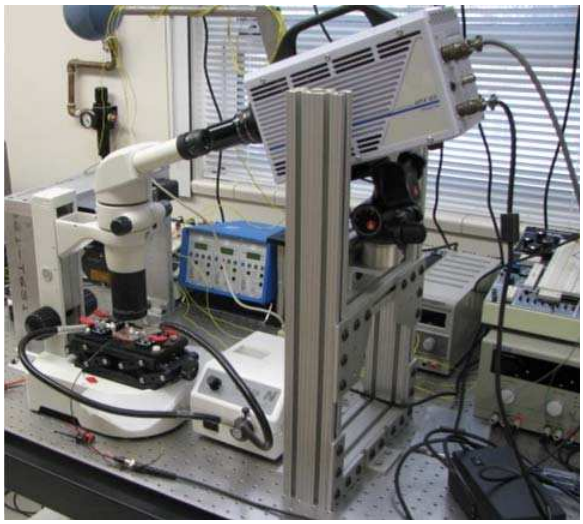

Figure E.6: A photograph of the microscopic photography station. The connection between the microscope and the high-speed camera is shown in the foreground. The sample holder is placed under the microscope and the gooseneck light pipes are in place.

vibrations within the laboratory which could have contaminated the measurements.

All components of this system were triggered and controlled through LabVIEW using a National Instruments PCI-6014 DAQ board and an NI BNC-2120 shielded connector block.

E.2.7 Microscopic photography station

A photomicrography system was used to take both static images and high-speed movies of the IPMC specimens for qualitative analysis of the deformation. A photograph of the setup is shown in Fig. E.6. A Nikon SMZ-800 stereoscopic zoom microscope (1–6.3x zoom) with a P-ED Plan 2x objective was used for magnification. Images were acquired with a Photron FASTCAM APX RS high-speed digital camera (the same camera described in Section 2.1.2) which was connected to one eyepiece of the microscope with a Martin Microscope MM-SLR adapter. With the addition of this adapter, images could be taken with total magnification exceeding 126x. A Nikon Instruments NI-150 High Intensity Illuminator was used to provide sufficient lighting for image acquisition via two gooseneck light pipes.

E.3 Preliminary experiments

In order to better understand the actuation mechanism and to learn how to handle the IPMC samples, a number of tests were run using a cantilevered strip of IPMC as discussed in Section E.2.3. The constraint system is shown in Fig. E.1. The cantilever tip displacement was monitored with the IPMC subjected to sinusoidal AC (ranging from 0.02 to 10 Hz) and DC excitations between 1 and

4 V. This range was chosen to test voltages both above and below the hydrolysis limit (the voltage at which water would begin to break down into hydrogen and hydroxide ions, 1.2 V [Shahinpoor and Kim, 2001]), above which performance was expected to degrade in time. The range of frequencies tested spanned the range of frequencies tested by Shahinpoor and Kim [2001] and Nemat-Nasser and Li [2000].

As noted in Table E.1 or Section E.2.3, the actual voltage drop across the IPMC differed from the no-load voltage for this set of experiments. In all results presented in this section, the voltage input reported is the no-load voltage input. Regardless of this issue, some meaningful results were obtained from these experiments.

To keep the test conditions consistent, all samples were soaked in deionized water for 30 min before each test (unless specified otherwise) and allowed to dry for 10 min until transient motion of the IPMC ceased. Samples were also handled with tweezers of latex gloves to prevent contamination of the sample surface as previously discussed.

E.3.1 Endurance tests: variation of tip deflection with time

The variation of the IPMC tip deflection was first measured over 600 cycles to determine if and how the performance, in this case the tip deflection, would degrade in time. Both the peak-to-peak tip deflection, Δh, shown in Fig. E.7, and the the mean height over each cycle relative to the starting position, $h_m = \Delta h/2 - h_{t=0}$, were monitored for a range of input voltages at a fixed frequency (1Hz). The results are presented in Fig. E.8 and show that there is generally little decay in Δh, holding a peak-to-peak amplitude within 97% of the maximum value over at least 600 cycles (60 sec) regardless of the input voltage. In all cases, there is some amount of time before the IPMC reaches a peak amplitude, somewhere between 50 and 200 cycles, as well as a slight mean motion. Neither of these show a clear trend with voltage. It is likely that these parameters are dependent on the hydration of the IPMC as well as the contact between the IPMC and the electrodes.

As shown in Table E.1, the actual voltage drop across the IPMC was smaller than indicated by the no-load voltage input in Fig. E.8. If the change in the voltage drop across the IPMC scales with the no-load voltage, then the voltage drop will by 3/8th of the value indicated in Fig. E.8. Thus, the voltages applied across the IPMC probably did not exceed the hydrolysis limit (1.2 V) and no solid conclusions can be drawn about whether performance will remain constant above this limit. Experiments by Kim et al. [2006] showed that under a 3 V, 0.5 Hz excitation, the IPMC peak-to-peak amplitude decayed to less than 50% of the initial amplitude over 600 cycles so some decay should be expected.

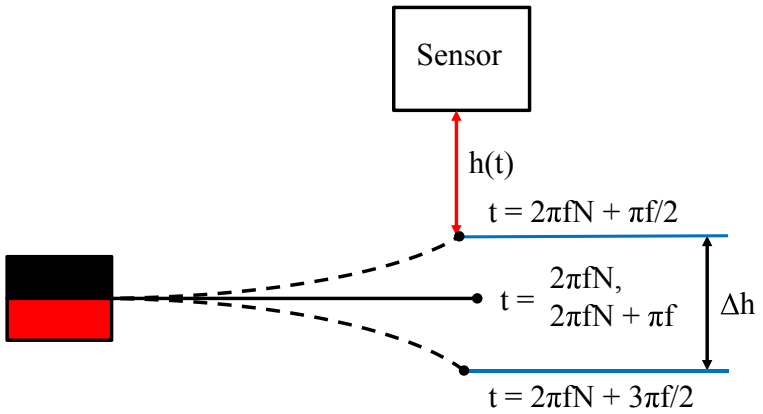

Figure E.7: A cartoon of the IPMC cantilever setup. The solid black line is the IPMC location at the beginning of every voltage cycle. The dotted lines mark the location of the maximum and minimum deflection. The clamp is drawn in red and black.

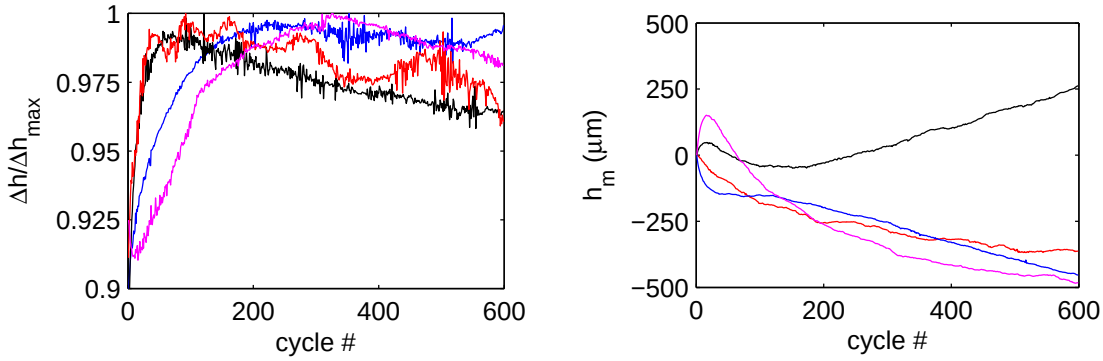

(a) Change in peak-to-peak amplitude

(b) Change in IPMC mean position

Figure E.8: (a): Change in the peak-to-peak amplitude, Δh. (b): Change in the mean height compared to the initial height, $h_m = \Delta h/2 - h_{t=0}$. In both, the input signals were 1 Hz sine waves with amplitudes of 1.2 V: red, 2 V: blue and black, and 3 V: magenta.

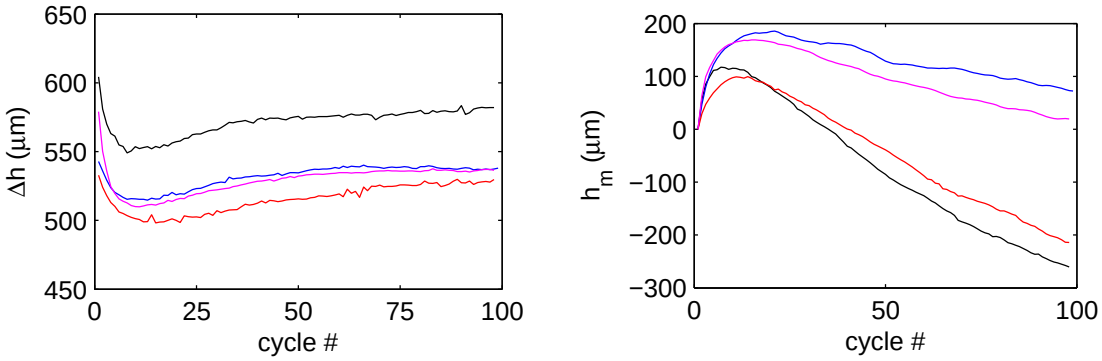

(a) Change in peak-to-peak amplitude

(b) Change in IPMC mean position

Figure E.9: Response of an IPMC to a 3 V, 1 Hz sine wave input when allowed to soak in deionized water for 6 min: black, 10 min: blue and red, and 30 min: magenta. The tests were run in the listed order. (a): Change in the peak-to-peak amplitude over 100 cycles. (b): Change in h_m, the mean amplitude compared to the initial height, over 100 cycles

E.3.2 Hydration tests

Experiments were performed after allowing the IPMC to rehydrate for various lengths of time to see how quickly the IMPC could reach a fully hydrated condition and thus perform optimally. Measurements were taken over 100 cycles with a 3 V, 1 Hz sine wave voltage input using the same setup as the endurance tests. The variation of Δh and h_m are shown in Fig. E.9. The change in Δh with time was similar for all hydration times. Also, there is no clear relationship between the mean amplitude and hydration time. Thus, the hydration times tested had little effect on the IPMC actuation and the minimal time to full hydration is likely less than 6 min. From observing the IPMC during rehydration, once submerged in water, the IMPC would curl along its length as it began to absorb water. After a few minutes this motion would cease. This cessation of motion appeared to be a good indication of when the sample was fully hydrated.

E.3.3 AC and DC excitation

The response of the IPMC to 2 and 2.5 V DC excitations are presented in Fig. E.10a. For these experiments, the voltage was applied as a step function, held for 30 sec, and then turned off. Measurements were taken for a total of 60 seconds capturing the step up and step down in voltage. In Fig. E.10a, the tip displacement from its position at time zero, h_d, reaches a maximum of 3000 μm after 10–15 sec. Thus, under AC actuation, it is not expected that the peak-to-peak tip deflection of the IPMC will increase for frequencies below about 0.05–0.1 Hz.

The response of the IPMC to sinusoidal AC excitations with no-load input voltages ranging from 1–4 V and frequencies from 0.05–0.5 Hz are shown in Fig. E.10b. In all cases, the peak-to-peak displacement increases with increasing voltage and decreases with increasing frequency as was found

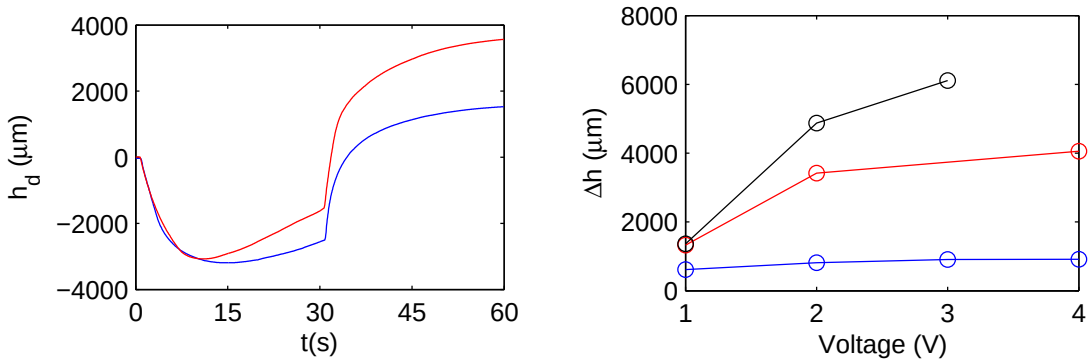

(a) DC actuation

(b) AC actuation

Figure E.10: (a): Response of a cantilevered IPMC strip to 2 V (blue) and 2.5 V (red) DC excitations. (b): Response of the IPMC to sine wave voltage signals at 0.05 Hz (black), 0.1 Hz (red), and 0.5 Hz (blue) over a range of input voltages

in several studies including Shahinpoor and Kim [2001]. Surprisingly, the actuation at low frequency (0.05 Hz) shows an even larger displacement than observed using DC actuation. This could be due to the difference in input (i.e., square wave input for the DC excitation and sine wave input for the AC excitation). As the mechanism for deformation is the transport of ions and water to the surface, for a DC excitation, the water is quickly accelerated toward the surface, and over a long period of time, may relax back and reduce the maximum achievable deformation. For the AC excitation, thought, the transport is more gradual and may lead to more fluid being transported to the surface when operated at low frequencies.

The peak-to-peak tip displacement with a 3 V, 0.5 Hz input was 0.9 mm. This matches well with Kim et al. [2006] who showed a displacement ranging from 0.75 to 1.25 mm over the first couple hundred cycles with the same voltage input. These experiments were performed with a 40 x 5 x 0.7 mm strip, which is nearly double the thickness of the IPMC strip used here, and thus one would expect a higher deflection for the present measurements. Again, noting the difference between the no-load and actual voltage across the IPMC, the actual voltage applied was smaller than Kim et al. [2006] and thus having a similar tip displacement seems reasonable.

E.4 Actuation of a rigidly bonded IPMC surface

Two different types of mechanisms were investigated for producing a dynamic roughness. In this section, a surface was selectively bonded to a substrate using a rigid conductive epoxy. In this setup, unbonded parts of the surface are free to actuate and any desired pattern can be formed by selectively adhering different parts of the surface. This actuation mechanism is similar to the actuation of a cantilevered sample in that it relies on stresses formed due to water and cation transport to cause

Figure E.11: The delaminated region of an otherwise rigidly bonded sheet of IPMC

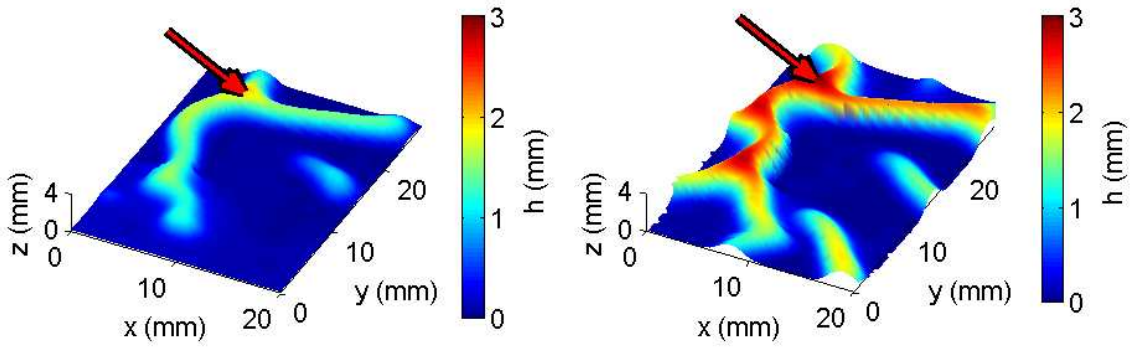

(a) Before testing

(b) After testing

Figure E.12: Scans of the static debonded region shown in Fig. E.11 are shown before testing in (a) and after testing in (b). The measurement location is indicated by the red arrow.

the surface to bend or bulge.

In the current experiments, this sort of dynamic roughness was studied on a delaminated portion of an otherwise rigidly bonded IPMC, where the setup was described in Section E.2.4. A photograph of the delaminated portion of the surface is provided in Fig. E.11. The deformation of this region was investigated under varying voltage inputs and various hydration conditions.

One of the major issues with using this sort of actuation mechanism was ensuring that the surface remained bonded over time. Using the laser scanning system, the surface shape was measured before and after all tests had been performed; the scans are shown in Fig. E.12. A change is noted in the shape and amplitude of the debonded region after the tests had been run. By limiting the range of actuation amplitudes, it is expected that further delamination could be prevented.

The bumps observed on the surface appeared once the surface was hydrated or actuated. The surface would relax back to a flat state after sitting for several hours. Running a voltage across the surface would quicken this relaxation by drying out the surface. After running all of the tests to be described, the surface no longer completely relaxed to a flat state, likely due to plastic deformation

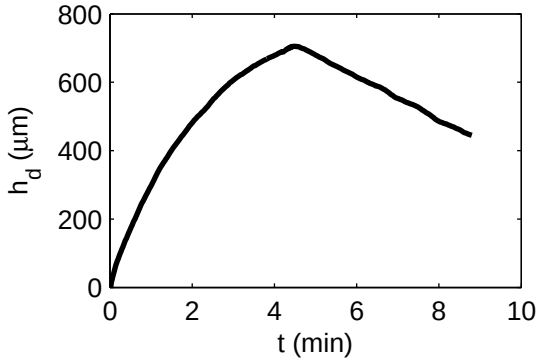

Figure E.13: The movement of the marked region in Fig. E.12 after hydrating the surface

of the surface. With a roughness such as this, the actuation amplitude should also be limited to prevent this irreversible deformation.

E.4.1 Hydration

Fig. E.13 shows the change in height of the corner of the bump marked with a red arrow in Fig. E.12a after hydrating the surface. In this set of measurements, deionized water was spread evenly over the entire surface using a foam brush and the change in the surface with no voltage applied was measured for 9 min. As the IPMC absorbed the water on the surface, the amplitude of the detached region grew at a rate near 5 μm/s and decreased to about 1 μm/s after some time. Once dry, the detached region started to shrink at a rate of about 1 μm/s. This growth with water absorption was expected as the IPMC was attached to the base electrode in a completely dry state, and thus any absorption of water will produce a stress that is relieved by deforming the surface.

In order to reduce the effect of hydration on measurements of the actuating surface, it was decided to wait until the surface appeared fully dry before running any tests. This would assure that the growth rate would be minimal and bounded by $dh/dt = \pm 1$ μm/s.

E.4.2 DC actuation

As with the cantilevered IPMC strips, actuation of the debonded region was studied under a DC voltage excitation. This would be useful for producing an "on/off" type of roughness that would either be continually activated or deactivated. In addition, it provides a means to determine the voltage that must be applied to offset the decrease in the roughness height due to dehydration for this particular case. Tests were run varying the voltage, the direction of the applied voltage, either "positive" where the top surface was the cathode or "negative" where the bottom surface was the cathode, and the surface hydration, either wet with a growth rate of 1 μm/s or dry with a decreasing amplitude at -1 μm/s. In these tests, a DC voltage was instantaneously applied across the IPMC

Voltage (V)	Voltage direction	Hydration	x_{90}	$\Delta h_{rise}(\mu\text{m})$	$\Delta h_{fall}(\mu\text{m})$
1	Positive	Wet	0.75	-17.8	4.4
2	Positive	Wet	0.93	216.4	128.2
3	Positive	Wet	0.84	387.0	172.4
3	Positive	Dry	0.65	851.4	-149.9
3.5	Positive	Dry	0.68	1309.3	-297.7
4	Positive	Dry	0.67	786.6	-121.8
4	Positive	Dry	0.87	824.5	-258.9
3.5	Negative	Wet	0.67	2309.7	-733.6
1	Negative	Dry	0.87	-7.6	-39.5
2	Negative	Dry	0.82	-144.5	-112.3
3.5	Negative	Dry	0.76	1778.7	-401.5
3.5 (#1)	Negative	Dry	0.71	1766.0	-622.1
3.5 (#2)	Negative	Dry	0.79	1549.9	-623.9
3.5 (#3)	Negative	Dry	0.82	1362.9	-666.3

Table E.2: Surface response to varying voltages and surface hydration. The first set of data are for positive voltages, the second set for negative voltages, and the final set for 3 tests run consecutively without rehydrating the surface.

and held for 30 sec (rising portion). Then the voltage was turned off and the sample was allowed to relax for 30 sec (falling portion). The results are summarized in Table E.2. In the table, x_{90} is the fraction of the rise time (30 sec total) for the roughness to reach 90% of its peak value. Δh_{rise} and Δh_{fall} are the change in the roughness height during the 30 sec the voltage was applied and the 30 sec after the voltage was removed, respectively.

While far from complete, the following statements can be made:

1. For a positive voltage on a wet surface, increasing the voltage increases Δh_{rise} and Δh_{fall} with no trend in x_{90}.

2. For a positive voltage on a dry surface, increasing the voltage shows no trend in Δh_{rise} nor Δh_{fall} and x_{90} is similar in all cases.

3. For a negative voltage on a dry surface, increasing the voltage increases Δh_{rise} and Δh_{fall}, with the Δh_{rise} becoming positive for large enough voltages (above 2 V) and decreases x_{90}.

4. For a given positive voltage, a wet surface has a smaller Δh_{rise} a larger Δh_{fall} that is positive, and a larger x_{90} as compared to a comparable dry surface.

5. For a given negative voltage, a wet surface has a larger Δh_{rise} and Δh_{fall} and a smaller x_{90} as compared to a comparable dry surface.

6. For a dry surface, a positive voltage has a smaller Δh_{rise}, Δh_{fall}, and x_{90} when compared to a negative applied voltage of the same magnitude.

From these statements, it appears that for a dry IPMC, the form easiest to maintain in experiments, a negative applied voltage (pulling cations and water to the base electrode) leads to a larger

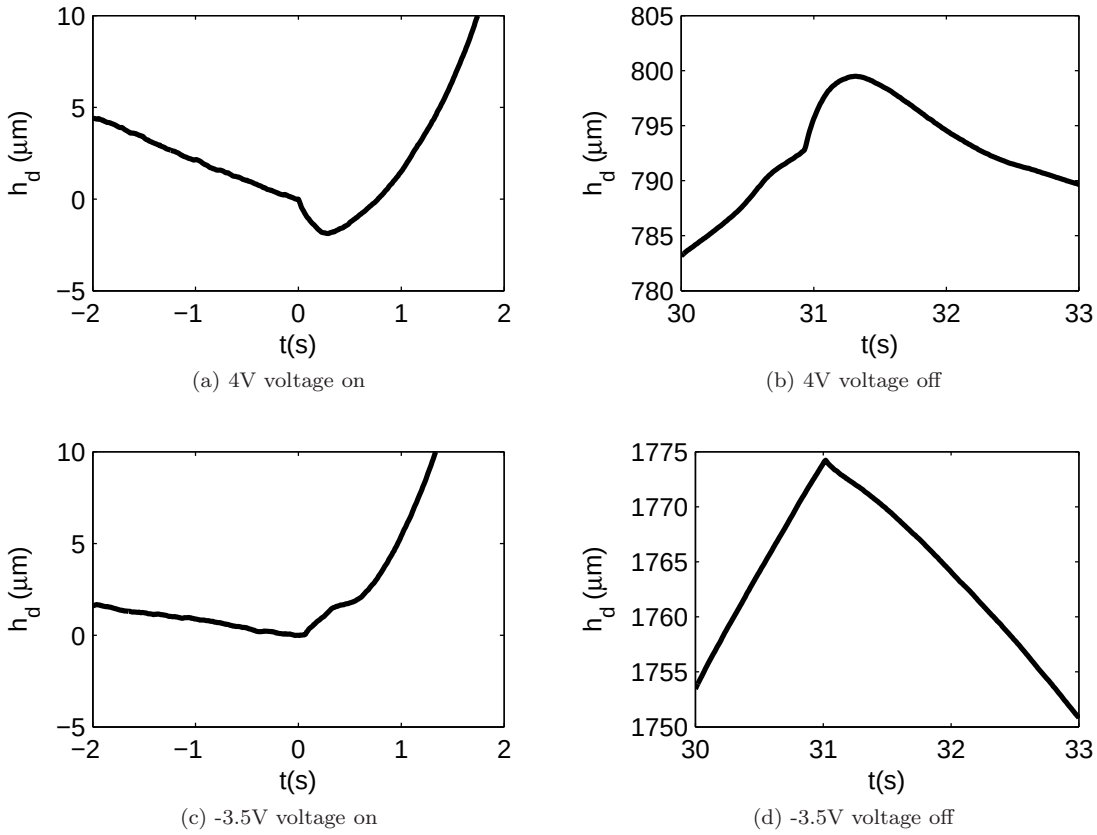

(a) 4V voltage on

(b) 4V voltage off

(c) -3.5V voltage on

(d) -3.5V voltage off

Figure E.14: The startup and shutdown response of the IPMC for positive and negative applied voltages

roughness amplitude, which is preferred. In addition, for a dry surface with a negative voltage, the change in amplitude clearly increases with voltage while this trend is not clear when applying a positive voltage. It should be noted thought, that at a fixed negative voltage, performance tends to be improved if a the surface is wet. Regardless, running with a negative DC voltage and a dry surface produces large amplitudes in a controlled manner.

The fact that both positive and negative voltages cause the surface to grow seems counterintuitive so the mechanism for this growth is investigated. Nemat-Nasser and Wu [2003] noted that when a DC voltage is applied to a cantilevered IPMC, it quickly bends toward the anode followed by a slow relaxation toward the cathode. That is, the initial movement is opposite the direction expected. This is observed in the height traces Fig. E.14 showing the height right when the voltage is applied and removed. For the positive case, there is a sharp overshoot in the amplitude in the direction opposite of the subsequent growth (or decay); toward the anode. On the other hand, this overshoot is not seen for a negative applied voltage and, if anything, shows a quick rise in the direction of subsequent movement as in Fig. E.14c, which would be in the direction of the anode.

While the change in direction of this sharp motion is understood when the cathode and anode

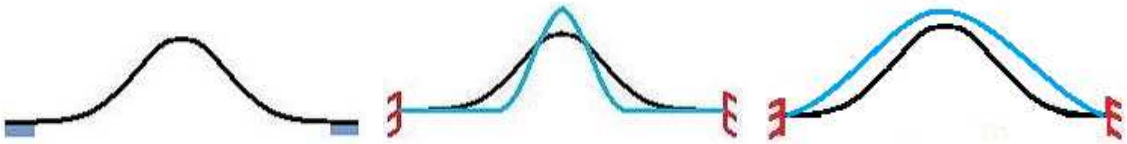

(a) Not actuated (b) Top cathode (c) Bottom cathode

Figure E.15: (a) A 2D cartoon of the delaminated IPMC surface. (b) The deformation under a positive voltage (top surface is the cathode). (c) The deformation under a negative voltage (bottom surface is the cathode). Black: unactuated, blue: actuated

are switched, the reason for a long-term increase in the roughness amplitude with both polarities is not immediately obvious. To help understand this, the following simple model is proposed.

In a cantilevered configuration, the application of a voltage across the IPMC causes a migration of cations from the anode to the cathode. This causes a compression on the anode side (due to a lack of ions and solvent/water) and an expansion on the cathode side (due to an increase in solvent/water), which causes a bending toward the anode as described in Shahinpoor and Kim [2001]. In the case of different constraints, such as the constrained configuration analyzed here, different results can be expected.

For simplicity, consider a 2D delaminated region forming a bump as shown in Fig. E.15a. Suppose that the bottom surface (nearest the substrate) is the anode and the top surface is the cathode (the positive configuration). When a voltage is applied (and ignoring the quick movement toward the anode at short times), ions will migrate across the thickness of the IPMC potentially causing an expansion of the cathode side and a compression of the anode side. The constraints prevent the top surface from expanding while the bottom surface contracts. The same goes for the opposite polarity case where the bottom will want to expand and the top will want to compress. Therefore, there must be a change in topology, which is dependent on the constraints.

First consider the case where the bump is firmly attached at its base so that it is essentially cantilevered on both ends. Then the topology shown in Figs. E.15b and E.15c may arise knowing that the IPMC will want to curl toward the anode, both of which result in a growing roughness height. It is likely that there is a minimum driving force (in this case voltage applied) to develop into these new shapes and grow vertically, hence there is a minimum voltage required for a dry surface with a negative voltage applied to grow upwards as supported by the results in Table E.2.

E.4.3 AC actuation

In addition to DC actuation, tests were run with AC signals to see if it would be feasible to oscillate a detached region dynamically. For AC actuation, both sine and square wave inputs were used. It was found that for the same peak-to-peak voltage, a square wave produced a larger change in the roughness amplitude than a sine wave. For example, a 3 V, 1 Hz sine wave produced an peak-to-

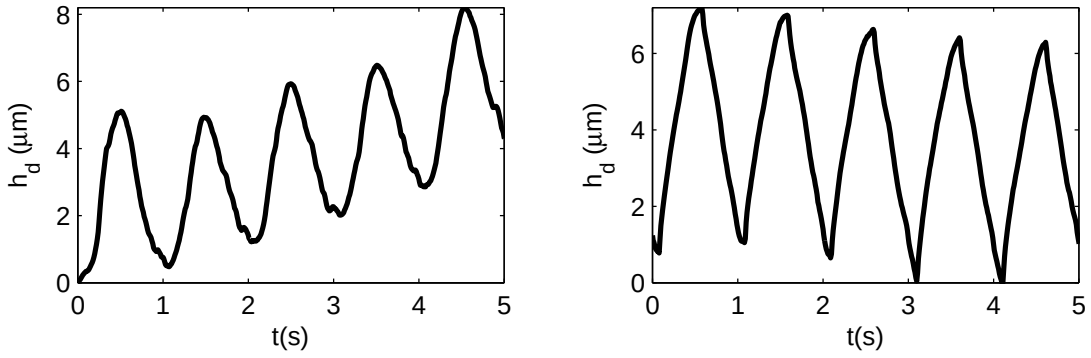

(a) Sine wave input (b) Square wave input

Figure E.16: (a): Response of the detached region to a 4 V, 1 Hz sine-wave voltage signal. (b): Response to a 3 V, 1 Hz square wave

peak amplitude of 3 μm while a square wave of the same voltage and frequency produced a 5–6 μm oscillation. The difference of response to the two input types is demonstrated in Fig. E.16 with the square wave actuation producing a triangle wave-like response.

Knowing that a negative DC voltage created a larger change in amplitude than a positive DC voltage, the amplitude of oscillation was increased by offsetting the square wave to oscillate between zero and some negative voltage. Also, by changing the duty cycle appropriately, the DC growth or decay from this offset could be removed. In the 3 V, 1 Hz case, an amplitude of 7 μm was achieved which is slightly better than for the sine or square waves alone, which produced amplitudes of 3 μm and 5–6 μm, respectively.

For lower frequency actuation large amplitudes could be obtained. With a 3.5 V, 0.25 Hz square wave with a 30% duty cycle, an amplitude of 180 μm was achieved as shown in Fig. E.17. It is important to note, though, that it took several cycles before this maximum amplitude was achieved. A similar phenomenon was noted by Kim et al. [2006] with cantilevered IPMC specimens. They note that this "time delay to reach the peak value of displacement" occurs because an IPMC specimen fully saturated with water does not actuate the best; the sample needs to lose water (through evaporation or hydrolysis during actuation) to reach some level where it will displace by an optimal amount. That is, having an IPMC membrane completely saturated with water makes it difficult for the surface to deform. By losing a little bit of this water, a balance is formed between the stiffness of the membrance and the force generated by water transport.

A compilation of the effects of the hydration, voltage level, and duty cycle are provided in Section E.4.4 for further review. Overall, a large magnitude oscillation is feasible, but only at low frequencies (under 1 Hz). Frequencies above 1 Hz show amplitudes on the order of 10 μm. This is much like a cantilevered IPMC sample where increasing the frequency decreases the achievable amplitude.

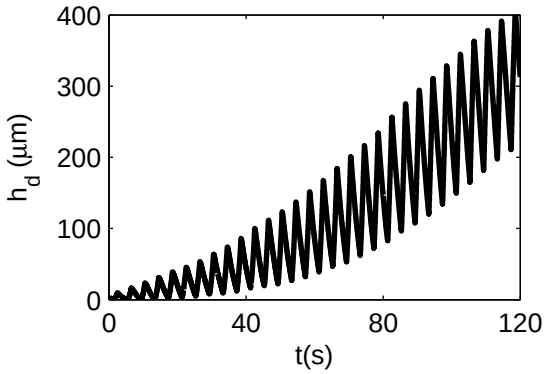

Figure E.17: Response of the detached region of the IPMC to a 30% duty cycle 0.25 Hz square-wave voltage input between 0 and -3.5 V

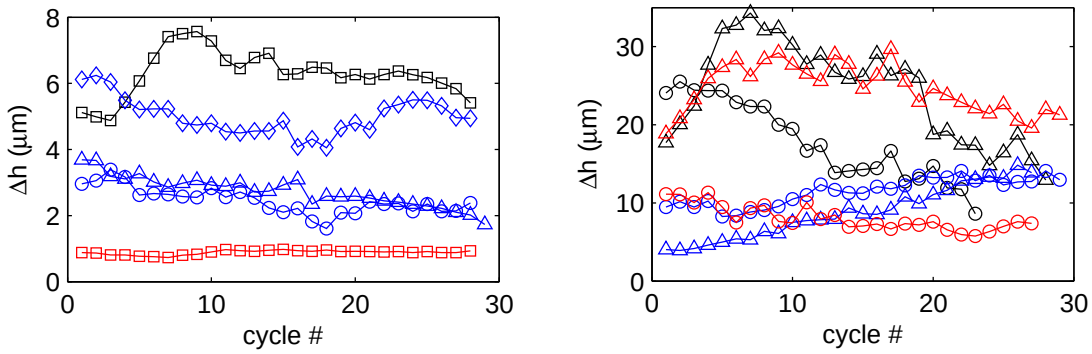

(a) Sine waves with no DC offset

(b) Square waves with no DC offset

Figure E.18: (a): IPMC response to sinusoidal inputs. Blue ○: 3.5 V, 1 Hz input with a dry surface, blue △: 4 V, 1 Hz input with a dry surface, blue ◊: 4 V, 1 Hz input with a wet surface, red □: 4 V, 10 Hz input with a dry surface, black □: 0.3 Hz, 3 V square wave with a dry surface. (b): IPMC response to different square wave inputs; two tests were run for each voltage-frequency pair indicated by the ○ and △ symbols. Black: 3.5 V, 0.25 Hz with 25% duty cycle and a dry surface, blue: same as black except the surface was wet, red: same as black except with a 50% duty cycle

E.4.4 Additional experiments

The variation in the detached roughness amplitude (as discussed in Section E.4) with time was investigated under varying input voltage excitations and varying levels of surface hydration, either allowing the surface to dry before running, labeled "dry", or hydrating the surface and running shortly after, labeled "wet". Figs. E.18a and E.18b show the roughness amplitude for sine and square wave inputs, respectively, with varying voltage and frequency. For a sine wave input, working with a "wet" surface improves the performance and acts similarly to a low frequency (0.25 Hz) square wave input. For the square wave input, though, working with a "wet" surface appears to either have no effect of decrease the performance. The change in performance with duty cycle is not conclusive from this figure, but it is important when a DC offset is applied as discussed next.

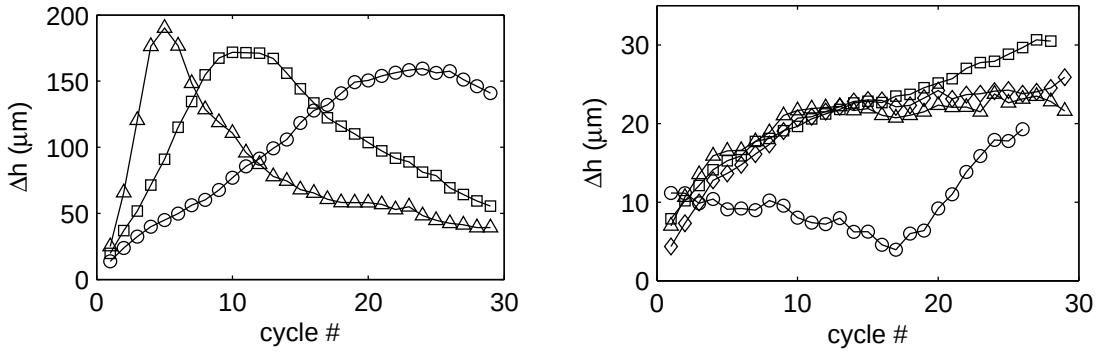

(a) Effect of duty cycle

(b) Effect of hydration

Figure E.19: (a): Effect of duty cycle on the peak-to-peak amplitude of a dry surface. The input was a 3.5 V square wave with a negative DC offset and a duty cycle of ○: 30%, □: 35%, and △: 50%. (b): Effect of hydration on peak-to-peak amplitude. The surface was hydrated and 4 consecutive sets of data were recorded without rehydrating the surface. The input was a 0.25 Hz, 3.5 V square wave with a 25% duty cycle. The symbols represent run ○: 1, □: 2, △: 3, and ◊: 4.

The effect of changing the duty cycle for a square wave input with a DC offset chosen to keep the voltage negative is presented in Fig. E.19a. This plot shows that as the duty cycle decreases, while the maximum amplitude does not change, the number of cycles to reach the maximum amplitude does. Thus using a shorter duty cycle will increase the usage time of the roughness, but it will also operate at a lower than maximum amplitude for the majority of its lifetime.

Using the same square wave input with a DC offset, the effect of the amount of hydration is presented in Fig. E.19b. From this plot, it is evident that the IPMC sample should actually be allowed to dry somewhat before operating to allow for the best actuation. Also, after hydrating once, the surface can operate for many cycles in a consistent manner.

Finally, the response to negative offset square wave inputs of varying voltage and frequency are compared in Fig. E.20a and the response to positive offset square wave inputs are compared in Fig. E.20b. From both sets of measurements, it is apparent that unless the frequency is low (even lower than 1 Hz), the actuation will be small. By comparing the two figures it is also apparent that the negative DC offset leads to a larger roughness amplitude as expected. In this case, the maximum amplitude is about 4 times larger than when using a positive DC offset.

E.5 Actuation of a nonrigidly bonded IPMC surface

In this section, the actuation of the IPMC using the setup described in Section E.2.5 will be discussed. First, the roughness and surface condition of the unactuated IPMC will be reviewed. This is followed by a presentation of quantitative measures of the surface actuation using the laser displacement system as well a qualitative view of the surface deformation offered by movies taken under a

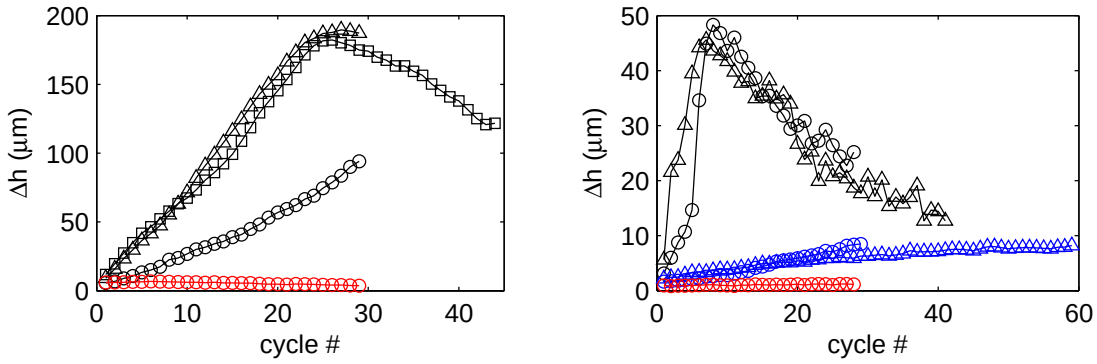

(a) Negative DC offset

(b) Positive DC offset

Figure E.20: (a): IPMC peak-to-peak amplitude response to a square wave input with a negative DC offset. Black: 3.5 V, 0.25 Hz square wave with a 30% duty cycle (○: first run), red: same as black except with a 1 Hz input. (b): IPMC peak-to-peak amplitude response to a square wave input with a positive DC offset. Black: 3.5 V, 0.25 Hz square wave with a 30% duty, blue: same as black, but with a 1 Hz input, red: same as black except a sine wave with no DC offset

Sample Label	Initial Surface	$h_t(\mu\text{m})$	$h_e(\mu\text{m})$	H	$k_{avg}(\mu\text{m})$	$s_{avg}(\mu\text{m})$
A	Rough	300	5	58	5.77	35.02
B	Rough	300	18	15	5.38	38.39
C	Smooth	170	10	15	11.33	41.31
D	Smooth	300	5	58	8.15	37.89
E	Smooth	300	18	15	10.87	34.06
F	Smooth	300	30	8	11.37	39.77

Table E.3: Static roughness parameters for different IPMC samples

microscope.

E.5.1 Static roughness

In this section, several different IPMC samples are considered, each with different properties including the initial roughness of the ion-exchange membrane, electrode thickness, and ion-exchange polymer thickness as summarized in Table E.3. This table lists the initial surface treatment (either smooth: no treatment, or rough: sanded with A400 sandpaper with an average particle size of 23.6 μm before depositing the electrode), the total IPMC thickness (h_t), the electrode thickness (h_e), and the parameter H, the ratio of the ion-exchange polymer thickness (defined as $h_t - 2h_e$) to the electrode thickness, h. Average measurements of the roughness height, k_{avg}, and element spacing, s_{avg}, are included and will be discussed below. The roughness height is defined as the height difference between a peak and the average height or the surrounding valleys. The element spacing is defined as the distance between consecutive peaks or valleys. As noted in Section E.2.6, the displacement sensor takes an average over the laser spot size of 30 μm so an underestimation of the height should be expected.

The average roughness height and spacing were extracted from a 200 μm long line scan along the surface. Due to the small roughness height, 40 measurements were taken at each point and averaged to help reduce the effects of noise. In addition, measurements were taken at 5–8 different locations to best characterize the mean static roughness. In order to calculate the roughness height and spacing, a peak finding method was used to capture the peaks and valleys.

In addition to these 1D scans for quick characterization of the surface, full 2D scans of the surface were taken to investigate the 3-dimensional shape of the roughness and gain insight into how the roughness was formed. These scans were performed over a 0.1 x 0.1 mm region and are presented in Fig. E.21. All of these measurements were taken with the IPMC in the constraint system described in Section E.2.5.

Images of the surface were taken under high magnification as well to gain further insight into the surface topology. Figs. E.22a and E.22b show one rough and one smooth sample, respectively. These images were taken using a Keyence VK-9700 color 3D laser scanning microscope[1]. While the rough surface looks as might be expected, the smooth surface is not completely smooth, but contains a number of cracks along the surface. This is why roughness is measured on the smooth surface and the deep cracks would explain why the roughness amplitude is higher for smooth surfaces.

Whether the smooth surface cracks or not depends on the thickness of the top electrode. This is verified in Fig. E.23 where smooth surface IPMC samples with thin and thick electrodes are compared using the microscope system described in Section E.2.7. On a macroscopic level the thin electrode surface appeared to have a mirror finish while the thick electrode surface looked frosty.

One other interesting feature of the smooth surface IPMC was a wrinkling that occurred when the surface was constrained and hydrated. This feature could not be obtained when debonding and rebonding the surface, but is shown in Fig. E.24. Perhaps this is a case where the thin electrode surface did buckle which was the expected mechanism for the dynamic actuation of the IPMC surface as discussed in Section E.1.

E.5.2 Dynamic roughness

In this section several aspects of the dynamic roughness are investigated. These include the change in roughness height with voltage and frequency, the repeatability of roughness actuation, the hydration needs of the surface, and finally the possibility of storing the actuator after use. The setup is shown in Fig. E.3.

Taking high-speed movies, the local variation of the surface can be viewed as shown in Fig. E.25. In this figure, two images are shown separated by half of the actuation cycle. When the top surface is acting as the anode, several black “holes” are seen on the surface, but when the top surface becomes the cathode, these “holes” are not observed. These “holes” are likely valleys in the surface

[1]Thanks to Michael Graham at Keyence for taking these preliminary images

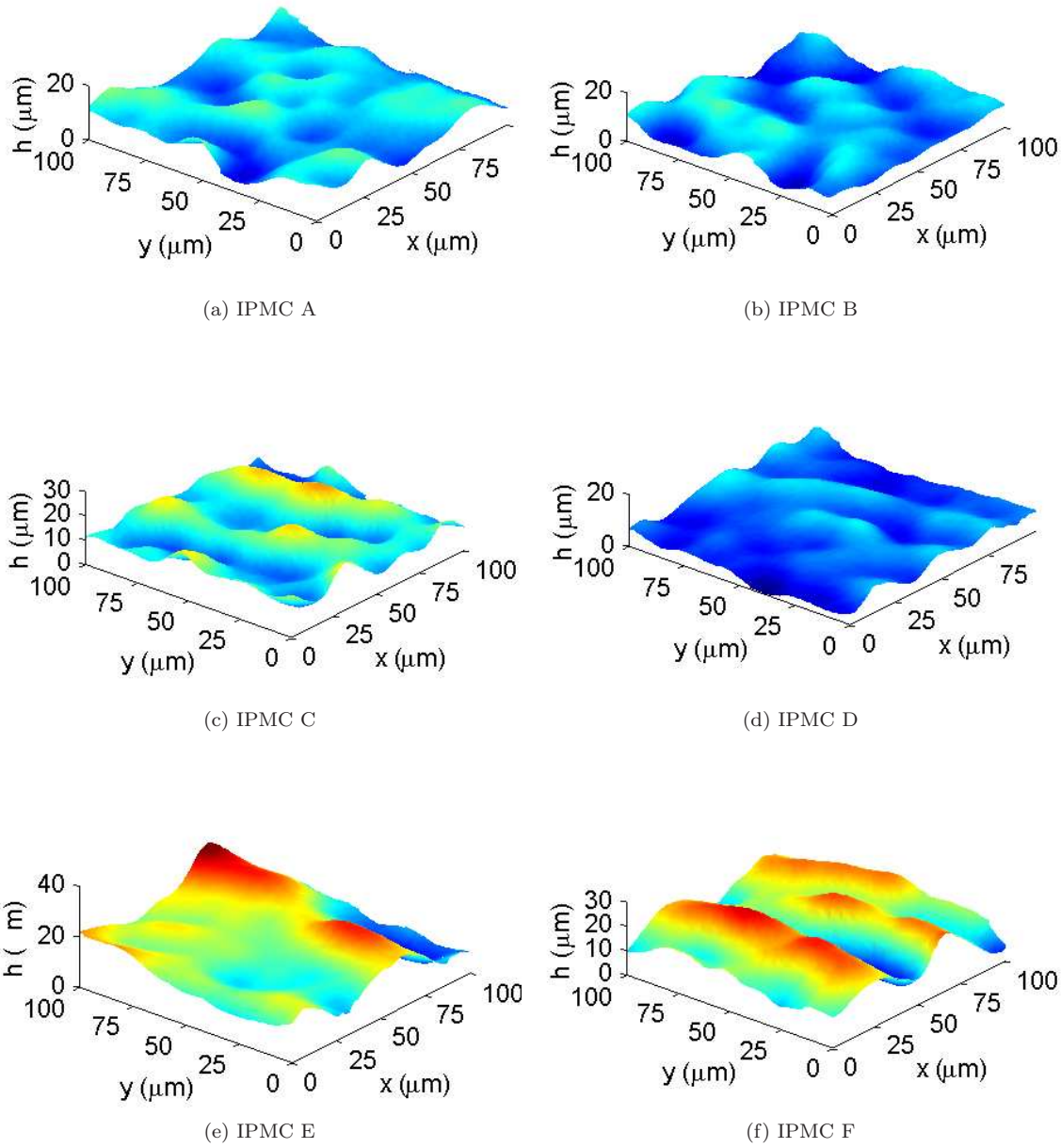

(a) IPMC A

(b) IPMC B

(c) IPMC C

(d) IPMC D

(e) IPMC E

(f) IPMC F

Figure E.21: Measurements of the static surface roughness over a 0.1×0.1 mm section of each of the IPMC samples. The colors range from 0 (blue) to 30 μm (red) in each image.

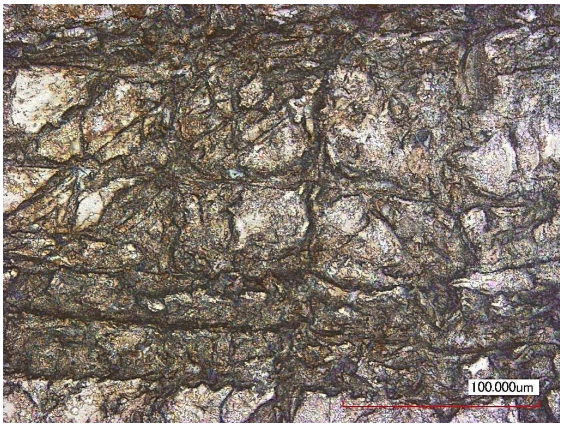

(a) Rough surface IPMC sample

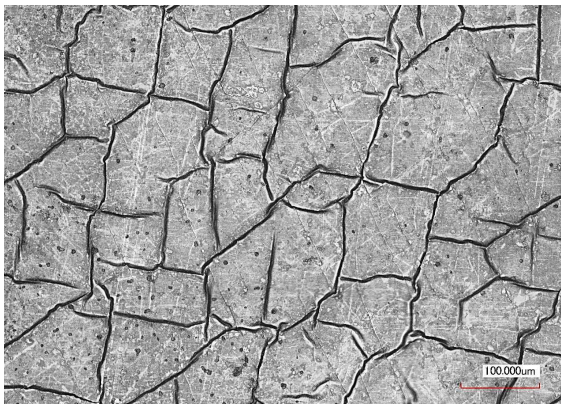

(b) Smooth surface IPMC sample

Figure E.22: Microscope images of representative (a): rough and (b): smooth IPMC surfaces. A scale is provided in the inset of each image.

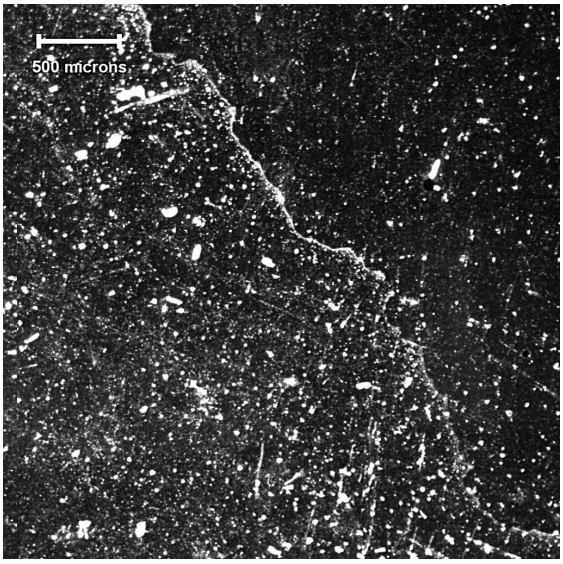

(a) Thin electrode

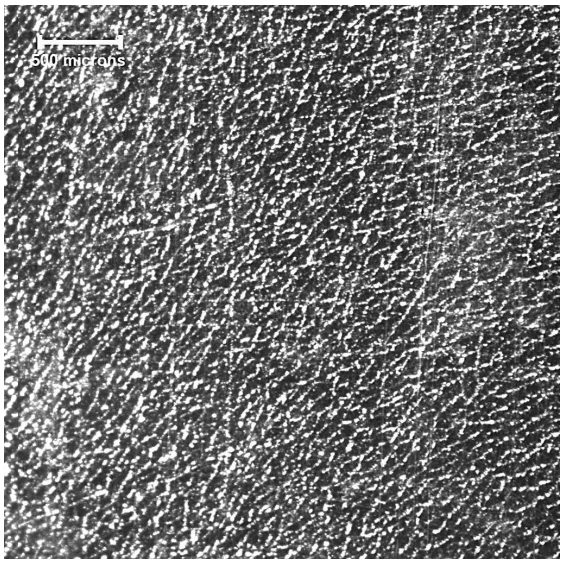

(b) Thick electrode

Figure E.23: Images of the surface of smooth IPMC samples with (a): a thin top electrode; sample D and (b) a thick top electrode; sample F. A scale is provided in the inset of each figure.

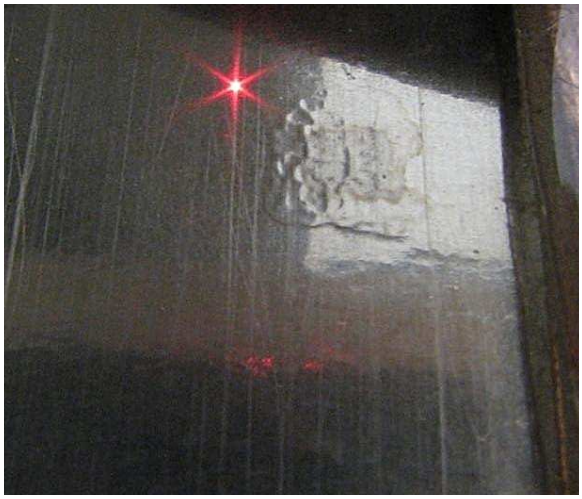

Figure E.24: The wrinkling of the smooth IPMC sample (sample D) is observed in the upper-right-hand corner of the image.

shielded from the light source by peaks in the roughness. When the surface topology changes during actuation these valleys likely rise up and thus the shadow cast by the surrounding peaks disappears. By moving the light source, these "holes" are no longer observed and regions that appear to be out of focus are viewed instead, leading the the interpretation of these regions as valleys below the focal plane of the microscope. Thus, the actuation viewed in the following experiments is likely linked with the movement of material in the valleys between static roughness elements.

E.5.2.1 Response to changes in voltage and frequency

In order to measure the effects of changes in voltage and frequency on the dynamic roughness performance, actuating portions of the surface were identified by a preliminary scan. It is not known exactly why only certain parts of the surface appeared to actuate, but it was expected that certain regions probably formed a better bond than others due to better electrical contact that may be linked to the distribution of the conductive gel. To identify actuating regions, 100 μm long line scans were performed in 2 μm steps near regions that appeared to be actuating (identified visually by a color change in the surface when actuated). During these scans the surface was actuated by a 2 V, 1 Hz square wave and measurements of the surface height were taken over 5 oscillation cycles at a rate of 40 measurements per cycle.

After scanning along a portion of the surface, oscillating regions were identified using the following steps. First, the mean amplitude in time was subtracted from each measurement location. Next, the FFT of the data was taken in time at each point and a band pass filter was used to extract information near the actuation frequency. Then, the inverse Fourier transform of the data was calculated. Finally, this filtered data was analyzed at each location and actuating regions were defined as regions where the maxima and minima were found at fixed intervals in time and consecutive maxima and minima

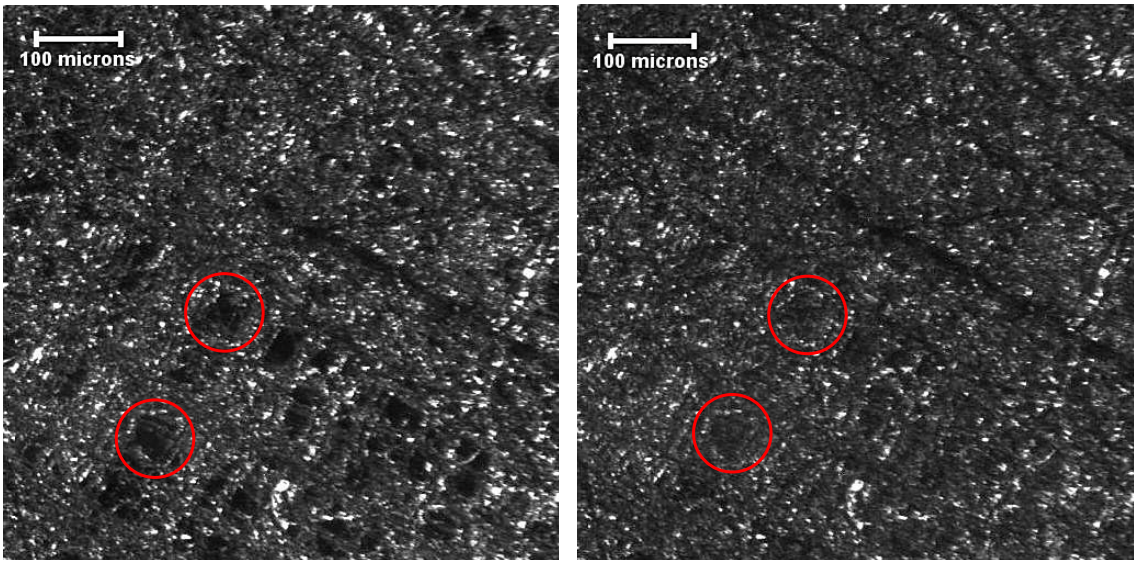

(a) Surface is positively charged (anode) (b) Surface is negatively charged (cathode)

Figure E.25: (a): Photograph of the IPMC when the surface is positively charged (anode). (b): Photograph of the IPMC when the surface is negatively charged (cathode) and attracting cations and water toward the surface. Two of the "holes" are circled in (a), and the corresponding regions without holes are circled in (b).

were separated by half a cycle.

The rms difference between the original signal and the filtered signal was about 0.9 μm, and thus the signal to noise ratio was low, of order 1 for input signals less than 2 V or higher than 10 Hz. After testing many samples it was found that while actuation was viewed on the roughened samples (e.g., IPMC samples A and B), actuation was not visible on smooth samples (e.g., IPMC samples C-F). For the smooth samples, the surface tended to delaminate from the base electrode, and thus no dynamic roughness was formed. Neither changing the conductive gel nor trying to improve the bonding method helped.

When a region of actuation was identified, measurements were taken at a point of maximum actuation for 200 cycles at a rate of 40 samples/cycle for a range of voltages and frequencies. The IPMC surface was rehydrated between each measurement to assure consistent actuation. Also, measurements were repeated after running through each voltage-frequency pair to ensure repeatability. The results are compiled in the contour plot in Fig. E.26 and show a power law decay in amplitude with increasing frequency and an exponential growth of amplitude with increasing voltage. The maximum deformation of 2.5 μm was at 4 V and 1 Hz, the lowest frequency and highest voltage tested.

Overall, the amplitude was relatively small, and showed trends similar to the delaminated roughness. Thus, while the surface could be actuated quickly, the amplitude was so small as to be unusable as a dynamic roughness in wind tunnel experiments.

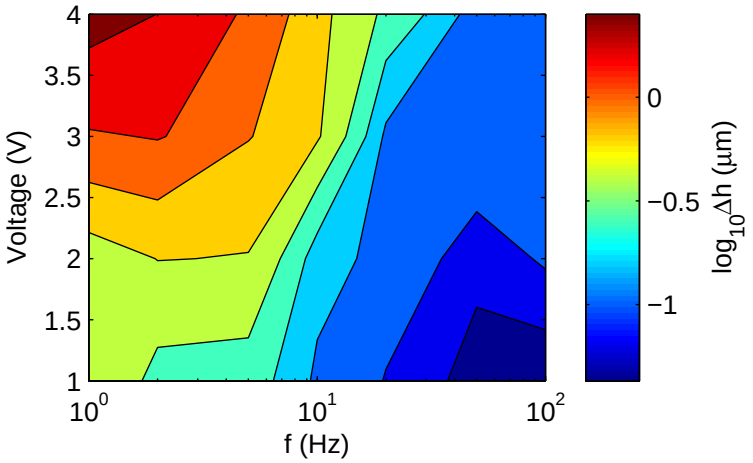

Figure E.26: Contour plot of the log of the roughness amplitude for each voltage-frequency pair

E.5.2.2 Repeatability

The repeatability of actuation was tested in several ways. To assure that the IPMC surface remained constrained in the same way between tests, scans were performed before and after actuation to assure that the surface returned to its original state. When running tests without rehydrating the surface between tests, the surface would return to, or near, its original state in all cases with an rms error of 0.85 μm. When rehydrating the surface before runs, the pre-run surface shape was different every time, but at the end of the tests, the surfaces always relaxed back to the same shape, again with an rms error around 1μm. The change in the shape of the surface before the run was likely due to varied levels of hydration, and thus varied swelling of the membrane.

It was also noted that the mean height of the actuating surface closely matched the shape of the relaxed surface. Only minor deviations were noted at the start of the measurement where the surface was hydrated. This helps to further validate the repeatability of actuation.

Consistent actuation was also assured by performing dynamic measurements over the same area several times to assure that actuation was always observed at the same locations. This was also done using the microscope system where regions of actuation were identified during each run (by looking for a appreciable change in brightness), and these actuating regions were compared visually between consecutive runs. Actuation was found to occur in the same region between runs, although the level of actuation decreased with time. By increasing the voltage input, actuation was once again viewed in these regions.

E.5.2.3 Hydration and surface storage

The hydration needs of the IPMC were evaluated by monitoring the actuation of a single point on the surface over a long time period at different voltages and frequencies. By observing the change

in the roughness height over time, the dehydration of the sample could be evaluated. Some initial measurements were used to verify that the roughness amplitude did not vary significantly over a large number of cycles as was needed to get an accurate representation of the roughness height. More tests were run over longer time periods to understand how long a sample could be used in situ, in a wind tunnel test, for example.

Tests were run with 2, 3, and 4 V inputs with a 2 Hz frequency. Under these conditions, little change in the actuation amplitude was viewed over a 10 minute period with a 2 V input, while a decay in the amplitude was noted for the 3 and 4 V cases. For the 3 V case, the decrease was about -1.6 nm/sec and for the 4 V case, it was -3.3 nm/sec, nearly double the 3 V case. Thus, a decay in peak-to-peak amplitude is shown for voltages well above the hydrolysis limit as initially expected.

Several tests indicate that the current method of constraining the IPMC cannot keep the IPMC in an operating condition for an extended period of time. Leaving the sample unattended in the constraint system for several days, the sample no longer actuated and appeared to have delaminated from the base electrode. A method of keeping the surface moist was tested, but this too lead to poor actuation when used at a later date. While the current setup is repeatable and usable for perhaps a few hours, for long-term operation, a different method of adhesion would be necessary.

E.6 Summary

From a series of cantilevered IPMC experiments, guidelines for handling, hydrating, and storing IPMC samples were developed. In addition, measurements of the tip deflection reliably repeated measurements in the literature.

For the detached roughness discussed in Section E.4 it was found that dynamic actuation was possible around a mean roughness at low frequencies on the order of 1 Hz. The largest peak-to-peak oscillations were observed by applying a square wave voltage signal across the IPMC with a negative polarity (i.e., with voltages ranging form 0 to some voltage, -V, measured with reference to the top surface) and 30% duty cycle. Although this method appears promising, it seems that large fluctuations are only possible at large time scales. Also, the actuating part of the surface is detached, and thus may, over time, cause the attached portion of the surface to delaminate if care is not taken. As the hydration or dehydration of the surface causes the mean roughness to change it would also be important to monitor the state of hydration.

Besides these drawbacks, it may be possible to develop a dynamic roughness for low frequency actuation using this actuation mechanism by selectively adhering the IPMC to a base electrode and patterning the desired detached regions. Using this more controlled setup could potentially create a usable low frequency dynamic roughness or a way to produce an on/off type of roughness that could easily reach its desired roughness within a second or so and reach amplitudes on the order of 1mm.

For the non-rigidly bonded IPMC sample actuation discussed in Section E.5, the surface roughness of the unactuated IPMC was studied first. For the rough IPMC samples (samples A and B), the roughness on the surface appeared to be entirely due to the roughening of the surface before electrode deposition. The average height of a protrusion was about 6 μm with a 35 μm spacing between protrusions for both thin and thick electrodes. For smooth surfaces the roughness amplitude was generally 2 times greater than the rough surface. Micrographs indicate that this roughness is actually due to a cracking of the surface. Furthermore, the roughness amplitude increases with electrode thickness, further indicating that the roughness measured is a result of cracking. In both cases, the actual roughness height was likely underestimated due to the spatial averaging of the 30 μm laser spot size.

With an AC actuation, the largest amplitude oscillations were observed for input signals above 2.5 V and below 10 Hz, but even in this range, the amplitude of actuation was limited to the order of several microns. Much like the delaminated roughness, the amplitude of actuation decreased with increasing frequency and decreasing voltage input. It should also be noted that although the IPMC does actuate under a low voltage, it draws a larger amount of current, particularly when a large sheet of IPMC is used. Thus, while the voltage is low, the power consumption of the IPMC is not, drawing currents in the range of 1–5 A, leading to power consumption on the order of 10 W.

From analysis of the videos produced with the photomicrography system as well as scans of the surface, the actuation of the surface was determined to occur at the end of the up-swing in the square wave voltage input (i.e., when the top electrode has a negative charge). This indicates that the actuation was due to water and ions traveling to and deforming the top surface of the IPMC. The concentration of water and ions near the surface would cause a swelling of the polymer exchange membrane, and this swelling would reduce the local stiffness of the material as discussed by Shahinpoor and Kim [2001], thus making the surface easier to deform.

Noting that deformation was observed on rough samples only, the cause of actuation can be hypothesized. As the surface was plated by a diffusion mechanism, the surface would be uniformly coated by platinum. Near the roughness peaks, the fraction of material that is plated is high compared to in the valleys so that the peaks of the roughness were likely more stiff than the valleys. As water flowed to the surface, the more compliant valley regions likely deflected more than the peaks causing the surface morphology to change as indicated in the micrographs. Besides the isolated case of a wrinkle pattern noted on a smooth surface, there was no concrete evidence for the hypothesized buckling mechanism for surface deformation, reducing the utility of this surface as a dynamic roughness.

Using the current findings, the actuation of the IPMC will likely be improved by minimizing the electrode thickness to promote deformation of valley regions on the surface (but not so thin that the electric field is degraded far from the electrodes). Furthermore, changing the voltage

input signal may help to create a more abrupt change in surface pressure that may further deform the surface. Nonetheless, a large change in roughness height is needed. The wind tunnel where testing was planned is discussed by Jacobi and McKeon [2011]. For their set of experiments between Re_τ = 900–1200, the viscous length scale was nearly 20 μm. Thus the measured roughness oscillations on the order of 2μm would produce a roughness of size $k^+ = 0.1$, which, regardless of the conversion between the roughness height, k, and the equivalent sandgrain roughness, k_s, would not exceed the requirement of $k_s^+ > 5$ to move from being a hydrodynamically smooth surface to a transitionally rough one. Roughness on the order of 200 μm, a 100-fold increase, would be necessary to produce a reasonable disturbance to the flow.

Bibliography

R. J. Adrian. On the role of conditional averages in turbulence theory. In *Turbulence in Liquids: Proc. of the Fourth Biennial Symposium on Turbulence in Liquids*, pages 323–332. Science Press, 1977.

R. J. Adrian. Conditional eddies in isotropic turbulence. *Phys. Fluids*, 22:2065–2070, 1979.

R. J. Adrian. Statistical properties of particle image velocimetry measurement in turbulent flow. In *Laser Anemometry in Fluid Mechanics III*. LADOAN-Instituto Superior Técnico, 1988a.

R. J. Adrian. Linking correlations and structure: Stochastic estimation and conditional averaging. In *Zoran P. Zaric Memorial International Seminar on Near-Wall Turbulence*. Hemisphere, 1988b.

R. J. Adrian, C. D. Meinhart, and C. D. Tomkins. Vortex organization in the outer region of the turbulent boundary layer. *J. Fluid Mech.*, 422:1–54, 2000.

J. Andreopoulos and D. H. Wood. The response of a turbulent boundary layer to a short length of surface roughness. *J. Fluid Mech.*, 118:143–164, 1982.

B. J. Balakumar and R. J. Adrian. Large- and very-large-scale motions in channel and boundary-layer flows. *Phil. Trans. Royal Soc. A*, 365:665–681, 2007.

P. R. Bandyopadhyay and A. K. M. F. Hussain. The coupling between scales in shear flows. *Phys. Fluids*, 27:2221–2228, 1984.

Y. Bar-Cohen. *Electroactive Polymer Actuators as Artificial Muscles: Reality, Potential, and Challenges*. SPIE Press, 2004.

J. S. Bendat and A. G. Piersol. *Random data: Analysis and measurement procedures*. John Wiley and Sons, 2nd edition, 1986.

K. M. Bobba. *Robust Flow Stability: Theory, Computations and Experiments in Near Wall Turbulence*. PhD thesis, California Institute of Technology, 2004.

J. Carlier and M. Stanislas. Experimental study of eddy structures in a turbulent boundary layer using particle image velocimetry. *J. Fluid Mech.*, 535:143–188, 2005.

P. Chakraborty, S. Balachandar, and R. J. Adrian. On the relationships between local vortex identification schemes. *J. Fluid Mech*, 535:189–214, 2005.

X. Chen and J. W. Hutchinson. Herringbone buckling patterns of compressed thin films on compliant substrates. *J. Appl. Mech.*, 71:597–603, 2004.

H. Choi, P. Moin, and J. Kim. Direct numerical simulation of turbulent flow over riblets. *J. Fluid Mech.*, 255:503–539, 1993.

M.S. Chong, A. E. Perry, and B. J. Cantwell. A general classification of three-dimensional flow fields. *Phys. Fluids A*, 2(5):765–777, 1990.

K. T. Christensen and R. J. Adrian. Statistical evidence of hairpin vortex packets in wall turbulence. *J. Fluid Mech.*, 431:433–443, 2001.

D. Chung and B. J. McKeon. Large-eddy simulation of large-scale structures in long channel flow. *J. Fluid Mech.*, 661:341–364, 2010.

F. H. Clauser. The turbulent boundary layer. *Adv. Appl. Mech.*, 4:1–51, 1956.

D. Coles. The law of the wake in the turbulent boundary layer. *J. Fluid Mech*, 1:191–226, 1956.

D. B. DeGraaff and J. K. Eaton. Reynolds-number scaling of the flat-plate turbulent boundary layer. *J. Fluid Mech*, 422:319–346, 2000.

J. C. del Álamo and J. Jiménez. Estimation of turbulent convection velocities and corrections to Taylor's approximation. *J. Fluid Mech.*, 640:5–26, 2009.

D. J. C. Dennis and T. B. Nickels. On the limitations of Taylor's hypothesis in constructing long structures in a turbulent boundary layer. *J. Fluid Mech.*, 614:197–206, 2008.

D. J. C. Dennis and T. B. Nickels. Experimental measurement of large-scale three-dimensional structures in a turbulent boundary layer. Part 2. Long structures. *J. Fluid Mech.*, 673:218–244, 2011.

V. Efros and P. -Å Krogstad. Development of a turbulent boundary layer after a step from smooth to rough surface. *Exp. Fluids*, 51:1563–1575, 2011.

E. T. Enikov and G. S. Seo. Analysis of water and proton fluxes in ion-exchange polymer-metal composite (IPMC) actuators subjected to large external potentials. *Sensor Actuat. A*, 122:264–272, 2005.

L. P. Erm and P. N. Joubert. Low-Reynolds-number turbulent boundary layers. *J. Fluid Mech.*, 230:1–44, 1991.

H. H. Fernholz and P. J. Finley. The incompressible zero-pressure-gradient turbulent boundary layer: an assessment of the data. *Prog. Aerospace Sci.*, 32:245–311, 1996.

K. A. Flack, M. P. Schultz, and T. A. Shapiro. Experimental support for Townsend's Reynolds number similarity hypothesis on rough walls. *Phys. Fluids*, 17, 2005.

K. A. Flack, M. P. Schultz, and J. S. Connelly. Examination of a critical roughness height for outer layer similarity. *Phys. Fluids*, 19, 2007.

O. Flores and J. Jiménez. Effect of wall-boundary disturbances on turbulent channel flows. *J. Fluid Mech.*, 566:357–376, 2006.

J. M. Foucaut, J. Carlier, and M. Stanislas. PIV optimization for the study of turbulent flow using spectral analysis. *Meas. Sci. and Tech.*, 15:1046–1058, 2004.

B. Ganapathisubramani, E. K. Longmire, and I. Marusic. Characteristics of vortex packets in turbulent boundary layers. *J. Fluid Mech.*, 478:35–46, 2003.

B. Ganapathisubramani, E. K. Longmire, and I. Marusic. Experimental investigation of vortex properties in a turbulent boundary layer. *Phys. Fluids*, 18, 2006.

Q. Gao, C. Ortiz-Dueñas, and E. K. Longmire. Analysis of vortex populations in turbulent wall-bounded flows. *J. Fluid Mech.*, 678:87–123, 2011.

G. Gioia and M. Ortiz. Delamination of compressed thin films. *Adv. Appl. Mech.*, 33:119–192, 1997.

M. Guala, M. Metzger, and B. J. McKeon. Interactions within the turbulent boundary layer at high Reynolds number. *J. Fluid Mech.*, 666:573–604, 2011.

F. R. Hama. Boundary-layer characteristics for smooth and rough surfaces. *Trans. SNAME*, 62: 333–351, 1954.

J. Hong, J. Katz, and M. P. Schultz. Near-wall turbulence statistics and flow structures over three-dimensional roughness in a turbulent channel flow. *J. Fluid Mech.*, 667:1–37, 2011.

R. Huang and Z. Suo. Wrinkling of a compressed elastic film on a viscous layer. *J. Appl. Phys.*, 91 (3):1135–1142, 2002.

Z. Huang, W. Hong, and Z. Suo. Evolution of wrinkles in hard films on soft substrates. *Phys. Rev. E*, 70:030601–1, 2004.

Z. Y. Huang, W. Hong, and Z. Suo. Nonlinear analyses of wrinkles in a film bonded to a compliant substrate. *J. Mech. Phys. Solid*, 53:2101–2118, 2005.

J. C. R. Hunt, A. A. Wray, and P. Moin. Eddies, stream, and convergence zones in turbulent flows. *Center for Turbulence Research Report*, CTR-S88:193–208, 1988.

N. Hutchins and I. Marusic. Large-scale influences in near-wall turbulence. *Phil. Trans. Royal Soc. A*, 365:647–664, 2007.

N. Hutchins, T. B. Nickels, I. Marusic, and M. S. Chong. Hot-wire spatial resolution issues in wall-bounded turbulence. *J. Fluid Mech.*, 635:103–136, 2009.

I. Jacobi and B. J. McKeon. Dynamic roughness perturbation of a turbulent boundary layer. *J. Fluid Mech.*, 668:258–296, 2011.

I. Jacobi, M. Guala, and B. J. McKeon. Characteristics of a turbulent boundary layer perturbed by spatially-impulsive dynamic roughness. *AIAA-2010-4474*, 2010.

J. Jeong and F. Hussain. On the identification of a vortex. *J. Fluid Mech.*, 285:69–94, 1995.

J. Jiménez. Turbulent flows over rough walls. *Annu. Rev. Fluid Mech.*, 36:173–196, 2004.

J. Jiménez, J. C. del Álamo, and O. Flores. The large-scale dynamics of near-wall turbulence. *J. Fluid Mech.*, 505:179–199, 2004.

R. D. Keane and R. J. Adrian. Optimisation of particle image velocimeters - Part I: double pulsed systems. *Meas. Sci. Technol.*, 1:1202–1215, 1990.

C. Kim. *Reduction of the Skin Friction Drag Using Transverse Cavities*. PhD thesis, Seoul National University, 2006.

J. Kim and F. Hussain. Propagation velocity of perturbations in turbulent channel flow. *Phys. Fluids A*, 5(3):695–706, 1993.

K. C. Kim and R. J. Adrian. Very large-scale motion in the outer layer. *Phys. Fluids*, 11(2):417–422, 1999.

K. J. Kim and M. Shahinpoor. A novel method of manufacturing three-dimensional ionic polymer-metal composites (IPMCs) biomimetic sensors, actuators and artificial muscles. *Polymer*, 43: 797–802, 2002.

K. J. Kim and M. Shahinpoor. Ionic polymer-metal composites: II. Manufacturing techniques. *Smart Mater. Struct.*, 12:65–79, 2003.

S. J. Kim, I. T. Lee, H.-Y. Lee, and Y. H. Kim. Performance improvement of an ionic polymer-metal composite actuator by parylene thin film coating. *Smart Mater. Struct.*, 15:1540–1546, 2006.

P. -Å. Krogstad, J. H. Kaspersen, and S. Rimestad. Convection velocities in a turbulent boundary layer. *Phys. Fluids*, 10(4):949–957, 1998.

J. LeHew, M. Guala, and B. J. McKeon. A study of convection velocities in a zero pressure gradient turbulent boundary layer. *AIAA-2010-4474*, 2010.

J. LeHew, M. Guala, and B. J. McKeon. A study of the three-dimensional spectral energy distribution in a zero pressure gradient turbulent boundary layer. *Exp. Fluids*, 51(4):997–1012, 2011.

P. M. Ligrani and P. Bradshaw. Spatial resolution and measurement of turbulence in the viscous sublayer using subminiature hot-wire probes. *Exp. Fluids*, 5:407–417, 1987.

R. Mathis, N. Hutchins, and I. Marusic. Large-scale amplitude modulation of the small-scale structures in turbulent boundary layers. *J. Fluid Mech.*, 628:311–337, 2009a.

R. Mathis, J. P. Monty, N. Hutchins, and I. Marusic. Comparison of large-scale amplitude modulation in turbulent boundary layers, pipes, and channel flows. *Phys. Fluids*, 21, 2009b.

B. J. McKeon and A. S. Sharma. A critical layer model for turbulent pipe flow. *J. Fluid Mech.*, 658: 336–382, 2010.

C. Millikan. A critical discussion of turbulent flows in channels and circular tubes. In *Proc. 5th Int. Cong. Appl. Mech.*, pages 386–392. Cambridge, 1938.

J. P. Monty and M. S. Chong. Turbulent channel flow: comparison of streamwise velocity data from experiments and direct numerical simulation. *J. Fluid Mech.*, 633:461–474, 2009.

J. P. Monty, N. Hutchins, H. C. H. Ng, I. Marusic, and M. S. Chong. A comparison of turbulent pipe, channel and boundary layer flows. *J. Fluid Mech.*, 632:431–442, 2009.

J. P. Monty, J. J. Allen, K. Lien, and M. S. Chong. Modification of the large-scale features of high Reynolds number wall turbulence by passive surface obtrusions. *Exp. Fluids*, 51:1755–1763, 2011.

W. R. B. Morrison, K. J. Bullock, and R. E. Kronauer. Experimental evidence of waves in the sublayer. *J. Fluid Mech.*, 47:639–656, 1971.

H. M. Nagib and K. A. Chauhan. Variations of von Karman coefficient in canonical flows. *Phys. Fluids*, 20, 2008.

V. K. Natrajan, Y. Wu, and K. T. Christensen. Spatial signatures of retrograde spanwise vortices in wall turbulence. *J. Fluid Mech.*, 574:155–167, 2007.

S. Nemat-Nasser. Micromechanics of actuation of ionic polymer-metal composites. *J. Appl. Phys.*, 92(5):2899–2915, 2002.

S. Nemat-Nasser and J. Y. Li. Electromechanical response of ionic polymer-metal composites. *J. Appl. Phys.*, 87(7):3323–3331, 2000.

S. Nemat-Nasser and Y. Wu. Comparative experimental study of ionic polymer-metal composites with different backbone ionomers and in various cation forms. *J. Appl. Phys.*, 93(9):5255–5267, 2003.

J. Nikuradse. Stromungsgesetze in Rauhen Rohren. *VDI-Forsch*, 361, 1933. (Engl. transl. 1950. Laws of flow in rough pipes. NACA TM 1292).

A. E. Perry and J. D. Li. Experimental support for the attached-eddy hypothesis in zero-pressure-gradient turbulent boundary layers. *J. Fluid Mech.*, 218:405–438, 1990.

W. Reif. *Squamation and ecology of sharks*. Courier Forschungsinstitut Senckenberg Nr. 78, 1985.

W. Sagong, C. Kim, S. Choi, W. P. Jeon, and H. Choi. Does the sailfish skin reduce the skin friction like the shark skin? *Phys. Fluids*, 20, 2008.

A. Savitzky and M. J. E. Golay. Smoothing and differentiation of data by simplified least squares procedures. *Anal. Chem.*, 36(4):1627–1639, 1964.

M. P. Schultz and K. A. Flack. Turbulent boundary layers on a systematically varied rough wall. *Phys. Fluids*, 21, 2009.

M. Shahinpoor and K. J. Kim. The effect of surface-electrode resistance on the performance of ionic polymer-metal composite (IPMC) artificial muscles. *Smart Mater. Struct.*, 9:543–551, 2000.

M. Shahinpoor and K. J. Kim. Ionic polymer-metal composites: I. Fundamentals. *Smart Mater. Struct.*, 10:819–833, 2001.

M. Shahinpoor and K. J. Kim. Ionic polymer-metal composites: III. Modeling and simulation as biomimetic sensors, actuators, transducers, and artificial muscles. *Smart Mater. Struct.*, 13: 1362–1388, 2004.

M. Shahinpoor, Y. Bar-Cohen, J. O. Simpson, and J. Smith. Ionic polymer-metal composites (IPMCs) as biomimetic sensors, actuators and artificial muscles — a review. *Smart Mater. Struct.*, 7:R15–R30, 1998.

M. Stanislas, L. Perret, and J.-M. Foucaut. Vortical structures in the turbulent boundary layer: a possible route to a universal representation. *J. Fluid Mech.*, 602:327–382, 2008.

H. Takenaka, E. Torikai, Y. Kawami, and N. Wakabayashi. Solid polymer electrolyte water electrolysis. *Int. J. Hydrogen Energy*, 7:397–403, 1982.

G. I. Taylor. The spectrum of turbulence. *Proc. R. Soc. Lond. A*, 164:476–490, 1938.

H. Tennekes and J. L. Lumley. *A First Course in Turbulence*. The MIT Press, 1972.

T. Theodorsen. Mechanism of turbulence. In *Proc. 2nd Midwestern Conf. on Fluid Mech.* Ohio State University, 1952.

C. D. Tomkins and R. J. Adrian. Spanwise structure and scale growth in turbulent boundary layers. *J. Fluid Mech.*, 490:37–74, 2003.

C. D. Tomkins and R. J. Adrian. Energetic spanwise modes in the logarithmic layer of a turbulent boundary layer. *J. Fluid Mech.*, 545:141–162, 2005.

A. A. Townsend. *The Structure of Turbulent Shear Flows*. Cambridge Univ. Press, 2nd edition, 1976.

M. J. Walsh. Turbulent boundary layer drag reduction using riblets. In *AIAA-1982-0169*. AIAA, 1982.

M. P Wernet. Temporally resolved PIV for space-time correlations in both cold and hot jet flows. *Meas. Sci. Technol.*, 18:1387–1403, 2007.

X. Wu and P. Moin. Direct numerical simulation of turbulence in a nominally zero-pressure-gradient flat-plate boundary layer. *J. Fluid Mech.*, 630:5–41, 2009.

Y. Wu and K. T. Christensen. Population trends of spanwise vortices in wall turbulence. *J. Fluid Mech.*, 568:55–76, 2006.

Y. Wu and K. T. Christensen. Spatial structure of a turbulent boundary layer with irregular surface roughness. *J. Fluid Mech.*, 655:380–418, 2010.

Y. Yang and D. I. Pullin. Geometric study of Lagrangian and Eulerian structures in turbulent channel flow. *J. Fluid Mech.*, 674:67–92, 2011.

J. Zhou, R. J. Adrian, S. Balachandar, and T. M. Kendall. Mechanisms for generating coherent packets of haripin vortices in channel flow. *J. Fluid Mech.*, 387:353–396, 1999.